Inaugural-Dissertation

zur Erlangung der Doktorwürde

der

Naturwissenschaftlich-Mathematischen

Gesamtfakultät

der

Ruprecht-Karls-Universität
Heidelberg

Vorgelegt von

MSc Katharyn M. Fletcher

aus Boston

Tag der mündlichen Prüfung: 18. April 2016

Thema

Quantum Chemical Study of Excited State Proton Transfer in Solvated Organic Molecules

Gutachter: Prof. Dr. rer. nat. Andreas Dreuw

Prof. Dr. rer. nat. Uwe H. F. Bunz

"When you feel homesick,' he said, 'just look up. Because the moon is the same wherever you go."

- Donna Tartt, *The Goldfinch*

Zusammenfassung

Quantenchemische Methoden haben der Untersuchung angeregter Zustände in der Photochemie mittlerer bis großer organischer Moleküle zu großen Fortschritten verholfen. Insbesondere die Untersuchung sogennanter *Übergangs-* und *Differenz*-Dichtematrizen ermöglichen die Visualisierung sogennanter *Detachment/Attachment*-Dichten und *Natural Transition* Orbitalen, die angeregte Zustände kompakt beschreiben. In dieser Arbeit werden hauptsächlich die zeitabhängige Dichtefunktionaltheorie (TD-DFT) und das algebraisch-diagrammatische Konstruktionschema (ADC) des Polarisierungspropagators als Methoden verwendet. Ein Überblick über die heute verfügbaren quantenchemischen Methoden zur Berechnung angeregter Zustände wird in Kapitel 2 gegeben. Diese Methoden werden auf verschiedene molekulare Systeme angewandt, von denen jedes seine spezifischen Herausvorderungen mit sich bringt. Gemeinsam haben diese Systeme jedoch Protonentransferprozesse, die im angeregten Zustand stattfinden.

Das erste in dieser Arbeit untersuchte System ist Pigment Yellow 101 (PY101), ein kommerziell verfügbares und hoch photostabiles, fluoreszierendes Gelbpigment. Mithilfe von TD-DFT wurden relaxierte Potentialoberflächen zwischen den stabilsten Isomeren des Pigments berechnet. Es zeigte sich, dass nach Anregung in den optisch erlaubten ersten elektronisch angeregten Zustand (S_1) sowohl intramolekularer Protonentransfer (ESIPT) als auch *cis-trans* Isomerisierung möglich sind. Hierbei erlaubt ein einfaches kinetisches Ratenmodell einen ersten Einblick in die Dynamik des Systems. Für die Anwendung solch einfacher Modelle werden Informationen über die relaxierten Potentialoberflächen und Geometrien benötigt. Die Durchfürung sehr rechenintensiver zeitabhängiger quantendynamischer Simulationen ist beim aktuellen Stand der Technik noch nicht möglich für Moleküle, die größer als PY101 sind. Aus diesem Grund ist die Entwicklung solcher Modelle wichtig. Die von dem in Kapitel 3 beschriebenen Modell berechneten Ergebnisse stimmen mit zeitaufgelösten Experimenten überein. Solche Modelle sind also überraschend vielversprechend. Die Ergebnisse des Projekts über PY101 werden in Kapitel 3 präsentiert.

Der Mechanismus zum Löschen der Fluoreszenz von Benzaldehyd in Wasser ist das Hauptthema von Kapitel 4. Eine Untersuchung mithilfe von TD-DFT entlang der Protonentransferkoordinate von einem expliziten Wassermolekül zum Benzaldehyd zeigt, dass ultraschneller, strahlungsfreier Zerfall vom optisch erlaubten S_3 ($\pi\pi^*$) in den S_1 ($n\pi^*$) unmittelbar nach der Photoanregung stattfindet und dass die Dynamik sich in diesem Zustand entwickelt. Es stellte sich heraus, dass sich Benzaldehyd entlang dieser Koordinate nicht als Photobase verhält, sondern ein Wasserstoffatom des Wassermoleküls aufnimmt, woraus zwei Radikale hervorgehen. Der danach stattfindende Elektronentransfer

zum Hydroxyl-Radikal führt zur Entstehung des Hydroxid-Ions, woran sich ein Protonenrücktransfer anschließt. Die Wiederherstellung des neutralen Systems im Grundzustand wird dadurch ermöglicht. Für die Untersuchung von diesem Löschmechanismus von Benzaldehyd in Wasser wurden die *Übergangs-* und *Differenz*-Dichten und Mulliken-Analysen mithilfe von ADC(2)-s berechnet. Diese Untersuchung wurde auf chemisch ähnliche Systeme erweitert. Zum Beispiel wurde die Anzahl an aromatischen Ringen bei den untersuchten Systemen erhöht.

In Kapitel 5 werden die Eigenschaften von auf Pyranin-basierten Photosäuren mithilfe von TD-DFT untersucht. Hierbei kommen Deskriptoren für angeregte Zustände zum Einsatz, die auf exzitonischen Wellenfunktionen basieren. Gegenstand sind Zustände mit Ladungstransfercharakter von den Substituenten zum aromatischen Kern. Die stärkeren Photosäuren, welche stärker elektronenziehende Substituenten besitzen, wiesen energetisch höherliegende Ladungstransferzustände auf. Diese Zustände lagen bei den schwächeren Photosäuren ungefähr 1 eV tiefer. *Single-Point*-Rechnungen entlang der Dissoziationskoordinate von neutralen Derivaten von Pyranin zeigten die Existenz eines andersartigen Elektronentransferzustandes auf, mit einem Ladungstransfer von dem Sauerstoffatom von der Photosäure zum Wassermolekül. Dieser Zustand sinkt energetisch entlang der Dissoziationskoordinate ab und wirkt dadurch möglicherweise dem ESPT-Prozess entgegen. In einer Photosäure mit stärker elektronenziehenden Substituenten, sinkt dieser Zustand weniger steil ab. Die genauere Bestimmung der Wirkung dieser zwei sehr unterschiedlichen Ladungstransferzustände auf die Eigenschaften der Pyranin-basierten Photosäuren erfordern weitere Untersuchungen. Detaillierte Vorschläge hierzu werden am Ende von Kapitel 5 präsentiert.

Im Großen und Ganzen, erwies sich die Vielfalt der zur Untersuchung von ESPT Prozessen verwendeten quantenchemischen Methoden für die in dieser Arbeit betrachteten(behandelten) organischen Systemen als sehr effekiv. Diese Tatsache zeigt außerdem, dass durch ihre Anwendung detaliierte Informationen über die Photochemie komplexer, biologisch und industriell relevanter Moleküle gewonnen werden können.

Abstract

The development of quantum chemical methods for the study of excited states had to major advancements in the ability to investigate the photochemistry of medium-sized to large organic molecules. In particular, tools for transition and difference density matrix analysis, allowing for the visualization of detachment/attachment, and difference density plots, along with natural transition orbitals, serve as compact descriptions of the excited state. Throughout this work, time-dependent density functional theory (TD-DFT) and the algebraic diagrammatic construction (ADC) scheme for the polarization propagator were used as the primary methods of investigation. An overview of the available quantum chemical methods for the study of excited states is given in Chapter 2. Several different molecular systems were studied, each presenting their own unique challenges, but unified under the theme of excited state proton transfer processes.

Pigment Yellow 101 (PY101), a commercially available and highly photostable fluorescent yellow pigment, is the first system studied. Relaxed scans of the potential energy surfaces connecting the most stable conformers of the pigment were computed using TD-DFT. It was found that PY101 undergoes excited state intramolecular proton transfer (ESIPT) and *trans-cis* isomerization after photoexcitation to the bright first singlet electronically excited state (S_1). A simple kinetic rate model is presented for gaining a first look at the dynamics of the system, and information obtained from the potential surface scans and geometry optimizations of PY101 is used as input. Time-dependent quantum dynamics simulations are not yet feasible for systems larger than PY101, and therefore the development of such models is important. The results from the kinetic model agree well with those from time-resolved experiments, indicating that such models are promising new tools. The results of the PY101 project are presented in Chapter 3.

The fluorescence quenching behavior of benzaldehyde in water is the primary subject of Chapter 4. TD-DFT calculations along the coordinate of proton transfer from an explicit water molecule to benzaldehyde show that photoexcitation is followed by ultrafast decay from the bright S_3 ($\pi\pi^*$) state to the S_1 ($n\pi^*$) state, where the system then evolves. Along this coordinate, benzaldehyde is found to act not as a photobase but rather abstracts a hydrogen atom from the water, forming as a result a pair of radicals. Subsequent electron transfer to the hydroxyl radical, forming a hydroxide anion, is followed by proton back transfer and restoration of the initial scenario. For the elucidation of the fluorescence quenching mechanism of benzaldehyde in water, tools for detachment/attachment densities and Mulliken population analyses, as implemented for ADC, were employed. This study was then extended to chemical relatives of benzaldehyde, for example by increasing the number of aromatic rings.

In Chapter 5, the photoacidic properties of a series of pyranine-based photoacids were studied using TD-DFT and a series of excited state descriptors based on the exciton wave function. Stronger photoacids exhibit higher lying states of charge transfer character from the substituents to the core, while these states are lower lying by about 1 eV in the weaker photoacids of the series. The stronger photoacids are characterized by more strongly electron-withdrawing substituents. In addition, single point calculations along the dissociation coordinate of neutral derivatives of pyranine reveals a second type of charge transfer state, going from the oxygen of the photoacid to the solvent molecule moeity, which crosses down over the course of the acid dissociation coordinate. It is suspected that this state may interfere with the excited state intermolecular (ESPT) process, as it does not cross down as rapidly in the case of a photoacid with more strongly deactivating substituents. More extensive study is necessary to fully describe the roles of these charge transfer states on the pyranine-based photoacids, and suggestions in this regard are made in detail at the end of Chapter 5.

On the whole, the breadth of quantum chemical methods used to study ESPT processes in a range of organic systems were highly effective in this regard. This speaks not only to the effectiveness of currently available methods for the study of excited states, but also has allowed for the obtainment of detailed insights into these complex systems of industrial and biological relevance.

Acknowledgements

First and foremost, I would like to thank Prof. Dr. Andreas Dreuw for the opportunity to learn about and research such an interesting variety of topics for the past four years. He was always encouraging and kind, regardless of how many questions or concerns I had. Thank you especially for the immensely helpful and interesting discussions!

I would also like to thank Dr. Shirin Faraji, who worked with me during the first project of my PhD. Dr. Faraji worked particularly closely with me during the development of the approximate kinetic model for the excited state dynamics of Pigment Yellow 101 and performed the calculations using this model presented in Section 3.6. During this time, she was not only a scientific advisor, but also showed me around Heidelberg and introduced me to some cool running routes.

I am indebted as well to Prof. Dr. Uwe Bunz and his group, particularly Jan Kumpf and Jan Freudenberg, for the experimental research motiving the study of aldehyde quenching.

I am very grateful to have worked with such a great group of people during this time. Thank you, Dreuw Group for being so awesome and for all of our discussions over coffee! I would especially like to thank Tim, Stefan, Tobi, and Felix for the nice atmosphere in the office, and Mary for being such a good friend and running partner. A big thank you as well to Jan Wenzel, who carefully read parts of this dissertation and gave me very helpful comments!

To my friends and family, thank you for always believing in me and making me feel closer to home. I love you Mom and Dan, Dad and April, Julie, and David.

Finally, thank you to my Georg, for always catching me. I love you infinitely.

Contents

List of Figures

List of Tables

Chapter 1

Introduction

Proton transfer reactions[1] make up some of the most common reactions in chemistry. Indeed it has been claimed that proton transfer between neighboring reactants is the most commonly occurring reaction in the biosphere[2]. Proton transfer processes range from the simple dissociation of acids and bases in water first introduced to chemistry students at the high school level, to proton transfer in enzymatic catalysis[3–5], to modulating the conformation of proteins[2]. Proton transfer reactions for organic molecules in the electronic ground state have been subject to extensive study for decades, and many examples are provided in the literature, see for example[6–9] for a small sampling. When irradiated with light, however, a molecule can be promoted from its stable ground state to electronically excited states, where its chemistry, including possible proton transfer reactions, is likely to change.

Once in the electronically excited state, many different photochemical processes can ensue. The literature provides more comprehensive overviews of photochemistry in general, see for example[10–13]. Initially, since the excited molecule is not only electronically but also vibrationally excited, it will relax to the ground vibrational level of the excited state potential energy surface. From here, one often-observed possibility is radiative decay back down to the electronic ground state, also known as fluorescence. A possible long-lived luminescent process is phosphorescence, which involves a change in spin multiplicity, i.e. from triplet to singlet. A system may also decay back to the ground state non-radiatively. Intersystem crossing (ISC) is the non-radiative transition between excited states of different spin multiplicity. Internal conversion (IC), in contrast, is the radiationless transition between excited states of the same spin multiplicity. Once back in the electronic ground state, the system will again vibrationally relax. The Stokes shift is the difference in energy between the emitted and absorbed photon, and therefore marks the difference between fluorescence and absorption.

In general, the larger and more complicated a molecule's structure, the more intricate and complex its manifold of electronically excited states, and thus the more variable the photochemistry. Moving along the excited state potential energy surface, different processes may be possible at different molecular coordinates of the system. For example, one may encounter a conical intersection between the excited state and the ground state with a dihedral rotation, allowing non-radiative decay to occur.

Proton transfer is also possible in the excited state, for example in systems like the organic molecules presented in this thesis. Along a hydrogen bond in a molecular system proton transfer from one part of the sytem to another may become feasible when the system has reached an electronically excited state via photoxcitation. If excited state proton transfer (ESPT) occurs from one part of a molecule to another part of the same molecule, excited state intermolecular proton transfer (ESIPT) is said to have transpired, while the simple acronym ESPT is used to describe intramolecular proton transfer between two distinct molecules in the excited state. Electron transfer (ET) may also occur before, after, or in conjunction with the proton transfer.

Excited state proton transfer reactions are ubiquitous in organic photochemistry. For example, several ESPT reactions occur in green fluorescent protein (GFP)[14–16], a protein known for its presence in the *Aequorea victoria* jellyfish[14, 17]. It explains the dual fluorescence in 3-hydroxyflavone[18] and has shown promise for explaining the binding protein binding properties[19, 20]. The applicability of ESPT is indeed very broad, ranging as well to optical probes for biomolecules [21–23] and polymer photostabilizers[24, 25] and white-light emitting materials[26, 27]. A longer list is provided by [28]. In some cases, proton transfer reactions are possible in the excited state but not in the ground state, leading for example to such phenomena as photoacidity, see for example [29–31].

Indeed, excited state chemistry can look very different from ground state chemistry, and it is therefore a main challenge in modern quantum chemistry to develop methods for appropriate description of the excited state. Massive advances in the fields of theoretical and computational chemistry in the past few decades have enabled chemists to gain insight into the excited state properties and processes of ever larger and more complex molecules. A selection of these methods, including in particular time-dependent density functional theory [32–34] and the algebraic diagrammatic construction scheme for the polarization propagator[35–38], will be described in Chapter 2 and then applied throughout this work. Overall, this work provides a new look and novel insight into the photochemistry of several organic systems.

Excited state proton transfer in various forms is a theme throughout, and the breadth of possibilities for such processes is highlighted. Chapter 3 focuses on Pigment Yellow 101, whose photostability and fluorescence have been baffling for decades but in recent

years have been explained[39–42]. In the scheme of this project, potential energy surfaces among the most stable isomers of Pigment Yellow 101 were computed. Excited state intermolecular proton transfer (ESIPT) leading to isomerization occurs very readily in PY101. The excited state dynamics of PY101 play out on the isolated surface of the first excited state, and neither ESIPT nor dihedral rotation to isomerization provide non-radiative decay routes to the electronic ground state. In addition to the extensive study on the excited state PES of PY101, a simple kinetic model for treating its excited state dynamics described.

Chapter 4 presents the central project of this thesis. Here, the fluorescence quenching of the quintessential benzaldehyde and several of its derivatives is described, giving for the first time a deep understanding of aromatic aldehyde photochemistry in polar, protic solvents. Benzaldehyde has been believed to be a photobase[43], exhibiting stronger basicity in the excited state than in the ground state. This would imply that ESPT occurs readily upon excitation. Here, this assumption is challenged, and the photochemistry of aromatic aldehydes in polar, protic solvents thoroughly ellucidated. The impact of this study on the field of organic synthesis at large will be discussed in the context of novel dialdehyde amine indicators, whose synthesis is also reported in recent literature[44].

In Chapter 5, a series of large pyranine-based photoacids[45–47] are investigated. These so-called "super" photoacids have an excited state $pK_a^* < 0$ and offer an array of properties for different applications, particularly those in vivo[47]. In this thesis, their excited state properties are computed and a new look at their photochemistries, particularly their varying abilities to dissociate in solution in the excited state, is obtained. The role of charge transfer in photoacid dissociation is also explored. Finally, in Chapter 6, the primary results of this work are summarized with particular attention to the individual impacts of these conclusions on the chemistry community at large. First, however, we turn our attention to Chapter 2 and an overview of the quantum chemical methods employed in this work.

As a final note, it should be mentioned that some of the results presented in this dissertation have been published by myself and my co-authors. These publications are

- **K. Fletcher, U. H. F. Bunz, and A. Dreuw**
Fluorescence quenching of aromatic aldehydes in water: photo-basicity vs. hydrogen atom abstraction
submitted for publication, **2016**.

- **K. Fletcher, A. Dreuw, and S. Faraji**
Potential energy surfaces and approximate kinetic model for the excited state dynamics of Pigment Yellow 101
Comp. Theo. Chem., **2014**, *1040-1041*, 177-185.

Chapter 2

Theoretical Methodology

Computational photochemistry, see for example [11, 13], involves the use of quantum chemical calculations and computer simulations to study light-induced chemical processes. Since a molecule can be excited to a higher electronic state through light absorption, the study of electronically excited states is the cornerstone of the field. Recent decades have witnessed significant progress in the study of excited states, and a helpful review on the available methods are provided in the literature[34]. One can think of these methods as belonging to two main classes: density-based and wave function-based methods. Which class is most appropriate depends on a multitude of factors, such as the chemical problem or the molecular system of interest. The selection of an excited state method also follows naturally from the ground state method of choice. Wave function-based methods necessitate an initial Hartree-Fock ground-state calculation in order to obtain an ab initio wave function[48]. In contrast, the ground state electron density from a density functional theory calculation forms the basis of excited state, time-dependent density functional theoretical studies. Since the chosen ground state method implicates the excited state method, approximations made in the ground state theory determine how accurate the following excited state calculations are.

In the following, these two classes of methods will be discussed in detail. The molecular Schrödinger Equation[49] and the Born-Oppenheimer Approximation[50] are introduced in Sections 2.1 and 2.2, respectively. In Section 2.3, wave function-based methods are presented, including Hartree-Fock theory[51–53], perturbation theory[54–56], configuration interaction[51, 57, 58], and coupled cluster methods[53, 59]. The algebraic diagrammatic construction[35–38] and the intermediate state representation thereof[60] are emphasized here as well. Density-based methods are described in Section 2.5, moving naturally from density functional theory (DFT)[61–66] to its time-dependent analog,

TD-DFT[32–34]. A discussion of the computation of absorption and fluorescence spectroscopy is given in Section 2.6, and the current methods used in the analysis of computed excited states are presented in Section 2.7.

2.1 The Molecular Schrödinger Equation

The molecular Schrödinger Equation[49] is the fundamental equation of quantum chemistry. It is a partial differential eigenvalue equation whose solution yields the energy of a particular system. For a system of N electrons and M nuclei, it is given by

$$\hat{H}(\vec{r};\vec{R})\Psi(\vec{r};\vec{R}) = E\Psi(\vec{r}), \tag{2.1}$$

where $\vec{r}$ and $\vec{R}$ are the electronic and nuclear coordinates, respectively. The physical state of the system is completely described by its wave function Ψ, and the probability density of finding electrons at $\vec{r} = \vec{r}_1\vec{r}_2...\vec{r}_N$ and nuclei at $\vec{R} = \vec{R}_1\vec{R}_2...\vec{R}_M$ is given by

$$\left|\Psi(\vec{r};\vec{R})\right|^2. \tag{2.2}$$

Indeed, in quantum mechanics, for every observable (here E) there corresponds a Hermitian operator (here $\hat{H}$). The only observable values of E are the eigenvalues of $\hat{H}$. What $\hat{H}$ looks like, as well the approximations that can be made to it, is the subject of the next section.

2.2 The Born-Oppenheimer Approximation

For a molecule with N electrons and M nuclei, the total Hamiltonian $\hat{H}$ is written in atomic units with the operator $\nabla = \frac{\partial}{\partial r/R}$ and the nuclear charges Z as

$$\begin{aligned}
\hat{H} = {} & -\frac{1}{2}\sum_{i=1}^{N}\nabla_i^2 - \sum_{i=1}^{N}\sum_{I=1}^{M}\frac{Z_I}{|r_i - R_I|} \\
& + \sum_{i=1}^{N}\sum_{j>i}^{N}\frac{1}{|r_i - r_j|} - \frac{1}{2}\sum_{I=1}^{M}\frac{\nabla_I^2}{2m_I} + \sum_{I=1}^{M}\sum_{J>I}^{M}\frac{Z_I Z_J}{R_I - R_J}
\end{aligned} \tag{2.3}$$

or in compact form as

$$\hat{H} = \hat{T}_e(\vec{r}) + \hat{V}_{eN}(\vec{r};\vec{R}) + \hat{V}_{ee}(\vec{r}) + \hat{T}_N(\vec{R}) + \hat{V}_{NN}(\vec{R}). \tag{2.4}$$

In Equation 2.4, $\hat{T}_e(\vec{r})$ gives the kinetic energy of the electrons, $\hat{V}_{eN}(\vec{r};\vec{R})$ the electron-nuclear Coulomb attraction, $\hat{V}_{ee}(\vec{r})$ the electron-electron Coulomb repulsion, $\hat{T}_N(\vec{R})$ the nuclear kinetic energy, and $\hat{V}_{NN}(\vec{R})$ the Coulomb repulsion of the nuclei. Therefore, the Schrödinger equation can be written as

$$\left[\hat{T}_e(\vec{r}) + \hat{V}_{eN}(\vec{r};\vec{R}) + \hat{V}_{ee}(\vec{r}) + \hat{T}_N(\vec{R}) + \hat{V}_{NN}(\vec{R})\right]\Psi(\vec{r};\vec{R}) = E\Psi(\vec{r};\vec{R}). \qquad (2.5)$$

At this point, a crucial approximation central to quantum chemistry was made by Max Born and Robert Oppenheimer[50]. Since nuclei are several thousand times heavier than electrons, the time scales of electronic and nuclear motion vary dramatically. Thus, a quasi-separable ansatz for the wave function can be adopted as

$$\Psi(\vec{r};\vec{R}) = \phi(\vec{r};\vec{R})\chi(\vec{R}), \qquad (2.6)$$

with the nuclear wave function $\chi(\vec{R})$ and the electronic wave function $\phi(\vec{r};\vec{R})$, which depends parametrically on the nuclear coordinates $\vec{R}$. Writing the wave function as a product of an electronic and a nuclear wave function means that the nuclei are treated in an external potential created by the electrons, but that they are independent of the motion of each individual electron. In this vein, the Hamiltonian is split into an electronic Hamiltonian $\hat{H}_e$ given by

$$\hat{H}_e = \hat{T}_e + \hat{V}_{eN} + \hat{V}_{ee} \qquad (2.7)$$

and a nuclear hamiltonian $\hat{H}_N$ given by

$$\hat{H}_N = \hat{T}_N + \hat{V}_{NN}. \qquad (2.8)$$

An important consequence of this approximation is the concept of the potential energy surface[53], which plots the total energy of a molecule as a function of the nuclear coordinates at varying geometries. The potential surface energy is given by

$$E(\vec{R}) = E_e(\vec{R}) + \hat{V}_{NN}. \qquad (2.9)$$

In essence, in building up the potential energy surface, one fixes the nuclei at a configuration $\vec{R}_i$, solves for the electronic motion at this configuration to obtain the electronic energy $E_e(\vec{R}_i)$ and the wave function $\Psi(\vec{r};\vec{R}_i)$, then repeats this procedure for all other geometries of interest.

While the Born-Oppenheimer approximation is applicable to the majority of quantum chemical problems, there are cases where its validity falters. In essence, it is applicable when the change in the electronic wave function with respect to the nuclear coordinates

is negligibly small in comparison with the nuclear mass[67]. In practice, this is true when electronic states are clearly energetically separate. The approximation breaks down, for example, at avoided crossings and conical intersections, i.e. places where electronic states become energetically close to each other. In these regions of the potential energy surface, the assumption that the nuclei may be treated in the field of all electrons is not valid, ergo the BO approximation does not hold[67].

Certain points on the potential energy surface, such as minima and transition states, are important to understand chemical reactivity. For both minima and saddle points, the gradient $\vec{g}$ for a system with N atoms and q_i individual degrees of freedom is defined by[53]

$$\mathbf{g}_i = \begin{pmatrix} (\frac{\partial E_{PES}}{\partial q_1})_i \\ (\frac{\partial E_{PES}}{\partial q_2})_i \\ \vdots \\ (\frac{\partial E_{PES}}{\partial q_N})_i \end{pmatrix} = 0.$$

The Hessian matrix is composed of second derivatives of the energy[53]

$$\mathbf{H} = \begin{pmatrix} \frac{\partial^2 E_{PES}}{\partial q_1^2} & \frac{\partial^2 E_{PES}}{\partial q_1 \partial q_2} & \cdots & \frac{\partial^2 E_{PES}}{\partial q_1 \partial q_N} \\ \frac{\partial^2 E_{PES}}{\partial q_2 \partial q_1} & \frac{\partial^2 E_{PES}}{\partial q_2^2} & \cdots & \frac{\partial^2 E_{PES}}{\partial q_2 \partial q_N} \\ \vdots & \vdots & \ddots & \vdots \\ \frac{\partial^2 E_{PES}}{\partial q_N \partial q_1} & \frac{\partial^2}{\partial q_N \partial q_2} & \cdots & \frac{\partial^2 E_{PES}}{\partial q_N^2} \end{pmatrix}.$$

Upon diagonalization of the Hessian, if one of its eigenvalues is negative, this means that one imaginary harmonic frequency (square root of the eigenvalue) exists. For first-order saddle points, chemically interpretable as transition states, exactly one imaginary frequency is present and for higher-order saddle points, more than one imaginary frequency exists. For true minima, however, no imaginary frequencies may be found[53].

There are many methods available for building up and characterizing points on a potential energy surface. Wave function-based methods, built up by the famous Hartree-Fock theory, are a natural starting point.

2.2.1 Conical intersections and minimum energy crossing point optimizations

The Born-Oppenheimer approximation falters in regions of the potential energy surface where electronic states approach each other energetically, for example at conical intersections (CIs)[68]. If the degeneracy is linearly lifted in displacements from a given intersection of two or more PESs, then a conical intersection (CI) is classified[68]. In

terms of a full description of the photochemistry of a variety of systems, these intersections become important. Indeed, when a system in a higher electronic state can reach a CI region, ultrafast radiationless decay to a lower-energy electronic state can ensue. For molecules, CIs are multidimensional "seams" rather than single points[69]. For example, for an intersection of two states in a molecular system, the intersection is effectively an $(N-2)$-dimensional hypersurface called the "seam space", where N is the number of internal coordinates of the system[12, 68]. The other two dimensions are designated for the "branching space," or the space where a displacement lifts the degeneracy[13]. Since radiationless transitions like internal conversion may take place in the area of a conical "seam," it is sometimes important to characterize such a seam by means of a CI optimization. Such an optimization is inherently different from a simple geometry optimization on a single, isolated potential energy surface, and is performed to find the so-called minimum energy crossing point (MECP)[69]. An algorithm for finding the MECP must provide a balanced description of the electronic structures of the involved states[70], and also must involve the constraint that the intersecting states have the same energy[69].

The two-dimensional branching space between electronic states I and J is spanned by the vectors g and h given by[71]

$$g^{IJ} = \hat{\nabla}_{\mathbf{R}}(E_I(\mathbf{R}) - E_J(\mathbf{R})) \tag{2.10}$$

and

$$h^{IJ} = \langle \Psi_I | \hat{\nabla}_{\mathbf{R}} | \Psi_J \rangle. \tag{2.11}$$

For electronic structure methods where analytic excited-state gradients are calculable, the g^{IJ} are analytically available. Several algorithms are in use today for the optimization of MECPs absent the requirement that the non-adiabatic coupling vector h^{IJ} be evaluated, including the penalty-constrained optimization algorithm by Levine et al.[72] and the branching-plane algorithm by Maeda et al[73]. Neither necessitates the computation of non-adiabatic couplings. As previously insinuated, these algorithms are of particularly important use to describe the photochemical processes in molecular systems around areas where radiationless transitions may be possible. However, it should be noted here that methods like CIS[34, 74, 75] and TD-DFT[32–34] (i.e. linear-response methods) fail to describe the topology of a concial intersection involving the reference state[76], which is usually taken to be the ground state. Thus, for describing S_1/S_0 crossings, a different reference state is required, which can be achieved by the employment of spin-flip methods[77–79].

2.3 Wave function-based methods

The separation of nuclear and electronic coordinates is followed by solving the electronic Schrödinger equation. However, this equation cannot be analytically solved and approximations must be made. Out of this necessity, the self-consistent field (SCF) methods Hartree-Fock (HF)[51–53] and Kohn-Sham density functional theory (DFT)[62] arise. A more detailed description of basic SCF methodology is provided in the literature[80]. SCF methods involve transforming the N-electron Schrödinger equation into a set of N differential equations for each electron. In turn, single-electron wave functions or orbitals are used to describe the individual electrons. These single-electron equations are coupled as a result of the electron-electron interaction potential. Each equation is implicitly dependent on the orbitals of the ensemble of electrons, and solutions for the single-electron orbitals must be consistent with the single-electron orbitals employed to calculate the electron-electron interaction potential. Both HF and DFT assume that the N-electron wave function can be written as an anti-symmetrized product of single-electron orbitals. This idea of the Slater determinant will be discussed in the following subsection. However, it should be kept in mind that HF and DFT do not transform the electronic Schrödinger equation to the set of single-electron equations equivalently.

My discussion of wave function-based methods begins with a description of Hartree-Fock theory. The fundamental assumption of HF is that each electron experiences the effect of all other electrons as an average field. In the limit of the complete basis set, the correlation energy is given as the energy difference between that of the exact system and that of the system in the HF limit. That is

$$E_{\text{corr}} = E_0^{\text{exact}} - E_0^{\text{HF}}. \tag{2.12}$$

Although HF often generates reasonable results for the equilibrium geometries of molecules in their electronic ground states, it is far from sufficient in the treatment of many problems of interest to the quantum chemist. The correlation energy E_{corr}, while generally only about < 5 % of the total energy[48], is often important. This is because it is of the same magnitude as, for example, energy barriers to reaction and differences between isomers. Methods treating electron correlation must therefore be employed.

After treating HF theory, more sophisticated wave function-based methods are discussed. In general, wave function-based ab initio methods can belong to the single-reference (includes coupled-cluster[53, 59, 81]), multi-reference[82–85], or configuration interaction[51, 57, 58] classes. Moving, for example, from HF to multi-configuration self-consistent field (MCSCF)[53], a few excited determinants are selectively included. Going further to complete active space SCF (CASSCF)[52], all excitations are considered

within a selected space of "active" orbitals. MCSCF and CASSCF compensate well for the single-determinant problems of HF, but they do not successfully treat dynamic correlation. For this, configuration interaction (CI)[51, 57, 58] is the most obvious choice. In any case, all of these methods have their foundation in HF, which will be discussed next. Several of the more advanced wave function-based methods are then treated once a thorough understanding of HF is gained.

2.3.1 Hartree-Fock Theory

Hartree-Fock theory[51, 53] begins with the assumption that the electrons of a system "ignore" each other, and that we can therefore write Ψ as the Hartree product

$$\Psi_{HP}(r_1, r_2, ..., r_N) = \phi_1(r_1)\phi_2(r_2) \cdots \phi_N(r_N). \tag{2.13}$$

The Hartree product does not, however satisfy the antisymmetry principle of Pauli[86], which states that a wave function describing electrons must be antisymmetric with respect to the interchange of any set of space-spin coordinates. The solution to this problem is the introduction of Slater determinants. The Hartree-Fock approximation[51] thus states that the wave function Ψ_0 is approximated by an antisymmetrized product of n orthonormal spin orbitals $\chi_i(\vec{x})$. Each of these spin orbitals is given as a product of a spin function α or β and a spatial orbital ψ. That is

$$\chi(x) = \begin{cases} \psi(r)\alpha(\omega) \\ \psi(r)\beta(\omega) \end{cases} .$$

The Slater determinant is then given by:

$$\Psi_0(x_1, x_2, ..., x_N) = \frac{1}{\sqrt{N!}} \begin{vmatrix} \chi_1(x_1) & \chi_2(x_1) & \cdots & \chi_N(x_1) \\ \chi_1(x_2) & \chi_2(x_2) & \cdots & \chi_N(x_2) \\ \vdots & \vdots & \ddots & \vdots \\ \chi_1(x_N) & \chi_2(x_N) & \cdots & \chi_N(x_N) \end{vmatrix} = |\Psi_0\rangle.$$

Here, all electrons are indistinguishable. Assuming that the electrons can be described by an antisymmetrized product (Slater determinant) means that each electron is subject to the Coulomb repulsion due to the average positions of all electrons. It is also notable that each electron experiences an "exchange" interaction as a result of the antisymmetrization[87]. The HF energy E_{HF} is given by $E_{HF} = \langle\Psi|\hat{H}_{el}|\Psi\rangle$. The variational theorem[88] holds, and the Slater determinant yielding the lowest energy offers the best approximation to the true Ψ.

In the HF method, our goal is therefore to determine the set of spin orbitals which minimize the energy. We need to apply the variational principle (see for example[53]) by minimizing the expectation value of the electronic Hamiltonian in the basis of the approximate many-particle wave function. In addition, we need to make certain that the orbitals χ remain orthonormal upon application of the variational principle. To this end, we employ Lagrange's method of undetermined multipliers[89]. We therefore have the constraint

$$\int \chi_i^*(r)\chi_j(r)dr = \delta_{ij} \tag{2.14}$$

and

$$f(i)|\chi(x_i)\rangle = \epsilon_i|\chi(x_i)\rangle \tag{2.15}$$

where ϵ_i is the Lagrangian multiplier giving the orbital energies[48]. The Fock operator is

$$f(i) = -\frac{1}{2}\nabla_i^2 - \sum_{I=1}^n \frac{Z_I}{|r_i - R_I|} + \sum_J (J_j(i) + K_j(i)) = h(i) + v^{HF}(i). \tag{2.16}$$

The electron-electron repulsion is given by $v^{HF}(i)$ and $h(i)$ describes the one-particle interactions.

The single electron orbitals $\chi(x)$ can then be employed to calculate the ground state energy, given by[48]

$$E_{HF} = \sum_i \int \chi_i^*(x_1)h(i)\chi_i(x_1)dx_1$$
$$+\sum_{i<j} \int \frac{\chi_i^*(x_1)\chi_j^*(x_2)\chi_i(x_1)\chi_j(x_2)(1-\hat{P})}{|x_1 - x_2|}dx_1 dx_2 \tag{2.17}$$

with the permutation operator $\hat{P}$. The permutation operator switches indices i and j, meaning electron x_1 is "moved" to orbital j and electron x_2 is in orbital i.

It must be emphasized here that E_{HF} does not include correlation energy and is therefore referred to as mean-field approach. Electronic Coulomb $J(i)$ and exchange $K(i)$ interactions are handled in the static field created by all of the electrons except for i. Extensive research followed the formulation of HF to include electron correlation, and an overview of post-HF methods are presented in the following sections.

2.3.2 Second quantization

The method of second quantization[48, 67, 90, 91] offers a useful alternative approach to many-body systems. Beginning with an orthonormal basis of orbitals, i.e. single-particle states, any many-particle state can be described using the set of occupation numbers

of the orbitals $|n_1 n_2...n\infty\rangle$. Assuming a multielectron system is to be treated, two requirments must be fulfilled. The first is that the occupation numbers may only have values of 0 or 1, as at maximum a single electron may occupy each orbital. The second is that, with respect to the permutation of a pair of electrons, the state $|n_1 n_2...n_\infty\rangle$ must be antisymmetric[67].

To this end, so-called creation $\hat{c}_p^\dagger$ and annihilation $\hat{c}_p$ operators are used which act on many-particle states[67]. The creation operator increases the occupation number n_p by one, i.e. it "creates" an electron, while the annihilation operator decreases the n_p by one, i.e. it "destroys" an electron. The creation and annihilation operators obey the anticommunication relations[48, 67]

$$\{\hat{c}_p, \hat{c}_q^\dagger\} = \hat{c}_p \hat{c}_q^\dagger + \hat{c}_q^\dagger \hat{c}_p = \delta_{pq} \tag{2.18}$$

and

$$\{\hat{c}_p, \hat{c}_q\} = 0 \tag{2.19}$$

and

$$\{\hat{c}_p^\dagger, \hat{c}_q^\dagger\} = 0. \tag{2.20}$$

The Pauli exclusion principle prevents the creation of an electron in an orbital where one already exists. Similarly, no electron can be annihilated in an orbital where no electron exists. As a result of this handy formalism, a one-particle operator in a multiparticle system may be written as[48]

$$\hat{O} = \sum_{pq} \langle p|h|q\rangle \hat{c}_p^\dagger \hat{c}_q, \tag{2.21}$$

while a two-particle operator can be expressed by

$$\hat{V} = \sum_{pqrs} \langle pq|rs\rangle \hat{c}_p^\dagger \hat{c}_q^\dagger \hat{c}_r \hat{c}_s \tag{2.22}$$

Finally, since the electronic Hamiltonian is simply the sum of one- and two-particle operators, it is in turn given by

$$\hat{H} = \sum_{pq} h_{pq} \hat{c}_p^\dagger \hat{c}_q + \frac{1}{2} \sum_{pqrs} \langle pq|rs\rangle \hat{c}_p^\dagger \hat{c}_q^\dagger \hat{c}_r \hat{c}_s. \tag{2.23}$$

2.3.3 Configuration Interaction Theory (CI)

Configuration interaction theory[51, 57, 58] involves the combination of a number of determinants variationally in order to treat dynamic correlation. The electronic many-body wave function is constructed as a linear combination of the ground state Slater determinant and so-called "excited" determinants. These excited determinants are formed by substituting virtual orbitals $\phi_a(r)$ for occupied ones $\phi_i(r)$.

Replacing one occupied with one virtual orbital yields "singly excited" Slater determinants $\Phi_i^a(r)$, while replacing two occupied with two virtual orbitals generates "doubly excited" Slater determinants $\Phi_{ij}^{ab}(r)$. The CI wave function can then be built up as

$$\Psi_{CI} = c_0\Phi_0(r) + \sum_{ia} c_i^a \Phi_i^a(r) + \sum_{iajb} c_{ij}^{ab} \Phi_{ij}^{ab}(r) + \sum_{ijkabc} c_{ijk}^{abc} \Phi_{ijk}^{abc}(r) + ... \tag{2.24}$$

The inclusion of all possible "excited" determinants and the substitution of this ansatz for the many-body wave function into the exact electronic Schrödinger equation leads to the Full-CI method. Full-CI solves the Schrödinger equation numerically exact within the chosen basis set. Truncation of the CI expansion immediately following the "singly-excited" determinants leads to the wave function ansatz

$$\Psi_{CIS} = \sum_{ia} c_i^a \Phi_i^a(r), \tag{2.25}$$

which characterizes the configuration interaction singles, or CIS method[34, 74, 75]. Note that $\Phi_0(r)$ is not present here, as it is uncoupled from the $\Phi_i^a(r)$ following Brillouin's theorem[51]. Substituting Ψ_{CIS} into the Schrödinger equation leads to the matrix equation

$$\mathbf{HX} = \omega\mathbf{X} \tag{2.26}$$

with $\mathbf{H}$ being the matrix representation of $\hat{H}$ in the space of singly-excited determinants, $\mathbf{X}$ as the matrix of the CIS expansion coefficients, and ω being the diagonal matrix of excitation energies. Building off of CIS is the expanded CIS(D) form, which offers a second-order perturbative correction to CIS[92].

2.3.4 Coupled Cluster Theory

Coupled cluster (CC) methods[53, 59] take a different approach in their attempt to describe electron correlation. CC involves a re-formulation of the electronic Schrödinger equation as a non-linear equation by parametrization via an exponential excitation operator. This allows for the computation of size-consistent approximations of the ground state for weakly-correlated systems. The HF approximation to the wave function is

taken to be the zero-order reference, and correlation energy is subsequently added by tacking on excitations. The full CI wave function can be written as

$$\Psi_{CI} = e^{\mathbf{T}}\Phi_0(r) \tag{2.27}$$

with the cluster operator

$$\mathbf{T} = \mathbf{T}_1 + \mathbf{T}_2 + \mathbf{T}_3 + ... + \mathbf{T}_n. \tag{2.28}$$

For example, considering double excitations,

$$\mathbf{T}_2 = \sum_{i<j}^{occ}\sum_{a<b}^{virt} t_{ij}^{ab}\Phi_{ij}^{ab} \tag{2.29}$$

$$.\hat{T} = \sum_{\mu} t_{\mu}\hat{\tau}_{\mu} \tag{2.30}$$

Including both singles and doubles excitations $\mathbf{T}_1$ and $\mathbf{T}_2$ yields the CCSD method[53, 59], while inclusion of all excitations from $\mathbf{T}_1$ to $\mathbf{T}_n$ gives full-CC. In general, then, the CC wave function is

$$\Psi_{CC} = (1 + \mathbf{T} + \frac{\mathbf{T}^2}{2} + \frac{\mathbf{T}^3}{3!} + ...)\Phi_0 \tag{2.31}$$

and the CC energy is determined by solving

$$E_{CC} = \langle\Phi_0|\hat{H}|e^{\mathbf{T}}\Phi_0\rangle. \tag{2.32}$$

Full-CI is equivalent to full-CC, including the same amount of determinants and yielding identical results. For the successful employment of CC theory for excited states, it is generally extended to LR-CC[93–95] or EOM-CC[96–99]. Commonly used schemes include CC2[100–102] and CC3[103, 104] as well.

2.3.5 Møller-Plesset Perturbation Theory

Perturbation methods in general separate the Hamiltonian into a zeroth-order part $\hat{H}_0$ and a correction part $\hat{H}_1$, i.e.

$$\hat{H} = \hat{H}_0 + \lambda\hat{H}_1, \tag{2.33}$$

which contains the perturbation parameter λ. In this vein, Møller-Plesset perturbation theory (MP)[55, 105] includes correlation energy as a small perturbation to the ground state determined by HF. First, the full Hamiltonian is split into the HF-operator F,

whose eigenfunctions $|\psi_i^{(0)}\rangle$ and eigenvalues are known, and a small perturbation V

$$H = F + V. \tag{2.34}$$

In turn, F is given by the sum of the one-particle interactions and the electron-electron repulsion

$$F = \sum_i f(i) = \sum_i h(i) + \sum_i v^{HF}(i) \tag{2.35}$$

and V can be written as

$$V = \sum_{ij} \frac{1}{r_{ij}} - \sum_i v^{HF}(i). \tag{2.36}$$

The next step is to substitute F into the Schrödinger equation and introduce an ordering factor λ. As a consequence, the eigenfunctions and eigenvalues are Taylor-expandable in λ[48]

$$(F + \lambda V)(|\psi_i^{(0)}\rangle + \lambda|\psi_i^{(1)}\rangle + \lambda^2|\psi_i^{(2)}\rangle + ...)$$
$$= (E_i^{(0)} + \lambda E_i^{(1)} + \lambda^2 E_i^{(2)} + ...)(|\psi_i^{(0)}\rangle + \lambda|\psi_i^{(1)}\rangle + \lambda^2|\psi_i^{(2)}\rangle + ...). \tag{2.37}$$

By intermediate normalization, it holds that[48]

$$\langle\psi_i^{(0)}|\psi_i^{(exact)}\rangle = \langle\psi_i^{(0)}|\psi_i^{(0)}\rangle + \lambda\langle\psi_i^{(0)}|\psi_i^{(1)}\rangle + \lambda^2\langle\psi_i^{(0)}|\psi_i^{(2)}\rangle = 1 \tag{2.38}$$

and thus

$$\langle\psi_i^{(0)}|\psi_i^{(n)}\rangle = 0 \qquad n = 1, 2, 3, ... \tag{2.39}$$

Collecting terms in λ yields a sequence of progressively higher-order estimates of the energy and the wave function. The zeroth-order correction is simply the sum of the orbital energies ($\sum_i \epsilon_i$). First-order correction, or MP(1), is equivalent to HF, and subtracts doubly-counted electronic Coulomb and exchange interactions. This first-order correction is given by the second term on the right-hand side of equation 2.40. MP(2) offers the first correction to HF. It includes the third term on the right-hand side of equation 2.40. In doing so, it introduces correlation effects that go beyond the mean-field, for example electron polarization. MP(3), in turn, offers the second correction to HF. The progression of correction to HF can best be seen in the expression for the MP energy, which is given in second order by

$$E_{MP(2)} = \sum_i \epsilon_i - \frac{1}{2}\sum_{ij}\langle ij||ij\rangle - \frac{1}{4}\sum_{ijab}\frac{\langle ij||ab\rangle\langle ij||ab\rangle}{\epsilon_a + \epsilon_b - \epsilon_i - \epsilon_j}. \tag{2.40}$$

In the next section, the algebraic diagrammatic construction (ADC) is presented, which is often looked upon as the excited state analog of MP(2).

2.4 The Algebraic Diagrammatic Construction of the Polarization Propagator

The algebraic diagrammatic construction scheme of the polarization propagator (ADC)[35–38] is an example of a method for computing excited states. ADC gets its name as it uses diagrammatic perturbation theory for the polarization propagator in many-body Green's function theory. The Hamiltonian operator is partitioned according to the Møller-Plesset framework. The polarization propagator works on the time-dependent, ground state wave function and thereby propagates the density fluctuations of a many-body system. The Lehmann representation of the polarization propagator is given by[106]

$$\prod_{pq,rs}(\omega) = \sum \frac{\langle\Psi_0|c_q^\dagger c_p|\Psi_n\rangle\langle\Psi_n|c_r^\dagger c_s|\Psi_0\rangle}{\omega + E_0^N - E_n^N} + \sum \frac{\langle\Psi_0|c_r^\dagger c_s|\Psi_n\rangle\langle\Psi_n|c_q^\dagger c_p|\Psi_0\rangle}{E_0^N - E_n^N - \omega} \tag{2.41}$$

with all electronically excited states denoted by Ψ_n and with Ψ_0 being the wave function of the ground state of energy E_0^N. The sum is performed over all electronically excited states with total energy E_n^N. The creation and annihilation operators are given by $c_q^\dagger$ and c_p, respectively. The polarization propagator has poles at $\omega_n = E_n^N - E_0^N$, which are the vertical excitation energies. It can also be written in the diagonal representation as

$$\prod(\omega) = \mathbf{X}^\dagger(\omega - \Omega)^{-1}\mathbf{X} \tag{2.42}$$

with the matrix of transition amplitudes $\mathbf{X}$ and the diagonal matrix of vertical excitation energies Ω. Alternatively, in the non-diagonal representation, it is written as

$$\prod(\omega) = \mathbf{f}^\dagger(\omega - \mathbf{M})^{-1}\mathbf{f} \tag{2.43}$$

with the matrix of effective transition moments $\mathbf{f}$ and the non-diagonal matrix representation of $\mathbf{M}$. The various approximation orders of ADC originate from the expansion of the Hamiltonian and transition moments with respect to a corresponding order of perturbation theory[35, 106]. For example, for ADC(2), one has

$$\mathbf{M} = \mathbf{M}^{(0)} + \mathbf{M}^{(1)} + \mathbf{M}^{(2)} \tag{2.44}$$

and

$$\mathbf{f} = \mathbf{f}^{(0)} + \mathbf{f}^{(1)} + \mathbf{f}^{(2)}. \tag{2.45}$$

This discussion serves as a foundation for ADC and its origins. In practice, it can also be derived using the intermediate state representation (ISR).

2.4.1 ADC via ISR

A practical way of deriving the ADC equations is through the intermediate state representation[60]. Applying the physical excitation operators $\hat{c}_J$ leads to a set of correlated electronically excited states

$$|\Psi_J^N\rangle = \hat{c}_J|\Psi_0^N\rangle \tag{2.46}$$

with the intermediate states $|\Psi_0^N\rangle$ and

$$\{\hat{c}_J\} = \{c_a^\dagger c_i; c_a^\dagger c_b^\dagger c_i c_j; .... \qquad i < j, a < b, ...\}. \tag{2.47}$$

The Gram-Schmidt orthogonalization scheme[107] is then used to build up an orthonormal basis of intermediate states, $\{|\tilde{\Psi}_J^N\rangle\}$. To do this, the scheme is used in succession on the excited states, starting from the exact ground state, followed by singly then doubly excited states, and so on. In this basis, the Hamiltonian is written forming the ADC matrix

$$\mathbf{M}_{IJ} = \langle\tilde{\Psi}_I^N|\hat{H} - E_0^N|\tilde{\Psi}_J^N\rangle \tag{2.48}$$

in which the system Hamiltonian has been shifted by E_0^N, which is of course the exact ground state energy. Solving

$$\mathbf{M}\mathbf{X} = \mathbf{X}\Omega, \tag{2.49}$$

which is known as the secular ISR equation, with $\mathbf{X}^\dagger\mathbf{X} = 1$, allows one to obtain the excitation energies $\Omega_n = E_n - E_0$. The exact excited states are yielded from the eigenvectors

$$|\Psi_n^N\rangle = \sum_J X_{nJ}|\tilde{\Psi}_J^N\rangle. \tag{2.50}$$

It follows that the dipole transition moments are given by

$$T_n = \langle\Psi_n^N|\hat{\mu}|\Psi_0^N\rangle = \sum_J X_{nJ}^\dagger\langle\tilde{\Psi}_J^N|\hat{\mu}|\Psi_0^N\rangle \tag{2.51}$$

and excited state properties in general are computable using

$$O_n = \langle\Psi_n^N|\hat{O}|\Psi_0^N\rangle = \sum_{I...J} X_{nJ}^\dagger X_{nJ}\langle\tilde{\Psi}_J^N|\hat{O}|\Psi_0^N\rangle \tag{2.52}$$

It is worth a reminder that employing ISR with Rayleigh-Schrödinger perturbation theory yields an expansion for $\mathbf{M}$ like in MP perturbation theory which allows truncation at the nth-order explansion to obtain the set of ADC(n) approximations. The class of ADC(n) methods are fully size-consistent with respect to transition moments and excited state properties and energies. They are also compact and Hermitian. This offers an advantage over CC, which is non-Hermitian, and CI, which (other than full CI) is

not size-consistent[108]. An example of a major advantage that the popularly employed ADC(2)-s scheme has over CC2 is that ADC(2)-s can describe conical intersections between two states of the same symmetry physically correct. Finally, it is notable that the transition and difference density matrix analyses, as described in Sections 2.7.1 and 2.7.2, respectively, are implemented into the ADC code in Q-Chem, allowing for a reliable and accurate description of excited state properties and impressive insight into the electronic structures of complex systems.

2.4.2 Structure of the ADC matrix

The second quantization formalism is often used in the derivation of expressions for the matrix elements of the ADC matrix, whereby strings of annihilation and creation operators must be evaluated for the IS basis to be constructed and the shifted Hamiltonian represented[35, 109]. Such explicit expressions for the matrix elements $\mathbf{M}_{\mu\nu}^{(n)}$ are provided in the literature[35, 38], while a qualitative discussion of the ADC matrix is given in this thesis. The ADC matrix $\mathbf{M}$ has a block structure made up of singles $(p-h)$ and doubles $(2p-2h)$ excited configurations[106]. For easier visualization, the basic structure of the ADC matrix is given in Figure 2.1.

FIGURE 2.1: The basic structure of the ADC matrix at different levels of perturbation theory. The ADC level of theory is giving followed by the corresponding level of perturbation theory at that ADC level in parentheses.

In the 0th and 1st order, the only non-zero block is the $[p-h, p-h]$ block. It is evident that for the three cases of ADC(2)-s[35, 60], ADC(2)-x[37, 67], and ADC(3)[38, 106, 110], the matrices are all of the same size, having the dimensions of a singles plus doubles matrix in CI theory. In the 2nd and 3rd orders, the matrix comprises the $[p-h, 2p-2h]$,

$[2p-2h, p-h]$, and $[2p-2h, 2p-2h]$ blocks as well. ADC(2)-x is an *ad hoc* extension of the ADC(2)-s formulation[37]. Use of ADC(2)-x in practice leads to a poor description of excitation spectra and excitation energies which are consistently underestimated[106]. ADC(3), while scaling like O(N^6) just as ADC(2)-x, offers a much better performance in the calculation of excitation spectra[106]. The interested reader will find explicit equations for the matrix elements of **M** in the literature[35, 38].

2.5 Density-based Methods

The history of density-based methods begins with the Thomas-Fermi-Dirac model (1926-1930)[111–113]. Fermion statistical mechanics were used to derive the kinetic energy for the so-called "Jellium" system. The Jellium system is a fictitious system composed of an infinite number of electrons which move in an infinite volume of space of uniform positive charge[53]. An approach exactly analogous to HF followed. The expression for the energy in terms of kinetic and potential contributions was constructed and the variational principle applied, yielding differential equations for the density ρ. Of course, this initial, rough density-based method was wrought with errors. A homogeneous electron gas model, while it may be reasonable for the description of systems where the density varies slowly, is not applicable for atoms and molecules where density quickly varies at different regions of the system space[114]. Thomas-Fermi theory[111, 112] fails to predict bonding among atoms in a molecular system, and the rough treatment of the kinetic energy leads to major errors in the total energy. In addition, since electron-electron interactions are classically described, the exchange interaction is not accounted for[115]. The second primitive forefather of modern density functional theory was the Hartree-Fock-Slater model (1951)[116]. This presented a sort of hybrid model, retaining wave functions but writing potentials in terms of ρ. It was simpler than HF and better than the Thomas-Fermi-Dirac model, but still not a solid enough theory for serious implementation.

2.5.1 Density Functional Theory

Modern density functional theory (DFT) is rooted in the two Hohenberg-Kohn theorems[61]. The first Hohenberg-Kohn theorem states that the ground-state density determines the external potential, and therefore determines the Hamiltonian $\hat{H}$ and the wave function Ψ. That is, there exists a unique one-to-one mapping between $\Psi(\vec{r}_1, ..., \vec{r}_n)$ and $\rho(\vec{r})$. In essence, we have a system of electrons moving in an external field $v(\vec{r})$ generated by the nuclei. To within a constant, $v(\vec{r})$ is a unique functional of the density. In turn, since $v(\vec{r})$ fixes the Hamiltonian, the full many-particle ground state $\Psi(\vec{r}_1, ..., \vec{r}_n)$ is a

unique functional of $\rho(\vec{r})$. The integral of the exact ground state density is related to the number of electrons n by

$$\int d\vec{r} \rho(\vec{r}) = n. \tag{2.53}$$

The density also gives us the positions and charges of the nuclei, which is all that is necessary to determine $\hat{H}$.

The second Hohenberg-Kohn theorem is essentially the variational principle for the electron density. The correct ground-state density minimizes the total energy. Together, the Hohenberg-Kohn theorems prove the existence of an energy functional $E[\rho]$.

Modern DFT is based on the ideas of Kohn and Sham (1965)[62], who recognized that for a real system of perfectly interacting electrons, there exists a fictitious, non-interacting system with the same ground state density as the real system. That is

$$\rho_0(r) = \rho_0^s(r) = \sum_i |\phi_i(r)|^2. \tag{2.54}$$

Thus, solving for the fictitious system should yield the correct information about the real system. Applying a variational principle on the artificial non-interacting system of electrons leads to the Kohn-Sham equations

$$\left[-\frac{1}{2} \nabla^2 + v_s(r) \right] \phi_i(r) = \epsilon_i \phi_i(r), \tag{2.55}$$

where ϵ_i is the Lagrangian multiplier for the orbital energies and and $i = 1, ..., n$.

This means that an external potential v_s, which, like in HF, includes the electron-nuclear attraction and mean-field Coulomb repulsion, can be found which describes all many-particle effects

$$v_s(r) = -\sum_I \frac{Z_I}{|r - R_I|} + \int dr' \frac{\rho(r')}{|r - r'|} + v_{xc}([\rho], r). \tag{2.56}$$

In turn, all differences between the interacting and non-interacting systems are covered by the so-called exchange-correlation (xc) potential. The ground state electronic energy is given by

$$E = E_T + E_V + E_J + E_{XC} \tag{2.57}$$

where E_T is the kinetic energy, E_V the electron-nuclear interaction energy, E_J the Coulomb self-interaction of $\rho(\vec{r})$, and E_{XC} the xc-energy.

Many options for xc-functionals are in use today, including LDA[64] (local density approximation), GGA (generalized gradient approximation), hybrid functionals (e.g.

B3LYP[117], BHLYP[118], etc.), meta-GGAs[119], and double-hybrid functionals (e.g. B2PLYP[120]). The exact potential remains, however, unknown.

2.5.2   Time-Dependent Density Functional Theory

Time-dependent DFT (TD-DFT) is the analog of DFT used for the calculation of electronically excited states. While DFT was based on the two Hohenberg-Kohn theorems, TD-DFT was based on the corresponding Runge-Gross theorem[32]. The Runge-Gross theorem states that the time-dependent potential uniquely determines the density. Just like in time-independent DFT, a non-interacting fictitious system is introduced

$$\imath \frac{\partial}{\partial t} \phi_i(rt) = \left[-\frac{1}{2} \nabla^2 + v_s(rt) \right] \phi_i(rt) \tag{2.58}$$

whose potential is given by:

$$v_s(rt) = v_s[\rho](rt) = v_{ext}(rt) + v_H[\rho](r) + \frac{\delta A_{xc}[\rho](rt)}{\delta \rho(rt)}. \tag{2.59}$$

Here, the exchange-correlation action functional A_{xc} has been introduced. It is here that Runge and Gross were erroneous. More detail about TD-DFT and the nature of the errors made can be found in the literature[33, 34]. In essence, no variational principle for the TD-densities exists. However, one can effectively "ignore" these errors, continue with the derivation, and end up with a method that is still often quite useful in the study of large molecular systems. Two methods may be used to obtain excitation energies and oscillator strengths with the time-dependent Kohn-Sham approach. The first, real-time DFT, involves propagation of the Kohn-Sham wave function in time[121, 122]. The second, linear-response TD-DFT[34, 48, 67] (LR-TD-DFT), is more commonly used and available with most quantum chemistry codes[34].

The density-matrix formalism is an convenient way of deriving the algebraic expressions for linear-response TD-DFT[34, 123]. LR-TD-DFT is effective when the external potential is small enough that the ground state structure of a system is not entirely disturbed. In essence, the linear response of the TD-Kohn-Sham equations are analyzed with respect to an externally applied oscillating electric field. To begin, the density is written using the KS orbitals $\phi_p(r)$, which are themselves the result of a ground state DFT calculation, as

$$\rho(rt) = \sum_i \psi(rt)\psi^*(rt) = \sum_{pq} P_{pq}(t)\phi_p(r)\phi_q^*(r). \tag{2.60}$$

Here, P_{pq} is the reduced density matrix[48]

$$P_{pq}(t) = \sum_i c_{pi}(t)c^*_{qi}(t) \tag{2.61}$$

with $c_{pi}(t) = \langle \phi_p | \psi_i(t) \rangle$. By substituting this expression for P_{pq} into equation 2.58, one is left with[48, 67]

$$i\frac{\partial}{\partial t}P_{pq}(t) = \sum_r (F_{pq}[\rho]P_{rq}(t) - P_{pr}(t)F_{rq}[\rho]). \tag{2.62}$$

Here,

$$F_{pq}[\rho] = \left\langle \phi_p \left| \frac{-1}{2}\nabla^2 + v_{ext}(rt) + v_H[\rho](r) + v_{xc}[\rho](r) \right| \phi_q \right\rangle. \tag{2.63}$$

One now makes the assumption that the time-dependent perturbation $g(rt)$ in $v(rt)$ is small, and as a result F_{pq} and P_{pq} may be expressed as an expansion in time. We now insert this into equation 2.62 to obtain a set of differential equations. The most elementary of these describes the zeroth-order contribution given by[48, 67]

$$\sum_r \{F^{(0)}_{pr}P^{(0)}_{rq} - P^{(0)}_{pr}F^{(0)}_{rq}\} = 0 \tag{2.64}$$

which is equivalent to the time-independent ground state DFT formalism. Here, $F^{(0)}_{pq} = \epsilon\delta_{pq}$ and $P^{(0)}_{pq} = \epsilon_{pq,p\in\text{occ}}$. The first order equations in linear-response theory are then[48, 67]

$$\begin{aligned}
i\frac{\partial}{\partial t}P^{(1)}_{pq}(t) &= \sum_r \{F^{(0)}_{pr}P^{(1)}_{rq} - P^{(1)}_{pr}F^{(0)}_{rq}\} \\
&+ \sum_r \{(F^{(1)}_{pr} + G_{pr})P^{(0)}_{rq} - P^{(0)}_{pr}(F^{(1)}_{rq} + G_{rq})\}
\end{aligned} \tag{2.65}$$

where $G_{pq} = \langle \psi_p | g(rt) | \psi_q \rangle$ and $F^{(1)}_{pq} = \langle \phi_p | \int dr_1 \int dt_1 \frac{\delta(v_H[\rho]+v_{xc}[\rho])}{\delta\rho(r_1 t_1)}\Delta\rho(r_1, t_1) | \phi_q \rangle$. If p and q denote occupied and virtual orbitals, the idempotency relation $\rho^2 = \rho$ for the density and $\sum_r P_{pr}P_{rq} = P_{pq}$ for the corresponding reduced density matrix means that the first order changes of $P^{(1)}_{pq}$ are non-zero. Equation 2.65 then is broken into a set of coupled equations for $P^{(1)ai}$ and $P^{(1)ia}$. Carrying out a Fourier transformation of these coupled equations with respect to time results in the working equations for TD-DFT[48, 67]

$$\begin{aligned}
\omega X_{ia} &= (\epsilon_a - \epsilon_i)X_{ia} + \sum_{jb}[\langle aj|ib\rangle + \langle aj|\delta v_{xc}|ib\rangle]X_{jb} \\
&+ \sum_{jb}[\langle ab|ij\rangle + \langle ab|\delta v_{xc}|ij\rangle]Y_{jb}
\end{aligned} \tag{2.66}$$

$$-\omega Y_{ia} = (\epsilon_a - \epsilon_i)Y_{ia} + \sum_{jb}[\langle ib|aj\rangle + \langle ib|\delta v_{xc}|aj\rangle]Y_{jb}$$
$$+ \sum_{jb}[\langle ij|ab\rangle + \langle ij|\delta v_{xc}|ab\rangle]X_{jb}. \tag{2.67}$$

Because the time-dependent perturbation $g(rt)$ is negligibly small, $\Delta P_{ia}(\omega)$ and $\Delta P_{ai}(\omega)$ may be renamed as Y_{ia} and X_{ia}, respectively, and the pseudo-eigenvalue matrix equation may be constructed[34, 48, 67]

$$\begin{pmatrix} \mathbf{A} & \mathbf{B} \\ \mathbf{B}^* & \mathbf{A}^* \end{pmatrix} \begin{pmatrix} \mathbf{X} \\ \mathbf{Y} \end{pmatrix} = \omega \begin{pmatrix} \mathbf{1} & \mathbf{0} \\ \mathbf{0} & \mathbf{-1} \end{pmatrix} \begin{pmatrix} \mathbf{X} \\ \mathbf{Y} \end{pmatrix}.$$

Here, the matrix elements in the case of a hybrid xc-functional are written as

$$A_{ia,jb} = \delta_{ij}\delta_{ab}(\varepsilon_a - \varepsilon_i) + (ja|ib) - c_{HF}(ji|ab) + (1 - c_{HF})(ja|f_{xc}|ib) \tag{2.68}$$

and

$$B_{ia,jb} = (ja|bi) - c_{HF}(jb|ai) + (1 - c_{HF})(ja|f_{xc}|bi) \tag{2.69}$$

with the coefficient c_{HF} being a measure of the amount of non-local Hartree-Fock exchange in the xc-functional. The so-called xc-kernel is given by f_{xc}. However, applying the adiabatic local density approximation[34] allows for the use of xc-functionals instead of xc-kernels for the practical use of TD-DFT. The well-known Tamm-Dancoff approximation (TDA)[124] is obtained by neglecting the $\mathbf{B}$ matrix.

2.5.3 Performance and limitations of TD-DFT

Density functional theory is computationally very cheap, having a formal scaling of at most N^3, where N is the number of basis functions[53]. When xc-functionals without non-local HF exchange are used, density-fitting approaches for two-electron integrals can be employed to make the calculations even more inexpensive[125–127].

TD-DFT can be extremely useful when used appropriately. It provides a good description of low-lying excited states, with errors in the excitation energies on the order of approximately 0.1-0.5 eV. This is similar to the errors found for wave function-based methods. All things considered, TD-DFT can therefore yield reasonable absorption spectra at a comparatively low cost[39, 128].

Though widely used for the computation of excited states, TD-DFT is not without its flaws. Generally speaking, the broad success of TD-DFT is for the computation of local excited states, like $n\pi^*$ and $\pi\pi^*$[48]. However, Rydberg and charge transfer states pose

significant problems. The failure to describe Rydberg states is well-documented in the literature[129, 130], and this discussion will focus on charge-transfer failure[131–134].

The separated charges in long-range CT states exhibit an electrostatic attraction resulting from the non-local HF exchange potential. Since TD-DFT in conjunction with local xc-functionals does not take this effect into account, CT states are described incorrectly[131] . This leads to errors in the excitation energies of several eV and physically incorrect potential energy surfaces[131, 132, 135]. The inability to reliably compute excitation energies originates from the self-interaction error[136] in the orbital energies, which are taken from ground state DFT.[132] In addition to the self-interaction error, the $\frac{1}{R}$ asymptotic behavior of CT excited states is also not accurately reflected with local xc-functionals in TD-DFT. Here, R is the distance coordinate between the separated charges. This is because of a self-interaction error in TD-DFT from electron transfer in the CT excited state.[132]

The first step to remedying the CT problem of TD-DFT is determining whether or not it in fact exists, and if so, to what extent. There are several ways to determine this. The easiest strategy is simply to examine the molecular orbitals or the attachement/detachment density plots. There are, however, other approaches, that are particularly useful in more difficult cases. For one, the excitation energies for long-range excited states exhibiting CT character, when computed using local xc-functionals with no HF exchange, are equal to the energy of the accepting MO minus that of the donating MO[131, 132, 135]. For these cases TDA and pure TD-DFT results are also identical. Looking at trends in the order of states using a variety of hybrid functionals can also help. Increasing the amount of HF exchange reduces the CT error. This reduces the artificial lowering of the CT excited states computed by non-hybrid functionals. As a result, the energies of states with CT character should go up with increasing amounts of HF exchange. From the Hellmann-Feynman theorem, the exchange-correlation energy is calculated by[53]

$$\int_0^1 \langle \Psi(\lambda)|\mathbf{V}_{xc}(\lambda)|\Psi(\lambda)\rangle d\lambda \tag{2.70}$$

with λ giving the degree to which the electrons interact. If there is no interaction, $\lambda = 0$, while for exact interaction, $\lambda = 1$. It follows that

$$E_{xc} = (1 - a)E_{xc}^{DFT} + aE_x^{HF} \tag{2.71}$$

where $a = 1 - z$ and z gives the amount of HF exchange. For example, $z = 0.5$ for the BHLYP functional. The posterchild for the series of hybrid functionals emerging from

this discussion is the B3LYP functional

$$E_{xc}^{B3LYP} = (1-a)E_x^{LSDA} + aE_x^{HF} + b\Delta E_x^B + (1-c)E_c^{LSDA} + cE_c^{LSDA} \qquad (2.72)$$

where $a = 0.20$, $b = 0.72$, and $c = 0.81$. In more difficult cases, such as intramolecular charge transfer, computing the so-called Λ-parameter, which determines the amount of CT character[137–140], can be useful. This calculates the degree of spatial overlap of the relevant MOS and then performs a weighted summation on the basis of the excited state wave function[138]. When $\Lambda = 1$, CT is not an issue, but as Λ approaches 0, the CT problem increases.

Another route to treating CT with TD-DFT is to include HF exchange at a long-range electron-electron interaction. To this end, $\hat{A}$ is partitioned into a short range part (first term on the right-hand side) and a long range part (second term on the right-hand side)

$$\frac{1}{r_{12}} = \frac{1 - erf(\mu r_{12})}{r_{12}} + \frac{erf(\mu r_{12})}{r_{12}} \qquad (2.73)$$

with $r_{12} = |r_1 - r_2|$. CAM-B3LYP[141], an example of such a long-range corrected functional, combines B3LYP[117] at short range with increasing amounts of HF exchange at the longer range.

2.6 Computation of absorption and fluorescence spectra

Molecules can be excited to higher electronic states by absorption of a photon, $E = h\nu$. The wavelengths of light necessary for electronic transitions to occur are generally within the UV-Visible region of the electomagnetic spectrum. These processes are very fast, occurring on the order of 10^{-15} s[142]. According to the Franck-Condon principle[143], electronic transitions take place much faster than the nuclei of the system can adapt, i.e. vertical transitions take place. The vertical transition from the electronic ground state to an excited state by light absorption is depicted in Figure 2.2. As a result of the vertical excitation, higher vibrational levels of the excited state can be populated.

Upon irradiation with light, an oscillating dipole is induced as a result of the response of the molecules of a sample to the applied field. Two identical charges q separated by a distance $\vec{d}$ have a dipole moment μ given by: $\mu = q\vec{d}$. As the molecule is excited by light, its electron density is redistributed, and the amount of charge separation that occurs is described by the polarizability α of the electron density. The polarizablility is described by $\alpha = \mu_{TM}/F_{el}$, with the transition dipole moment μ_{TM} and the electrical force F_{el}.
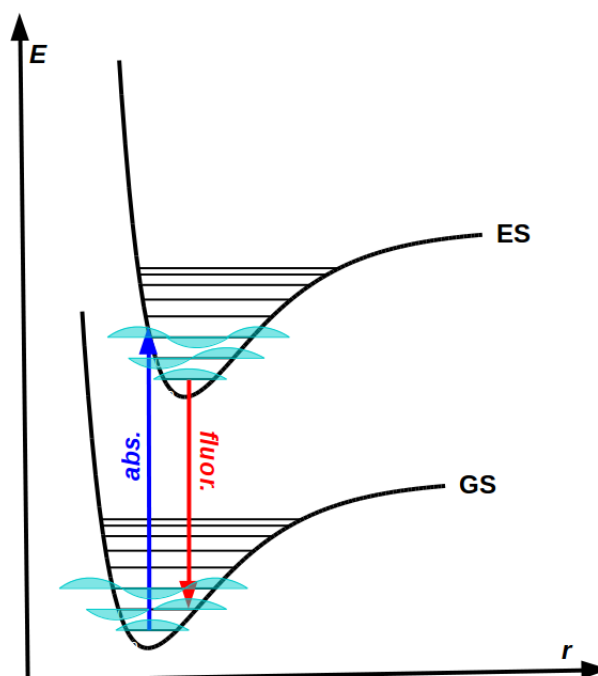
FIGURE 2.2: The Franck-Condon Principle

The transition moment integral[144] can be written as

$$\mu_{TM} = \int \Psi_f^* \mu \Psi_i d\tau \tag{2.74}$$

with Ψ_f and Ψ_i being the wave functions of the final and initial states, respectively, and μ being the dipole moment of the molecule. The strength of an electronic excitation is then determinable by the oscillator strength f, which is proportional to $(\mu_{TM})^2$[145]. The oscillator strength is a unit-less value, and will be used throughout this work to rate the strengths of the various electronic transitions presented.

2.7   Analysis of electronically excited states

Computation of the electronic spectra of a system is frequently accompanied by a study of the nature of the excited states for that system. Often times, it is sufficient to study simply the MOs involved in a given electronic transition. Looking at the MOs gives insight into the nature of a transition, for example if it is an $n\pi^*$ or $\pi\pi^*$ transition. The orbitals involved in the transition can in this sense be used to determine the order of excited states and to compare this order to that for similar molecules. MO analysis is indeed a good approach if the excited state is represented by one major singly-excited Slater determinant. It can become extremely difficult to comb through the electronic structure of excited states if the excited state wave function is an expansion of several

Slater determinants with coefficients of the same magnitude[34]. In these instances, one goes beyond MOs and employs the tools offered by transition density analysis, such as natural transition orbitals, or difference density analysis, such as attachment and detachment density plots (Att/Det plots).

2.7.1 Transition density analysis

The transition density $T(r)$ couples the electronic ground state with a given excited state. The transition density matrix $(\mathbf{T})_{ia}$ is a rectangular matrix of the dimensions $n_{occ} \times n_{virt}$ that can be used to obtain a compact description of an electronic excitation via a decomposition into so-called natural transition orbitals (NTOs). The transition density matrix is given by[34]

$$(\mathbf{T})_{ia} = \langle \phi_i | \hat{T}(r) | \phi_a \rangle. \tag{2.75}$$

Since it cannot directly be diagonalized, one applies the corresponding orbital transformation of Amos and Hall[146]. Based on a singular value decomposition of the $(\mathbf{T})_{ia}$, it yields pairs of occupied and virtual NTOs[147–149]. The decomposition of the transition density matrix is written using the unitary matrices $\mathbf{U}$ and $\mathbf{V}$ as[150]

$$\mathbf{D}^{0\alpha,[MO]} = \mathbf{U} diag(\sqrt{\lambda_1}, \sqrt{\lambda_2}, ...) \mathbf{V}^T \tag{2.76}$$

$\mathbf{U}$ gives the set of initial (hole) orbitals, while $\mathbf{V}^T$ the set of final (electron) orbitals. In this way, only a select number of configurations are required to describe the electronically excited states. Indeed, NTOs are extremely useful in determining the ordering of the states, since an electronic transition can be described by a single NTO pair. This holds even in cases where the canonical MO basis indicates that the transition is very mixed. Natural orbitals (NOs) offer another tool for excited state analysis. In contrast to NTOs, natural orbitals (NOs) are obtained by diagonalizing the ground state single-electron density, and are thus eigenfunctions of the spinless one-particle electron-density matrix[148].

2.7.2 Difference density analysis

Another option for investigating electronically excited states beyond the simple MO picture are attachment and detachment densities. For this purpose, analysis of the difference density matrix is necessary. Difference density analysis is indeed frequently

performed[151–154]. The difference density matrix is defined as[34]

$$\Delta = \mathbf{P}_{ES} - \mathbf{P}_{GS} \tag{2.77}$$

where $\mathbf{P}_{ES}$ is the single-electron density matrix of the excited state, and $\mathbf{P}_{GS}$ the corresponding matrix of the ground state. Diagonalizing Δ yields Att/Det plots[155, 156]

$$\mathbf{U}^\dagger \Delta \mathbf{U} = \delta. \tag{2.78}$$

Here, $\mathbf{U}$ is the unitary transformation matrix which contains the eigenvectors of the difference density. The diagonal matrix containing the eigenvalues is given by δ. The diagonal matrix δ can be split into two matrices $\mathbf{A}$ and $\mathbf{D}$, representing the attachment and detachment densities, respectively. The detachment density is the sum of all eigenvectors of the difference density matrix whose eigenvalues are negative. The attachment density is, in contrast, the sum of all NOs of the difference density matrix whose occupation numbers are positive, weighted by the absolute value of their occupation. Thus[34]

$$.\Delta = \mathbf{A} - \mathbf{D} \tag{2.79}$$

In practice, detachment density can be seen as the part of the single-electron ground state density that is removed during the electronic transition. Attachment density is the rearrangement of this density. Taken together, the Att/Det plots characterize the transition from D $\rightarrow$ A. This offers another important advantage over MO analysis, as one can view electronic transitions as if they corresponded to simple single-orbital replacements. Examples of applications beyond those performed in this work are found in the literature[157–160].

2.8   Computational treatment of solvation

It is well-known that the interactions between solute and solvent can strongly impact molecular structures, energies, and properties, see for example[161–163]. This motivates the need to model such interactions in order to compare computation with experimental data, since experiments are often carried out in solution. One route to take in this regard is to use discrete interaction modeling, for example one can treat the majority of a solvated system classically with molecular mechanics, while employing quantum mechanics only for the most chemically relevant part of said system[164–166]. Another approach is to use continuum solvation models.[167–170] In such models, the solute is embedded in a cavity existing within a continuous solvent described by its macroscopic properties.
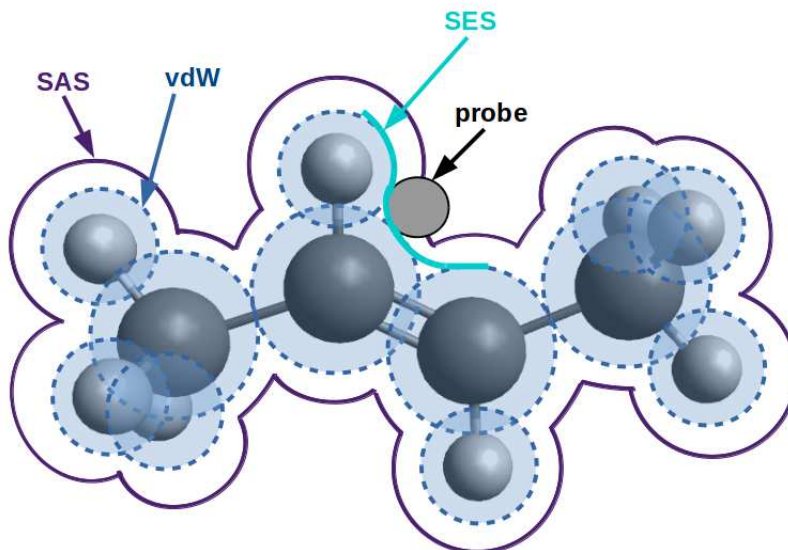
FIGURE 2.3: The van der Waals, solvent accessible surface, and solvent excluded surface for an example system.

For contiuum solvation models, there are several ways to effectively define the cavity housing the solute. One initially places overlapping van der Waals spheres centered on the nuclei of the molecule, thus generating the so-called van der Waals (vdW) surface. A thorough explanation of these surfaces along with more extensive visualizations are given in the literature[171]. The solvent accessible surface (SAS) what is traced by the center of a probe sphere as it moves along the spheres of the vdW surface. In contrast, the solvent excluded surface (SES) is what is traced by the most inside-facing (i.e. toward the solute) point of the probe sphere as it moves along the vdW surface. These surfaces are depicted in Figure 2.3 for improved visualization of the cavity construction. The physical problem is simple: a charge density inside a cavity (Γ) existing within a solvent continuum with dielectric permittivity ε. Within this model, the polarization of the solute's charge distribution (ρ_M) must obey the Poisson equation[172]

$$- \nabla[\varepsilon(\mathbf{r}) \nabla V(\mathbf{r})] = 4\pi \rho_M(\mathbf{r}) \tag{2.80}$$

with $V_R(\mathbf{r})$ being the reaction potential resulting from the polarization of the dielectric and $V_M(\mathbf{r})$ resulting from ρ_M. Here,

$$V(\mathbf{r}) = V_M(\mathbf{r}) + V_R(\mathbf{r}) \tag{2.81}$$

where $V_R(\mathbf{r})$ is the reaction potential generated by the polarization of the dielectric and $V_M(\mathbf{r})$ arises from ρ_M. By introducing an apparent surface charge density (σ) on the

cavity, the reaction potential can be written as[172]

$$V_R = V_\sigma(\mathbf{r}) = \int_\Gamma \frac{\sigma(\mathbf{s})}{|\mathbf{r} - \mathbf{s}|} d^2\mathbf{s}. \tag{2.82}$$

How σ is specifically defined gives rise to a series of PCM-type models, such as DPCM[173], IPCM[174], SCIPCM[174], IEFPCM[173, 175–193], and C-PCM[182, 193]. C-PCM, as will become evident in the discussions to follow, is the implementation of COSMO in the PCM framework.

2.8.1 The conductor-like screening model (COSMO)

The conductor-like screening model (COSMO)[194, 195] belongs to the class of apparent surface charge dielectric continuum models (ASMs)[195]. This means that a cavity Γ is first built which separates the solute from the solvent (dielectric continuum). A set of m surface segments at positions $\underline{t}_I$ with areas s_i describe the cavity. A set of apparent surface charges $\underline{q} = q_1, ..., q_m$ on the m segments gives the dielectric polarization of the solvent. A set of linear equations $\underline{\underline{A}}q + \underline{\underline{B}}Q = 0$ is then used to calculate these charges. Here, Q represents the charge distribution of the solute, and $\underline{\underline{A}}$ and $\underline{\underline{B}}$ are linear operators constructed based on the boundary condition. Defining $\underline{\Phi} = \Phi_1, ..., \Phi_m$ as the solute electrostatic potential on the cavity, the increase in energy of the system as a result of the polarization of the continuum is given by $E_{tot} = 0.5\Phi$[195].

COSMO employs a scaled boundary condition in lieu of the exact dielectric boundary condition, which is the case for other ASMs. For use of the exact boundary condition, the linear operators $\underline{\underline{A}}$ and $\underline{\underline{B}}$ are[195]

$$\underline{\underline{A}}_D = \underline{\underline{\mathbf{E}}}^\perp - \frac{4\pi\varepsilon}{\varepsilon - 1}\underline{\underline{\mathbf{S}}}^{-1} \tag{2.83}$$

and

$$\underline{\underline{B}}_D = \underline{\underline{\tilde{E}}}^\perp. \tag{2.84}$$

The $m \times m$ matrix $\underline{\underline{\mathbf{E}}}^\perp$ provides the normal component of the electric field due to the polarization charges $\underline{q}$ and acting on each surface segment, and the operator $\underline{\underline{\tilde{E}}}^\perp$ yields the normal component of the solute electric field on the segments. According to electrostatics[196], dielectric screening energies scale according to

$$f(\varepsilon) = \frac{\varepsilon - 1}{\varepsilon + x} \tag{2.85}$$

where ε is of course the dielectric permittivity of the medium and $x = 0 - 2$. This means that the screening effects in solvents like water, which is a strong dielectric ($\varepsilon = 78.4$),

can be readily approximated by those of a conductor ($\varepsilon = \infty$)[194]. COSMO takes advantage of this idea and employs the comparatively simple boundary conditions for a conductor, while scaling the screening charges with the function $f(\varepsilon)$ according to the desired solvent. The COSMO operators are then given by[195]

$$\underline{\underline{A}}_C = \underline{\underline{V}} \tag{2.86}$$

and

$$\underline{\underline{B}}_C = f(\varepsilon)\underline{\underline{\tilde{V}}}. \tag{2.87}$$

Here, V is the matrix that generates the electrostatic potential resulting from the polarization charges on the individual surface segments. $\underline{\underline{V}}$ is the Coulomb matrix of surface segments, whose diagonal elements give the self-potential of a charge q_i spread out over the area s_i of segment i. $\underline{\underline{\tilde{V}}}$ is the corresponding operator which generates the electrostatic potential of the solute on the segments[195]. In the original formulation of COSMO, x was set to 0.5, which is ideal for neutral systems[193]. It is also known that $x = 0.5$ yields results of sufficient accuracy until a dielectric constant $\varepsilon = 2$. The implementation of COSMO within the PCM framework results in the C-PCM method, which will be discussed in more detail in the following.

2.8.2 The conductor-like polarizable continuum model (C-PCM)

The C-PCM model, another popular ASM, was first formulated by Barone and Cossi in 1998[182] and the following discussion closely follows the description of the method presented there. All presented equations in this subsection can be found in this reference as well. First, one acknowledges that the molecular Hamiltonian will be perturbed by the solvent. That is,

$$\hat{H} = \hat{H}^0 + \hat{V} \tag{2.88}$$

with $\hat{H}^0$ as the Hamiltonian of the solute in gas phase and $\hat{V}$ representing the electrostatic interactions between the solute and solvent. A cavity is built up by a set of spheres centered on the atoms of the solute molecule, then evened out to yield the solvent-excluding surface. It is then broken down into a set of surface segments called tesserae i of areas S_i and charges q_i. One can then write the conductor-like boundary condition

$$V(\overrightarrow{r}) + \sum_i^{tesserae} V_{q_i}(\overrightarrow{r}) = 0 \tag{2.89}$$

with V describing the electrostatic potential resulting from the solute charges and V_{q_i} that resulting from the polarization charges. Variational minimization via an SCF procedure yields the free energy of the solute

$$G = \langle \Psi | \hat{H}^0 | \Psi \rangle + \frac{1}{2} \langle \Psi | \hat{V} | \Psi \rangle. \tag{2.90}$$

The vector of polarization charges, $\overrightarrow{Q}$ is given by

$$\mathbf{A} \overrightarrow{Q} = -\overrightarrow{V} \tag{2.91}$$

with the matrix elements of A

$$A_{ii} = 1.07 \sqrt{\frac{4\pi}{S_i}} \tag{2.92}$$

and

$$Aij = \frac{1}{|\overrightarrow{r}_i - \overrightarrow{r}_j|}. \tag{2.93}$$

Partitioning the potential such that one obtains a set of charges Q^N for the nuclei and Q^e for the electrons, one can write the Hamiltonian as

$$\mathbf{H} = \mathbf{H}^0 + \frac{1}{2}(\mathbf{j} + \mathbf{y}) + \frac{1}{2}\mathbf{X} + \frac{1}{2}U_{NN} \tag{2.94}$$

with the gas phase Hamiltonian

$$\mathbf{H}^0 = \mathbf{h}^0 + \frac{1}{2}G^0 + V_{NN}. \tag{2.95}$$

Here, $\mathbf{j}$ describes the interactions between electronic charges and solute nuclei, and $\mathbf{y}$ those between nuclear charges and solute electrons. $\mathbf{X}$ gives the interactions between the electronic charges and the electrons, and U_{NN} those between nuclear charges and nuclei.

In the COSMO model, one scales the polarization charges such that Gauss law is valid for the total polarization charge. In this respect, the charges are multiplied by a factor $\frac{\varepsilon-1}{\varepsilon}$ with the dielectric constant ε. For the surface polarization charges, one therefore has

$$\sum_i q_i^N = q_{Gauss}^N = -\frac{\varepsilon-1}{\varepsilon} \sum_n^{nuclei} Z_n \tag{2.96}$$

and

$$\sum_i q_i^e = q_{Gauss}^e = \frac{\varepsilon-1}{\varepsilon} N^e. \tag{2.97}$$

These conditions are not perfectly upheld in practice as a result of numerical and physical errors.

Recalling the expression of the molecular free energy in solution, here taking only electrostatic (es) interactions into account,

$$G_{es} = \langle \Psi | \hat{H}^0 | \Psi \rangle + \Delta G_{es} \tag{2.98}$$

where

$$\Delta G_{es} = \frac{1}{2} \sum_{i}^{tesserae} q_i V_i. \tag{2.99}$$

Should one consider non-electrostatic interactions as well, the free energy derivatives become

$$G^{\alpha} = G_{es}^{\alpha} + G_{cav}^{\alpha} + G_{diss}^{\alpha} + G_{rep}^{\alpha} \tag{2.100}$$

with the nuclear coordinate α. The free energy of cavity formation is given by G_{cav}, and G_{diss} with G_{rep} give the dispersion and repulsion terms, respectively.

Remembering the scaling factor $\frac{\varepsilon-1}{\varepsilon}$, one can write a highly computationally applicable equation for ΔG_{es}^{α}, for which a charge derivative calculation is not necessary

$$\Delta G_{es}^{\alpha} = \sum_{i} q_i V_i^{\alpha} + \frac{1}{2} \frac{\varepsilon}{\varepsilon - 1} \sum_{ij} A_{ij}^{\alpha} q_i q_j. \tag{2.101}$$

The free energy derivatives, given in equation 2.100, are employable in optimizations for the computation of relaxation caused by the solvent environment.

Solvation models are used throughout this work to effectively and inexpensively treat the effects of a solvent environment on the photochemical processes investigated. Though a quantum chemical investigation begins with an initial treatment of the system in the gas phase, the development and use of explicit and implicit solvation models is necessary for comparison with experimental spectra.

Chapter 3

Pigment Yellow 101: Potential energy surfaces and kinetic modeling for excited state dynamics

3.1 Motivation and Background

Pigment Yellow (PY101), more formally known as 2,2'-dihydroxy-1,1'-naphthalazine, is one of few fluorescent yellow pigments that are commercially available[197]. It has been known since 1899 and boasts a long industrial past[198–200], having been used, for example, as viscose pigment and printing ink[39]. Despite its widespread industrial applicability, its unique fluorescent properties and high photostability were historically not well understood. Computation of the excited states of PY101 has led to significant insight into its photochemistry. For example, the S_1 state of PY101 is a $\pi\pi^*$ optically allowed state characterized by a HOMO-LUMO transition[39, 40]. In contrast, the S_1 state for its non-fluorescent relative, 1,1-Napthaldazine, is a forbidden $n\pi^*$ state. By way of a conical intersection with the electronic ground state along the bending mode of the central bisazomethine unit, efficient nonradiative decay of 1,1-Napthaldazine is possible[39, 40]. This bending mode does not open up a nonradiative deactivation channel in PY101, however. The excited state dynamics of PY101 have been studied with time-resolved spectroscopy in past work[41]. Notably, the experimental transient absorption spectra and calculated amplitude spectra[41] indicated that in order to describe the decay of the S_1 state of PY101, five time constants $\tau_1 = 150$ fs, $\tau_2 = 3$ ps, $\tau_3 = 63$ ps,

$\tau_4 = 500ps$, and $\tau_5 = 1.3$ ns are needed[41], suggesting a potentially complicated excited state dynamics picture.

Past analysis of the S_1 potential energy surface led to the development of a model for the excited state dynamics of PY101[41, 42]. To this end, stable isomers, depicted in Figure 3.1, in the electronic ground and S_1 states were identified. Combining the knowledge of these stable isomers with experimentally-determined spectral signatures of the intermediates, the foundation for description of the excited state dynamics was set. This model, together with initial relaxed scans of the S_1 surface, suggested that most of the initial population of the excited state will reach only the *exo-trans*-diol (**Ax**) minimum before decaying fluorescently back down to the electronic ground state[42]. This *exo-trans*-diol form is indeed the most energetically stable. A minority of the population may reach the *exo-trans*-keto (**Bx**) isomer via excited-state intramolecular proton transfer (ESPT). A still smaller population was thought to be able to reach the **Cx** and **Ex** minima via *trans-cis exo-endo* isomerizations[42].

The computational study of photoinitiated processes in medium-sized and large molecules is currently a staggering challenge in modern theoretical chemistry. Particularly challenging is the computation of dynamic quantities such as time scales, reaction rates, and quantum yields. PY101 not only exhibits fascinating photochemistry, it is also relatively large (42 atoms) and therefore ideal as a model for these types of investigations. The electronic struture problem must be reliably solved and nuclear motion taken into consideration. It is best if both of these aspects contain significant quantum effects with predictability. The main challenge, however, is that full quantum dynamics calculations for systems of more than approximately 20 degrees of freedom are reasonably feasible. In fact, even the calculation of the potential energy surfaces, which are important ingredients in a quantum dynamics simulation, is impossible to undertake with desirable accuracy. It is therefore critical to develop simple kinetic models for treatment of larger systems which allow for at least a qualitative photochemical understanding. In this vein, one follows in the footsteps of Rice-Ramsperger-Kassel-Marcus theory, transition state theory, or the Arrhenius equation[201–204]. The development of such models should not only aid in the interpretation of time-resolved spectroscopic measurements, but also help to develop and design new experiments. PY101 is ideal for such purposes, particularly as it has been thoroughly investigated both empirically and theoretically. This project is therefore twofold. The first part involves the computation of relaxed surface scans along photochemically relevant coordinates. This is done also considering solvent effects in the ground state. The second part deals with the development of a non-equilibrium kinetic rate model for the purposes of simulating the excited state kinetics and determining the importances of the different conformers. Since PY101 has an reactive, isolated S_1

state, multi-state and non-adiabatic effects should not determine the photochemistry. In principle, its dynamics can therefore be treated as *hot* ground state dyanamics.

The six most stable ground state conformers are shown in Figure 3.1. These are *exo-trans*-diol (**A**), *exo-trans*-keto (**B**), *endo-trans*-diol (**C**), *endo-trans*-keto (**D**), *exo-cis*-diol (**E**), and *exo-cis*-keto (**F**). Section 3.3 provides a more detailed discussion of the structural intricacies of PY101, and Section 3.4 discusses the static properties of PY101 in the excited state. In Section 3.5, relaxed surface scans are presented for the important reaction coordinates connecting these six conformers in the first excited state and the corresponding energy barriers are estimated from these potential curve calculations, i.e. full transition state searches and optimizations were not performed. The barriers reported from the recent literature[205] were determined in the same way. In Section 3.6, the kinetic model used to estimate the distribution of the S_1 population of PY101 among the corresponding excited state conformers **Ax**, **Bx**, **Cx**, and **Ex**, is presented. The efficacy of the model is described in relation to experimental data. First, however, the computational details are provided in Section 3.2.

(A) *exo-trans*-diol **(B)** *exo-trans*-keto **(C)** *endo-trans*-diol

(D) *endo-trans*-keto **(E)** *exo-cis*-diol **(F)** *exo-cis*-keto
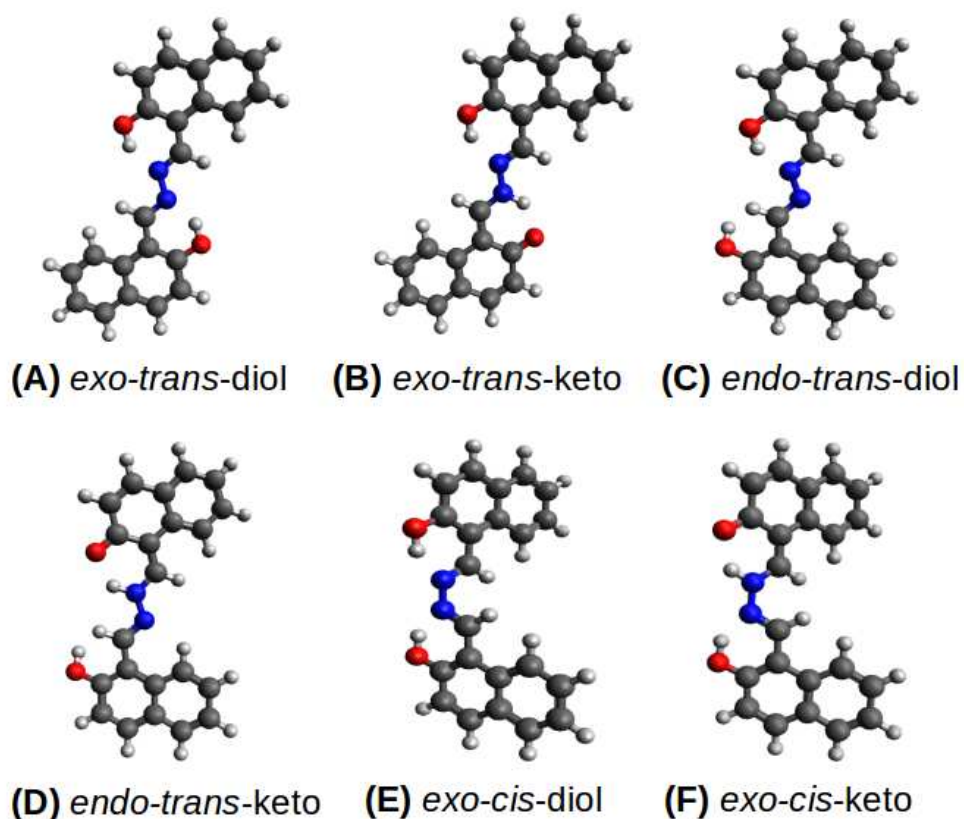
FIGURE 3.1: The six most stable ground state isomers of PY101.

It should be noted at this time that some of the information presented in this chapter has been previously published by myself and co-authors as

K. Fletcher, A. Dreuw, and S. Faraji, Potential energy surfaces and approximate kinetic model for the excited state dynamics of Pigment Yellow 101, *Comp. Theo. Chem.*, **2014**, *1040-1041*, 177-185.

3.2 Computational Methods

Ground state optimizations presented in the literature[205] were performed using density functional theory[61, 62, 64] in combination with the Becke-half-and-half-Lee-Yang-Parr (BHLYP)[118] and B3LYP[117] exchange-correlation (xc) functionals. All calculations reported from the most recent literature on PY101[205] were done using the ORCA[206] and Q-Chem[207] program packages. It should be noted that the DZP basis set implemented in ORCA is not the same basis set as Dunning's origingal double-ζ plus polarization basis set[208]. TD-DFT in ORCA using hybrid functionals also forces the use of the Tamm-Dancoff-Approximation (TDA)[124]. Møller-Plesset perturbation theory of second order (MP2)[55] was also used[42]. Prior work revealed that the optimized geometries of PY101 in the ground state were independent of the xc-functional/basis set combination chosen[40, 42]. Benchmarking of the most important slice through the S_1 potential energy surface, the twisting coordinate around the C-N-N-C central dihedral angle, with respect to RI-CC2[209, 210] calculations showed that the BHLYP/DZP level of theory yields accurate results[137]. The charge transfer failure of TD-DFT[131, 132, 134, 135] contributes to the error in the curves computed along this coordinate, as there is a strong charge-transfer character for the geometry at a 90°torsion angle. The BHLYP functional was selected instead of the long-range corrected CAM-B3LYP[141], for example, because BHLYP has been shown to generate reliable results for a variety of reactions. The use of BHLYP can, however, still lead to a slight underestimation of the charge transfer states. For the C-N-N-C twisting coordinate, this error is a mere 0.1 eV[137].

Ground and excited state geometries optimized and presented here were computed using DFT and TD-DFT[32–34],respectively, and employing the BHLYP xc-functional and the cc-pVDZ[208, 211, 212] basis set as implemented in Gaussian. It should be noted that the half-and-half BHLYP functional implemented in Gaussian is not the same as Becke's original[118]. In the case of **Fx**, the computed maximum displacements for convergence, when calculated using the analytically computed Hessian over the course of the frequency calculation, do not fully converge but are extremely close to the cutoff criteria. Thus, these structures are likely extremely close to the real stationary point, especially since convergence in the optimization calculation is achieved, where an estimated Hessian is used. Geometric parameters and vertical excitation energies are computed both in the
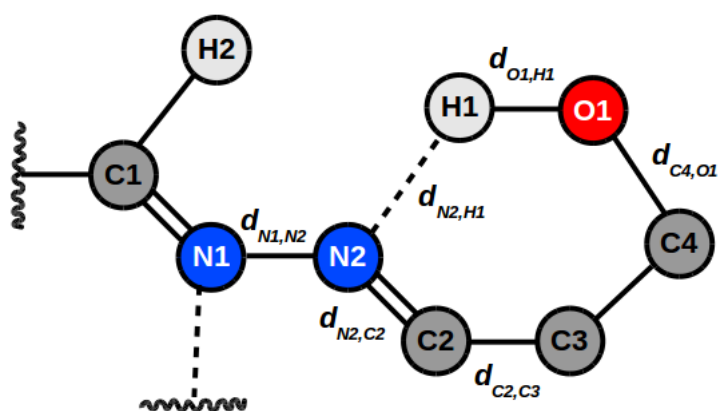
FIGURE 3.2: Geometric parameters for of PY101 for comparison of the isomers.

gas phase and employing the C-PCM model[182, 193] to treat solvation in water. Vertical excited states were also computed using the C-PCM model for dimethylsulfoxide (DMSO). Additional features in the expermiental absorption and fluorescence spectra of PY101 arose when solvated in DMSO[41]. Therefore, a look into potential solvent effects is valuable. As will be shown in this work, solvation in water and DMSO yield nearly identical results. Relaxed surface scans along the S_1 state were carried out among the six most stable conformers and the energy barriers among these estimated. The effect of solvation in the S_1 state is also treated. All calculations were performed using Gaussian 09, Revision D.01[213].

3.3 Structure of PY101

A search of the potential energy surface in previous work led to the identification of six most stable isomers of PY101. In this section, they are presented in detail both in the ground state and in the first singlet electronically excited state, employing both gas phase and C-PCM models. The relevant bond lengths and angles for distinguishing the isomers are given in Figure 3.2 and their values presented in Tables 3.1, 3.2, 3.3, and 3.4. While this type of structural analysis has been performed before, it has only been done for PY101 in the gas phase. Therefore, the C-PCM model to treat solvation in water is used here for the first time in order to gain an understanding of how the structures, and thus potential photochemical properties, of PY101 may differ in solution compared to in vacuum.

Comparing first the central N-N bond length in Tables 3.1 and 3.2. These do not change with any significance moving from gas phase to solution. Indeed, the vast majority of the structural characteristics are uneffected. However, there are a couple of striking

Isomer	$d_{N1,N2}$	$d_{N2,C2}$	$d_{C2,C3}$	$d_{C4,O1}$	$d_{O1,H1}$	$d_{N2,H1}$	$\angle C1,N1,N2,C2$	$\angle N2,C2,C3,C4$
A	1.368	1.284	1.445	1.325	0.980	1.720	-180.0	0.000
B	1.351	1.283	1.448	1.329	0.973	1.753	-180.0	0.000
	1.351	1.325	1.381	1.241	1.707	1.032	-180.0	0.000
C	1.373	1.285	1.445	1.325	0.981	1.711	-177.7	0.900
D	1.350	1.327	1.381	1.240	1.724	1.030	-177.9	-0.500
E	1.369	1.280	1.451	1.326	0.979	1.723	70.90	-0.900
F	1.361	1.283	1.447	1.325	0.977	1.731	35.70	2.700
	1.361	1.328	1.381	1.238	1.732	1.024	35.70	1.000

TABLE 3.1: Geometric parameters of the six most stable ground-state isomers of PY101 in gas phase, optimized at the BHLYP/cc-pVDZ level of theory.

differences. For one, on one side of **B**, the $d_{O1,H1}$ distance is about 0.05 eV longer in solution than in the gas phase. This may imply an easier transition from **B** to **A** in the ground state. In addition, the **D** isomer loses its central dihedral angle of $-0.500°$ when solvation is treated. This could imply less flexibility of this angle in the ground state. Still, overall, these effects are extremely modest to miniscule, and no observed change in the ground state potential energy surface of PY101 is expected.

Isomer	$d_{N1,N2}$	$d_{N2,C2}$	$d_{C2,C3}$	$d_{C4,O1}$	$d_{O1,H1}$	$d_{N2,H1}$	$\angle C1,N1,N2,C2$	$\angle N2,C2,C3,C4$
A	1.369	1.284	1.447	1.329	0.982	1.708	-180.0	0.000
B	1.353	1.282	1.449	1.332	0.975	1.742	180.0	0.000
	1.353	1.321	1.387	1.247	1.754	1.028	180.0	0.000
C	1.374	1.284	1.447	1.329	0.984	1.701	-178.6	0.400
D	1.354	1.321	1.387	1.246	1.767	1.027	-179.2	0.000
E	1.369	1.280	1.452	1.330	0.981	1.705	66.30	-0.300
F	1.364	1.283	1.447	1.329	0.979	1.716	36.30	2.000
	1.364	1.322	1.389	1.247	1.748	1.022	36.30	0.600

TABLE 3.2: Geometric parameters of the six most stable ground-state isomers of PY101 using C-PCM for water, optimized at the BHLYP/cc-pVDZ level of theory.

Comparing now the ground state geometric parameters with those for the excited state optimized geometries in both the gas phase and employing C-PCM to treat solvation. First, $d_{N1,N2}$ decreases here appreciably, by about 0.05-0.07 Å. Indeed, this distance is also shorter for the structures optimized in solution than in the gas phase. The second distance considered, $d_{N2,C2}$, is increased in the excited state compared to the ground

state, by about 0.02-0.06 Å. The $d_{C2,C3}$ distance is decreased by about 0.04-0.05 Å in most cases, but in **D**, the distance is lengthened by about 0.02 Å. Overall, the $d_{C4,O1}$ and $d_{O1,H1}$ distances do not vary appreciably, however, for **D** and **B**, the $d_{O1,H1}$ are increased by almost 0.1 Å in the excited state, indicating a potential facilitation of ESPT processes for these isomers in the excited state. Looking at the final distance compared, $d_{N2,H1}$, an increase in the excited state is observed in most cases, though this increase is not particularly appreciable. Still, for **E**, for example, the distance is increased by about 0.08 Å, indicating possibly easier ESPT in the excited state.

Isomer	$d_{N1,N2}$	$d_{N2,C2}$	$d_{C2,C3}$	$d_{C4,O1}$	$d_{O1,H1}$	$d_{N2,H1}$	$\angle C1,N1,N2,C2$	$\angle N2,C2,C3,C4$
A	1.308	1.329	1.412	1.319	0.989	1.672	-180.0	0.000
B	1.312	1.323	1.415	1.326	0.977	1.720	-180.0	0.000
	1.312	1.330	1.414	1.250	1.632	1.047	-180.0	0.000
C	1.310	1.328	1.413	1.317	0.992	1.661	-179.3	0.000
D	1.316	1.326	1.416	1.248	1.656	1.044	-179.5	-0.900
E	1.305	1.336	1.417	1.315	0.997	1.634	14.90	-1.300
F	1.313	1.324	1.419	1.321	0.982	1.695	9.40	0.900
	1.313	1.338	1.413	1.246	1.664	1.036	9.40	-3.900

TABLE 3.3: Geometric parameters of the S_1 state isomers of PY101 in gas phase, optimized at the BHLYP/cc-pVDZ level of theory.

The dihedral angles are compared next. Rotation about a dihedral angle is generally characterized by a higher barrier than ESPT, particularly for ESPT over such short distances as observed for PY101. Interestingly, for example, the $\angle C1, N1, N2, C2$ angle for **E** is decreased by over 20° in the excited state compared to the ground state. Most other angles remain effectively the same. For **E**, the final angle $\angle N2, C2, C3, C4$ is also decreased marginally in the excited state, however this should have very little if any impact on the dynamics.

Finally, the geometric parameters for the excited state structures in the gas phase and employing C-PCM for water are compared. First, the $d_{N1,N2}$ distance is slighltly decreased, hindering dihedral rotation about this angle in solution compared to in the gas phase. Indeed, this angle is also smaller by about six degrees for **Ex** in solution compared to the gas phase. for **Dx**, to a lesser extent for **Bx**, the $d_{O1,H1}$ distance is increased when the C-PCM model is employed. That is, ESPT is likely facilitated in solution compared to the gas phase. For the most part, the structural changes are, however, modest, and it is likely that only small changes in barriers among the excited states will occur moving from gas phase to solution. The overall picture of the excited

Isomer	$d_{N1,N2}$	$d_{N2,C2}$	$d_{C2,C3}$	$d_{C4,O1}$	$d_{O1,H1}$	$d_{N2,H1}$	$\angle C1,N1,N2,C2$	$\angle N2,C2,C3,C4$
A	1.293	1.341	1.403	1.323	0.989	1.673	-180.0	0.000
B	1.298	1.332	1.408	1.327	0.980	1.711	180.0	0.000
	1.298	1.340	1.407	1.254	1.675	1.041	180.0	0.000
C	1.296	1.341	1.403	1.322	0.991	1.664	-179.8	0.000
D	1.300	1.338	1.406	1.252	1.693	1.040	-179.8	-0.200
E	1.295	1.346	1.408	1.320	0.999	1.617	9.000	-0.800
F	1.301	1.333	1.411	1.324	0.984	1.678	1.700	0.100
	1.301	1.344	1.410	1.253	1.676	1.032	1.700	-0.700

TABLE 3.4: Geometric parameters of the S_1 state isomers of PY101 using C-PCM for water, optimized at the BHLYP/cc-pVDZ level of theory.

state dynamics should, however, remain the same. To obtain a sense of which structures will be most commmon among the excited state population, the relative energies of the isomers are compared next.

Isomer	B3LYP/DZP[42]	BP86[214, 215]/DZP[42]	MP2/6-31G*[42]	BHLYP/DZP[42]	BHLYP/cc-pVDZ	BHLYP/cc-pVDZ (C-PCM)
A	0.00	0.00	0.00	0.00	0.00	0.00
B	0.21	-	0.35	0.25	0.28	0.19
C	0.50	-	0.41	0.48	0.45	0.40
D	0.64	0.67	0.68	0.66	0.68	0.54
E	0.26	0.24	0.18	0.27	0.27	0.25
F	0.44	0.38	0.35	0.50	0.53	0.41

TABLE 3.5: Relative energies (eV) of the six most stable ground state conformers of PY101.

Tables 3.5 and 3.6 show the relative energies of the six most stable isomers of PY101 in the S_0 and S_1 states, computed at various levels of theory both in gas phase and using the C-PCM model. While thorough benchmarking of the TD-DFT methods had revealed that the BHLYP functional was necessary to accurately describe the PY101 system, several methods are used for comparing the relative energies of the isomers in the ground and excited states. Regardless of method, the **A**/**Ax** structure is consistently found to be the most stable, followed by **B**/**Bx**. Overall, the relative energies are all in remarkably good agreement. The **A(x)** and **B(x)** structures are followed by the **E(x)**

isomer in stability. Indeed, in the ground state, the **B** and **E** isomers are almost identical in stability, while only in the excited state is **Bx** about 0.14 eV lower in energy than **Ex**. Isomers **C** and **F** also have approximately the same energy in the ground state, while in the S_1, **Fx** is 0.26 eV lower in energy that **Cx**. Isomer **D(x)** is the least stable throughout.

Isomer	B3LYP/DZP	BHLYP/DZP	BHLYP/cc-pVDZ	BHLYP/cc-pVDZ (C-PCM)
Ax	0.00	0.00	0.00	0.00
Bx	0.07	0.13	0.15	0.12
Cx	0.51	0.49	0.48	0.42
Dx	0.46	0.59	0.55	0.48
Ex	0.22	0.27	0.28	0.26
Fx	-	0.23	0.26	-

TABLE 3.6: Relative energies of the six most stable excited state conformers of PY101.

Due to the consistent relative stability of **Ax** compared to all other isomers, most of the excited state population is expected to both initially land in and remain in this form. Indeed, Ahmedova et al. also found that the diol isomer is the most common form of 4,4ʹ-dihydroxy-1,1ʹ-napthaldazine[216], further supporting that the diol form should be the most stable for PY101 and its relatives. Potentially, some population may move to **Bx**, but an ease of proton back transfer to restore **Ax** means that this will likely be the most common form by far. Since the employment of the C-PCM model to treat solvation in water does not seem to change the ordering of which states are most stable, it is unlikely that the presence of a polar, protic solvent will largely impact the excited state dynamics of PY101, beyond perhaps stabilizing transition states to ESPT and lowering those barriers. With this initial understanding of the ground and excited state structures of PY101, we now turn our attention to the static excited state properties of the system.

3.4   Static excited state properties of PY101

Since the **A** isomer is expected to be immediately populated after photoexcitation of PY101, the vertical excitation energies and oscillator strengths of the five lowest singlet electronically excited states of the most stable **A** isomer of PY101 are presented in Table

3.7. The S_1 has an excitation energy of 3.47 eV and the prominent oscillator strength. This is a bright state of $\pi\pi^*$ character, representing a HOMO-LUMO transition. The molecular orbitals involved in this transition are shown in Figure 3.3. The first excited state is comparatively isolated, with the other singlet states lying relatively close together starting about 0.7 eV above the S_1. The four lowest states are all varying $\pi\pi^*$ states, while the S_5 is an $n\pi^*$ state. Of the states other than S_1, the S_3 is the only one exhibiting a noteworthy oscillator strength. Still, it lies over 1 eV above the S_1 and is therefore unlikely to become populated to a large degree. Comparing the excitation energies in the gas phase versus using the C-PCM model for water, a lowering of the S_1 excitation energy by 0.19 eV is observed. Other than small energetic changes, the excited states appear uneffected by the solvent model. The S_1 is still the brightest $\pi\pi^*$ and relatively isolated energetically, and therefore the excited state population will necessarily evolve along this state.
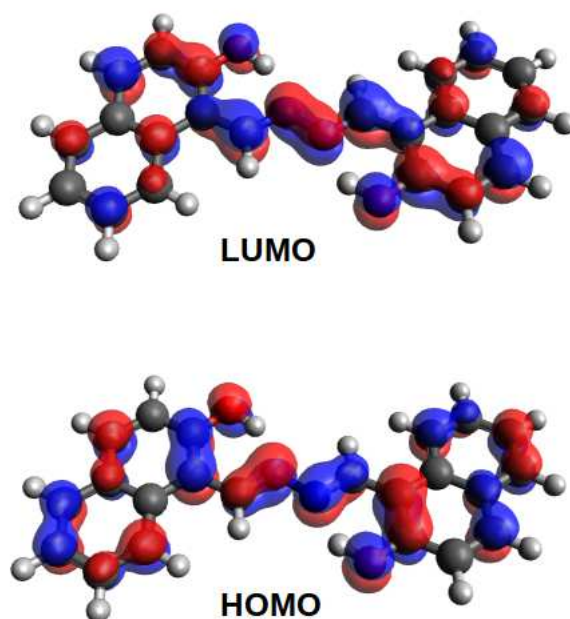
FIGURE 3.3: The HOMO and LUMO orbitals involved in the predominant $\pi\pi^*$ transition for the S_1 state of **A**.

Though the **A(x)** isomer is clearly the most energetically stable and likely to be most extensively populated immediately post-excitation, it is still worthwhile to compare how the properties of the bright S_1 state may vary among the other isomers. Indeed, the S_1 is in all cases the bright state, varying merely in its excitation energy to varying degrees. The highest excitation energy is observed to the **Ex** structure, while the lowest is to the **Fx** isomer. The range of excitation energies spans about 0.7 eV, which is considerable, although an isolated S_1 state is observed in all cases. Comparing C-PCM to gas phase computations, the excitation energies are consistently lowered by about 0.2

State (g)	Excitation energy (eV)	Oscillator strength	Character
S_1	3.47	1.026	$\pi\pi^*$
S_2	4.17	0.000	$\pi\pi^*$
S_3	4.49	0.217	$\pi\pi^*$
S_4	4.56	0.000	$\pi\pi^*$
S_5	4.62	0.000	$n\pi^*$
State (H_2O)	Excitation energy (eV)	Oscillator strength	Character
S_1	3.28	1.368	$\pi\pi^*$
S_2	4.07	0.000	$\pi\pi^*$
S_3	4.44	0.496	$\pi\pi^*$
S_4	4.49	0.000	$\pi\pi^*$
S_5	4.61	0.001	$n\pi^*$
State (DMSO)	Excitation energy (eV)	Oscillator strength	Character
S_1	3.28	1.365	$\pi\pi^*$
S_2	4.07	0.000	$\pi\pi^*$
S_3	4.44	0.490	$\pi\pi^*$
S_4	4.49	0.000	$\pi\pi^*$
S_5	4.61	0.001	$n\pi^*$

TABLE 3.7: Vertical excitation energies, oscillator strengths, and excited state characters for the 5 lowest singlet excited states of **A** in the gas phase and using the C-PCM for water and DMSO. All calculations were performed at the TD-DFT/BHLYP/cc-pVDZ level of theory.

eV in solution, but no dramatic changes to the excited state dynamics can be expected on this basis alone.

Armed with this understanding of the ground and excited state structures and excitation energies of PY101, the potential energy surface is now examined in more detail, yielding qualitative yet thorough insight into the excited state dynamics of PY101.

3.5   Potential energy surfaces

Five time constants are necessary for a description of the decay of the S_1 state of PY101[41]. They were identified from experimental transient absorption spectra and computed amplitude spectra and are $\tau_1 = 150$ fs, $\tau_2 = 3$ ps, $\tau_3 = 63$ ps, $\tau_4 = 500$ ps, and $\tau_5 > 1.3$ ns. Previously, a thorough search of the S_1 potential energy surface was performed, identifying 16 stable conformers of PY101[42]. While the majority were too high-energy for them to reasonably impact the excited state dynamics of PY101, 6 were selected for more thorough study. These are the 6 isomers depicted in Figure 3.1. As previously discussed, **A(x)** is the most stable isomer of PY101, followed by **B(x)** which is only 0.15 eV higher (see Table 3.6). The previous model for the photoinduced dynamics of PY101, described here in the introduction, is further clarified and extended in this

Isomer (g)	Excitation energy (eV)	Oscillator strength
A	3.47	1.026
B	3.27	0.931
C	3.53	1.002
D	3.29	0.901
E	3.92	0.746
F	3.22	0.812
Isomer (H_2O)	Excitation energy (eV)	Oscillator strength
A	3.28	1.368
B	3.06	1.217
C	3.34	1.368
D	3.09	1.198
E	3.78	1.092
F	3.04	1.076
Isomer (DMSO)	Excitation energy (eV)	Oscillator strength
A	3.28	1.365
B	3.06	1.214
C	3.34	1.364
D	3.09	1.195
E	3.78	1.089
F	3.05	1.074

TABLE 3.8: Vertical excitation energies and oscillator strengths of the S_1, HOMO-LUMO ($\pi\pi^*$) excitation for the six isomers of PY101 in the gas phase and using the C-PCM for water and DMSO. All calculations were performed at the TD-DFT/BHLYP/cc-pVDZ level of theory.

thesis. Relaxed surface scans in S_1 are performed connecting the six most stable isomers of PY101 and energy barriers are estimated on the basis of these curves. It should be noted that for all computed curves, the ground state equilibrium structures serve as the starting points from where photoexcitation followed by isomerization occurs.

Initial photoexcitation of PY101 results in the population of the Franck-Condon region of the S_1 state, and from here the vast majority (about 90 percent) of PY101 molecules will stay in the diol form[41]. Fluorescence back to the S_0 state may also occur, corresponding to the $\tau_3 = 63$ ps rate constant. The Franck-Condon region is rapidly depopulated and an excess energy of 0.46 eV is then available to populate **Ax**, **Bx**, **Ex**, and **Fx**. Since their relative energies are so high and the transition to them would involve dihedral rotation, which generally involves a high barrier, **Cx** and **Dx** are unlikely to be reached. The potential surface scans computed here allow one to qualitatively judge which isomers will be most likely to be populated upon photoexcitation of PY101.

Looking at the structures in Figure 3.1, it is clear that three main processes are necessary to convert among the isomers: excited state intramolecular proton transfer (ESIPT), dihedral angle rotation, and a combination of the two. In several molecular relatives

of PY101, ESIPT has also been observed[217]. In light of this, a relaxed scan in S_1 is first performed along the ESIPT coordinate from the OH-group of **Ax** to its nearest neighboring nitrogen, forming **Bx** as a result. The potential energy curves computed in the gas phase and employing the C-PCM model to treat solvation in water are shown in Figure 3.4.
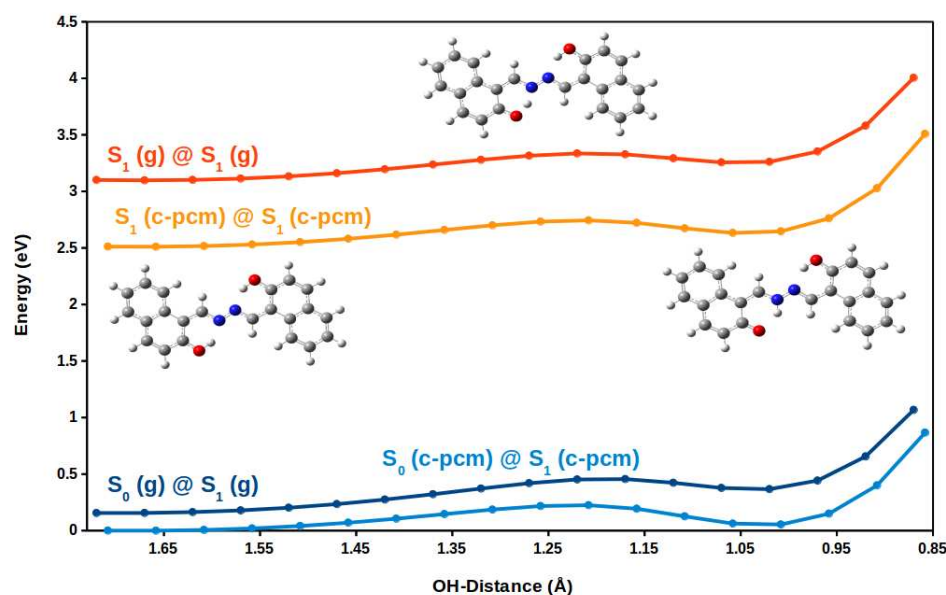
FIGURE 3.4: Potential surface scans for the transition from **Ax** to **Bx** both in the gas phase and employing the C-PCM model for water.

While the total energy of the curves is lower when the C-PCM model is used, the overall picture of the ESIPT process appears uneffected. Therefore, it is expected that solvation of PY101 in polar, protic solution should result in the same excited state dynamics as in the gas phase. The barrier to ESIPT in the gas phase from **Ax** $\rightarrow$ **Bx** is only about at most 0.23 eV, and should therfore be readily overcome with the initial excess energy of 0.46 eV. In the ground state (at S_1), it is 0.30 eV. The barrier in solution is at most 0.23 in the excited state and at most 0.22 in the ground state (at S_1). Therefore, ESIPT takes place more readily in the excited state than in the ground state in the gas phase, while having roughly the same barrier in solution both in the S_0 and S_1.

Prior work, along with experimental studies, had indicated that the **Ex** and **Fx** structures, being the second most-stable pair of isomers after **Ax** and **Bx**, should also be readily populated after photoexcitatin of PY101. Since **Fx** had been computed at the BHLYP/DZP level of theory to be more energetically stable than **Ex**, the **Fx** minimum is seen as being where most of the ES population in this region should accumulate. From here, *trans-cis* isomerization is possible. Along with these ideas, the large structural differences between the ground and excited state *cis* conformers indicate that **Fx** and **Ex** have long fluorescence lifetimes and are thus assigned the rate constant $\tau_4 =$

500 ps. The last experimental signal, being the result of a long-lived photoproduct has consequentially been interpreted to be the absorption spectrum of isomer **F**[41, 42].
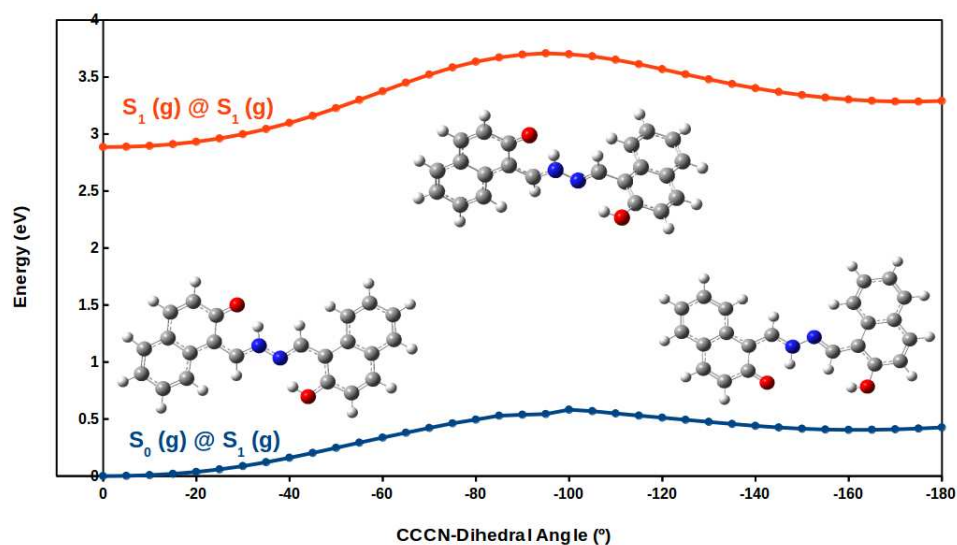
FIGURE 3.5: Potential surface scans for the transition from **Bx** to **Dx** in the gas phase.

Relaxed surface scans were also performed along the C-N-N-C rotation coordinate of the bisazomethine unit, moving from the *trans* to the *cis* isomers. That is, the S_1 surface was optimized moving from **Ax** → **Ex** and **Bx** → **Fx**. In addition, the pathway from **Ax** → **Fx** was also computed, combining dihedral rotation and ESPT for the transition. The energy barriers, again estimated from the relaxed scans, are at most 0.9 eV from **Ax**→ **Ex** and only 0.52 eV from **Bx** → **Fx**. For the case of **Bx** → **Fx**, the relaxed scan was performed to an angle of 93°towards **Fx** for the barrier estimation. This curve is shown in Figure 3.6. In the opposite direction, the barrier from **Ex** to **Ax** was at most 0.6 eV, which is slightly smaller than in the original direction, but still very large compared to the barriers to ESIPT. On the whole, these higher barriers to C-N-N-C dihedral rotation indicate that the *cis* isomers are much less likely to be populated than their *trans* counterparts. Still, some population may accumulate in the **Fx** and **Ex** forms. Therefore it is important to know which of the two is the more likely candidate for population increase upon photoexictation, in order that the observed long-lived photoproduct be identified. **Fx** is slightly more stable energetically than **Ex**, and the barrier from **Fx** → **Ex** is at most 0.15 eV, while the opposite direction, from **Ex** → **Fx**, of about at most 0.13 eV, is similar. These barriers are very similar to those for the ESIPT processes connecting **Ax** and **Bx**, and therefore should the *cis* isomers be reached, ESIPT is likely to occur.

In addition to dihedral rotation about the central bisazomethine unit, torsion of the C-C-C-N angle leading to *exo-endo* isomerization is another possibility. Thus, pathways from **Ax**/**Bx** to **Cx**/**Dx** are investigated. Due to the higher relative energies of the **Cx**
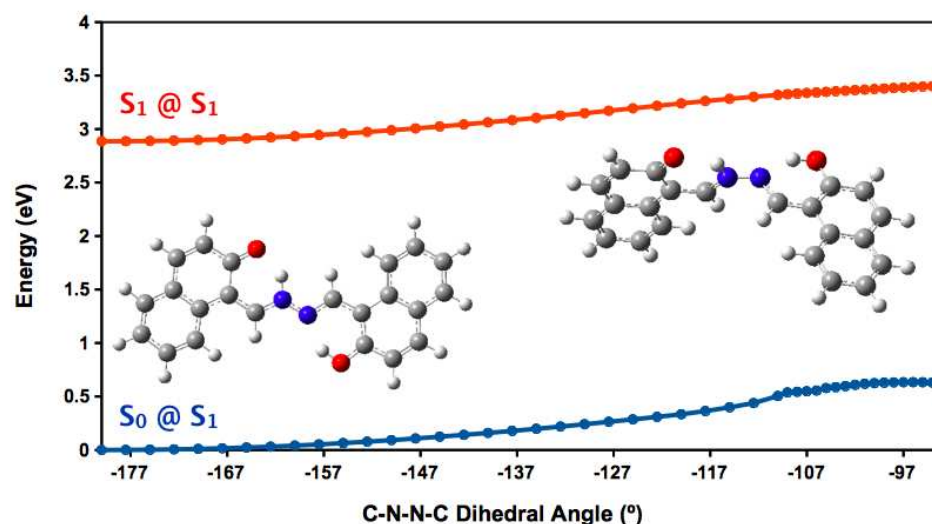
FIGURE 3.6: Potential surface scans for the transition from **Bx** to a 93°rotated structure towards **Fx** in the gas phase.
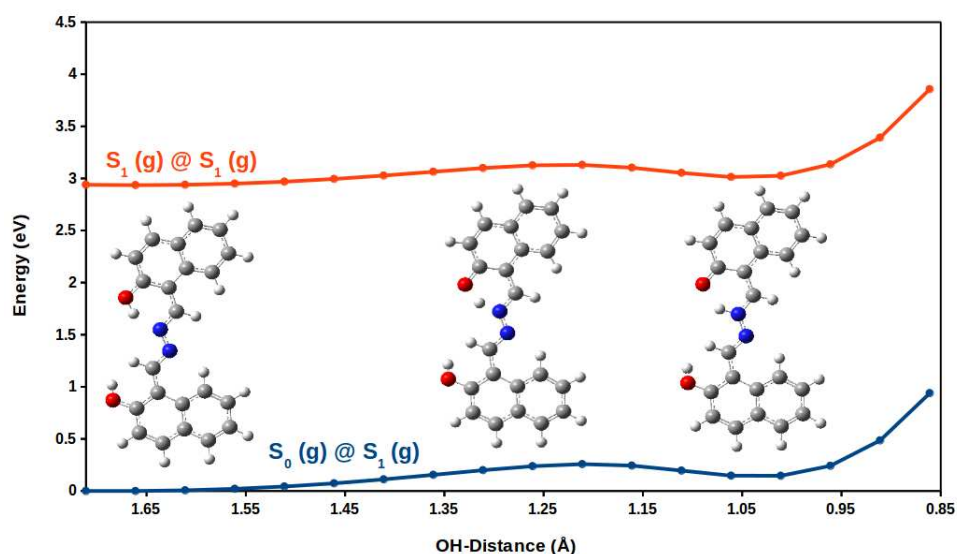
FIGURE 3.7: Potential surface scans for the transition from **Cx** to **Dx** in the gas phase.

and **Dx** isomers, it had been previously assumed that they would not be populated to any appreciable degree after photoexcitation. Still, they are considered here in light of the appreciable excess energy initially available to the system for interconversion among the isomers. Relaxed surface scans optimized in S_1 were computed again going halfway from **Ax**→**Cx**, i.e. to a structure with a dihedral angle of about 96°, and fully from **Bx**→**Dx**. The latter has an estimated barrier of at most 0.8 eV, with the reverse process requiring 0.4 eV. The former process estimated pseudobarriers, computed simply as the difference between the 96°rotated structure in S_1 and the S_1 minimum, of about 1 eV and about 0.6 eV, respectively. These barriers are of course prohibitively large. In addition, it was hypothesized that the barriers for these processes may be impacted by

solvation due to the increased charge transfer character at the twisted structure[137]. For completeness, the ESIPT coordinate was also scanned going from $\mathbf{Cx} \rightarrow \mathbf{Dx}$, echoing the findings for $\mathbf{Ax} \rightarrow \mathbf{Bx}$ and $\mathbf{Fx} \rightarrow \mathbf{Ex}$. The relaxed scans for the the $\mathbf{Cx} \rightarrow \mathbf{Dx}$ ESIPT coordinate are shown in Figure 3.7. Indeed the barrier from $\mathbf{Cx} \rightarrow \mathbf{Dx}$ is estimated to be at most 0.19 eV, while the opposite process necessitates at most 0.12 eV. Therefore, ESIPT in PY101 can readily occur across the board. Still, because the barriers to these *endo* forms are prohibitively high, it is unlikely that they will be populated and thus they will not play a role in the S_1 dynamics of PY101.
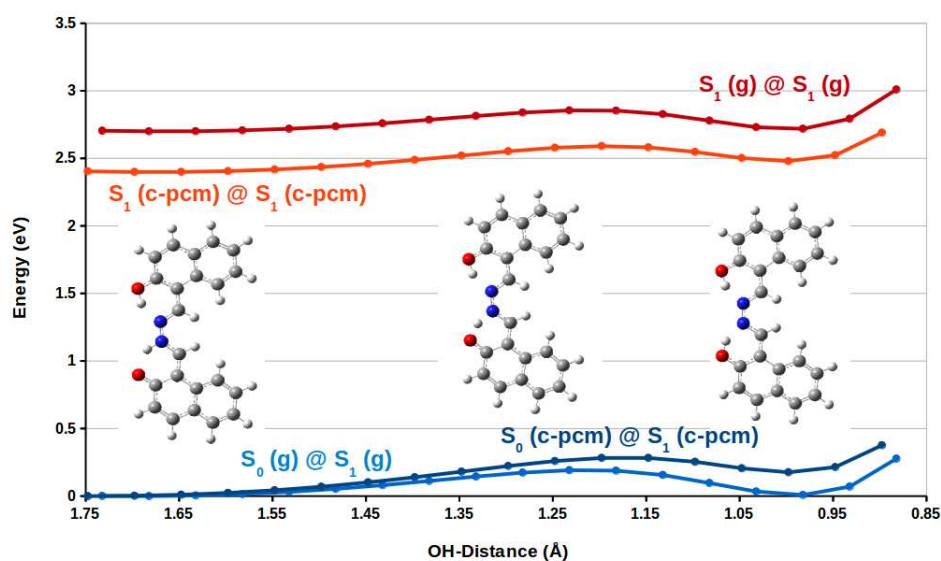
FIGURE 3.8: Potential surface scans for the transition from $\mathbf{Fx}$ to $\mathbf{Ex}$ both in the gas phase and employing the C-PCM model for water.

Figure 3.9 summarizes the barriers reported in the literature[205] connecting the six most stable conformers of PY101. These barriers were determined using TDA/TD-DFT, which were employed in the next section describing the kinetic modeling. Obviously, the differences between these reported values and the full TD-DFT results discussed in detail here are negligible, further supporting the excited state picture of PY101 presented here. The ESIPT processes studied, $\mathbf{Ax} \rightarrow \mathbf{Bx}$, $\mathbf{Cx} \rightarrow \mathbf{Dx}$, and $\mathbf{Fx} \rightarrow \mathbf{Ex}$ all require around 0.1-0.2 eV to take place, making them the most energetically feasible excited state isomerizations for PY101. Dihedral rotation of the central bisazomethine C-N-N-C angle, leading to *trans-cis* isomerization, requires roughly four to eight times as much energy as ESIPT. Thus, these rotations are less likely to occur. Still, given the low relative energies of the $\mathbf{Ex}$ and $\mathbf{Fx}$ isomers, rotation may still be possible, in particular for the case of $\mathbf{Bx} \rightarrow \mathbf{Fx}$. Dihedral rotation of the C-C-C-N angle leading to *exo-endo* isomerization is similarly unlikely due to the relatively high estimated barriers. In addition, since the $\mathbf{Cx}$ and $\mathbf{Dx}$ isomers have the highest relative energies, it is all but certain that they can be neglected in a discussion of the excited state dynamics of PY101.
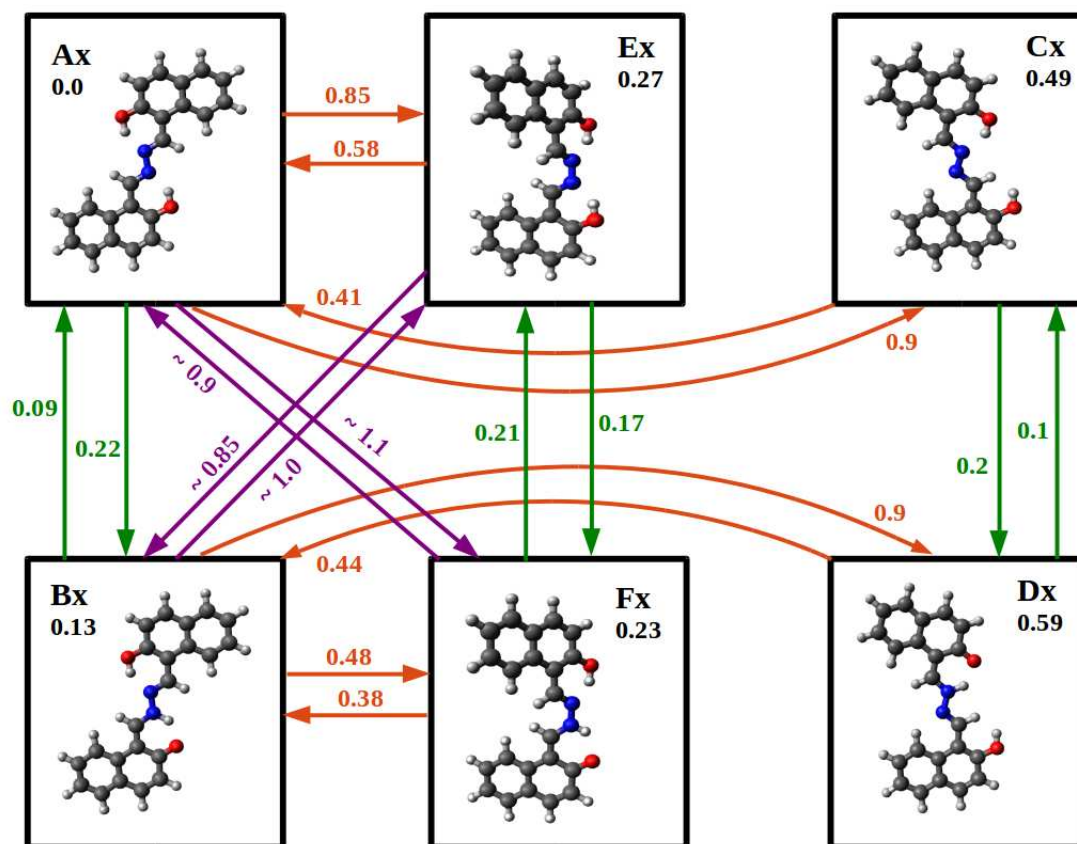
FIGURE 3.9: Summary of the results used for the testing of the non-equilibrium kinetic rate model. Relative energies for the different PY101 isomers and the estimated energy barriers for converting between them are presented in eV. For these computations, the TDA/TD-DFT/BHLYP level of theory was employed, treating the system in the gas phase.

The following model is proposed for the excited state dynamics of PY101. The excited PY101 molecules gain a significant amount of initial excess energy upon photoexcitation of **A**. This initial excess energy comes from the fact that the Franck-Condon point is found 0.27 eV above the exo-trans minimum of **Ax**. Also, in the corresponding experiment, the wavelength of the excitation pulse was 387 nm. That is, the pulse is 25 nm blue-shifted to the maximum absorption of the S_1 band at 411 nm, adding another 0.19 eV to the initial excess energy. This means that on aveage, a total of 0.46 eV excess energy is availabe to overcome the barriers to the other isomers of PY101 in the excited state. Note that this relates to a local vibrational temperature of PY101 in the S_1 state of about 4000K. With this initial excess energy, the ESIPT barrier for **Ax**→**Bx** isomerization is rapidly overcome. From **Bx**, further decay to **Fx** followed by a return to **Ax** is possible. Some of the excited state population may also reach **Ex** from **Fx** via ESIPT, but will then likely return back to **Fx** via the reverse ESIPT process. The previously computed absorption spectrum of **F** indicates that is is the spectrum of the remaining photoproduct of the excited state dynamics[42]. Once returned to **Ax** and after cooling,

fluorescent decay from **Ax** to **A** occurs. With this discussion, a preliminary prediction of the excited state dynamics of PY101 is gained, based on the extensive computation of the potential energy surface along possible photochemical reaction coordinates in the S_1 state. To summarize in short:

$$\mathbf{Fx} \leftarrow \mathbf{Ex} \leftarrow \mathbf{Ax} \leftrightarrow \mathbf{Bx} \rightarrow \mathbf{Fx} \tag{3.1}$$
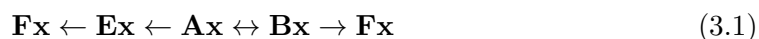
We now look to the development of an approximate kinetic model for the dynamics of PY101 and similar molecules in the excited state.

3.6 Approximate kinetic model for excited state dynamics

The qualitative understanding of areas of S_1 potential energy surface of PY101 most important to its photochemistry can be used for further, more quantitative investigation. In principle, one can develop statistical rate models for the simulation of excited state dynamics using the ingredients of the relative energies of the conformers and the energy barriers required for the movement among them. Because photo-initiated processes, by nature of being out of equilibrium, frequently take place on several coupled potential energy surfaces, such models are very often not applicable. However, the excited state dynamics of PY101 occur on an isolated S_1 surface, making it an ideal backbone for the development and testing of such models. In addition, time-resolved experimental results are known for PY101. Accurate quantum dynamics and semi-classical calculations of the excited state dynamics for molecules larger than PY101 are currently not feasible. Thus, the development of such models is imperative. The relative energies and barrier heights, reported in the literature[205], are given in Figure 3.9 and used in the testing of the kinetic model provided here. These relative energies and barrier heights, computed at the TDA-TDDFT/BHLYP/DZP level in ORCA, do not vary appreciably from the calculations performed using full-TD-DFT which are presented here. Therefore, knowledge of the excited state potential energy surface of PY101 is again confirmed, and regardless of minor changes to the method used, the kinetic model should yield consistently similar results.

Two pieces of information must be kept in mind in order to simulate the non-equilibrium kinetics of PY101's photochemistry. First, the details of the S_1 potential energy surface must be known. Second, one must consider the available excess energy E_{xs}, which depends on the initial amount of excess energy and how much dissipation occurs over the course of the reaction time. Thus, it can readily be described by the following

mono-exponential decay function

$$E_{xs}(t) = E_{xs}(t_0)e^{k_{diss}t} \tag{3.2}$$

in the case of PY101 the initial excess energy $E_{xs}(t_0)$ was determined to be 0.35 eV. The dissipation rate k_{diss} was taken to be 10^{12} s^{-1}, 2×10^{11} s^{-1}, and 10^{11} s^{-1}. These values match typical cooling times for systems similar to PY101[218–220].

Employing an adapted rate model for the separate reactions and setting up a kinetic model to be solved by propagation in time offers a clear way of including the barrier heights and relative energies of the potential energy surface. On the basis of the calculation of all relevant energy barriers among the energy surfaces connecting the different conformers of PY101 in the excited state, the computation of thermal rate constants for each first order reaction becomes possible. This is done in accordance with the Arrhenius ansatz. For example, for the reaction from **Ax** to **Bx**, one has

$$k_{AxBx}(E_{xs}(t)) = Ae^{\frac{-E_a}{kT+E_{xs}}}. \tag{3.3}$$

Here, E_a is the energy barrier, $E_{xs}(t)$ the excess energy available, kT is the available thermal energy, and $A = 10^{12}$ s^{-1}. The taken value of A is representative of photochemical reactions, and is the inverse of the time needed to reach an energy barrier. It is well-established that barrierless reactions take place on the timescale of several femtoseconds to picoseconds.

The potential energy curves computed in the literature[205] form the basis of this model, as the experimental excess energy, energy barriers, and fluorescence lifetimes are required input. Upon excitation, **Ax** is populated with an initial excess energy of 0.35 eV[205], presenting the initial condition. Full TD-DFT results presented here indicate that 0.46 eV initial excess energy is available. Using the three dissipation rates in three simulation runs, the energy dissipation over the course of the reaction is observable. Since the results are for all purposes independent of the dissipation rate, the rate $k_{diss} = 10^{11}$ s^{-1} is used for presentation. Several important reaction pathways were considered. These are the forward reactions starting from **Ax**: **Ax→Bx**, **Ax→Ex**, and **Ax→Fx**, in addition to the back reactions: **Bx→Ax**, **Ex→Ax**, and **Fx→Ax**. Fluorescent decay is also considered via: **Ax→A**. Several consecutive reactions were also accounted for in the model. These are **Bx→Fx**, **Ex→Fx**, and the radiative decay **Fx→F**. The first six reaction rates depending on the excess energy available were calculated according to equation 3.3 using the energy barriers calculated in the literature and presented in Figure 3.9 in parentheses. The experimentally determined value, $k_{AxA} = 1.58 \cdot 10^{10}$ s^{-1}, was used, however, for the fluorescence rate for **Ax→A**. This is the inverse of the

63 ps fluorescent lifetime. Analogously, the empirical decay rate of $k_{FxF} = 2 \cdot 10^9$ s^{-1} was used for **Fx**→**F**. Notably, *exo-endo* isomerization reactions are not considered, since these do not play a large role in the excited state dynamics, as their energy barriers are too high. The kinetic model accounts for competitive reaction pathways occurring in parallel, along with the set of consecutive pathways. The change in population of **Ax** in the context of this model is given, as an example, by

$$
\begin{aligned}
\frac{d}{dt}P_{Ax}(t) = &[-k_{AxBx}(t) - k_{AxEx}(t) - k_{AxFx}(t) - k_{AxA}]P_{Ax}(t) \\
&+ k_{BxAx}(t)P_{Bx}(t) + k_{ExAx}(t)P_{Ex}(t) + k_{FxAx}(t)P_{Fx}(t).
\end{aligned}
\tag{3.4}
$$

The reaction rates depend implicitly on time, since they are dependent on the excess energy E_{xs}, which is itself time-dependent. Using the set of equations for all noted populations, the kinetic model was propagated in time steps of 1 ps for up to 1 ns. The initial condition $Ax = 1$ at $t = 0$ was used. More detail on the results is provided in the literature[205], but a brief summary is provided in the following. The depopulation of the **Ax** population is effectively immediate following photoexcitation, and the **Bx** conformer is populated by a ballistic ESIPT process. The new **Bx** population decays ultrafast back to **Ax**, as well as to the **Fx** isomer. As a result, the lifetime of the **Bx** population is extremely short, which agrees well with the previous experimentally determined lifetime of 3 ps for the **Bx** population. Following a repopulation of **Ax**, the population of **A** is seen to increase as a result of the overwhelming fluorescent decay process **Ax**→**A**. A minor population reaches **Ex** through the reaction **Ax**→**Ex** directly following photoexcitation, but the back reaction **Ex**→**Ax** leads to an almost complete repopulation of **Ax**. The form **Fx** also exhibits a noteworthy initial population via the consecutive reaction **Ax**→**Bx**→**Fx** and the direct reaction **Ax**→**Fx**. From here, the fluorescent decay reaction **Fx**→**F** is possible, generating the photoproduct **F**.

The results of this model reflect the experimentally determined kinetics very well. Indeed, the previously determined photochemistry of PY101, previously elucidated purely on the basis of qualitative interpretation of the S$_1$ potential energy surface, is corroborated by the results of this model. This is surprising due to the relative crudeness of the model when compared to full-scale quantum dynamics simulations, and important as such rate models could be of much use in future studies of large systems. Indeed, it is shown that it is reasonable to use such models for investigating the excited state dynamics of organic chromophores characterized by an isolated S$_1$ surface. In these cases, non-adiabatic and multi-state effects do not dominate the dynamics, making rate models applicable. The use of such models requires thorough study of the potential energy surface and computation of relevant energy barriers, as well as consideration of energy dissipation. It can therefore be extremely computationally involved. Still, initial insight

into the expected quantum dynamics can result. This is of high importance particularly for larger systems for which full dynamics simulations are not yet possible.

3.7   Conclusion

First, the structure of PY101 is described on the basis of crucial bond lengths and angles, both in the ground and excited states, as well as in the gas phase and employing the C-PCM model to treat solvation in water. These initial measurements provide insight into which coordinates of transition may be facilitated in the excited state, particularly in the case of solvated PY101 versus in vacuum. Overall, the structural changes are modest. A notable increased OH distance for isomers **D** and **B** upon excitation is noted, potentially leading to facilitated ESIPT in that state. This distance is again increased when the excited state system is treated as being in solution versus the gas phase. Thus, ESIPT processes may more readily occur in polar solution. Still, the effects are unlikely to distort the overall picture of the excited state dynamics, and PY101 is thus expected to behave in solution as described here in the gas phase. Comparing the relative energies of the isomers of PY101 in the S_0 and S_1 states, both in the gas phase and in solution, it is clear that $\mathbf{A(x)}$ is the most stable conformer in all cases and at all levels of theory. The second most stable conformer is $\mathbf{B(x)}$. $\mathbf{D(x)}$ is clearly the least stable of the six. Therefore, generally $\mathbf{Ax}$ will be immediately populated post-excitation, and the excited state dynamics will play out from this state.

Next, the static excited state properties of PY101 both in the gas phase and employing the C-PCM model to treat solvation in water are described. The S_1 state of PY101 is a bright $\pi\pi^*$ state, characterized by a HOMO-LUMO transition. The lowest four singlet electronically excited states are all $\pi\pi^*$ transitions, and the lowest $n\pi^*$ state is S_5. For all isomers, the S_1 is the bright state, and excitation energies range from 3.22-3.92 eV in the gas phase, and 3.04-3.73 eV using C-PCM. The lowest vertical excitation energy to S_1 is exhibited by **F**, and the highest by **E**. Excitation energies are overall about 0.2 eV lower when computed with C-PCM than in the gas phase.

A detailed analysis of the potential energy surfaces of the S_0 and S_1 states of PY101 was then performed, describing the landscape among the six most stable conformers of PY101. These surfaces provide an initial interpretation of the excited state dynamics of PY101, and indeed allow for predictions of the photochemical processes that are likely to occur. PY101 has been here reinvestigated in depth, also including a look at the modest influence of solvation models on the system. Relaxed scans on the S_1 surface were computed at the TD-DFT/BHLYP/cc-pVDZ level of theory connecting

the relevant pathways among the six most stable conformers: *exo-trans* diol (**Ax**), *exo-trans* keto (**Bx**), *endo-trans* diol (**Cx**), *endo-trans* keto (**Dx**), *exo-cis* diol (**Ex**), and *exo-cis* keto (**Fx**). Energy barriers were estimated based on the computed S_1 surfaces, and it was found that barries involving ESIPT were much lower than those involving dihedral rotation.

In the second part of this project, a non-equilibrium adapted rate model was presented and employed for the test case of PY101 to estimate the kinetics and significance of possible excited state processes. Here, the computed relative energies and estimated energy barriers served as input. PY101 is an ideal test case for such simple models, as its dynamics play out on an isolated S_1 surface. This means that multi-state and non-adiabatic effects are negligible, and the excited state dynamics can be treated like *hot* ground-state kinetics. Experimental fluorescence lifetimes were taken into account and the energy-dependent Arrhenius rate constants were calculated for each reaction pathway. Within this advanced kinetic model, the excited state populations for **Ax**, **Bx**, **Ex**, and **Fx** were simulated, along with the restoration of the ground state population of **A** and the formation of the ground state photoproduct **F**. First order kinetic equations for the model were solved by propagation in time, where the initial condition was that, upon photoexcitation, the population of **Ax**= 1 at $t = 0$.

The results of applying the kinetic rate model to the PY101 system are summarized as follows. The population of **Bx** if strongly populated through ESIPT from **Ax** rapidly after photoexcitation. **Bx** is, however, the shortest-lived population and decay either to **Ax** by proton back-transfer or to **Fx** by *trans-cis* isomerization is imminent. Overall, the obtained kinetics agree surprisingly well with experimental findings and serve to confirm previously-made assignments of the intermediates, which had resulted from qualitative inspection of the PES and relative energies only. It can therefore be concluded that such adapted rate models are appropriate for simulating the excited state dynamics of large chromophores, under the condition that the dynamics plays out on an isolated S_1 surface.

Simple kinetic models like the one presented in this work are important because accurate quantum-dynamical and semi-classical treatments of the excited state dynamics of molecules larger than PY101 are not currently feasible. However, it is critical to note that such models are limited to cases where the photochemistry of a given system can be seen as *hot* ground state chemistry. In short, time-dependent quantum dynamics simulations remain the gold standard. However, for the treatment of such large systems, the development of such approximate kinetic models are very useful for an initial look at the dynamics, and are indeed for some cases still the only option.

Chapter 4

Fluorescence Quenching of Aromatic Aldehydes

4.1 Motivation and Background

Amines serve as analytes for a multitude of applications[221–223]. They are used to detect food spoiling[224–227], for producing pharmaceuticals and colorants[228, 229], and for the preparation of biological buffer compounds and surfactants[228], among other uses. Currently, a number of chemosensory approaches for detecting amines exists, such as artificial receptor libraries, water-soluble conjugated polymers, and collections of hydrophobic porphyrin dyes[230]. Highly active trifluoromethyl-substituted ketones and selected 1,3-diketones are also used[221–223, 225–229, 231–240]. These indicators operate by a change of color upon reaction with an amine. In most cases, however, colorimetric or fluorimetric amine recognition takes place in organic solvents.

Recently, water-soluble distyrylbenzenes containing aldehyde groups were synthesized and shown to be excellent fluorescence-based turn-on indicators for amines[44]. Such fluorophores also carrying solubilizing and fluorescence-augmenting branched oligoethyleneglycol chains were studied in previous work[241] and, recently, a thorough account of their amine-sensing capabilities was discussed[242]. Prior work has focused on using cruciform (XF) fluorophores[243–250]. A fluorescence change of tetrahydroxy-XFs[251] is caused by interaction with simple amines. Hinging on the acidity of an amine, hydrogen bonding or direct deprotonation of the phenolic XFs takes place, yielding a color change in emission that is influenced by the structure of the amine. Primary, secondary, and 1,n-diamines can be detected with aldehyde-substituted distyrylbenzenes and cruciform dialdehyde fluorophores, which exhibit, however, either no or barely any fluorescence in water. Their structures are shown in Figures 4.1 and 4.2. In contrast, the addition

products with an amine, forming an aminal, a hemiaminal, or an imine exhibit strong fluorescence[242].
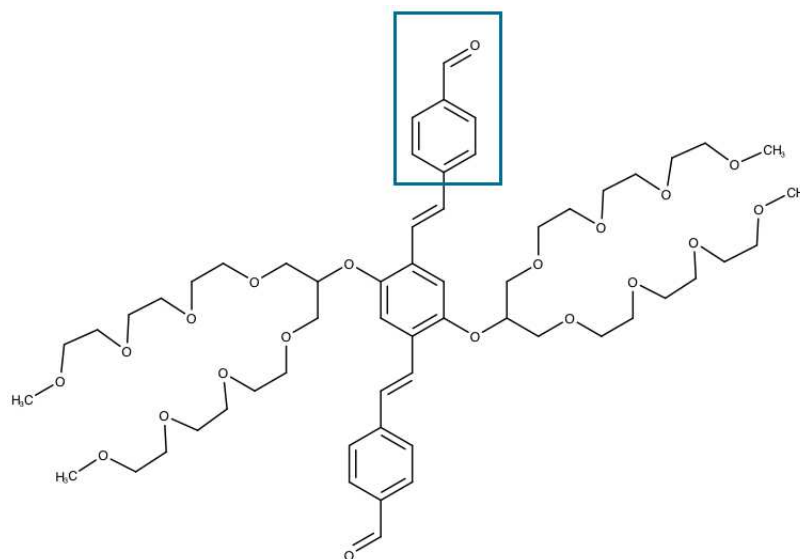
FIGURE 4.1: Distyrylbenzene fluorophore with aldehyde groups.
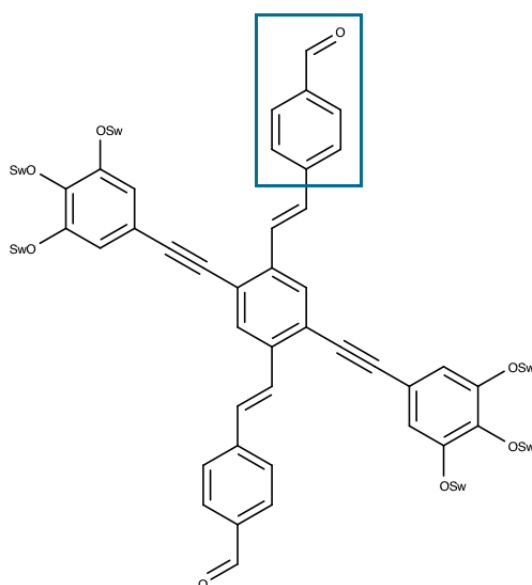
FIGURE 4.2: Cruciform fluorophore with aldehyde groups.

A mechanism was proposed based on preliminary calculations to explain the fluorescence quenching of the dialdehydes in water[242] It has been suggested that the distyrylbenzene aldehydes may act as excited state bases in aqueous solution and that excited state protonation of the aldehydes takes place. DFT-based calculations indicated that electron transfer also occurs from the newly formed hydroxide anion to the cationic protonated aldehyde, yielding radical formation. Upon subsequent non-radiative decay to the electronic ground state, the hydrogen atom is transferred back to the OH radical, and the original hydrogen-bonded aldehyde is restored[242]. In this project, the previously

proposed mechanism is reinvestigated using state-of-the-art quantum chemical methods in conjunction with explicit and implicit solvation models. Benzaldehyde, which represents the basic structural motif common to the distyrylbenzene aldehydes and the unit containing the site of proposed proton transfer, is the starting point. Following an overview of the literature on benzaldehyde, being as it is extremely well-studied, the mechanism of fluorescence transfer is elucidated. A series of modifications are then made to the aldehyde, looking at specific cases, varying substituents, solvents, and the length of the conjugated aromatic system. Attention is also briefly paid to an imine analog. As a whole, this work provides a comprehensive look at fluorescence quenching in aromatic aldehyde systems, which is not only of vital importance to the synthesis of amine indicators, but also to synthetic organic chemistry as a whole.

It should be noted here that some of the information presented in this chapter has been previously submitted for publication by myself and my co-authors as

K. Fletcher, U. H. F. Bunz, and A. Dreuw
Fluorescence quenching of aromatic aldehydes in water: photo-basicity vs. hydrogen atom abstraction, *submitted for publication*, **2016**.

4.2 Literature overview

Here, a summary of the main experimental and theoretical studies of benzaldehyde is given as the information is relevant to our investigation. Benzaldehyde (BA) is a quintessential aromatic carbonyl which exhibits strong phosphorescence but only weak fluorescence. Importantly, no emission can be experimentally observed for BA in water[252]. BA possesses a 3-state intersection region formed by the S_1 ($n\pi^*$) and the two closely-lying, lower-energy T_2 ($\pi\pi^*$) and T_1 ($n\pi^*$) states[253–255]. The S_2 state is also $\pi\pi^*$. Intersystem crossing (ISC) from $S_1 \rightarrow T_2$ occurs extremely quickly with a rate constant of 8.03×10^{10} s^{-1} (computational)[253] or 2.4×10^{10} s^{-1} (experimental)[256]. It follows from El-Sayed's rule[257] that this ultra-fast ISC is due to a large spin-orbit matrix element[253, 254] and is encouraged by a small energetic barrier[253, 255]. We therefore take into consideration both triplet and singlet excited states in the revelation of the fluorescence quenching mechanism in water.

Protonated BA, expected to result from the quenching mechanism, has also been studied recently. In an investigation of monosubstituted benzenes, the proton affinities of BA and its relatives were reported to be about 0.87-1.30 eV (20-30 kcal/mol) higher in the lowest singlet excited $\pi\pi^*$ state with respect to the ground state[258]. At the MP2/6-31G* level of theory, the site of BA protonation was confirmed to be the carbonyl oxygen[259]. In

its protonated form, BA's *syn* conformation is 0.08 eV (8 kJ mol^{-1}) more stable than its *anti* conformation[260]. At the CC2/cc-pVDZ and CC2/aug-cc-pVDZ levels of theory, the photofragmentation spectrum of BA was computed. Here, the lowest $\pi\pi^*$ transition of the protonated form is red-shifted in comparison to the neutral BA[261]. This finding is confirmed by CASSCF and CASPT2 calculations[258]. The electronic and vibrational spectra of protonated benzaldehyde-water clusters ([BA·(H$_2$O)$_{n\leq5}$]H$^+$) have also been studied experimentally. When $n \leq 2$, in the ground state, the additional proton is found on BA. However, when $n > 2$, proton transfer takes place to the solvent, thus forming H$_3$O$^+$. Once BA is photoexcited to the $\pi\pi^*$ state, BA is protonated. This, along with the other studies on protonated BA, consistently imply that the proton affinity of BA is increased in the excited state. BA thus is presumed to be a photobase[43], and in the problem of BA in water, ESPT is expected to take place.

The assumption that BA acts as a photobase in aqueous solution is challenged by the wealth information about ketone and aldehyde photochemistry as pertaining to organic synthesis[262, 263]. The Dauben-Salem-Turro rules[264], which use correlation diagrams in the classification of photochemical reactions, assume that said reactions are controlled by the formation of primary products with diradical characteristics. Photochemical processes of ketones and aldehydes in organic solvents subject to continuous near-UV irradiation are expected to undergo radical reactions. In this light, hydrogen transfer, rather that ESPT, would naturally be expected. Therefore, the central question for this study becomes: in protic solvents such as water, is BA a photobase which undergoes ESPT, or does it rather behave like a diradical, undergoing excited-state hydrogen transfer (ESHT)?

The computation of electronic spectra of benzaldehyde in the gas phase is the starting point of this investigation. The literature provides a thorough overview of vapor phase spectroscopy of BA[265], and vacuum UV spectra of BA have been known for over 50 years[266–268]. The first band of the gas phase spectrum at room temperature is weak and appears at 3.34 eV[269, 270]. It arises from an $n\pi^*$ transition to the first singlet electronically excited state. The remaining bands, found at 4.51 eV (S$_2$) and 5.34 eV (S$_3$) are likely $\pi\pi^*$ transitions, and a fourth band is identified at 6.36 eV[268]. Computations of the spectra of BA include MS-CASPT2 calculations, which reasonably agree with empirical results. The first five valence singlet excitation energies occur between 3.71 and 6.23 eV[154]. As a first step in the investigation of the fluorescence quenching of benzaldehyde, the gas phase spectroscopy of BA is benchmarked using a series of TD-DFT functionals and high-level ADC(2)-s and ADC(3) methods.

4.3   Computational Methods

Ground state optimizations for benzaldehyde with explicit water molecules in its vicinity $(BA \cdot (H_2O)_n$ with $n = 0 - 2)$ were carried out using density functional theory (DFT)[64] at the DFT/CAM-B3LYP[141]/cc-pVDZ level of theory in both gas phase and employing the C-PCM solvation model. Indeed, all ground state optimizations of all aldehydes studied in this work were carried out at the CAM-B3LYP/cc-pVDZ level of theory using the C-PCM model, with the exception of geometries used in gas phase vertical excitation calculations, which were of course optimized in the gas phase.

For a benchmarking of the quantum chemical methodology, the vertical excitation energies of BA in the gas phase were carried out using time-dependent DFT (TD-DFT)[32–34] in combination with CAM-B3LYP, BHLYP[214], B3LYP[117], ωB97X[271], and B2PLYP[120] functionals. Calculations using the algebraic diagrammatic construction scheme for the polarization propagator of second order (ADC(2))[35, 60] and third order (ADC(3))[38, 106, 110] yielded benchmark results for comparison with TD-DFT. For the benchmark studies, Dunning's correlation consistent cc-pVDZ and cc-pVTZ basis sets[208, 211, 212] were used.

Since the quenching mechanism crucially involves the presence of a polar, protic solvent, the influence of said solvent must also be benchmarked. Solvation is modeled using the conductor-like polarizable continuum model (C-PCM)[182, 193] with up to explicit water molecules in the neighborhood of BA. The solvent's response to the vertical excitation is treated both using linear response and state-specific methods for non-equilibrium solvation[190, 272]. The solvent cavity is defined by Bondi radii multiplied by a scaling factor of 1.2. Lange and Herbert provide further information about discretization schemes for PCMs[273, 274]. All benchmark and ADC-level calculations were carried out using Q-Chem 4.1[207, 275] and 4.2[276], and a locally modified version of 4.3, while all relaxed surface scans are performed using the CAM-B3LYP/cc-pVDZ level of theory in conjunction with equilibrium C-PCM solvation as implemented in Gaussian 09, Revision D.01[213]. Finally, it should be noted that the energy barriers reported throughout this chapter were estimated on the basis of the computed potential energy surfaces, and an explicit transition state search and optimization was not performed. Thus, the exact energy barriers are at most equal to the values reported here.

4.4   Benzaldehyde in the gas phase

Benzaldehyde in the gas phase is the starting point of this study. The results of TD-DFT and ADC calculations are presented in Table 4.1 along with literature values for

comparison. Here, the most accurate method is ADC(3), as it exhibits a statistical error of only around 0.2 eV for common organic systems[110]. The S_1, S_2, and S_3 states are of $n\pi^*$, $\pi\pi^*$, and $\pi'\pi^*$ characters, respectively. The S_3 state is the bright state here, and its oscillator strength hovers around 0.27 for all methods.

Method	S_1	S_2	S_3
Experiment[255, 268]	3.34	4.51	5.34
B3LYP	3.59 (0.000)	4.74 (0.018)	5.27 (0.233)
B3LYP/6-31G*[277]	3.69	4.78	5.31
BHLYP	3.98 (0.000)	5.20 (0.022)	5.54 (0.213)
CAM-B3LYP	3.78 (0.000)	5.06 (0.018)	5.50 (0.231)
CAM-B3LYP/cc-pVTZ	3.80 (0.000)	4.98 (0.019)	5.40 (0.243)
B2PLYP	4.02 (0.000)	5.24 (0.022)	5.56 (0.205)
ω-B97X	3.85 (0.000)	5.17 (0.016)	5.63 (0.219)
MS-CASPT2[154]	3.71	4.33	4.89
ADC(2)-s	3.72 (0.000)	5.00 (0.010)	5.82 (0.310)
ADC(3)	3.83 (0.000)	4.73 (0.008)	5.66 (0.265)
ADC(3)/cc-pVTZ	3.80 (0.000)	4.64 (0.010)	5.44 (0.257)

TABLE 4.1: Vertical excited states of isolated benzaldehyde. Excitation energies (in eV) and oscillator strengths (in paranthesis) are given as computed employing a palate of levels of theory. Experimental data is provided for comparison. Unless otherwise noted, the basis set used is cc-pVDZ basis set.

The $n\pi^*$ (S_1) excitation energy is overestimated by 0.5 eV when compared to experiment, while the $\pi\pi^*$ and $\pi'\pi^*$ excitation energies are only off by 0.2 eV. The reason for these deviations lies in the use of a small basis set with not enough diffuse basis functions. Indeed, it common knowledge that diffuse Rydberg states mix into valence states in small organic systems, thereby decreasing their excitation energies. Accurately reproducing the gas phase spectrum of benzaldehyde is not the purpose of this work, however. Rather, the focus is on elucidating the excited state properties in solution, where Rydberg states are of much less significance.

Standard hybrid functionals do not yield results that agree with benchmark calculations, as seen in Table 4.1. The B3LYP functional generates excitation energies that are about 0.2 eV lower than ADC(3) calculations. The use of BHLYP and B2PLYP functionals overestimate the excitation energies for the $n\pi^*$ and $\pi\pi^*$ states. Although data generated by the B3LYP functional appears to most closely agree with experiment, this functional is, due to its known charge-transfer failure[131, 132, 278], not appropriate for studying proton and electron transfer in BA·H_2O systems. For the study of charge transfer processes, long-range corrected functionals such as CAM-B3LYP and ω-B97X are necessary.

The results in Table 4.1 indicate that none of the tested levels of theory agree very well with experimental data. Still, The TD-DFT/CAM-B3LYP/cc-pVDZ level of theory

yields results in closest agreement to the ADC(3) benchmarks. TD-DFT/CAM-B3LYP, ADC(2), and ADC(3) results all describe a high oscillator strength for the $\pi'\pi^*$ (S_3) state, and this is indeed in good agreement with experiment.
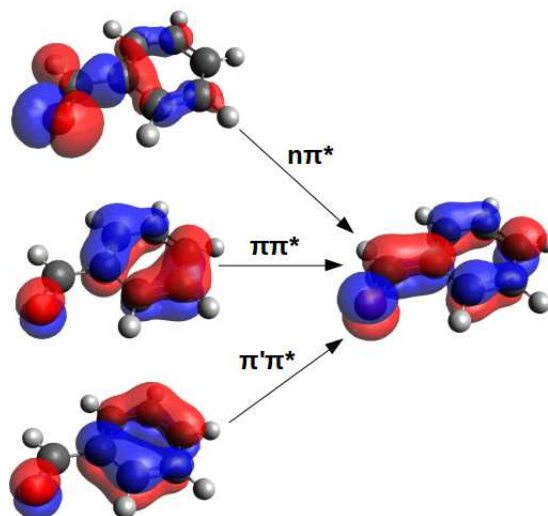
FIGURE 4.3: The Hartree-Fock molecular orbitals of the $n\pi^*$ (S_1, T_1), $\pi\pi^*$ (S_2), and $\pi'\pi^*$ (S_3, T_2) states.

In light of the high ISC rate described in the literature review, the triplet manifold cannot be ignored. ADC(2)/cc-pVDZ calculations for the lowest triplet excited states of BA in the gas phase have also been computed. The vertical excitation energy to T_1 is 3.48 eV, lying only 0.24 eV below S_1. This state is, like S_1, an $n\pi^*$ state. The T_2 state has a vertical excitation energy of 3.52 eV, which is a mere 0.04 eV above the T_1 state. The T_2 state is of $\pi'\pi^*$ character. Indeed, these results agree extremely well with previous data found in the literature (Section 4.2). Figure 4.3 shows the frontier molecular orbitals involved in these transitions.

A solid understanding of the excited state properties of BA in the gas phase has thus been obtained. Still, the focus of this project is on fluorescence quenching in polar, protic solvents. Therefore, it is a logical next step to look at how the static properties of BA change in the presence of a solvent.

4.5   Static properties of solvated benzaldehyde

Our purpose lies in the study of benzaldehyde in polar, protic solution. Thus, it is crucial that the explicit and implicit discription of the solvation of BA be effective. Vertical excited states were calculated at the TD-DFT/CAM-B3LYP/cc-pVDZ level of theory for the first three singlet electronically excited states of BA·H_2O, and the results were compared to ADC(2)/cc-pVDZ and ADC(3)/cc-pVDZ benchmark calculations. Table

4.2 provides the excitation energies (eV) and oscillator strengths for the $BA \cdot (H_2O)_n$ systems, with $n = 0 - 2$. A comparison of the $BA \cdot H_2O$ system in gas phase to that using non-equilibrium C-PCM solvation for water is first drawn. The $\pi'\pi^*$ (S_3) state, which exhibits the highest oscillator strength, has a slightly higher excitation energy in the gas phase than in aqueous solution. It is noted here that the electronic structure of the three lowest singlet states, $n\pi^*$ (S_1), $\pi\pi^*$ (S_2), and $\pi'\pi^*$ (S_3), matches that for BA in the gas phase. This notation for the excited states will be used throughout the discussion in this chapter. For a clear visualization of these states, attachment/detachment density plots are shown in Figure 4.14. As for the case of BA in the gas phase, the CAM-B3LYP functional is again found to appropriately describe the system. The excitation energy for the S_1 state, for example, is only 0.05 eV off from the ADC(2) result, and the bright S_3 state is only off by 0.06 eV.

Evaluating the solvation model is the next step. One to two explicit water molecules are included for this purpose. This explicit consideration is combined with standard non-equilibrium solvation as well as with a first-order, perturbative approximation to the state specific (SS) approach[279, 280], i.e. the ptSS method[281]. The linear response contribution is computed employing the zeroth-order transition density (ptLR). Calculated solvatochromic shifts quantitatively agree with experimental data when ptSS and ptLR are combined[281].

The number of explicit water molecules in the vicinity of BA also has a minor effect on the system. That is, more explicit water molecules do lead to an only slightly more accurate description of BA in aqueous solution. Shown in Table 4.2 are the three lowest vertically excited states computed at the TD-DFT/CAM-B3LYP/cc-pVDZ, ADC(2)/cc-pVDZ, and ADC(3)/cc-pVDZ levels of theory for the BA, $BA \cdot H_2O$, and $BA \cdot (H_2O)_2$ systems. Standard non-equilibrium C-PCM was used. For all numbers of explicit water molecules the $\pi'\pi^*$ is the bright state. Using explicit water molecules is necessary in addition to the implicit solvation model to describe the solvated system. Still, one water molecule is sufficient for the realm of this investigation. Previous calculations had shown only a 0.04 eV difference in excitation energies for the bright state when first order terms are included in the PCM correction beyond the simple 0th order correction. Thus, standard LR-CPCM in combination with an explicit water molecule was deemded sufficient for modeling the solvation of BA in water.

Relatively inexpensive TD-DFT/CAM-B3LYP/cc-pVDZ calculations agree well with ADC(2) results for all model systems, making CAM-B3LYP/cc-pVDZ a good method of choice for the remainder of the study. Also important is the fact that the data does not vary much with the number of explicit water molecules, and therefore one water is used for future calculations. It should be noted here that the experimental absorption

System	$n\pi^*$	$\pi\pi^*$	$\pi'\pi^*$
BA			
-CAM-B3LYP (gas phase)	3.78 (0.00)	5.06 (0.02)	5.50 (0.23)
CAM-B3LYP+LR-CPCM	3.91 (0.00)	4.98 (0.03)	5.36 (0.33)
ADC(2) (gas phase)	3.72 (0.00)	5.00 (0.01)	5.82 (0.31)
ADC(2)+LR-CPCM	3.86 (0.00)	4.97 (0.02)	5.72 (0.32)
BA·H_2O			
-CAM-B3LYP (gas phase)	4.03 (0.00)	5.05 (0.02)	5.50 (0.28)
-CAM-B3LYP+LR-CPCM	4.15 (0.00)	4.94 (0.04)	5.31 (0.39)
ADC(2) (gas phase)	3.96 (0.00)	4.99 (0.01)	5.76 (0.36)
ADC(2)+LR-CPCM	4.07 (0.00)	4.93 (0.02)	5.63 (0.38)
ADC(3) (gas phase)	4.10 (0.00)	4.74 (0.01)	5.62 (0.31)
ADC(3)+LR-CPCM	4.25 (0.00)	4.70 (0.02)	5.52 (0.33)
BA·$(H_2O)_2$			
CAM-B3LYP+LR-CPCM	4.25 (0.00)	4.85 (0.04)	5.23 (0.40)
ADC(2)+LR-CPCM	4.14 (0.00)	4.86 (0.02)	5.51 (0.40)

TABLE 4.2: Excitation energies (eV) and oscillator strengths (in parentheses) for the lowest excited singlet states of BA·$(H_2O)_n$ with $n = 0, 1, 2$ in combination with a C-CPM model for aqueous solution, as computed at the TDDFT/CAM-B3LYP/cc-pVDZ level of theory and compared to the ADC(2) benchmark.

spectrum of BA in water reveals S_2 and S_3 peaks at 4.35 eV (285 nm) and 4.95 eV (250 nm)[282]. The S_1 state cannot be seen in the spectrum. The deviations here with the computational results in Table 4.2 are common because vibrational contributions are not taken into account in the calculations.

4.6 Mechanism of fluorescence quenching of aromatic aldehydes in water

The equilibrium geometry of BA·H_2O in the ground state is the initial structure in our study, when BA is photo-excited in aqueous solution and the fluorescence is subsequently quenched and the excitation energy converted into heat. In this initial strucuture, the distance between the hydrogen-bonded H of water and carbonyl O is 1.86 Å. To determine whether BA acts as a photobase, as previous studies strongly indicate, or rather as an H-abstractor, a relaxed surface scan along the excited state "protonation" coordinate of BA was computed. Of course, the aim is also to determine whether or not hydrogen or proton transfer is a relevant quenching channel, as had been previously proposed. Here, the distance between the H of water and the carbonyl oxygen was shortened in steps of 0.01 Å, optimizing in the S_1 state and allowing all other parameters to relax on the S_1 potential energy surface. Although the bright state is the S_3 state, Kasha's rule[10, 283] implies that ultrafast decay will occur to the S_1 state immediately after excitation, thus

making optimization on the S_1 state most appropriate. The TD-DFT/CAM-B3LYP/cc-pVDZ level of theory was used, employing the equilibrium, linear-response C-PCM to treat solvation in water, as implemented in Gaussian 09, Revision D.01[213]. Figure 4.4 shows single point calculations performed along this computed proton/hydrogen coordinate at the S_1 optimized geometries using non-equilibrium, linear-response C-PCM solvation. The ground and first four singlet electronically excited states are shown, along with the lowest two triplet states. The minimum of the S_0 surface at S_1 optimized geometry is used as the zero point reference. The accuracy of the applied TD-DFT approach has been tested by single point calculations along this coordinate using ADC(2)-s, which yields potential energy curves in qualitative agreement with those obtained at the TD-DFT/CAM-B3LYP level. These curves are shown in Figure 4.4 as well.

Using non-equilibrium solvation modeling, the transfer barrier in the S_1 state is estimated to be at most 0.51 eV, while it is slightly decreased to at most 0.42 eV when equilibrium solvation is employed. Compared to the 1.3 eV excess energy available to the system, defined as the energy difference between the initially excited S_3 state at the ground state equilibrium geometry and the energy of the geometrically relaxed S_1 state, the barrier is easily overcome. At the TD-DFT/CAM-B3LYP/cc-pVDZ/C-PCM level of theory, the T_2 state is also $n\pi^*$, and at OH distances shorter than approximately 1.1 eV, the S_2, T_2, S_1, and T_1 states are all effectively degenerate. Thus, the excited state population all "lands" in the same place along the excited state surface, from which non-radiative decay is then feasible. As previously discussed, ultra-fast ISC from $S_1 \rightarrow T_2$ is observed in the gas phase[253–256] due to a large spin-orbit matrix element, in agreement with El-Sayed's rule. In principle, quantum dynamics calculations would be necessary to quantitatively assess the described quenching mechanism. Also, the situation of the fourfold degeneracy at distances shorter that 1.1 Å favors ISC from the singlet to the triplet manifold. Still, because of the longer lifetimes of triplet states, we hypothesize that quenching in the singlet manifold from $S_1 \rightarrow S_0$ occurs on a quicker timescale than ISC. It is safe to say that low-lying triplet states likely play no role in the quenching of BA in water.

In computing this relaxed surface scan optimized in S_1, the assumption has been made that Kasha's rule is applicable. However, when applying Kasha's rule, it is important to note that it does not hold universally[10]. Famous exceptions of the rule include azulene and its derivatives, see for example [284–288] among others, where the S_2-S_1 energy difference is too large for competitive IC to occur. Generally, it can be said that when the S_2-S_1 energy diffence becomes larger than approximately 1 eV, the applicability of Kasha's rule must be questioned[289]. Kasha's rule indeed depends on the energy gap law, which states that the rate constant of IC or ISC increases exponentially as the energy gap between two electronic states decreases[290]. As a result, when the S_2-S_1
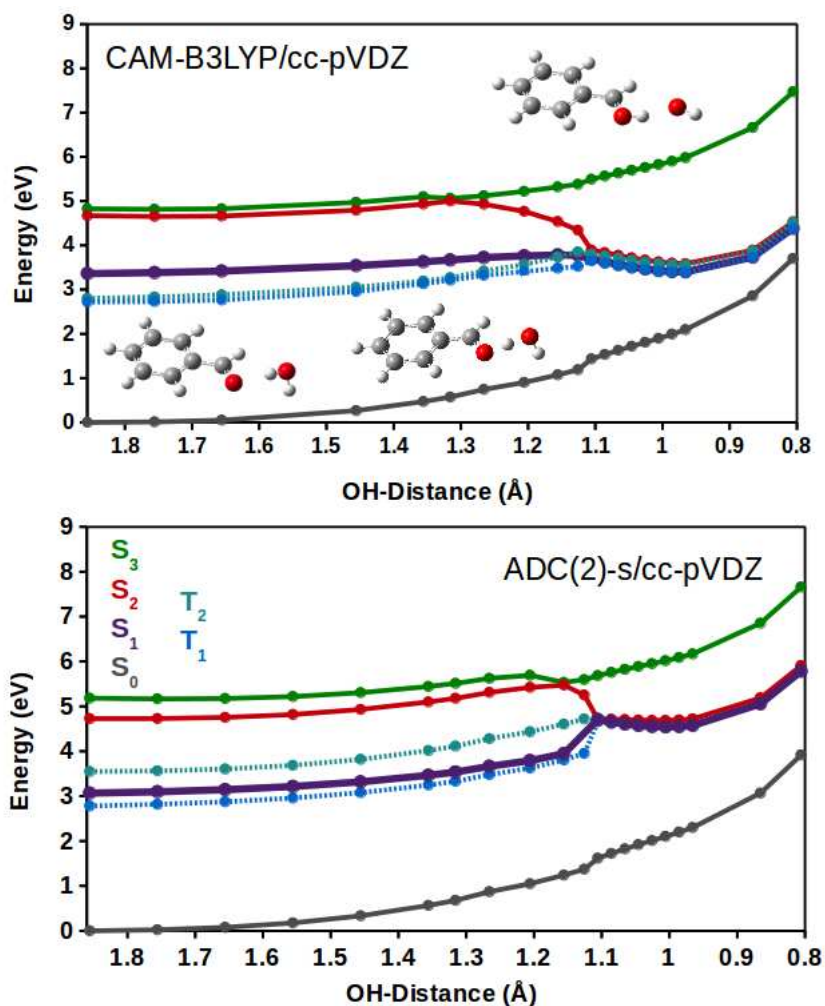
FIGURE 4.4: Potential energy surfaces of the lowest singlet and triplet states of BA·H_2O along the ESHT coordinate from water to the carbonyl of BA, computed at the TD-DFT/CAM-B3LYP and ADC(2)-s levels of theory, employing linear-response, non-equilibrium C-PCM to treat solvation in water.

energy gap is significantly smaller than the S_1-S_0 energy gap, IC from S_2 to S_1 will be much faster than fluorescence from S_2.

Looking to the specific case of the BA·H_2O system, the application of Kasha's rule must be scrutinized. As it is, the energy gap between the bright S_3 state and the S_1 state is, as shown in Figure 4.4 for the S_1 optimized scan, quite large and not appreciably smaller than the gap between S_1 and S_0. Attempting to optimize in the bright S_3 state starting from the ground state equilibrium OH distance of 1.86 Å, immediate IC to S_2 occurs. Following now the S_2 state starting from the same OH distance of 1.86 Å, a significant decrease in the S_2-S_1 energy gap is observed compared to the S_1-optimized scan. Indeed, the S_2-S_1 energy gap drops from more than 1 eV when optimization is performed in S_1 to only 0.5 eV when optimization takes place in S_2. Continuing along the S_2 optimized coordinate, the energy gap shortens even more to around 0.4 eV. Compared to the S_1-S_0

energy gap at the S_2 optimized geometry, which is approximately 4 eV, this 0.4-0.5 eV is indeed significantly smaller. From this alone, one may hypothesize that in the very early stages of the quenching mechanism after photoexcitation, the majority of the population will move from the relaxed S_2 to the S_1 via IC, and subsequently the dynamics will take place primarily in the S_1.

In order to better discern where the conical intersections between the S_3/S_2 and S_2/S_1 states lie, which of course allow for immediate nonradiative decay via IC from the bright S_3 to the S_1, minimum energy crossing point (MECP)[69] optimizations were carried out in Q-Chem 4.3[276] at the TD-DFT/CAM-B3LYP/cc-pVDZ level of theory employing the C-PCM model and using the branching-plane[73] MECP method. Between the S_3 and S_2 states, a conical intersection was found at the geometry of the BA·H_2O system having a distance between the hydrogen bonded O of the carbonyl and the H of water of 1.745 Å. For this structure, the bond length of the C double-bonded to O is 1.266 Å, and the point of intersection lies with an excitation energy of 4.60 eV above the ground state at that geometry. Similarly, a conical intersection between the S_2 and S_1 was found at an OH distance of 1.696 Å and a CO bond length of 1.257 Å. Here, the intersection is 3.88 eV above the ground state. We see therefore that OH distances within 0.2 Å of the ground state equilibrium bond distance, two CIs allow for the rapid initial decay to S_1, further supporting the application of Kasha's rule to this system.

As the quenching mechanism and the exact electronic picture of the excited states along the transfer coordinate is disciphered, three technically-possible routes for post-excitation photodynamics are entertained. First, the system could evolve along the S_3 ($\pi\pi^*$) surface, which is rather unlikely. Second, the system could undergo rapid decay to the S_2 state and evolve here. In light of the above discussion regarding Kasha's rule, it is also unlikely that the majority of the excited population will remain in this state. In the third, and the most likely scenario, initial ultrafast internal conversion (IC) to the S_1 ($n\pi^*$) state occurs. As previously stated, this is in agreement with Kasha's rule and it is therefore the situation dominating the photochemistry. This scenario will therefore be analyzed in the bulk of the following discussion.

It has already been established that the energetic barrier to hydrogen/proton transfer is readily overcome in the S_1 state. The computed coordinate strongly indicates that this is indeed the major channel of fluorescence quenching of BA in aqueous solution. The question remains, however, whether BA is indeed a photobase. To answer this question, analyses of electronic excitations were computed using tools for natural transition orbital, attachment/detachment and difference densities, and Mulliken populations. Mulliken analysis of the partial charges of the BA/BAH and H_2O/OH fragments in the S_1 state, as shown in Figure 4.5, demonstrates that the total charges of the BAH and OH remain

small over the course of the transfer coordinate. Indeed, they are at most around 0.2. This indicates that the transfer of both an electron and a proton, i.e. a *hydrogen atom* is taking place in the S_1 state. Therefore, BA undergoes ESHT rather than the popularly assumed ESPT. At distances of less than 0.97 Å, the ground state is energetically very close to the S_1 state, and decay to the S_0 is anticipated. This non-radiative decay is accompanied by electron transfer from the electronically excited BAH radical to the OH radical, forming BAH^+ and OH^-. The analysis of Mulliken charges confirms this as well, as BAH in the ground state clearly has a positive charge of about +0.9 while OH has a corresponding negative charge of -0.9. The PES of the electronic ground state then indicates that the proton will transfer back once the S_0 is reached, restoring the neutral $BA \cdot H_2O$ situation.
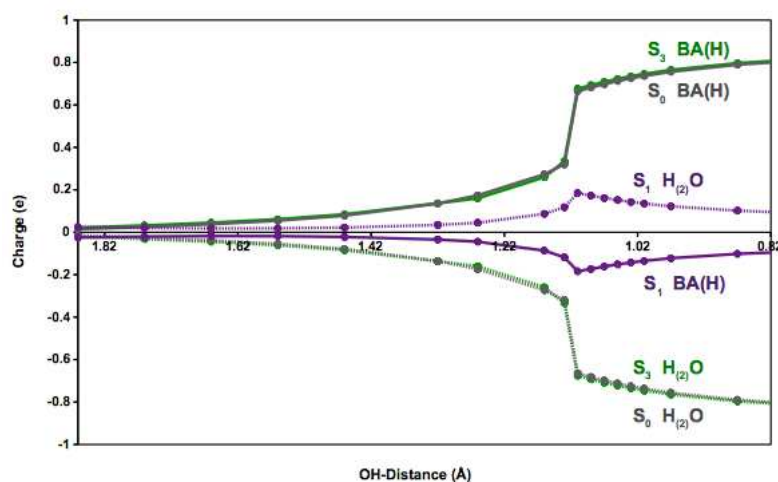
FIGURE 4.5: Mulliken charges for the S_0, S_1, and S_3 states of the $BA \cdot H_2O$ system calculated at the ADC(2)-s level of theory. In the ground and S_3 states, ESPT takes place from water to the aldehyde, while in the S_1 state, a hydrogen atom is transferred instead. Thus in the S_1, the sum of partial charges for both the aldehyde and hydroxide moeities hover around 0 throught the course of the ESHT coordinate.

The fact that ESHT and not ESPT from water to the carbonyl of benzaldehyde is occuring, is substantiated by examination of the attachment/detachment density plots. Attachment (A) and detachment (D) densities are obtained through diagonalization of the difference density matrix. The detachment density is effectively the part of the ground state density that is removed and rearranged to be attachment density during the electronic transition. Taken together, the A/D densies thus characterize the electronic transition $D \rightarrow A$. The sum of A and D corresponds to the difference between the electron densities between the ground state and the excited state of interest, in our case the S_1. A major strongpoint of this analysis is to capture all MO contributions to an electronic transition in one image. The A/D density plots for the lowest five singlet electronically excited states of the $BA \cdot H_2O$ system at ever shorter distances between the carbonyl O and the H of water are shown in Figures 4.6 through 4.9.
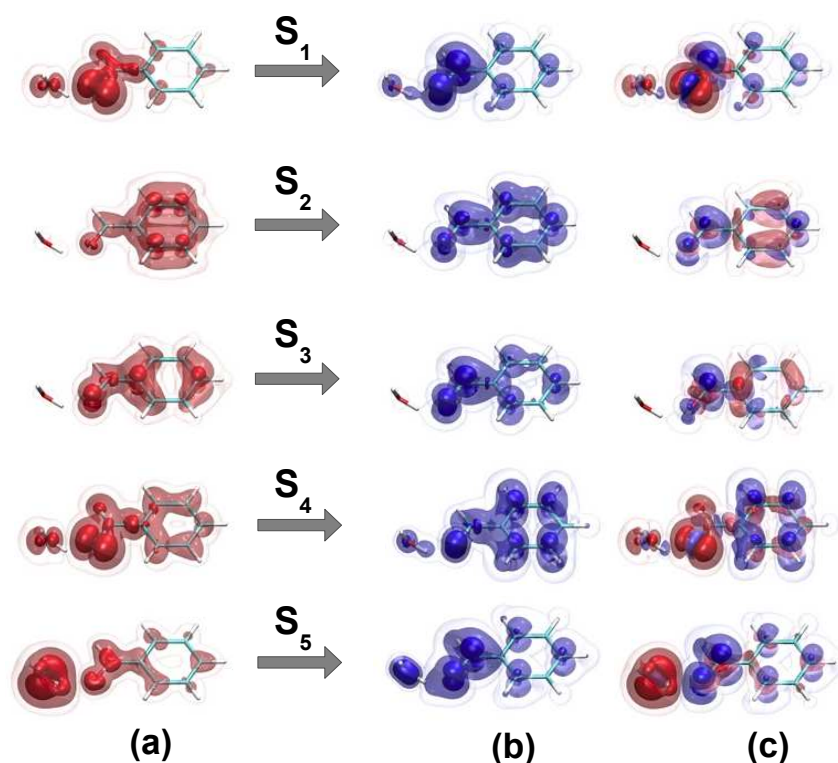
FIGURE 4.6: Detachment (red) and attachment (blue) densities for the lowest five singlet electronically excited states of the BA·H_2O system optimized in S_1 at an OH-distance of 1.56 Å.

Inspecting the A/D plots for the lowest five singlet electronically excited states along the S_1 optimized scan shown in Figures 4.6 through 4.9 at OH distances of 1.56 Å, 1.32 Å, 1.13 Å, and 0.97 Å, a higher-lying CT state is revealed which crosses down from the S_5 position to the S_1 position over the course of the scan. At OH distances of 1.1 Å and shorter, this state, now in the S_1 position, is degernate with the S_2 state of almost identical CT character. That is, the S_1 $n\pi^*$ not only increases in CT character along the scan, but a second CT state moves down over the course of the ESHT coordinate, and both states are energetically degenerate at the minimum in S_1 lying at an OH distance of 0.97 Å. One possible result of this fact is that in other systems, having an S_1 state of $n\pi^*$ character may not be the only condition leading to quenching via the ESHT-based mechanism. If a higher lying state exhibiting CT from water to the carbonyl of the aldehyde crosses down over the course of the OH distance coordinate to below the original S_1 of a related system, quenching via ESHT may still be observed.

As we have seen and the A/D picture confirms, the S_1 state is initially an $n\pi^*$ transition. As the water molecule approaches the oxygen of the carbonyl, the detachment density goes from depicting a lone pair on the oxygen of the carbonyl to a lone pair on the hydroxide moeity. That is, the S_1 state becomes of ever increasing charge transfer character. This indicates again that a simple proton transfer is not taking place in the
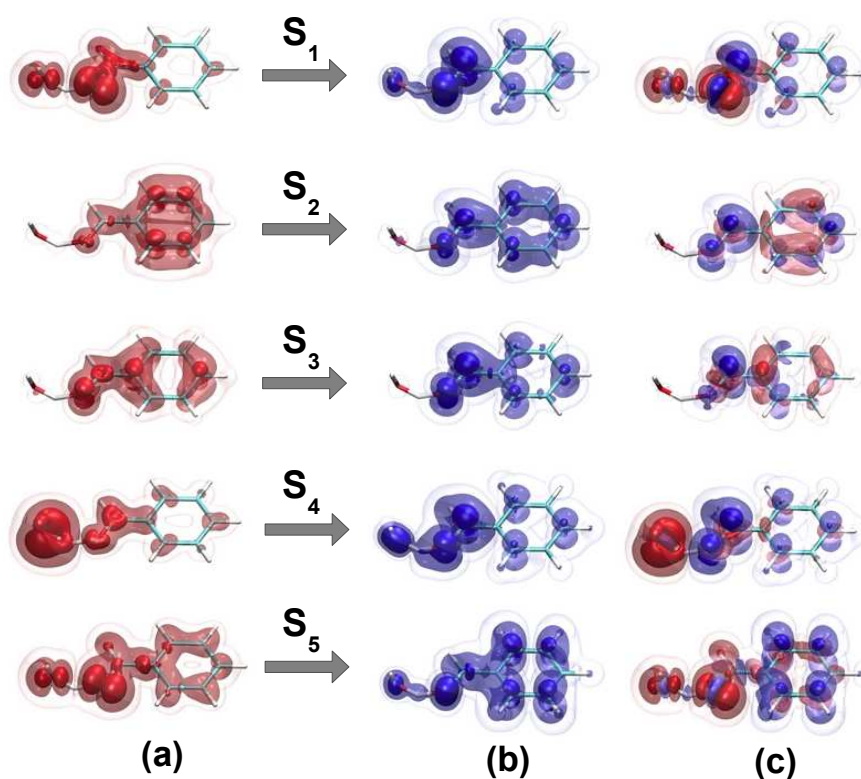
FIGURE 4.7: Detachment (red) and attachment (blue) densities for the lowest five singlet electronically excited states of the BA·H$_2$O system optimized in S$_1$ at an OH-distance of 1.32 Å.

S$_1$ state, but rather the transfer of a hydrogen atom occurs. In decaying back down to the S$_0$, we see therefore see the opposite process: electron transfer occurs initially back to the hydroxide, forming the anionic pair, and proton transfer follows, restoring the neutral ground state scenario.

Finally, a third excited state analysis tool that confirms the observed mechanism is the study of natural transition orbitals (NTOs). NTO analysis offers an additional window into the excited states of this system[148], as they offer a compact picture of the excited state[291–293]. An investigation of the NTOs of BA·H$_2$O again supports the conclusion that CT occurs from the hydroxide moeity to the carbonyl. The NTOs along the S$_1$ state of the system at the same OH distances used for A/D analysis are provided in Figure 4.10.

In general, at and around the transition state, NTO analysis shows low-lying excited states of CT character. The picture obtained from A/D density analysis is corroborated by looking at the NTOs along the coordinate. Again, we see that at an OH distance of around 1.1 Å, electron transfer occurs, indicating that a proton and an electron are transferred to the carbonyl of BA. Thus, we see yet again that, assuming the system
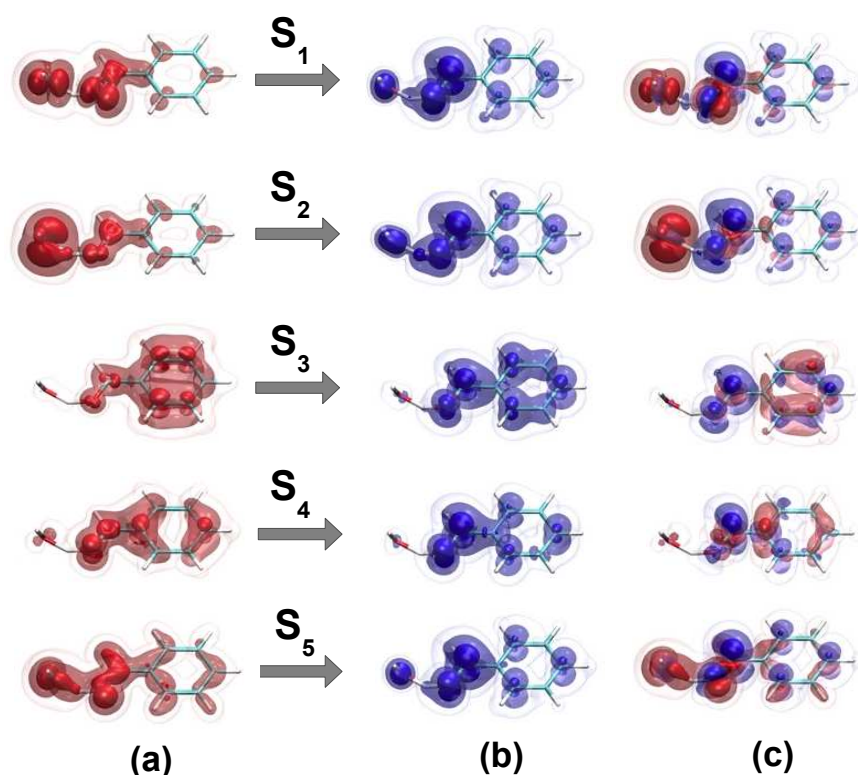
FIGURE 4.8: Detachment (red) and attachment (blue) densities for the lowest five singlet electronically excited states of the BA·H$_2$O system optimized in S$_1$ at an OH-distance of 1.13 Å.

evolves along the S$_1$ state in accordance with Kasha's rule, ESHT rather than ESPT occurs.

Though because of Kasha's rule and the existence of conical intersections between the S$_3$/S$_2$ and S$_2$/S$_1$ states, the vast majority of the excited population of BA·H$_2$O is expected to initially decay ultrafast to S$_1$, one may reasonably assume that it is at least possible that some of the excited population decays only ultrafast from S$_3$ to S$_2$. The scenario where the population evolves on the S$_2$, $\pi\pi^*$ surface is entertained in the following. To study this possibility in more detail, a relaxed surface scan was performed along the same OH distance coordinate as the S$_1$ optimized scan under the same conditions, i.e. starting at the ground state equilibrium OH distance of 1.86 Å and carrying out the optimizations at the TD-DFT/CAM-B3LYP/cc-pVDZ level of theory and employing the equilibrium, linear-response C-PCM model to treat solvation in water. As before, the OH distance was progressively shortened in steps of 0.01 Å. Single point calculations were then performed using the S$_2$ optimized geometries along the scan at the ADC(2)-s/cc-pVDZ level of theory, at OH distances of 1.86 Å, 1.66 Å, 1.46 Å, 1.26 Å, 1.16 Å, and 0.97 Å in order to obtain A/D density plots for comparison with those computed at the S$_1$ optimized geometries. The results are as follows. The original S$_2$ $\pi\pi^*$ state
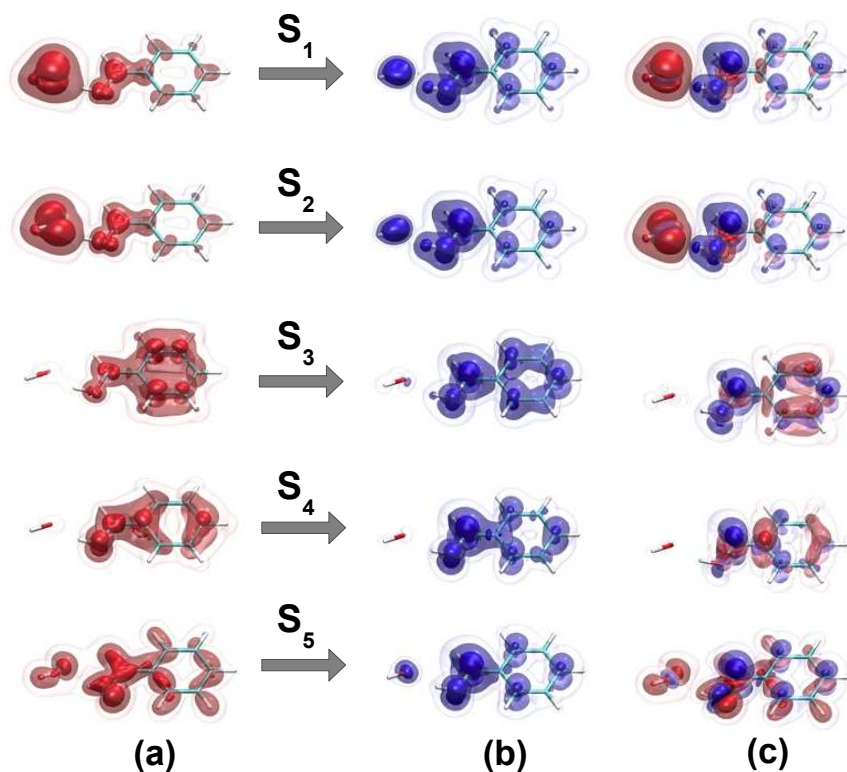
FIGURE 4.9: Detachment (red) and attachment (blue) densities for the lowest five singlet electronically excited states of the BA·H_2O system optimized in S_1 at an OH-distance of 0.97 Å.

moves up to the S_3 position at around 1.1 Å. As was observed in the S_1-optimized scenario, a CT state exhibiting transfer from water to the carbonyl moves down from the S_4 position at an OH distance of 1.46 Å to the S_2 position at a distance of 1.1 Å. Again, the $n\pi^*$ state is originally the S_1 state, and this S_1 state gains in similar CT character as the OH distance between the H of water hydrogen-bonded to the O of the carbonyl is progressively shortened. It is observed again that after an OH distance of 1.1 Å, the S_2 and S_1 states are practically degenerate, leading to the same mechanism. In summary, due to the energetic degeneracy and nearly identical CT characters of the two lowest singlet electronically excited states at OH distances shorter than 1.1 Å, as observed in both the S_2 and S_1 optimized scans, it can be concluded that the same mechanism of fluorescence quenching should be observed in both scenarios.

Of course, in reality, a small amount of the excited state population may indeed evolve on the S_3 ($\pi'\pi^*$) state. In this much less likely case, the estimated energy barrier to proton/hydrogen atom transfer is at most 0.51 eV. This is, however, computed for the scan optimized in S_1, and therefore it is an upper bound for the estimated barrier. Looking back at the Mulliken charges, we note again that the transfer of a proton rather than a hydrogen atom appears to occur, as is the case in the ground state. Indeed, BAH as a charge of +0.9 and OH of -0.9 at smaller OH distances as shown in Figure 4.5. At
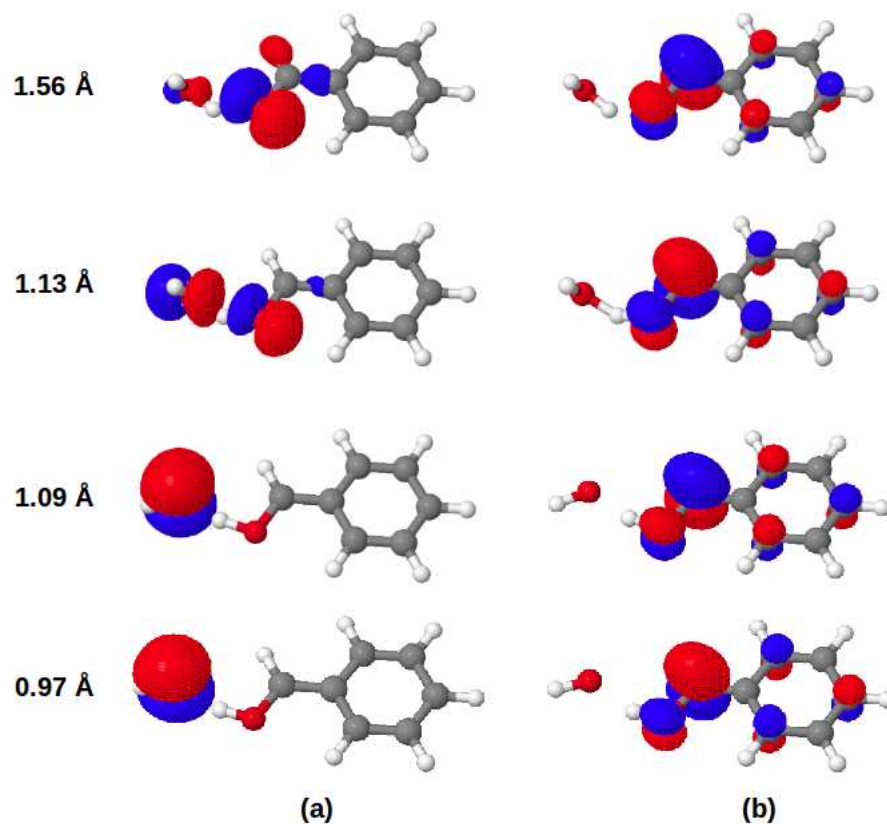
FIGURE 4.10: The NTOs for the S_1 state at OH distances of 1.56 Å, 1.13 Å, 1.09 Å, and 0.97 Å over the course of the hydrogen transfer process.

about 1.35 Å, this state is strongly coupled to the S_2 state, and some of the population could therefore move down into the "well" at 0.97 Å and be quenched. The S_3 state itself continues to increase in energy, making ESPT even less feasible.

The possible quenching mechanisms are summarized in Figure 4.11. Following Kasha's rule, the system evolves along the S_1 state where ESHT, rather than ESPT, occurs and is indeed the route to fluorescence quenching of BA in polar, protic solvents. This stands in contrast to popular belief that BA is a photobase and demonstrates that the basicity of BA is not necessarily increased upon photo-excitation.

The S_1 state clearly determines the photochemistry of BA in aqueous solution. However, this mechanism, while important for aldehydes exhibiting a lowest $n\pi^*$ singlet electronically excited state in solution, does not provide satisfactory elucidation the quenching mechanism in the larger amine indicators. Extensions of the understanding of aldehyde photochemistry in solution are provided in the following sections.
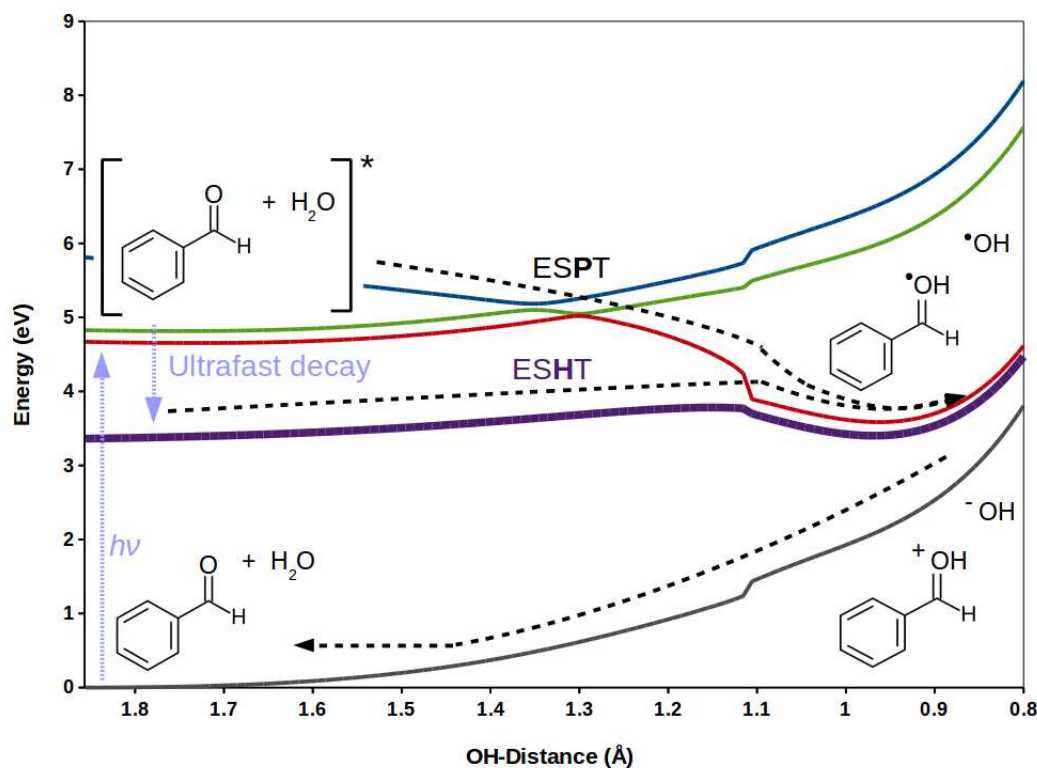
FIGURE 4.11: The mechanism of fluorescence quenching of BA in polar, protic solution.

4.7 Solvent, substituent, and imine effects on fluorescence quenching

Benzaldehyde is well-known to exhibit a relatively low solubility of < 7 g/L in water. It is, however, highly soluble in ethanol. In principle, the excited states of BA·H_2O and BA·EtOH are almost identical. The ADC(2)-s/cc-pVDZ vertical excitation energies are presented in Tables 4.3 (BA·H_2O) and 4.4 (BA·EtOH).

Environment	S_1	S_2	S_3	S_4
Gas Phase	3.96 (0.00)	4.99 (0.01)	5.76 (0.36)	6.62 (0.00)
	$n - \pi^*$	$\pi - \pi^*$	$\pi - \pi^*$	$n - \pi^*$
Water	4.07 (0.00)	4.93 (0.02)	5.63 (0.38)	6.88 (0.31)
	$n - \pi^*$	$\pi - \pi^*$	$\pi - \pi^*$	$n - \pi^*$

TABLE 4.3: Excitation energies (eV) and oscillator strengths (in parentheses) for the four lowest singlet electronically excited states of BA·H_2O in gas phase and in water, as computed using the ADC(2)/cc-pVDZ level of theory.

When computed in the gas phase, the excitation energies differ as little as 0.02 eV. The differences become slightly larger when the excited states are computed using a corresponding C-PCM model for solvation. Then, the excitation energies differ by about 0.1 eV. In analogy to BA·H_2O, the excited states of BA·EtOH in gas phase and in ethanol

Environment	S_1	S_2	S_3	S_4
Gas Phase	3.96 (0.00)	4.98 (0.01)	5.74 (0.39)	6.19 (0.00)
	$n - \pi^*$	$\pi - \pi^*$	$\pi - \pi^*$	$n - \pi^*$
Ethanol	4.06 (0.00)	4.92 (0.02)	5.60 (0.42)	6.54 (0.00)
	$n - \pi^*$	$\pi - \pi^*$	$\pi - \pi^*$	$n - \pi^*$

TABLE 4.4: Excitation energies (eV) and oscillator strengths (in parentheses) for the four lowest singlet electronically excited states of BA·EtOH in gas phase and in ethanol, as computed using the ADC(2)/cc-pVDZ level of theory.

agree quite well, indicating that the presence of ethanol as a solvent does not appreciably affect the neutral BA·EtOH system. The order of the excited states is indeed the same.

Employing the CAM-B3LYP/cc-pVDZ level of theory with equilibrium C-PCM to model solvation in ethanol a relaxed surface scan was performed along the hydrogen transfer coordinate of the BA·EtOH system. As was highly anticipated due to the presence of a S_1, $n\pi^*$ state, the same mechanism for fluorescence quenching is observed as was previously described for the aldehyde system in water. Due to the high solubility of BA in EtOH, experiments can very readily be performed for comparison with our results. Again, the excess energy is computed and the barrier to ESHT estimated based on the curve. The excess energy is 1.28 eV, which agrees almost perfectly with the excess energy for the BA·H_2O system of 1.29 eV. In the BA·H_2O system, the esimated barrier to H-transfer is at most 0.42 eV, and thus the 1.29 eV excess energy is more than sufficient for the ESHT process to be carried out. In the case of the BA·EtOH system, the barrier is a mere 0.19 eV at most, making it even more readily overcome. Of course, this difference is minor compared to the available excess energy and therefore no experimentally observed difference is expected. However, this lowering of the barrier in an alcohol compared to water is also observed in the case of BA in methanol (MeOH), where the S_1 barrier based on an analogously computed relaxed scan in that state was an estimated 0.17 eV. Therefore, one can conclude that the transition state is stabilized in the presence of a slightly less polar alcohol, thereby lowering the barrier to ESHT. Perhaps this stabilization results from less competing H-bonding by the alcoholic solvents compared to water, thus facilitating the ESHT. Still, it is important to note that this effect is rather insignificant and this study of solvents serves primarily to demonstrate that, as long as the aldehyde has a lowest $n\pi^*$ state in a polar, protic solvent, the same mechanism as observed in the initial case of BA·H_2O will ensue.

Of course, one may also consider if substituents have any measurable effect on the quenching mechanism, particularly because charge transfer processes are involved. Again, it is observed that, as long as a lowest $n\pi^*$ state is present, the same mechanism will be observed. However, the amount of initial excess energy is effected by the activating or

deactivating character of the substituents on the benzaldehyde ring. The fluorescence of aromatic systems is known to be influenced by their substituents, with electron-donating ones generally enhancing fluorescence and electron-withdrawing ones causing quenching[294]. To reiterate, three potential mechanisms for the fluorescence quenching in polar, protic solvents have been determined. In the first and least likely case, the system evolves along the S_3 surface after photoexcitation. This scenario is associated with the transfer of a *proton* from water to the carbonyl of the aldehyde. In the second case, the system undergoes initial ultrafast decay to the S_2 state, where it evolves and eventually becomes degenerate with the S_1 state at OH distances shorter than about 1.1 Å. It is most likely, however, that the system initially decays ultra-fast to the S_1 state, where *hydrogen* atom transfer is confirmed to be the prevailing mechanism. This second case is far more likely and will dominate the photochemistry of the aromatic aldehydes.

Electron withdrawing substituents, for example cyano groups, pull charge from the ring and could potentially facilitate the initial transfer of a hydrogen atom to the carbonyl group of the aldehyde. Activating groups, such as the methoxy substituents studied here, donate charge to the ring and could thus slow down the mechanism in S_1. However, in the unlikely even that the mechanism plays out in S_3, activating groups would logically facilitate the process. It should be noted that the protonation equilibria of benzaldehydes has been computationally studied[295], and proton transfer in the ground state between nitric acid and benzaldehyde has also been investigated[296]. Here, the focus is of course on hydrogen transfer in the excited state and the effect of substituents on the previously outlined quenching mechanism. As such, the effect of such substituents is not substantial, and the lowest singlet electronically excited state is consistently of $n\pi^*$ character. Table 4.5 shows the computed initial excess energies and estimated energy barriers for the calculated hydrogen transfer coordinates for the systems and solvents studied. As before, the initial excess energies are computed to be the energy difference between the Franck-Condon point of the S_3 state and the energy of the geometrically relaxed S_1 state.

System	Solvent	Excess energy	Barrier in S_1
BA·H_2O	H_2O	1.29	0.42
BA·EtOH	EtOH	1.28	0.19
BA·MeOH	MeOH	1.28	0.17
p-OCH_3-BA·H_2O	H_2O	1.01	0.42
p-CN-BA·H_2O	H_2O	1.24	0.41
3,4,5-CN-BA·H_2O	H_2O	1.40	0.42
3,4,5-OH-BA·H_2O	H_2O	0.49	0.42
p-NO_2-BA·H_2O	H_2O	0.87	0.41

TABLE 4.5: Excess energies and estimated energy barriers for the calculated hydrogen transfer coordinates for a variety of systems and solvents. All energies are in eV.

Assuming the photo-excited system evolves in the S_1 state, neither the presence of electron donating nor withdrawing substituents should have a measurable effect on whether or not the neutral hydrogen atom is transferred. However, a lowering of the S_1 state is observed in the case of, for example, 3,4,5-tricyanobenzaldehyde·H_2O compared to 3,4,5-trihydroxybenzaldehyde·H_2O. The computed initial excess energy for the 3,4,5-tricyanobenzaldehyde·H_2O system is about 1.40 eV, wich is a marginal increase of about 0.11 eV compared to BA·H_2O. In the case of 3,4,5-trihydroxybenzaldehyde·H_2O, the excess energy is a mere 0.49 eV, which is only just sufficient to overcome the esimated 0.42 eV barrier. The presence of deactivating substituents appears to stabilize the $n\pi^*$ transition of the first electronically excited state. The case of p-nitrobenzaldehyde·H_2O, with an initial excess energy of 0.87 eV, stands in contrast to this observed trend. Overall, some minor tuning of the efficiency of the mechanism is thus expected to be possible by adding substituents and changing solvents. Still, based on the relaxed surface scans computed for all cases in Table 4.5, the mechanism confirmed for BA·H_2O is indeed the same, and the observed effects have no major impact on the observation of quenching via the ESHT channel.

Experimental studies of novel amine indicators, framing the larger motivation for this project, were described in depth in the introduction to this chapter. The dialdehyde indicators ceased to fluoresce in water, while addition products that formed an aminal, hemiaminal, or imine were not quenched. Thus arose the question as to whether or not small amines also exhibit the fluorescence quenching mechanism observed for BA, or if the differences between the two groups are present already at this level. Here, the carbonyl -O is replaced with an NCH_3 group, and a relaxed surface scan is again performed at the TD-DFT/CAM-B3LYP/cc-pVDZ level of theory and optimized in the S_1 state. Shown in Figure 4.12 (A), it is clear that the mechanism observed for BA does not play out.

Interestingly, the first excited state is incredibly low-lying, as a result of the rotation of the C-C-N-C dihedral angle at the optimized S_1 geometry. Thus, a relaxed scan in S_1 of this dihedral was also carried out from the planar structure to a right angle, at increments of 1 degree, as shown in Figure 4.12 (B). It is observed that, as the dihedral angle becomes increasingly right, a non-radiative decay route opens up from $S_1 \rightarrow S_0$. Therefore, while the mechanism determined for BA is not relevant here, fluorescence is still quenched. It is therefore concluded that the mechanisms determined for these small systems cannot be generalized to predict the photochemistry observed for the large amine indicators.

Longer, extended π-systems are needed to investigate the mechanism of quenching for the larger amine indicators. For these larger structures, the S_1 state is no longer $n\pi^*$,
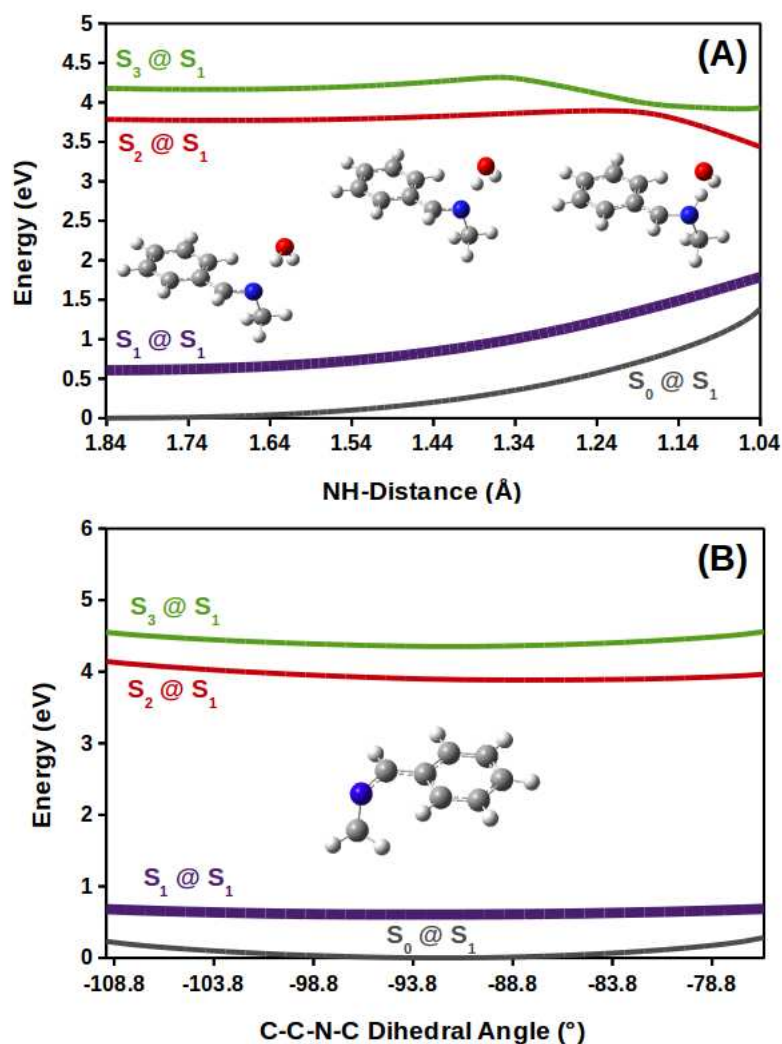
FIGURE 4.12: ESHT coordinate (A) and dihedral rotation of the C-C-N-C dihedral angle for benzylidenemethylamine. Relaxed scans are computed at the TD-DFT/CAM-B3LYP/cc-pVDZ level of theory using equilibrium, linear-response C-PCM to treat solvation in water and optimized in the S_1 state.

but rather, as we will see, $\pi\pi^*$. In this case, possibilities of ESPT or other non-radiative decay channels such as via ISC have been discussed. These differences will be elucidated at length in the following sections.

4.8 Size of the π-delocalized system

In this section, a series of aromatic aldehydes of increasing size, shown in Figure 4.13, are discussed. For BA and other aromatic aldehydes with a lowest $n\pi^*$ state, ESHT is the mechanism of fluorescence quenching in aqueous solution. However, increasing the size of the conjugated system alters the ordering of the excited states, and quenching

may occur via other routes, like dihedral angle rotation of a double bond between two phenyl rings, ISC, or some other channel.

$n = 0, 1, 2, 3$
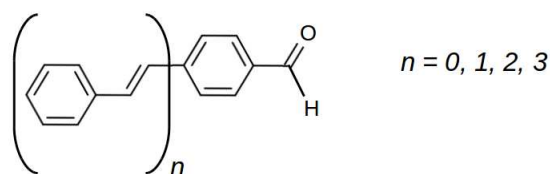
FIGURE 4.13: The series of aromatic aldehydes of increasing size studied in this investigation.

First, each aldehyde is discussed individually. A summary discussion of size effects on quenching is then given.

4.8.1 $n = 0$

This is of course the case of simple BA, though for the sake of easy comparison, a review of the excited states of BA in aqueous solution is given. Table 4.6 provides the excitation energies and oscillator strengths for the lowest singlet and triplet electronically excited states of BA. The characters of the three lowest singlet and triplet states, most relevant to the discussion to follow in the coming sections, are given in Figure 4.14. The A/D and difference densities, computed using TD-DFT, elucidate where the states of different characters lie.

S_1	S_2	S_3	S_4	S_5
3.96 (0.000)	5.02 (0.033)	5.40 (0.337)	6.62 (0.338)	6.79 (0.490)

T_1	T_2	T_3	T_4	T_5
3.20	3.37	4.17	4.51	5.24

TABLE 4.6: Excitation energies (eV) and oscillator strengths (in parentheses) for the five lowest singlet and triplet electronically excited states of BA·H_2O using C-PCM to treat solvation in aqueous solution, as computed at the TD-DFT/CAM-B3LYP/cc-pVDZ level of theory.

The S_1 state is, of course, $n\pi^*$, and lies about 0.75-0.60 eV above the two lowest triplet states. Figure 4.13 also provides the nomenclature for these three critical states that will be used consistently throughout this discussion. The S_1 and T_2 states are $n\pi_a^*$, the S_2 and T_3 are $\pi_i\pi_b^*$, and the S_3 and T_1 are $\pi_j\pi_b^*$. The quenching mechanism proceeds via ESHT in the $n\pi_a^*$ state.

FIGURE 4.14: Detachment (a), attachment (b), and difference (c) density plots for the lowest singlet and triplet excited states of $n = 0$, computed at the TD-DFT/CAM-B3LYP/cc-pVDZ level of theory using C-PCM for water.

4.8.2 $n = 1$

The A/D density plots of the lowest singlet and triplet electronically excited states of the $n = 1$ system, computed as vertical excitations at the TD-DFT/CAM-B3LYP/cc-pVDZ level of theory, using non-equilibrium C-PCM for water, is shown in Figure 4.15. Table 4.7 gives the vertical excitation energies for these lowest states common to BA and the $n = 1$ systems. Notably, the bright $\pi_j\pi_b^*$ state, which was S_3 for BA, has shifted down to be S_1, while the energy of the $n\pi_a^*$ state is essentially unchanged. The ordering of the triplet states remains the same, but the excitation energy of the lowest $\pi\pi^*$ triplet state is lowered in energy by about 1 eV.

Since the $n\pi_a^*$ singlet state is no longer the lowest, the ESHT mechanism was hypothesized to fail for this case. Figure 4.16 shows the relevant potential energy surfaces along the H/H^+ transfer coordinate for the $n = 1$ system. The initial excess energy, computed as the difference between the total energy of the system at the Franck-Condon point of the S_1 surface minus that of the relaxed S_1 system at an OH-distance of 1.83 Å, is a mere 0.4 eV. Since the bright state is no longer higher-lying and thus no initial ultrafast

S$_1$	S$_2$	S$_3$	S$_4$	S$_5$
3.85 (1.311)	3.92 (0.000)	4.72 (0.018)	4.97 (0.002)	5.34 (0.006)

T$_1$	T$_2$	T$_3$	T$_4$	T$_5$
2.12	3.28	3.34	4.04	4.08

TABLE 4.7: Excitation energies (eV) and oscillator strengths (in parentheses) for the five lowest singlet and triplet electronically excited states of the $n = 1$ system using C-PCM to treat solvation in aqueous solution, as computed at the TD-DFT/CAM-B3LYP/cc-pVDZ level of theory.

FIGURE 4.15: Detachment, attachment, and difference density plots for the lowest singlet and triplet excited states of $n = 1$, computed at the TD-DFT/CAM-B3LYP/cc-pVDZ level of theory using C-PCM for water.

decay to the S$_1$ occurs, this is to be expected. The 0.4 eV available is nowhere near sufficient energy to cross the barrier estimated to be at most 1.2 eV based on the PES. In addition, at an OH-distance of about 1 Å, no reorientation of the hydroxide moeity has taken place as was the case for BA in water. Therefore, the mechanism observed for BA and assumed to hold for aromatic aldehydes with a lowest singlet $n\pi^*$ state is not valid for this case.

Since this first system which consists of two rings joined by a central C-C-C-C dihedral angle, is of course a very close relative of the popularly studied stilbene. It is therefore natural to examine the possibility of dihedral rotation to *trans-cis* isomerization of the system. Stilbene photoisomerization has been extensively studied both experimentally[297–314] and theoretically[315–330]. Both the *cis-trans* and *trans-cis* directions of
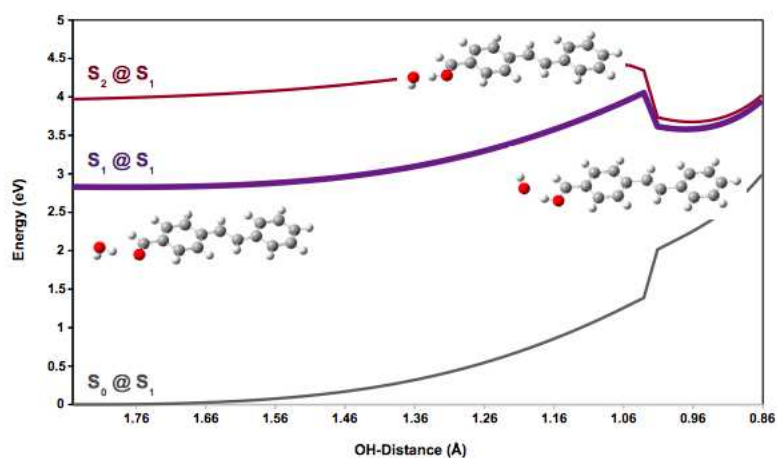
FIGURE 4.16: Potential energy surfaces, calculated at the TD-DFT/CAM-B3LYP/cc-pVDZ level of theory, of the lowest singlet electronically excited states of the $n = 1$ system. Optimization is carried out in the S_1 state at decreasing OH distances between the hydrogen of water and the carbonyl oxygen. Steps of 0.02 Å are taken and solvation is treated using the linear-response, equilibrium C-PCM model for water.

isomerization have been studied, and recent dynamical simulations of *cis-trans*[326–330] and *trans-cis*[316, 317, 331] show that both cases involve essentially the same mechanism[331]. These involve an initial weakening of the central C-C double bond resulting from the electronic excitation, followed by dihedral rotation about this bond and subsequent de-excitation due to an avoided crossing close to a conical intersection between the potential surfaces of the S_1 and S_0[331]. Dynamical simulations of *trans-cis* isomerization indicate that the dihedral rotation key to non-radiative decay takes place on a longer timescale[331] than for *cis-trans* isomerization, where rotation is immenently observed post-excitation[326–330]. Still, *trans-cis* isomerization occurred on the timescale of only several ps. It should be noted that these simulations involved stilbene being irradiated with a 150 fs (FWHM) laser pulse and photon energy of 3.1 eV, which agreed with the density-functional energy gap between HOMO and LUMO. While for *cis-trans* isomerization the rotation is directly induced, for *trans-cis*, electronic excitation not only weakens the central double bond, but also induces vibrations involving this bond which cause the isomerization. In the singlet manifold, the presence of an avoided crossing restores the original central double bond in the electronic ground state[331].

For the $n = 1$ aldehyde, a similar mechanism should in principle be possible. The central C-C bond length in the ground state is 1.343 Å, while in the S_1 state, at equilibrium geometry following excitation from the ground state, it is 1.420 Å. This indicates a weakening of the central C-C double bond resulting from the excitation. Examining the A/D plots as well for the S_1 state of the $n = 1$ system shows that electron density is shifted from the central bond to the C-C single bonds that flank the original double bond. As is the case for stilbene, the bond order of the $n = 1$ system is decreased upon

photoexcitation, leading to the possibility of free rotation about this bond and resulting fluorescence quenching. This possibility will be reexamined in the cases of the larger aldehydes as well.

4.8.3 $n = 2$

Increasing the size of the conjugated system again, a further lowering of the bright S_1, $\pi_j\pi_b^*$ state by about 0.47 eV occurs, as well as a further increase in its oscillator strength. Unlike for the case of $n = 0$, the higher lying singlet states exhibit significantly lower oscillator strengths and $\pi_j\pi_b^*$ is decidedly the dominant transition. The triplet states are also lowered in their excitation energies, with the T_1 now lying about 1.4 eV below the T_1 of BA. The states are summarized in Table 4.8, and the A/D plots associated with them are shown in Figure 4.17.

S_1	S_2	S_3	S_4	S_5
3.38 (2.219)	3.92 (0.000)	4.35 (0.009)	4.69 (0.010)	4.71 (0.010)

T_1	T_2	T_3	T_4	T_5
1.82	2.49	3.31	3.34	3.89

TABLE 4.8: Excitation energies (eV) and oscillator strengths (in parentheses) for the five lowest singlet and triplet electronically excited states of the $n = 2$ using C-PCM to treat solvation in aqueous solution, as computed at the TD-DFT/CAM-B3LYP/cc-pVDZ level of theory.

Of course, since the lowest state is not $n\pi^*$, the mechanism outlined for BA will not be observed. Indeed, assuming the excited state behavior observed in the $n = 1$ system is also to be seen here, the system evolving along the S_1 state should not undergo non-radiative decay in the singlet manifold. In this case, however, the triplet $n\pi^*$ state (T_4), is practically degenerate with the S_1. Therefore, ISC from the S_1 to the T_4 is theoretically possible. IC to the T_3 may well then ensue, since the T_3 lies only 0.03 eV below T_4. Non-radiative decay may well thus occur via a complex set of processes involving both the singlet and triplet manifolds.

The possibility of dihedral rotation about the C-C-C-C dihedral angle between rings closest to the aldehyde is considered next. Here, the bond order of the double bond between the two most central carbon atoms should not decrease upon excitation to the extent that it does for $n = 1$. This is evidenced by the A/D plots, which show density moving from both C-C double bonds on each side of the central ring to the single bonds. That is, less density overall is shifted from the double bonds to the single bonds, and therefore the double bonds do not decrease in bond order to the same extent as for $n =$ upon excitation. This central C-C bond therefore does not allow for the dihedral
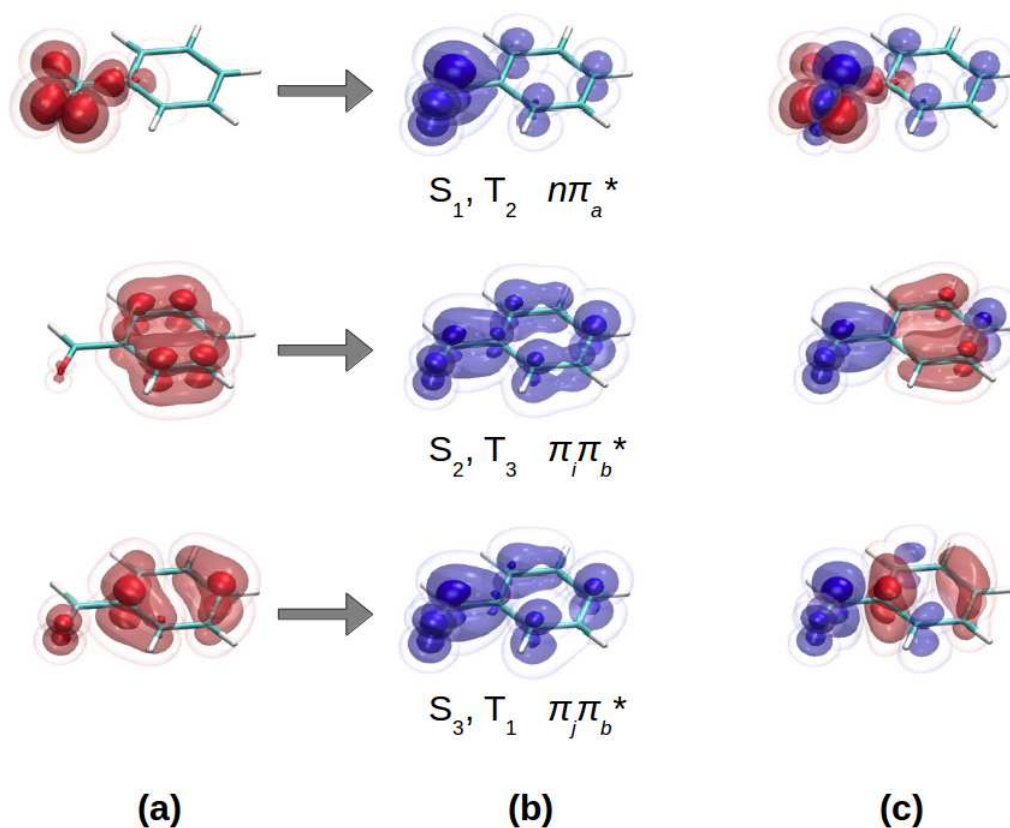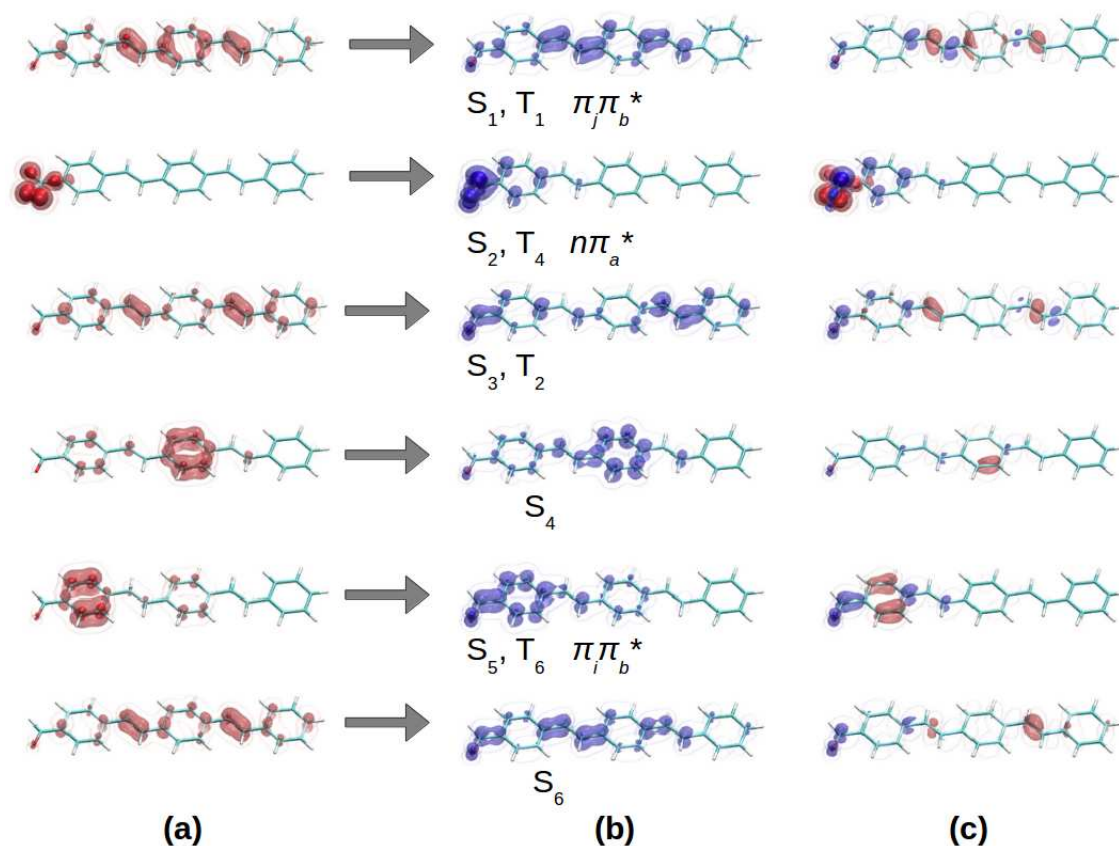
FIGURE 4.17: Detachment, attachment, and difference density plots for the lowest singlet and triplet excited states of $n = 2$, computed at the TD-DFT/CAM-B3LYP/cc-pVDZ level of theory using C-PCM for water.

rotation in stilbene upon excitation. Hence, quenching via this route is not an option. Indeed, this is substantianted by the bond lengths in the ground and excited states. In the ground state, the double bonded C atoms share a bond length of 1.344 Å, while at the equilibrium geometry in the excited state, it is 1.401 Å, i.e. the bond order of the original double bond does not change appreciably upon excitation and rotation should be significantly less feasible.

4.8.4 $n = 3$

An aldehyde with four aromatic rings is the largest system considered in this study. Sorting the excited states naturally becomes a more complicated process, which is why the lowest seven electronically excited states are shown in Figures 4.18 and 4.19, along with Table 4.9. A complex manifold of several $\pi\pi^*$ excited states exists above the $n\pi^*$ state, and the clear $\pi_i\pi_b$ state exhibited by the smaller systems is not present in the lowest seven singlet states, though the S_7 is shows similar A/D plots to those of this $\pi_i\pi_b$ state in the other systems. Compared to the $n = 2$ structure, the bright S_1, $\pi_j\pi_b$ has shifted further down to by 0.2 eV to a vertical excitation energy of 3.18 eV. In doing

so, it loses its degeneracy with the T_4 state. It is also notable that the S_2 state is not an $n\pi^*$ state, as it was for the $n = 1$ and $n = 2$ systems, but rather a $\pi\pi^*$ state very similar to the S_1. The $n\pi^*$ state appears first in the S_3 and T_5 states. The S_1 and T_1 states are of the same character, as are the S_2 and T_2 states. Since again the lowest singlet state is not $n\pi^*$, but yet again rather a $\pi_j\pi_b$ state, the quenching mechanism outlined for BA does not hold. In addition, because of the lack of degeneracy between the $\pi_j\pi_b$ and any triplet state, ISC does not seem as likely. ESHT/ESPT is not expected to yield quenching.
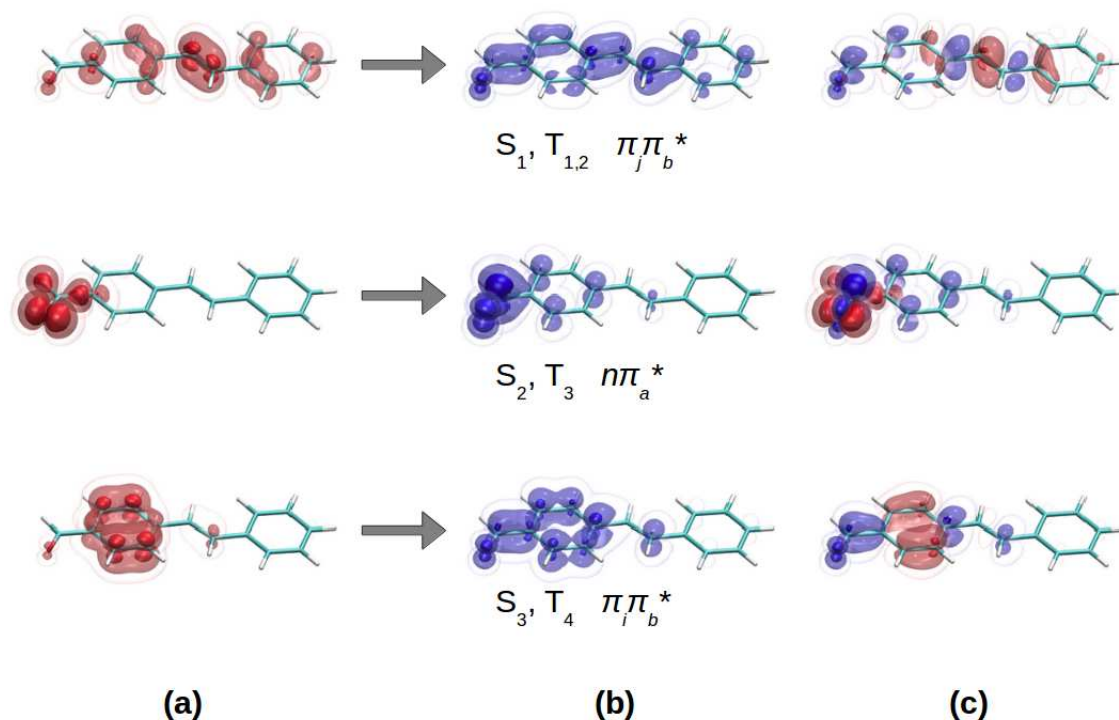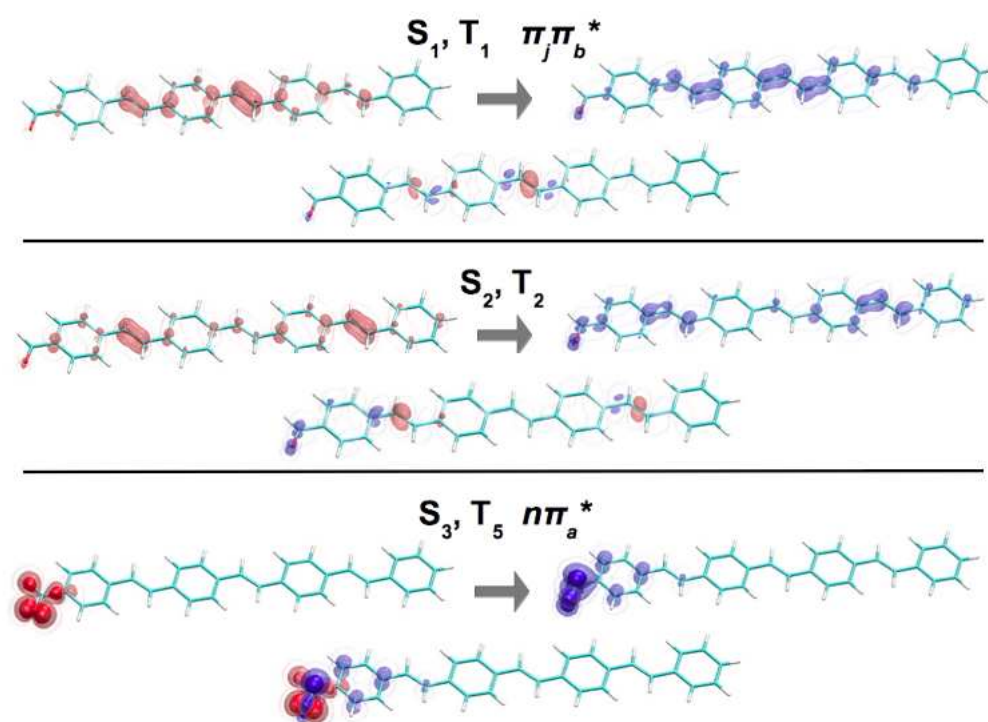

FIGURE 4.18: Detachment, attachment, and difference density plots for the lowest singlet and triplet excited states of $n = 3$, computed at the TD-DFT/CAM-B3LYP/cc-pVDZ level of theory using C-PCM for water.

S_1	S_2	S_3	S_4	S_5	S_6	S_7
3.18	3.87	3.92	4.58	4.62	4.69	4.702
(3.130)	(0.009)	(0.000)	(0.099)	(0.122)	(0.021)	(0.014)
T_1	T_2	T_3	T_4	T_5	T_6	T_7
1.71	2.14	2.69	3.33	3.35	3.78	4.04

TABLE 4.9: Excitation energies (eV) and oscillator strengths (in parentheses) for the five lowest singlet and triplet electronically excited states of the $n = 3$ using C-PCM to treat solvation in aqueous solution, as computed at the TD-DFT/CAM-B3LYP/cc-pVDZ level of theory.
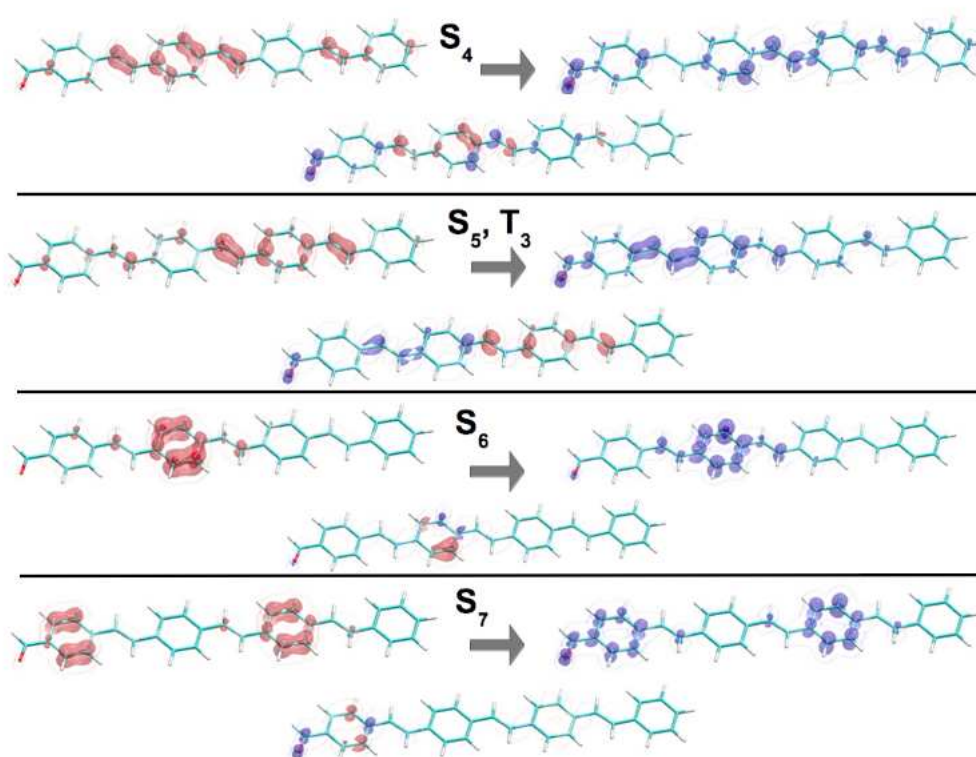
FIGURE 4.19: Detachment, attachment, and difference density plots for the lowest singlet and triplet excited states of $n = 3$, computed at the TD-DFT/CAM-B3LYP/cc-pVDZ level of theory using C-PCM for water.

For this largest aldehyde, like for the $n = 2$ sytem and for the same reasoning, dihedral rotation of the C-C-C-C angle in the para position relative to the aldehyde group is unlikely to be present as a quenching channel. Indeed, the bond length of the central C-C double bond of this angle is 1.344 Å in the ground state and 1.377 Å in the excited state, evidencing almost no change in the strength of the bond or bond order upon excitation. Since ISC/IC channels do not seem to be open and rotation is not feasible, this system, which is longer than the fluorophores depicted in Figures 4.1 and 4.2, may well fluoresece in aqueous solution.

4.8.5 Summary of size effects

In order to visualize how the size of the conjugated system influences the ordering of the excited states and, thereby, the possible fluorescence quenching routes, Figure 4.20 plots the vertical excitation energies for the main $n\pi_a^*$, $\pi_i\pi_b^*$, and $\pi_j\pi_b^*$ singlet and triplet electronically excited states for all of the systems considered in the above discussion. The $n\pi_a^*$ state is slightly lower, by about 0.5 eV, in the triplet than in the singlet manifold for all systems. The excitation energy also does not exhibit any significant energetic changes with increased system size. The $\pi_i\pi_b^*$ state moves from the S_2 to the S_3 position going

from the $n = 0$ to the larger systems, while exhibiting a minor decrase in excitation energy of about 0.1-0.2 eV. As is the case for $n = 0$, this state should not play any significant role in the photochemistry of the aromatic aldehydes.
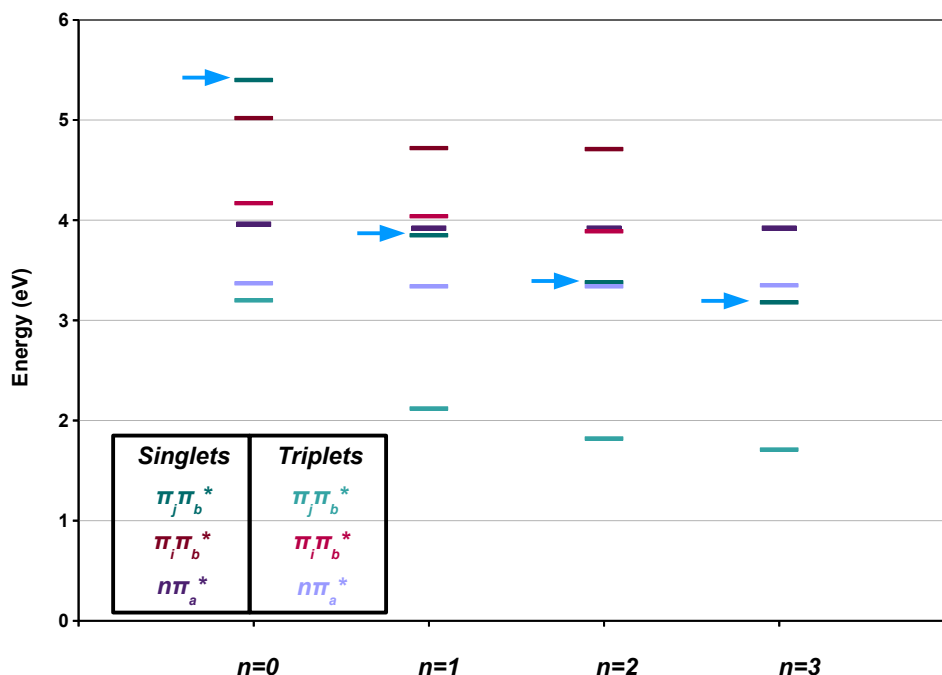
FIGURE 4.20: Comparison of the ordering of the $n\pi_a^*$, $\pi_i\pi_b^*$, and $\pi_j\pi_b^*$ singlet and triplet electronically excited states for the $n = 0, 1, 2$, and 3 systems, computed at the TD-DFT/CAM-B3LYP/cc-pVDZ level of theory using C-PCM for water. The bright state for each structure is marked with a blue arrow.

The change most significant to the photochemistry of the aldehyde series involves the bright $\pi_j\pi_b^*$ state. Here, a sharp decrease in the excitation energy to this state is observed with the addition of one ring, i.e. for $n = 1$. For this state, it is nearly degenerate with the $n\pi_a^*$ state, however. With increased system size, the bright $\pi_j\pi_b^*$ state moves ever lower energetically. This change occurs both in the singlet and triplet manifolds. Several options for the impact of this trend on the photochemistry of the aldehydes follow. First, for the $n = 2$ system, the $\pi_j\pi_b^*$ (S$_1$) state is practically degenerate with the $n\pi^*$ (T$_2$) triplet state. Therefore, intersystem crossing from the S$_1$ to the T$_2$ could ensue. Since T$_2$ is an $n\pi^*$ state, ESHT may well be a possible route for quenching. For $n = 1$, the S$_1$ and T$_2$ states are not degenerate, but still relatively close energetically, so that ISC could likely occur somewhere near the equilibrium geometry on the potential energy surface. Still, for $n = 1$, it has been established that the alternative route via stilbene-like dihedral rotation is another possibility. Finally, the $n = 3$ system exhibits, as previously described, a signficantly more complicated series of both singlet and triplet excited states. The bright $\pi_j\pi_b^*$ (S$_1$) state is also very low-lying compared to most of the other states, particularly lying below the triplet $n\pi_a^*$. Still it lies only about 0.5 eV above

the T_3 state, as indicated in Table 4.9. Therefore, for this largest system, ISC from S_1 to T_3, followed by IC from T_3 to T_2, and then from T_2 to T_1, is a possibility. The T_1 state, lying very low with an excitation energy of only 1.71 eV, may then be coupled in neighboring areas of the potential energy surface to the S_0 state, where non-radiative decay could then occur. This largest system is also longer than the cruciform dialdehyde fluorophore which known to exhibit quenching. Another possibility is therefore that up to the $n = 2$ system can quench via ESHT, ESPT, or a series of ISC and IC processes, while the $n = 3$ sytem is fluorescent.

This detailed description of the excited states of the $n = 0, 1, 2, 3$ aldehyde series offers an initial look into what photochemical processes may be possible for aromatic aldehydes of varying size after photoexcitation. Of course, more elaborate calculations, including accurate potential energy surfaces and even quantum dynamics calculations would be necessary to elucidate what processes take place without a doubt. Still, this thorough description and ordering of the excited states confidently points to the possible routes of interest for further investigation.

4.9 Conclusion

Novel water-soluble distyrylbenzenes appended with aldehyde groups were recently synthesized and found to be excellent fluorescence-based turn-on indicators for amines. Indeed, primary, secondary, and 1,n-diamines were shown to be detectable with aldehyde-substituted distyrylbenzenes and cruciform dialdehyde fluorophores. However, these cutting-edge amine indicators exhibited either no or barely any fluorescence in water. Since benzaldehyde, a quintessential aromatic aldehyde, was the smallest common structure contained in the indicators, it served as a perfect starting point for what became a thorough investigation of fluorescence quenching of aromatic aldehydes in polar, protic solution.

Benzaldehyde in the gas phase has been studied quite extensively in its own right. In addition, experimental data indicates that it, like the amine indicators, does not fluoresce in water. Up until now, it was unclear as to whether benzaldehyde acts as a photobase in aqueous solution, or rather a hydrogen-abstractor. While much information about ketone and aldehyde photochemistry as pertaining to organic synthesis indicates that benzaldehyde should undergo ESHT, a plethora of studies claimed that it was a photobase, i.e. ESPT should occur.

After a thorough benchmarking of TD-DFT methods against high-level ADC(2)-s calculations, the TD-DFT/CAM-B3LYP/cc-pVDZ level of theory was chosen as the best

level of theory to describe the system. In addition, the presence of aqueous solution was treated explicitly, through the addition of one water molecule in the vicinity of the carbonyl, and implicitly using the C-PCM model for water.

The mechanism of fluorescence quenching of benzaldehyde in water was then determined. Since ESPT had been the hypothesized route of fluorescence quenching, the coordinate most appropriate to study was the shortening of the OH distance between the hydrogen of water and the carbonyl oxygen. First, potential energy surfaces of the lowest electronically excited states of the BA·H_2O system were computed at the TD-DFT/CAM-B3LYP/cc-pVDZ level of theory, optimized in the S_1, $n\pi^*$ state. Solvation was treated with equilibrium, linear-response C-PCM for water as implemented in Gaussian 09. The efficacy of the method was tested yet again with single-point calculations performed at select S_1-optimized geometries along the coordinate using ADC(2)-s/cc-pVDZ and non-equilibrium C-PCM. The ADC(2)-s calculations qualitatively confirm the accuracy of the TD-DFT computed relaxed scan. In addition, tools for natural transition orbital, attachment/detachment and difference densities, as well as for Mulliken populations, were employed at the ADC(2) level. It was confirmed that ESHT rather than ESPT occurs. That is, benzaldehyde is not in fact a photobase, but rather abstracts a hydrogen atom from the neighboring water molecule. This ESHT leads to the formation of a pair of BAH and OH radicals. Once transfer is complete, the ground state lies energetically very close to the S_1 state, and through electron transfer from the BAH radical to the OH radical, BAH^+ and $OH-$ are formed. This is followed by back transfer of a proton and subsequent non-radiative relaxation to the ground state, restoring the initial neutral scenario. To extend the study for more widespread applicability in organic synthesis, a series of variations on the benzaldehyde system were then considered. In addition, the effects of an alcoholic solvent as opposed to water were investigated. The presence of an alcoholic solvent decreased the barrier to ESHT, as estimated from the corresponding potential energy surfaces. In addition, the presence of deactivating substituents on the benzene ring increased the amount of initial excess energy available to the system, perhaps facilitating the ESHT process. The effects here were extremely moderate, however, and are unlikely to have any visible effect on experimental observations. Finally, the benzylidenemethylamine system was also studied, since experimental studies of the amine indicators had shown that addition products forming an aminal, hemiaminal, or imine were not quenched. Therefore, the small benzylidenemethylamine was the initial test case for the applicability of the mechanisms determined for one-ring systems to observed quenching in the larger indicators. Indeed, due to the rotation of the C-C-N-C dihedral angle, which appears to lead to a conical intersection between the S_1 and S_0 states, doest not fluoresce. This implies that the mechanisms for the smaller systems, while important in their own right, are not applicable for the larger amine indicators.

Finally, the effect of the size of the aromatic system was studied, growing the system from 1 to 4 rings. While aromatic aldehydes exhibiting a lowest $n\pi^*$ state will undergo ESHT as benzaldehyde does, for systems of increasing size, the bright $\pi\pi^*$ state moves increasingly in terms of its vertical excitation energy. The quenching mechanism observed for benzaldehyde in water was shown to be invalid for the larger molecules. For a system with two rings, similar to stilbene, dihedral rotation is a possible quenching route. For the larger systems, however, no appreciable decrease in bond order of the central C-C double bond is expected upon photoexcitation, and thus such rotation is not feasible. For the system with three rings, the lowest $\pi\pi^*$ singlet state is practically degenerate with the $n\pi^*$ triplet state, making quenching routes based on ISC potentially possible. For the largest system with four rings, this degeneracy is broken, and the system is hypothesized to indeed fluoresce in water.

Overall, the course of this project has lead to a detailed understanding of the fluorescence quenching mechanisms of a broad series of aromatic aldehydes in polar, protic solvents. In addition, the question of ESHT versus photobasicity for the quintessential benzaldehyde has finally been settled, having widespread implications for organic synthesis.

Chapter 5

Excited state properties of pyranine-derived super-photoacids

5.1 Motivation and Background

Organic aromatic molecules exhibiting enhanced acidity in the first electronically excited state compared to the ground state are termed *photoacids*[46]. Photoacidity is commonly observed in dye molecules[332–336], proteins[337, 338], and aromatic alcohols[339–361]. Indeed, excited-state proton transfer (ESPT) from an excited photoacid to a neighboring solvent molecule[2, 353, 360, 362–372] has been extensively studied. 8-hydroxypyrene-1,3,6-trisulfonate, or **HPTS**, is a popular compound in ESPT studies due to its low toxicity[47] and high solubility in aqueous solution[373]. The absorption and emission spectra of **HPTS** lie in the visible region and it is very soluble in water.[364, 374–380]. Importantly, the pKa of **HPTS** drops from 7.3 in the ground state[381] to a mere 1.4 in the excited state[382]. In studies of photoacidity, water is often used as the proton-accepting solvent due to its high polarity and ability to, within the hydrogen-bonded environment, both stabilize and accept protons[45]. However, for a class of photoacids called *super-photoacids*, proton transfer to DMSO and other polar, aprotic solvents is also possible.[353, 383]. Super-photoacids are characterized by an excited state pKa* < 0.

While **HPTS** serves as an excellent model to study photoacidity, it has one major practical flaw: *in vivo* studies are not feasible, since the negatively charged sulfonic acid substituents hinder cell permeability[384]. In addition to the pressing need to develop photoacids which are usable *in vivo*, there has also been a push in recent years towards developing stronger photoacids and super-photoacids[47]. Recently, two main classes of

93

photoacids based on the **HPTS** model were synthesized and their properties examined. These groups are the **HPTA Group**, including **HPTA**, **1A**, **1B**, **1C**, **1D**, and **1E**, and the **MPTA Group**, including **MPTA**, **2A**, **2B**, **2C**, **2D**, and **2E**. The structures of all investigated photoacids are presented in Figure 5.1. The experimental data inspiring this computational study is thoroughly reported in the literature[45–47], but the key points focused on in this dissertation will be described in the following.
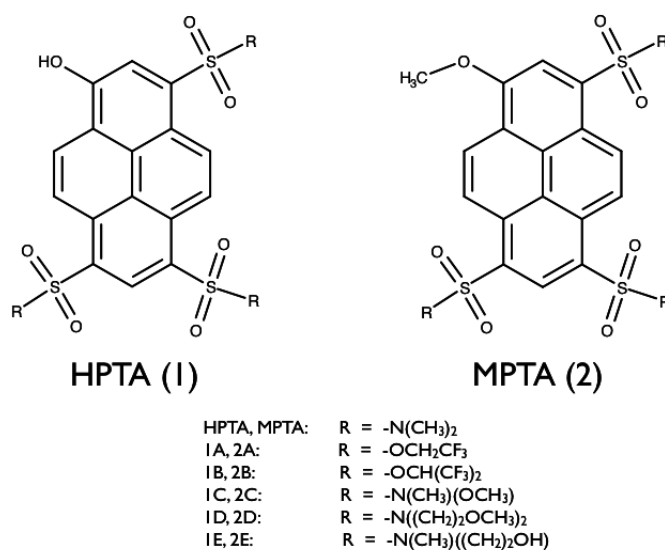
FIGURE 5.1: Structures of the investigated pyranine-based photoacids.

First, there appears to be a strong correlation between photoacidity of a given photoacid and the amount of charge transfer (CT) in the excited state[45]. The photoacid **1B**, having the most strongly deactivating substituents, is the strongest photoacid[45]. The question of where CT is occuring is yet to be answered, however. Semiempirical CIS calculations in conjunction with implicit treatment of solvation indicated significant CT characterizes the S_3, S_4, and S_5 states[45]. Here, CT took place from the sulfonamide substituents to the pyrene core for **MPTA**. Oddly, experimental results had hinted that CT occuring the opposite direction, i.e. from the ring to the substituents, was a cause for stronger photoacidity. Also notable was the fact that the stronger photoacids contained the more deactivating substituents[45]. Thus, the charge redistribution processes involved in enhancing photoacidity are still subject to more advanced investigation. In addition, the observable second excited state, found to arise from the S_3-S_5 in the calculations) may be important for photoacidity, and the energy difference between the S_1 and spectroscopically observed S_2 state increases as photoacidity increases.

An increased static dipole moment of the photoacids in the excited state was found to be the most important indicator of excited state photoacid strength[45]. Excitation and emission spectra exhibit bathochromic shifts in solvents of higher polarity, and indeed the stronger the shift in emission, the higher the excited state polarity[45]. On the

whole, altering substituents leads to a range of photoacids with varying properties. All photoacids are, however, photostable enough for ultrasensitive fluorescence spectroscopy and have high quantum yields[47]. The goal of this work is therefore to study the excited state properties of the synthesized photoacids in order to gain a sense of how charge transfer character, static dipole moment, substituents, and solvent environments can influence their properties and degrees of photoacidity. More detail regarding previous experimental results as they pertain to this investigation is given for easy reference in Section 5.3.

This chapter is organized as follows. First, a benchmarking study of a series of functionals for time-dependent density functional theory (TD-DFT) is undertaken for the model case of **HPTA** in the gas phase. Next, the **HPTA Group** and **MPTA Group** are investigated and compared in terms of the ordering and characters of their excited states in the gas phase and using the C-PCM model to treat solvation in aqueous solution. The absorption and emission spectra for **HPTA** were computed for a series of solvents of varying dielectric constants and the results are compared with experiment. Throughout, several excited state descriptors following from the exciton picture of the excited state are used for intelligent analysis of exchange-correlation (xc) functionals and characterization of the excited states beyond the primitive molecular orbital (MO) picture. These descriptors are presented in the next Section, 5.2. To elucidate the excited state photophysics with respect to the ESPT process for the photoacids, rigid scans along the acid dissociation coordinate were performed for **HPTA** in the gas phase and employing the linear-response, non-equilibrium C-PCM model for water. The results are compared with additional single point calculations performed for **1A** at select OH distances along the dissociation coordinate. This will be the subject of Section 5.6.

5.2   Computational Methods and Benchmarking

Time-dependent density functional theory (TD-DFT) is the method of choice in our investigation of the excited states of large **HPTA-** and **MPTA-based** photoacids. Indeed, it is an exremely popular and at times even crucial method for the study of medium-sized to large molecules. Still, TD-DFT is not without its shortcomings. Particulary the study of charge-transfer (CT) states, Rydberg states, and electronic excitations of extended π-conjugated systems can be problematic. In this light, a series of excited-state descriptors based on the exciton wave function were recently developed[385, 386]. This initial development was then extended for the case of TD-DFT[387]. The exciton wave function is built from the one-particle transition density matrix. Diagonistic information, not only about the natures of the excited states but also regarding popular

xc-functionals, is gained from these excited-state descriptors based on the electron-hole model.

The spatial distribution of the electron and hole in the exciton picture, along with correlation effects, provide the basis for the benchmarking analysis performed in this study. Benchmarking using TD-DFT has to be intelligent in the case of large photoacids, and more advanced benchmark methods such as the algebraic-diagrammatic construction of second order (ADC(2)-s) become prohibitively expensive. Our focus is on two primary measures of the amount of charge transfer in an excited state. First, the mean of the distance between electron and hole is given by[385, 387]

$$d_{h \to e} = |\langle \overrightarrow{x}_e - \overrightarrow{x}_h \rangle| = |\langle \overrightarrow{x}_e \rangle - \langle \overrightarrow{x}_h \rangle|. \tag{5.1}$$

which is the distance between the charge centers. Second, the root-mean-square (rms) of this distance, written as[385, 387]

$$d_{exc} = \sqrt{\langle |\overrightarrow{x}_e - \overrightarrow{x}_h|^2 \rangle} \tag{5.2}$$

is also used in our comparisons, as it includes contributions due to dynamic charge separation and is called the exciton size. The covariance links these two charge transfer measures in that[385, 387]

$$d_{exc}^2 = d_{h \to e}^2 + \sigma_h^2 + \sigma_e^2 - 2 \times COV \tag{5.3}$$

with the rms sizes of the electron and hole distributions being σ_e and σ_h, respectively. The covariance is given by[385, 387]

$$COV = \langle \overrightarrow{x}_h \cdot \overrightarrow{x}_e \rangle - \langle \overrightarrow{x}_h \rangle \cdot \langle \overrightarrow{x}_e \rangle. \tag{5.4}$$

Finally, the Pearson correlation coefficient[385, 387]

$$R_{eh} = \frac{\langle \overrightarrow{x}_h \cdot \overrightarrow{x}_e \rangle - \langle \overrightarrow{x}_h \rangle \cdot \langle \overrightarrow{x}_e \rangle}{\sigma_h \sigma_e} \tag{5.5}$$

is used in our comparisons. This coefficient quantifies electron-hole correlation effects and ranges from -1 to 1. For no correlation, R_{eh} is zero, while a negative R_{eh} indicates dynamic "repulsion" of the electron and hole. A positive R_{eh} signifies, in contrast, that a "bound exciton" is present[387]. In the more commonly used MO picture, it is assumed that the electron-hole correlation is zero. This is, however, an oversimplification that is not always warrented. Taken together, these descriptors free one from the dependence on using molecular orbitals for assignment of excited states. Particularly in cases where there are multiple contributions to the character of the excited state, as is incidentally

the case with such large photoacids, the use of molecular orbitals is cumbersome and not particularly definitive. Since CT has been indicated as being a factor influencing photoacidity, understanding how varying xc-functionals describe the CT states is critical. In the following, the benchmarking results comparing these parameters are first presented for the **HPTA** system in the gas phase. This data is shown in Table 5.1.

	Excitation Energy (eV)	fosc	$d_{h \to e}$	d_{exc}	COV (Å^2)	R_{eh}
B3LYP						
S_1	3.1356	0.4350	0.5359	4.7987	-0.2234	-0.0201
S_2	3.5393	0.0099	0.7572	4.7880	0.4332	0.0378
S_3	3.7184	0.0015	3.8074	6.0432	0.4065	0.0357
S_4	3.7990	0.0543	2.5849	5.8497	0.2242	0.0167
S_5	3.8967	0.0083	3.7503	5.9211	-0.0184	-0.0018
BHLYP						
S_1	3.5223	0.5596	0.4565	4.3620	0.7103	0.0702
S_2	3.9505	0.0165	0.2503	3.9807	1.4834	0.1582
S_3	4.6995	0.0066	0.3299	3.8389	0.8500	0.1060
S_4	4.7659	0.3124	0.7611	4.3231	0.3501	0.0373
S_5	4.9749	0.1367	0.3979	4.0679	1.2356	0.1328
ω-B7X						
S_1	3.6013	0.5669	0.4079	4.1584	1.3385	0.1352
S_2	3.9540	0.0506	0.2145	3.7839	2.0185	0.2205
S_3	4.8149	0.0055	0.2695	3.6053	1.4440	0.1832
S_4	4.9506	0.2286	0.8850	4.0369	1.1826	0.1323
S_5	5.0531	0.3208	0.3864	3.9093	1.8475	0.1968
CAM-B3LYP						
S_1	3.4605	0.5297	0.4993	4.3732	0.7489	0.0735
S_2	3.8469	0.0280	0.2388	3.9751	1.5452	0.1641
S_3	4.6082	0.0034	0.5487	4.0063	1.1214	0.1252
S_4	4.6538	0.2742	0.6304	4.3590	0.5636	0.0576
S_5	4.8083	0.1277	0.6461	4.2475	1.8893	0.1823

TABLE 5.1: Vertical excited states and relevant excited state descriptors computed for **HPTA** in the gas phase and employing the B3LYP, BHLYP, ω-B97X, and CAM-B3LYP xc-functionals for TD-DFT. In all cases, the cc-pVDZ basis set was used.

The excitation energies calculated using the BHLYP, ω-B97X, and CAM-B3LYP functionals are all in generally good agreement with each other. For B3LYP, the excitation energies are significantly lower, particularly for the S_3, S_4, and S_5 states, where the difference is approximately 1 eV compared to the data for the other functionals. Moving to

the oscillator strengths, these also indicate with their agreement the same ordering of the excited states for all functionals. Again, the results for the functionals excluding B3LYP are in best agreement. For all states, the S_1 is the bright state, while the S_4 and S_5 also exhibit non-negligible oscillator strength. The mean of the electron-hole distance, $d_{h \to e}$, shows more significant variation among the functionals. Here, $\omega - B97X$ and BHLYP are in closest agreement with each other, while differences to CAM-B3LYP are still not appreciable. For B3LYP, however, the S_3, S_4, and S_5 states are characterized by very large electron-hole distances of 3.8074 Å, 2.5849 Å, and 3.7503 Å, respectively. This is compared to the around 0.5-0.8 Å for the other functionals. Of course, this is to be expected. Large electron-hole distances indicate high CT character for the excited states, and it is known that the energies of CT states are often falsely lowered for B3LYP. Indeed, TD-DFT/B3LYP is generally assumed to not be reasonable for the study of charge transfer or proton transfer because of its well-documented charge-transfer failure.[131–134] This trend is echoed for the case of d_{exc}, which also indicates much larger rms electron-hole distances for the S_3, S_4, and S_5 states computed using B3LYP versus the other functionals, which exhibit remarkable agreement. The covariance also shows agreement among the BHLYP, ω-B97X, and CAM-B3LYP functionals, though there is more variation than with the other parameters. Covariances computed with B3LYP, however, notably disagree, again pointing to B3LYP as an outlier method that is not appropriate for futher use. Finally, R_{eh} values tend to hover around 0-0.2 for all states in all cases, though slightly negative values are observed in the S_1 and S_5 states calculated with B3LYP. For the other functionals, the values are in very reasonable agreement and support again the efficacy of these methods in the description fo the excited states of the photoacids. Considering the need to treat charge transfer states, a long range functional like CAM-B3LYP is the most logical choice and the TD-DFT/CAM-B3LYP/cc-pVDZ level of theory will be employed for the rest of the study. Ground and excited state optimizations were carried out using Gaussian 09, Revision D.01 in the gas phase and employing the C-PCM model, as specified throughout the discussion[213]. Vertical excitations utilizing the tools for the excited state descriptors were carried out using Q-Chem 4.3[276].

5.3 Previous experimental findings

Before delving into the computed properties of the photoacids, a summary of the pertinent experimental data on this selection of photoacids is given in the following. The photoacids in this study represent a novel class of pyranine-derived photoacids with potential applicability *in vivo*. While most common photoacids are unable to dissociate in non-aqueous solution within their excited state lifetimes, the photoacids studied here

generally have the ability to dissociate in solvents like DMSO and alcohols. Indeed, **1B** and **1E** undergo ESPT in H_2O, MeOH, and EtOH. **1B**, the strongest photoacid of the **HPTA Group**, has ESPT rate constants of 3×10^{11} s^{-1} in H_2O, 8×10^9 s^{-1} in MeOH, and 5×10^9 s^{-1} in EtOH. For the case of **1E**, those rate constants show more variability, at 7×10^{10} s^{-1}, 4×10^8 s^{-1}, and 2×10^8 s^{-1}, respectively. Table 5.2 shows the ground state pK_as and excited state pK_a^*s for the **HPTA Group** of photoacids[46].

	HPTS	HPTA	1A	1B	1C	1D	1E
pK_a	7.3	5.6	4.7	4.4	5.6	5.7	5.6
pK_a^*	1.4	-1.0	-2.7	-3.9	-1.2	-0.8	-0.9

TABLE 5.2: Ground state pK_as and excited state pK_a^*s for the **HPTA Group**, as reported in the literature[47].

We shift our focus now to the trends in absorption and emission spectra. First, it should be noted that the **HPTA Group** and **MPTA Group** exhibit trends that are very much alike, as one would expect because the electronic effect of a proton and a -CH_3 group are very similar. Even with respect to different solvents, the groups exhibit similar solvatochromic behavior with respect to solvent polarity. Here, the main difference only lies in the presence of ESPT in protic and aprotic, highly basic solvents. Both excitation and emission spectra demonstrate a bathochromic shift in solvents of higher polarity, though the shift is more extreme in emission than in excitation. This indicates that the photoacid has a higher polarity in the excited state than in the ground state. A change in the permanent dipole moment was indeed shown to be an important indicator of excited state acidity[45]. A large change in the permanent dipole moment was computed for all compounds. This change is seen as evidence for charge transfer taking place before proton transfer, causing stronger photoacidity. Still, the direction of charge transfer could not be determined in previous experimental or computational work.

ROH	HPTA	1A	1B	1C	1D	1E
$\lambda_{abs,max}$	2.94 eV	2.91 eV	2.99 eV	2.89 eV	2.90 eV	2.93 eV
	(422 nm)	(426 nm)	(414 nm)	(429 nm)	(427 nm)	(423 nm)
$\lambda_{em,max}$	2.62 eV	2.58 eV	2.53 eV	2.58 eV	2.59 eV	2.60 eV
	(473 nm)	(480 nm)	(490 nm)	(481 nm)	(478 nm)	(476 nm)
RO$^-$	HPTA	1A	1B	1C	1D	1E
$\lambda_{abs,max}$	2.51 eV	2.40 eV	2.36 eV	2.44 eV	2.48 eV	2.50 eV
	(494 nm)	(516 nm)	(526 nm)	(509 nm)	(499 nm)	(495 nm)
$\lambda_{em,max}$	2.27 eV	2.22 eV	2.20 eV	2.23 eV	2.25 eV	2.26 eV
	(547 nm)	(558 nm)	(564 nm)	(555 nm)	(551 nm)	(548 nm)

TABLE 5.3: Excitation and emission spectra for the neutral excited photacid (ROH) and its deprotonated counterpart (RO$^-$) for the **HPTA Group**, as reported in the literature[47].

Excitation of the photoacid generates a vibrationally relaxed excited state acid which then initiates the ESPT process. An important indicator of ESPT efficiency is the ratio of emission intensity of the neutral species to that of the corresponding excited state base. Thus, increasing photoacidity leads to decreasing neutral photoacid fluorescence intensity. For **1A** and **1B**, nearly quantitative ESPT in DMSO is observed, while for **HPTA**, **1C**, **1D**, and **1E**, emission of the excited state acid is detectable. Table 5.3 shows the absorption and emission maxima for the neutral excited photoacids (ROH) and corresponding deprotonated species (RO$^-$) in water for the **HPTA Group**. This will be referenced in the following sections with respect to the computational results presented here.

Finally, the energy difference between the first and second excited states, as observed for the **HPTA Group** in DMSO, are given in Table 5.4. The spectroscopically observable S$_2$ was found in quantum chemical calculations to be the S$_3$, S$_4$, and S$_5$ states. This difference was found to increase with increased photoacidity, and will also be examined in the calculations to follow.

Photoacid	ΔE(S$_2$-S$_1$)
HPTS	0.277 eV (2236 cm^{-1})
HPTA	0.345 eV (2786 cm^{-1})
1A	0.436 eV (3520 cm^{-1})
1B	0.478 eV (3857 cm^{-1})
1C	0.406 eV (3277 cm^{-1})
1D	0.337 eV (2722 cm^{-1})
1E	0.337 eV (2718 cm^{-1})

TABLE 5.4: Energy differences between the first and the second spectroscopically observable excited states, determined in DMSO[45].

The trends to keep in mind going forward with the computations presented in the following are summarized as follows. First, electron-withdrawing substituents on the pyrene core lead to increased photoacidity. Second, the increase in the static dipole moment in the excited state is a critical characteristic of excited state acidity. Related to these focal points is the strong correlation of photoacidity and the amount of charge transfer in the excited state. Finally, both the absorption and emission spectra exhibit a bathochromic shift in solvents of higher polarity, and a more extensive shift in emission than in excitation indicates that the molecule has a higher polarity in the excited state than in the ground state. We look now to the static properties of the **HPTA Group** and **MPTA Group** photoacids, employing the quantum chemical analysis tools described in Section 5.4 to increase our understanding of their excited state properties.

5.4 Static properties of pyranine-based photoacids

The vertical excited states for the series of **HPTA-** and **MPTA-based** photoacids were then computed in the gas phase and using the C-PCM model to treat solvation in water. Here, the geometries used were optimized in the gas phase at the DFT/CAM-B3LYP/cc-pVDZ level of theory in Gaussian 09, Revision D.01. The structures **1B** and **2B** exhibited computed displacements very close to the cutoff criteria but not fully converged, when over the course of a frequency calculation the analytically computed Hessian is employed. These structures are still likely extremely close to the real stationary points, in particular because convergence was reached when the estimated Hessian in the geometry optimization procedure was employed. Since semiempirical CIS calculations had indicated that significant CT in the S_3, S_4, and S_5 states occurred[45], the excited state descriptors employed in the benchmarking analysis were computed here as well. Particularly the electron-hole distance measures, $d_{h\to e}$ and d_{exc}, are useful for the diagnosis of states of high CT character. Because it had been reported[45] that the S_3, S_4, and S_5 states move down below the dark S_2 state as a result of treating implicit solvation in acetonitrile, the excited states and their descriptors are also computed here for **HPTA** and **MPTA** in acetonitrile. Jung et al. noted here as well that the accuracy of their employed methods is rather low and hinted that perhaps these states are more energetically close together than they report. These CT states may then very well play a large role in the photophysical properties of the photoacid series.
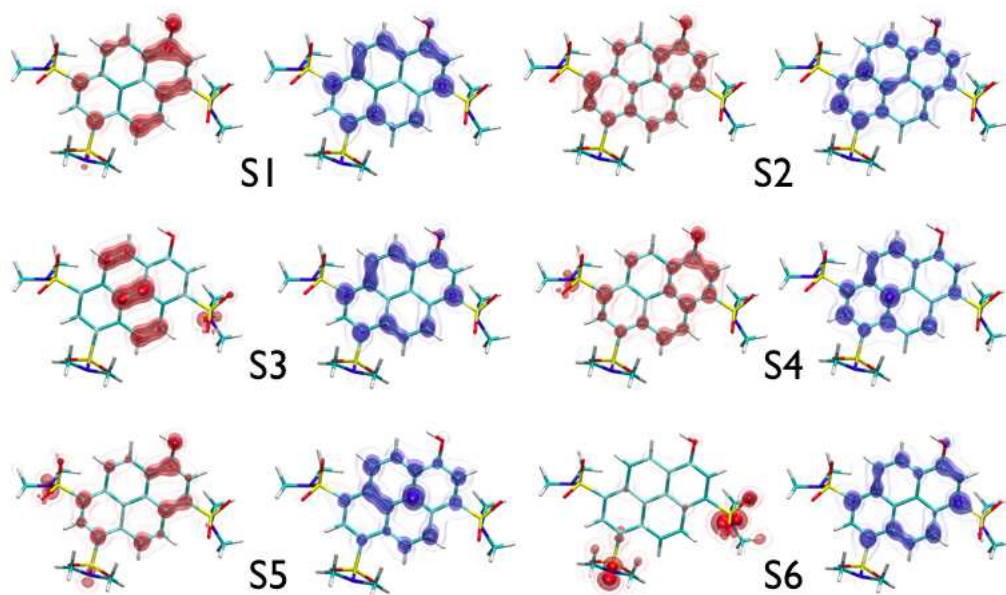
FIGURE 5.2: Attachment and detachment densities for the S_1-S_6 states of **HPTA** in the gas phase.
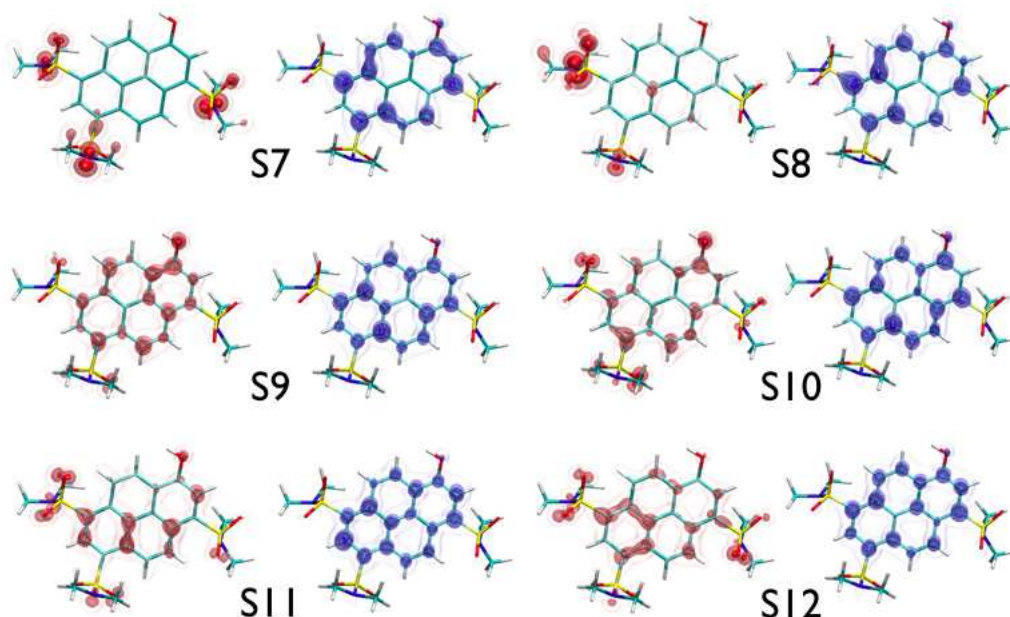
FIGURE 5.3: Attachment and detachment densities for the S_7-S_{12} states of **HPTA** in the gas phase.
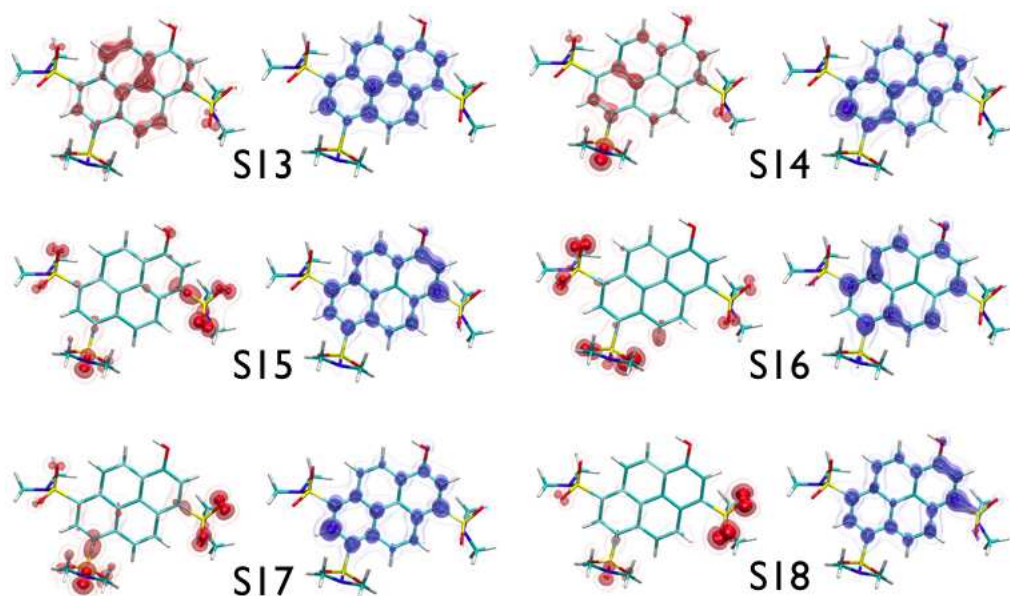
FIGURE 5.4: Attachment and detachment densities for the S_{13}-S_{18} states of **HPTA** in the gas phase.

The complete ste of data for the vertical excited state analysis of all computed photoacids are provided in Tables 5.5 (**HPTA**), 5.7 (**1A**), 5.8 (**1B**), 5.9 (**1C**), 5.10 (**MPTA**), 5.12 (**2A**), 5.13 (**2B**), and 5.14 (**2C**). Here, the gas phase and C-PCM data are shown side by side for easier comparison. The attachment and detachment densities of the first 20 singlet electronically excited states are given for **HPTA** (Figures 5.2, 5.3, 5.4, and 5.5) and **1B** (Figures 5.6, 5.7, 5.8, and 5.9) in the gas phase. **1B** was chosen for comparison with HPTA because of it was the strongest photoacid in the series according
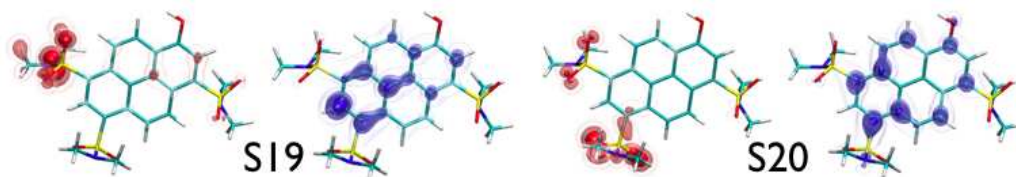
FIGURE 5.5: Attachment and detachment densities for the S_{19}-S_{20} states of **HPTA** in the gas phase.
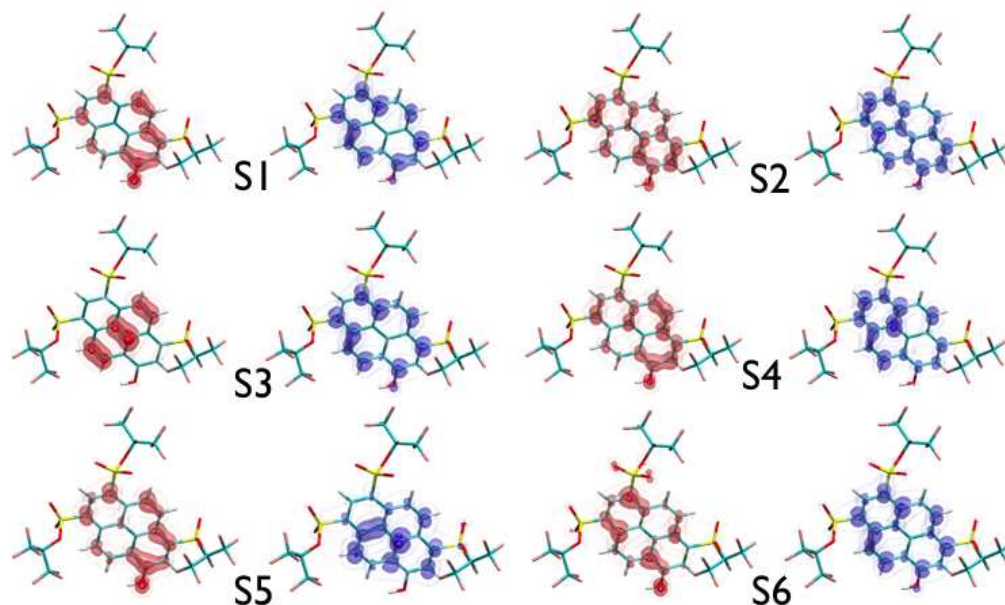
FIGURE 5.6: Attachment and detachment densities for the S_1-S_6 states of **1B** in the gas phase.

to experiment[45–47]. These two exemplary cases illustrate the deepest contrasts between the excited state characters of the different photoacids. The excited states of **HPTA** are discussed first. The S_1 state is the bright state, and the A/D plots in Figure 5.2 show some charge transfer is occuring away from the oxygen on the OH group. The S_2 and S_3 states have low oscillator strengths and exhibit short CT distances mainly centered on the pyrene core. Next, the S_4 and S_5 states, like S_1, demonstrate some CT away from the oxygen of OH. They also have significant oscillator strenghts of about 0.27 and 0.13, respectively. Starting with S_6, many of the higher-lying excited states involve CT from the substituents to the pyrene core. This presence of strong CT is reflected in the values for $d_{h \to e}$ and d_{exc} shown in Table 5.5, which are approximately 2.07 Å and 5.31 Å respectively, for the S_6 state. This is of course a marked contrast to the S_2 state, for example, which exhibited $d_{h \to e}$ value of only 0.24 Å. As reported in Table 5.2, the pK_a^* of **HPTA** is -1.0, while **1B** is the strongest photoacid with a p$K_a^* = -3.9$. It
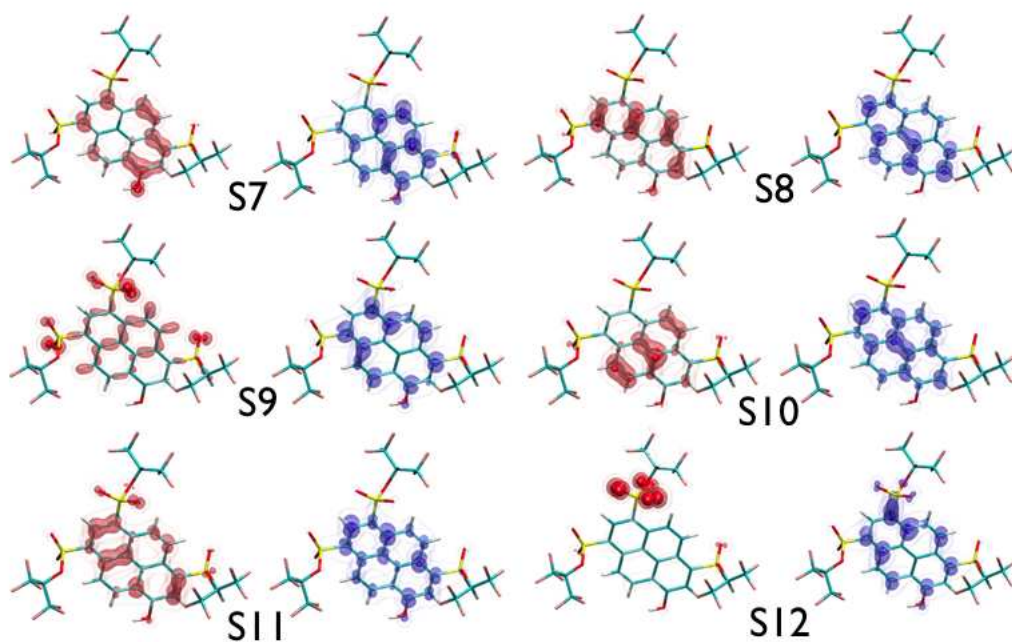
FIGURE 5.7: Attachment and detachment densities for the S_7-S_{12} states of **1B** in the gas phase.
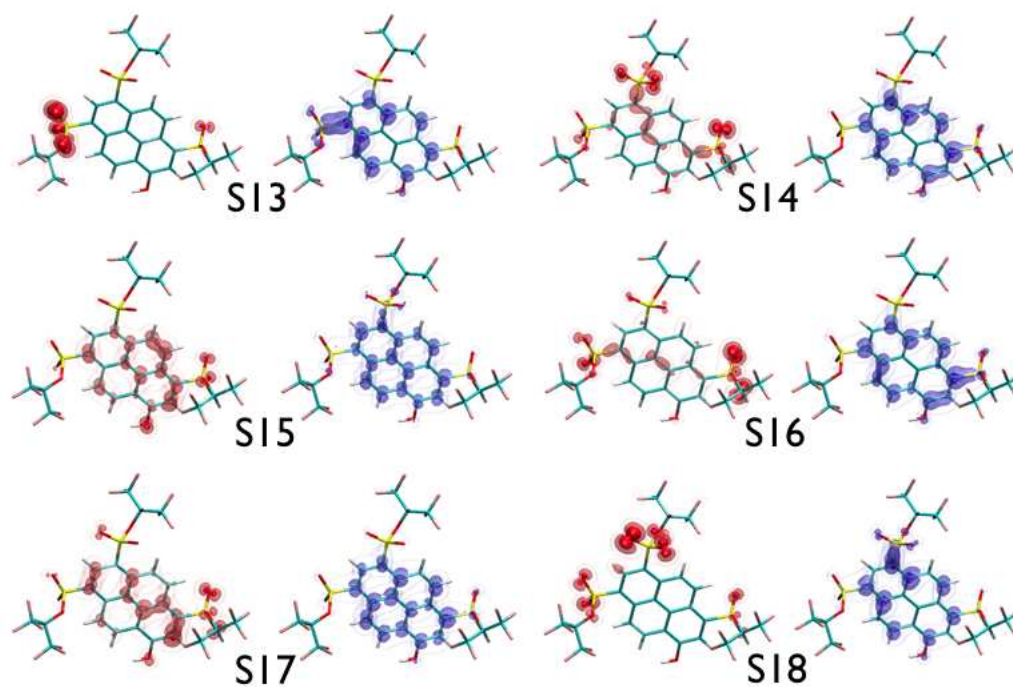
FIGURE 5.8: Attachment and detachment densities for the S_{13}-S_{18} states of **1B** in the gas phase.
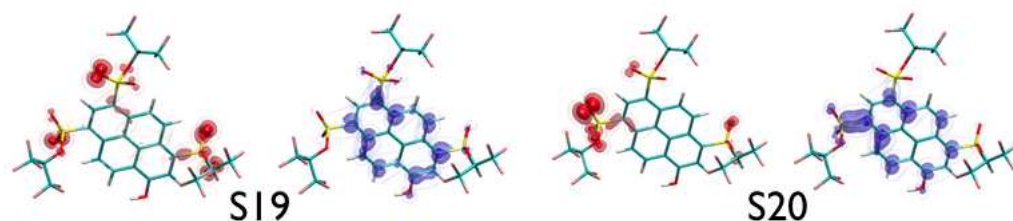
FIGURE 5.9: Attachment and detachment densities for the S_{19}-S_{20} states of **1B** in the gas phase.

	Gas Phase				C-PCM			
	EE	**fosc**	$\mathbf{d}_{h \to e}$	$\mathbf{d}_{exc}$	**EE**	**fosc**	$\mathbf{d}_{h \to e}$	$\mathbf{d}_{exc}$
S_1	3.45	0.534	0.50	4.37	3.35	0.711	0.51	4.37
S_2	3.85	0.027	0.24	3.97	3.84	0.028	0.29	3.97
S_3	4.60	0.003	0.54	4.00	4.55	0.061	0.61	3.98
S_4	4.65	0.277	0.65	4.36	4.60	0.384	0.35	4.32
S_5	4.80	0.131	0.63	4.24	4.79	0.144	0.41	4.06
S_6	4.93	0.018	2.07	5.31	4.92	0.013	2.35	5.26
S_7	5.03	0.011	1.51	5.43	5.05	0.013	1.75	5.48
S_8	5.09	0.045	2.52	5.27	5.09	0.047	2.18	5.38
S_9	5.33	0.053	0.06	4.44	5.30	0.085	0.35	4.23
S_{10}	5.40	0.010	0.50	4.28	5.39	0.320	0.09	4.19
S_{11}	5.49	0.401	0.59	4.39	5.53	0.471	0.84	4.35
S_{12}	5.64	0.207	0.53	4.37	5.68	0.021	0.45	4.30
S_{13}	5.76	0.080	0.12	4.27	5.76	0.101	0.13	4.40
S_{14}	5.81	0.105	0.89	4.21	5.80	0.112	0.77	4.05
S_{15}	5.92	0.027	1.25	4.79	6.04	0.017	1.58	4.75
S_{16}	5.97	0.014	1.91	5.06	6.05	0.073	1.80	4.79
S_{17}	6.02	0.013	1.59	4.75	6.11	0.023	1.23	4.69
S_{18}	6.04	0.001	2.20	5.01	6.21	0.004	1.37	4.81
S_{19}	6.08	0.077	2.80	4.92	6.29	0.004	1.30	4.72
S_{20}	6.16	0.017	3.34	5.31	6.37	0.014	3.36	5.18

TABLE 5.5: Excited state parameters for the lowest 20 singlet electronically excited states of **HPTA** in the gas phase and employing the C-PCM model to treat solvation in water. The excitation energies (EE) are given in eV, while the sizes $d_{h \to e}$ and d_{exc} are in Å.

is therefore of interest to discuss the differences in the static properties between these two systems of different photoacidities. The complete set of values for the excited state descriptors computed for this system are given in the gas phase and employing C-PCM for solvation in water in Table 5.8.

As noted previously, the A/D plots for the lowest 20 vertically excited singlet states of **1B** are presented in Figures 5.6, 5.7, 5.8, and 5.9. As is the case for **HPTA**, the S_1

	EE	fosc	$d_{h\rightarrow e}$	d_{exc}
S_1	3.35	0.715	0.51	4.37
S_2	3.84	0.028	0.29	3.97
S_3	4.55	0.064	0.62	3.99
S_4	4.60	0.387	0.34	4.32
S_5	4.79	0.142	0.41	4.06
S_6	4.92	0.014	2.34	5.26
S_7	5.05	0.013	1.72	5.48
S_8	5.09	0.047	2.19	5.38
S_9	5.30	0.087	0.35	4.22
S_{10}	5.39	0.322	0.09	4.19
S_{11}	5.53	0.471	0.85	4.36
S_{12}	5.68	0.023	0.48	4.31
S_{13}	5.76	0.101	0.12	4.39
S_{14}	5.80	0.111	0.77	4.05
S_{15}	6.04	0.011	1.34	4.72
S_{16}	6.05	0.078	1.87	4.83
S_{17}	6.11	0.024	1.21	4.69
S_{18}	6.21	0.004	1.38	4.82
S_{19}	6.29	0.004	1.32	4.72
S_{20}	6.36	0.013	3.36	5.18

TABLE 5.6: Excited state parameters for the lowest 20 singlet electronically excited states of **HPTA** using C-PCM for acetonitrile. The excitation energies (EE) are given in eV, while the sizes $d_{h\rightarrow e}$ and d_{exc} are in Å.

of **1B** is the main bright state with an oscillator strength of 0.509, lying about 0.1 eV below the S_1 state of **HPTA**. The S_1 state of **1B** also shows CT away from the oxygen of the OH group, in indeed the same fashion as for **HPTA**'s lowest singlet electronically excited state. The next four states are also of the same character and energetic order as is the case for **HPTA**. It is first with the S_6 state that a significant difference between **1B** and **HPTA** is observed. The S_6 of **1B** has an excitation energy of 5.28 eV and a low oscillator strength of 0.01. Looking at the A/D densities, no significant charge transfer from the substituents to the ring is observed for this state, as it was so clearly for **HPTA**. Indeed, the value of $d_{h\rightarrow e}$ is only about 0.43 Å, while it was 2.07 Å in the case of **HPTA**. The lowest state exhibiting similarly strong CT from the substituents to the pyrene core for **1B** is the S_{12} state, with a vertical excitation energy of 5.96 eV. This is more than 1 eV higher than the lowest CT state for **HPTA**. Like **HPTA**, the higher lying excited states of **1B**, shown in Figures 5.7, 5.8, and 5.9, are a similar group of states with strong CT character from the substituents to the pyrene core. In the literature[45], substantial CT was found in this same direction in the S_3-S_5 states from the semiempirical CIS calculations. As previously touched upon in the introduction to this chapter, this result is somewhat startling, as experimental data had indicated that CT from the ring to the substituents was a cause for stronger photoacidity. These states lie > 1 eV above the bright S_1 state. Thus, the extent to which they move down over

	Gas Phase				C-PCM			
	EE	**fosc**	$\mathbf{d}_{h \to e}$	$\mathbf{d}_{exc}$	**EE**	**fosc**	$\mathbf{d}_{h \to e}$	$\mathbf{d}_{exc}$
S_1	3.39	0.487	0.64	4.35	3.27	0.654	0.65	4.35
S_2	3.87	0.019	0.30	3.90	3.86	0.020	0.33	3.90
S_3	4.46	0.020	0.31	3.81	4.40	0.022	0.36	3.83
S_4	4.72	0.369	0.83	4.22	4.65	0.529	0.78	4.22
S_5	4.89	0.082	0.08	3.87	4.85	0.088	0.10	3.83
S_6	5.28	0.010	0.13	4.41	5.26	0.001	0.17	4.34
S_7	5.37	0.032	0.39	3.86	5.30	0.052	0.57	3.96
S_8	5.64	0.539	0.46	3.97	5.59	0.853	0.17	3.96
S_9	5.73	0.018	1.05	4.72	5.75	0.047	0.45	3.86
S_{10}	5.78	0.074	0.28	4.19	5.84	0.135	0.18	4.12
S_{11}	5.85	0.034	1.78	5.18	5.91	0.101	0.27	4.05
S_{12}	5.87	0.117	2.33	5.03	6.08	0.002	3.00	5.23
S_{13}	5.92	0.078	1.71	4.77	6.13	0.002	3.27	5.33
S_{14}	5.94	0.068	1.03	4.60	6.15	0.001	3.74	5.39
S_{15}	6.12	0.002	1.43	4.62	6.26	0.007	1.07	4.42
S_{16}	6.35	0.003	0.44	3.75	6.31	0.002	0.41	3.88
S_{17}	6.39	0.013	0.52	4.80	6.46	0.022	0.51	4.58
S_{18}	6.43	0.000	0.99	5.14	6.55	0.136	0.30	4.44
S_{19}	6.46	0.007	2.26	5.10	6.60	0.019	0.49	4.00
S_{20}	6.51	0.000	0.62	4.92	6.63	0.330	0.22	4.02

TABLE 5.7: Excited state parameters for the lowest 20 singlet electronically excited states of **1A** in the gas phase and employing the C-PCM model for water. The excitation energies (EE) are given in eV, while the sizes $d_{h \to e}$ and d_{exc} are in Å.

the course of acid dissociation may more clearly indicate what role, if any, they have in the differing photoacidities of the series.

It was determined in the literature that the energetic difference between the spectroscopically observable S_2 (i.e. S_3-S_5 from the semiempirical CIS calculations) state and the S_1 state correlated positively with photoacid strength[45]. These differences were on the scale of around 0.27-0.48 eV. This matches roughly the energy difference between the S_2 and S_1 state in the TD-DFT/CAM-B3LYP/cc-pVDZ computations presented here. In our calculations, the difference between S_2 and S_1 increases only by about 0.1 eV going from, for example, **HPTA** to the stronger **1B**. In addition, it increases by around 0.1-0.15 eV again when the C-PCM model is employed to implicitly treat solvation. The S_1 state, looking to the attachment and detachment densities, does involve a minor CT from the O of the OH group to the neighboring ring on the pyrene core. The S_2 state, however, involves negligible CT. Therefore, it is unlikely that the energy difference between these two is a good benchmark of photoacidity. Looking instead to the higher-lying states and in particular their $d_{h \to e}$ values, a noticeable shift upwards of states of CT character is observed for the stronger photoacids. This was of course touched upon already in this discussion, pointing to the shift of the lowest CT state

	Gas Phase				C-PCM			
	EE	fosc	$d_{h\to e}$	d_{exc}	EE	fosc	$d_{h\to e}$	d_{exc}
S_1	3.36	0.509	0.67	4.36	3.23	0.671	0.68	4.36
S_2	3.86	0.018	0.32	3.91	3.84	0.019	0.37	3.91
S_3	4.44	0.023	0.36	3.83	4.36	0.023	0.40	3.84
S_4	4.70	0.343	0.88	4.21	4.62	0.503	0.86	4.22
S_5	4.88	0.097	0.10	3.90	4.84	0.097	0.05	3.86
S_6	5.28	0.010	0.11	4.43	5.25	0.001	0.16	4.39
S_7	5.36	0.031	0.43	3.84	5.28	0.055	0.61	3.92
S_8	5.64	0.555	0.38	3.94	5.59	0.870	0.12	3.98
S_9	5.74	0.027	0.90	4.59	5.73	0.040	0.49	3.86
S_{10}	5.78	0.110	0.49	4.01	5.83	0.182	0.06	3.94
S_{11}	5.88	0.239	0.25	3.94	5.88	0.060	0.21	4.20
S_{12}	5.96	0.011	3.03	5.19	6.20	0.005	0.94	4.17
S_{13}	5.99	0.006	3.05	5.25	6.26	0.007	1.16	4.60
S_{14}	6.11	0.002	1.33	4.73	6.29	0.016	2.53	5.00
S_{15}	6.30	0.004	0.99	3.99	6.35	0.001	2.71	5.08
S_{16}	6.34	0.003	1.10	4.86	6.38	0.006	0.22	4.74
S_{17}	6.39	0.001	0.77	4.65	6.53	0.217	0.14	4.56
S_{18}	6.45	0.004	2.75	5.28	6.56	0.051	0.55	4.33
S_{19}	6.49	0.024	1.01	4.99	6.60	0.157	0.73	4.55
S_{20}	6.56	0.003	2.76	5.20	6.64	0.078	0.54	4.61

TABLE 5.8: Excited state parameters for the lowest 20 singlet electronically excited states of **1B** in the gas phase and employing the C-PCM model for water. The excitation energies (EE) are given in eV, while the sizes $d_{h\to e}$ and d_{exc} are in Å.

exhibiting transfer from the substituents to the pyrene core of **1B** to S_{12} with an excitation energy of 5.96 eV, compared to the placement of this type of state at S_6 with an excitation energy of 4.93 eV for the weaker photoacid **HPTA**. Indeed, the S_6 of **HPTA** has a $d_{h\to e}$ of around 2 Å while these distances for the strong **1B** are all below 1 Å until S_{12}.

The pattern of a larger energetic difference between the S_1 state and the lowest strong CT state with increased photoacidity was observed for the entire class of photoacids investigated here. As has been established for **HPTA**, the S_6 is the lowest CT state and has an excitation energy of 4.93 eV. The difference in excitation energies between this S_6 and the bright S_1 is about 1.47 eV. **1C** has a similar pK_a^* to **HPTA** of -1.2. The excited state properties for **1C** in the gas phase and using C-PCM to treat solvation in water are shown in Table 5.9. In the gas phase, the lowest strongly CT state is also the S_6 and has a difference in excitation energy with the S_1 of a 1.47 eV as well. The stronger photoacids **1A** and **1B** have pK_a^* values of -2.7 and -3.9, respectively. The full results for **1A** are given as computed in the gas phase and using C-PCM for water in Table 5.7, while those for **1B** follow in Table 5.8. For **1A**, the bright S_1 state lies at 3.39 eV in the gas phase and the lowest state of substantial CT character is the S_{12} with an

	Gas Phase				C-PCM			
	EE	**fosc**	$\mathbf{d}_{h \to e}$	$\mathbf{d}_{exc}$	**EE**	**fosc**	$\mathbf{d}_{h \to e}$	$\mathbf{d}_{exc}$
S_1	3.44	0.530	0.56	4.37	3.31	0.699	0.59	4.37
S_2	3.87	0.023	0.27	3.94	3.85	0.023	0.33	3.94
S_3	4.55	0.012	0.35	3.93	4.48	0.034	0.42	3.89
S_4	4.71	0.323	0.93	4.33	4.63	0.483	0.76	4.27
S_5	4.84	0.097	0.23	4.09	4.82	0.114	0.05	3.86
S_6	4.90	0.044	3.05	5.33	5.03	0.022	1.88	5.31
S_7	4.91	0.010	2.99	5.46	5.07	0.008	2.23	5.52
S_8	5.12	0.003	3.70	5.39	5.23	0.004	2.90	5.27
S_9	5.30	0.016	0.26	4.69	5.28	0.047	0.42	4.33
S_{10}	5.37	0.020	0.17	4.02	5.35	0.030	0.94	4.56
S_{11}	5.42	0.007	2.17	5.09	5.53	0.484	1.17	4.62
S_{12}	5.59	0.642	0.74	4.31	5.56	0.416	1.72	4.81
S_{13}	5.68	0.006	1.57	5.16	5.71	0.026	0.12	4.09
S_{14}	5.71	0.005	0.99	4.80	5.78	0.020	0.45	4.58
S_{15}	5.77	0.050	0.56	4.60	5.83	0.110	1.10	4.53
S_{16}	5.86	0.109	1.15	4.41	5.94	0.062	1.49	4.99
S_{17}	5.90	0.085	2.67	5.18	6.05	0.012	2.95	5.36
S_{18}	5.96	0.041	2.42	4.86	6.09	0.018	2.96	5.00
S_{19}	5.97	0.006	1.60	4.69	6.19	0.005	1.55	4.78
S_{20}	6.06	0.003	2.42	5.14	6.28	0.003	0.32	4.23

TABLE 5.9: Excited state parameters for the lowest 20 singlet electronically excited states of **1C** in the gas phase and employing the C-PCM model for water. The excitation energies (EE) are given in eV, while the sizes $d_{h \to e}$ and d_{exc} are in Å.

excitation energy of 5.87 eV. Thus, the difference in excitation energy between the S_{12} and S_1 is about 2.48 eV, or roughly 1 eV greater than the similar difference observed in the weaker photoacids **HPTA** and **1C**. Similarly for the strongest photoacid **1B**, the energy difference beteween the lowest CT state and the bright S_1 is 2.61 eV. For the **MPTA**-based photoacids studied, i.e. **MPTA**, **2A**, **2B**, and **2C**, this same pattern is also observed.

Attention is now paid to the differences in excited state properties between the photoacids treated in the gas phase, as described in the above discussion, and employing the C-PCM model to treat solvation in water and, for **HPTA** and **MPTA**, in acetonitrile as well. In the presence of a solvent, the bright state is marginally energetically stabilized by about 0.1-0.15 eV. The lowest state of strong CT character, however, shifts upward in excitation energy. For **1B**, the difference in excitation energy between the S_{12} exhibiting CT and the S_1 was 2.61 eV in the gas phase, while using C-PCM for water, it jumps to a 3.05 eV difference. A similar but slightly smaller jump for **1A** is exhibited for this energy difference, from 2.48 eV to 2.81 eV. This data is shown as well in Figure 5.10, which shows the correlation between photoacidity and excitation energies of the S_1 state and the lowest CT state for the **HPTA**, **1A**, **1B**, and **1C**. Evidently,

	Gas Phase				C-PCM			
	EE	fosc	$d_{h \to e}$	d_{exc}	EE	fosc	$d_{h \to e}$	d_{exc}
S_1	3.43	0.613	0.49	4.41	3.30	0.775	0.61	4.41
S_2	3.86	0.028	0.19	3.98	3.84	0.026	0.29	3.98
S_3	4.53	0.002	0.25	3.92	4.49	0.018	0.44	3.95
S_4	4.69	0.306	0.47	4.48	4.59	0.432	0.50	4.41
S_5	4.85	0.103	0.72	4.21	4.81	0.142	0.53	4.14
S_6	4.92	0.010	1.18	5.23	4.87	0.004	2.13	5.18
S_7	5.04	0.005	1.14	5.47	5.01	0.005	1.30	5.47
S_8	5.08	0.045	2.09	5.25	5.07	0.044	2.23	5.36
S_9	5.30	0.010	0.13	4.58	5.27	0.026	0.37	4.30
S_{10}	5.38	0.026	0.18	4.25	5.34	0.165	0.24	4.42
S_{11}	5.48	0.209	0.78	4.61	5.53	0.615	0.48	4.32
S_{12}	5.63	0.431	0.54	4.29	5.64	0.157	0.66	4.53
S_{13}	5.74	0.081	0.12	4.10	5.73	0.059	0.31	4.07
S_{14}	5.79	0.101	0.51	4.09	5.77	0.117	0.41	3.99
S_{15}	5.90	0.021	1.23	4.73	6.02	0.006	0.81	4.75
S_{16}	5.95	0.010	2.07	5.08	6.07	0.060	2.02	4.77
S_{17}	6.05	0.019	2.21	4.70	6.09	0.048	1.65	4.75
S_{18}	6.07	0.003	2.75	5.15	6.19	0.004	1.60	4.84
S_{19}	6.11	0.062	2.67	4.95	6.30	0.008	2.46	4.92
S_{20}	6.15	0.019	3.35	5.33	6.34	0.008	1.59	4.77

TABLE 5.10: Excited state parameters for the lowest 20 singlet electronically excited states of **MPTA** in the gas phase and employing the C-PCM model for water. The excitation energies (EE) are given in eV, while the sizes $d_{h \to e}$ and d_{exc} are in Å.

for the weakest photoacids **HPTA** and **1C**, the CT state is lower lying than for the stronger photoacids, while the excitation energy of the bright S_1 state remains relatively constant regardless of pK_a^*. Finally, the vertical excited states were computed as well for **HPTA** and **MPTA** in acetonitrile. It was reported in the literature[45] that the S_3, S_4, and S_5 states move below the dark S_2 state in acetonitrile. However, no relevant change in the lowest six excited states was observed for **HPTA** and **MPTA** treating solvation in acetonitrile when compared to water. The tables showing the full results for the computations treating acetonitrile solvation are Tables 5.6 and 5.11.

As presented in Section 5.3, experimental data suggested that the stronger photoacids contained more deactivating substituents. This would indicate that pulling charge away from the pyrene core may ease acid dissociation, and by extension charge transfer from the substituents to the pyrene core may hinder dissociation. A similar correlation is shown here as well, with the energetic distance between CT states exhibiting transfer from the substituents to the pyrene core lying higher for the stronger photoacids, i.e. **1A** and **1B**, than for the weaker ones, i.e. **HPTA** and **1C**. This discussion on the whole hints that a larger energy difference between states of strong CT character from the

	EE	fosc	$d_{h \to e}$	d_{exc}
S_1	3.30	0.780	0.60	4.41
S_2	3.84	0.026	0.29	3.98
S_3	4.49	0.018	0.43	3.94
S_4	4.59	0.438	0.49	4.41
S_5	4.81	0.140	0.53	4.14
S_6	4.87	0.004	2.10	5.17
S_7	5.01	0.005	1.29	5.47
S_8	5.07	0.044	2.23	5.36
S_9	5.27	0.027	0.37	4.30
S_{10}	5.34	0.166	0.24	4.42
S_{11}	5.52	0.616	0.49	4.32
S_{12}	5.64	0.160	0.67	4.53
S_{13}	5.73	0.059	0.31	4.07
S_{14}	5.77	0.116	0.41	3.99
S_{15}	6.02	0.006	0.85	4.75
S_{16}	6.07	0.059	2.03	4.77
S_{17}	6.09	0.050	1.72	4.76
S_{18}	6.17	0.004	1.61	4.84
S_{19}	6.29	0.008	2.57	4.95
S_{20}	6.34	0.008	1.47	4.73

TABLE 5.11: Excited state parameters for the lowest 20 singlet electronically excited states of **MPTA** using C-PCM for acetonitrile. The excitation energies (EE) are given in eV, while the sizes $d_{h \to e}$ and d_{exc} are in Å.
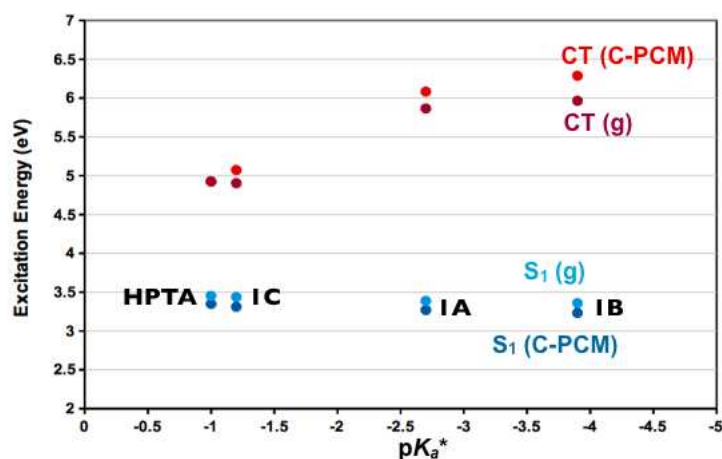
FIGURE 5.10: Correlation of pK_a^* versus excitation energy for the bright S_1 state and the lowest state of strong CT character for the photoacids **HPTA**, **1A**, **1B**, and **1C**, computed in the gas phase and using the C-PCM model for water.

substituents to the pyrene core may be a cause for the corresponding strong photoacidities of the pyranine-based photoacids. It is important to emphasize however that these differences really only provide a first primitive look into what states and factors could be of influence on the photophysics. In order to gain a better understanding of especially

	Gas Phase				C-PCM			
	EE	fosc	$d_{h \to e}$	d_{exc}	EE	fosc	$d_{h \to e}$	d_{exc}
S_1	3.37	0.571	0.65	4.39	3.22	0.719	0.76	4.39
S_2	3.88	0.019	0.27	3.90	3.86	0.021	0.34	3.90
S_3	4.36	0.006	0.26	3.82	4.34	0.010	0.33	3.83
S_4	4.76	0.389	0.84	4.29	4.65	0.525	0.88	4.27
S_5	4.94	0.054	0.15	3.80	4.87	0.071	0.26	3.78
S_6	5.18	0.002	0.24	4.56	5.14	0.006	0.29	4.51
S_7	5.34	0.028	0.50	3.94	5.27	0.051	0.64	4.07
S_8	5.67	0.357	0.26	4.09	5.62	0.894	0.23	3.95
S_9	5.69	0.186	0.87	4.48	5.75	0.029	0.45	3.83
S_{10}	5.75	0.084	0.28	4.01	5.77	0.075	0.26	4.30
S_{11}	5.85	0.216	1.56	4.73	5.84	0.181	0.10	3.84
S_{12}	5.87	0.005	0.54	5.29	6.03	0.001	3.29	5.15
S_{13}	5.89	0.072	1.55	4.70	6.10	0.001	2.30	5.28
S_{14}	5.92	0.014	0.36	5.03	6.12	0.002	2.75	5.41
S_{15}	6.10	0.006	1.30	4.65	6.20	0.011	1.21	4.65
S_{16}	6.35	0.008	0.39	4.05	6.29	0.008	0.46	3.99
S_{17}	6.37	0.030	0.88	4.58	6.41	0.049	0.38	4.57
S_{18}	6.44	0.002	0.98	5.02	6.51	0.075	0.38	4.52
S_{19}	6.47	0.013	1.78	5.01	6.54	0.024	0.51	3.87
S_{20}	6.51	0.002	0.90	5.14	6.59	0.241	0.19	4.07

TABLE 5.12: Excited state parameters for the lowest 20 singlet electronically excited states of **2A** in the gas phase and employing the C-PCM model for water. The excitation energies (EE) are given in eV, while the sizes $d_{h \to e}$ and d_{exc} are in Å.

the role of CT in the ESPT process, the dissociation coordinate must be studied.

5.5 Absorption and emission spectra in a series of solvents

The solvents employed in this part of the study and their dielectric constants are summarized in Table 5.15. All geometry optimizations converged during the geometry optimizations, carried out in Gaussian at the DFT/CAM-B3LYP/cc-pVDZ level of theory for the ground state and using corresponding TD-DFT for the excited state. However, the excited state optimizations generally only converged in this respect, but came only extremely close to convergence in the frequency calculation. Gaussian uses an analytically calculated Hessian in frequency computations, while an estimated Hessian is used for optimizations, leading to a discrepancy in some cases.

Treating solvation implicity for this series of solvents, the absorption and emission spectra were computed for **HPTA**. For the case of absorption, both linear-response and state-specific non-equilibrium C-PCM were employed for the treatment of solvation. The absorption and emission data are reported in Figure 5.11. Experimental observations showed a bathochromic shift resulting from solvent polarity. Since this shift was

	Gas Phase				C-PCM			
	EE	**fosc**	$\mathbf{d}_{h \to e}$	$\mathbf{d}_{exc}$	**EE**	**fosc**	$\mathbf{d}_{h \to e}$	$\mathbf{d}_{exc}$
S_1	3.34	0.597	0.69	4.41	3.18	0.737	0.79	4.41
S_2	3.87	0.018	0.30	3.91	3.84	0.021	0.38	3.92
S_3	4.34	0.007	0.29	3.83	4.30	0.010	0.36	3.85
S_4	4.73	0.367	0.91	4.29	4.62	0.502	0.97	4.28
S_5	4.92	0.062	0.11	3.84	4.85	0.072	0.23	3.83
S_6	5.18	0.002	0.25	4.57	5.13	0.008	0.31	4.54
S_7	5.32	0.031	0.55	3.94	5.25	0.057	0.68	4.06
S_8	5.67	0.268	0.28	4.14	5.61	0.914	0.28	3.97
S_9	5.69	0.276	0.63	4.31	5.73	0.024	0.48	3.82
S_{10}	5.74	0.134	0.49	3.96	5.76	0.060	0.28	4.28
S_{11}	5.85	0.268	0.09	3.84	5.81	0.196	0.24	3.86
S_{12}	5.94	0.005	3.04	5.23	6.13	0.006	0.70	4.34
S_{13}	5.97	0.005	3.13	5.31	6.19	0.008	0.67	4.60
S_{14}	6.09	0.005	1.33	4.76	6.27	0.025	2.02	4.93
S_{15}	6.26	0.012	1.09	4.25	6.32	0.001	2.76	5.16
S_{16}	6.35	0.013	0.31	4.65	6.36	0.010	0.50	4.73
S_{17}	6.41	0.009	0.35	4.53	6.49	0.128	0.55	4.39
S_{18}	6.46	0.004	2.09	5.27	6.52	0.105	0.25	4.29
S_{19}	6.50	0.031	1.33	5.03	6.55	0.198	0.81	4.48
S_{20}	6.55	0.002	2.74	5.26	6.56	0.008	1.21	4.96

TABLE 5.13: Excited state parameters for the lowest 20 singlet electronically excited states of **2B** in the gas phase and employing the C-PCM model for water. The excitation energies (EE) are given in eV, while the sizes $d_{h \to e}$ and d_{exc} are in Å.

more pronounced in the emission spectra than in excitation, it was concluded that the photoacid polarity is higher in the excited state than in the ground state. This trend is not observed in our computations, though we do note a strong red shift of the emission with respect to excitation, which agrees with experiment (Table 5.3).

A large change in the permanent dipole moment was found in experiment to be a strong indicator of excited state photoacidity. This change in dipole moment is reportedly indicative of CT taking place before ESPT, causing stronger photoacidity. The dipole moment of **HPTA** in the series of solvents, optimized in the ground and first exited states for each dielectric constant of the medium, is given in Figure 5.11. The change in dipole moment does not seem to vary at all with increasing dielectric constant, though a minor increase in both is observed moving from about $\epsilon = 10$ to about $\epsilon = 25$. Indeed, a slight increase in both moments is observed as ϵ approaches 80, though this change is not expected to be of much observed significance. Still, our results confirm an increase in the dipole moment for the excited state compared to the ground state, as reported in the literature.

Thus far, only the static excited state properties of the photoacids have been investigated. Though the change in dipole moment upon excitation and subsequent relaxation

	Gas Phase				C-PCM			
	EE	fosc	$d_{h\to e}$	d_{exc}	EE	fosc	$d_{h\to e}$	d_{exc}
S_1	3.42	0.614	0.58	4.41	3.27	0.764	0.69	4.41
S_2	3.88	0.023	0.23	3.94	3.86	0.023	0.33	3.95
S_3	4.46	0.003	0.27	3.89	4.42	0.015	0.38	3.89
S_4	4.75	0.352	0.88	4.38	4.63	0.493	0.86	4.32
S_5	4.89	0.082	1.50	4.56	4.85	0.098	0.13	3.84
S_6	4.91	0.025	1.66	4.84	4.98	0.018	1.82	5.25
S_7	4.95	0.003	3.33	5.44	5.04	0.007	2.17	5.51
S_8	5.10	0.001	3.47	5.44	5.19	0.008	1.41	5.07
S_9	5.25	0.002	0.43	4.86	5.25	0.020	0.78	4.50
S_{10}	5.34	0.022	0.37	4.03	5.30	0.027	2.07	4.95
S_{11}	5.40	0.005	2.15	5.12	5.52	0.109	2.03	5.04
S_{12}	5.63	0.667	0.69	4.33	5.57	0.875	0.29	4.29
S_{13}	5.67	0.016	0.68	4.90	5.70	0.004	0.38	4.44
S_{14}	5.71	0.003	1.37	4.75	5.74	0.011	0.54	4.51
S_{15}	5.76	0.049	0.85	4.62	5.79	0.122	0.72	4.27
S_{16}	5.84	0.132	0.82	4.27	5.91	0.061	1.46	5.01
S_{17}	5.89	0.059	2.76	5.35	6.01	0.014	2.58	5.47
S_{18}	5.96	0.010	1.55	4.84	6.11	0.019	2.88	4.84
S_{19}	6.01	0.016	2.98	4.86	6.14	0.006	1.55	4.85
S_{20}	6.06	0.003	2.28	5.18	6.28	0.016	0.68	4.37

TABLE 5.14: Excited state parameters for the lowest 20 singlet electronically excited states of **2C** in the gas phase and employing the C-PCM model for water. The excitation energies (EE) are given in eV, while the sizes $d_{h\to e}$ and d_{exc} are in Å.

Solvent	Dielectric constant (ϵ)
Dichloromethane (DCM)	8.9300
Isopropanol (IP)	19.2640
Ethanol (EtOH)	24.8520
n,n-Dimethylformamide (DMF)	37.2190
Dimethylsulfoxide (DMSO)	46.8260
Water	78.3553

TABLE 5.15: Summary of the solvents employed in the study of absorption and emission spectra of HPTA.

of the S_1 state indicates that CT may indeed play a role in the photophysics, this role is impossible to discern in the purely static picture. We thus now turn our attention to the deprotonation coordinate of **HPTA** in water. In addition, we look as well at a combination of explicit and implicit solvation modeling in our treatment of the photoacid dissociation.
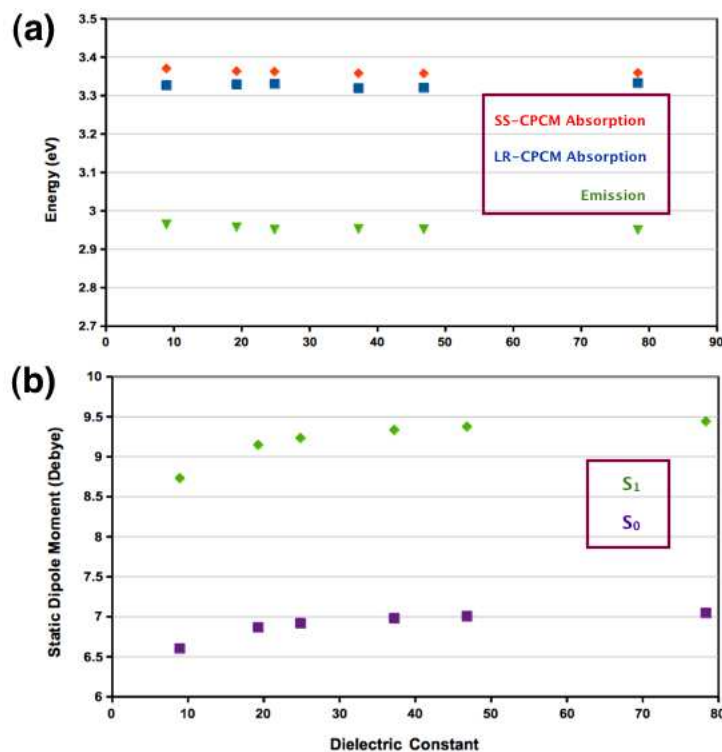
FIGURE 5.11: (a) Absorption and emission and (b) ground and excited state static dipole moments of **HPTA** in the solvent series.

5.6 Dissociation of HPTA and 1A

In order to obtain a first look at the photophysics of the pyranine-based photoacids, the acid dissociation coordinate of **HPTA**·H_2O was studied. Starting from the equilibrium **HPTA**·H_2O structure, single point calculations were performed at intervals of 0.05 Å, manually pulling the proton on **HPTA** towards the oxygen of H_2O while holding all other coordinates constant. Attachment/detachment densities and the set of excited state descriptors were computed. It should be noted that the **HPTA** structure used for the rigid scan holds one substituent rotated slightly inward compared to the fully optimized geometry used for the relaxed scan. The single point calculations were carried out at the TD-DFT/CAM-B3LYP/cc-pVDZ level of theory both in the gas phase and employing the C-PCM model for water. These rigid scans are depicted in Figure 5.12. In the gas phase, a higher-lying state appears to cross down over the course of the dissociation coordinate, moving to become S_1, while in solution, the rigid S_1 curve is comparatively isolated and much flatter than in the gas phase, indicating potentially facilitated ESPT.

For **HPTA**·H_2O, the equilibrium distance between the H of the photoacid and the O of the explicit water molecule is 1.70 Å. Table 5.16 provides the excited state information for this structure in the gas phase and using C-PCM. Table 5.17 then gives the results
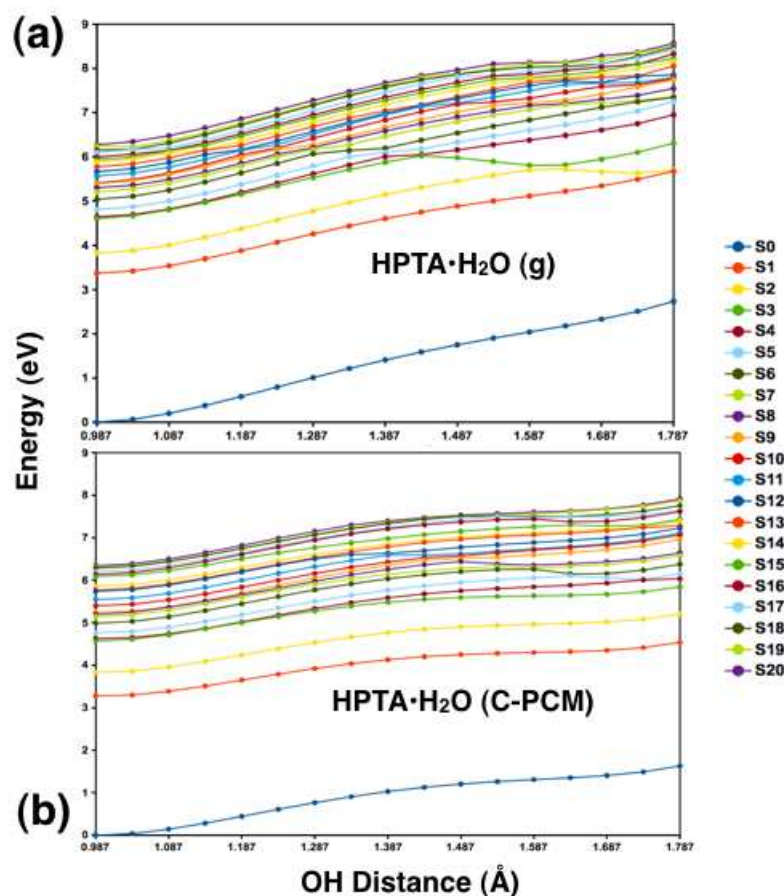
FIGURE 5.12: Single point calculations along the dissociation coordinate of **HPTA**·H$_2$O (a) in the gas phase and (b) computed using the non-equilibrium C-PCM model to treat solvation in water.

at the end of the dissociation coordinate for a distance of 0.96 Å. These OH distances correspond in Figure 5.12 between the O and H of the -OH group on the photoacid of 0.987 Å and 1.787 Å, respectively. Initially, at equilibrium, the excited states lie similarly to the case of **HPTA** without the additional water molecule: the lowest states all involving small amounts of CT centered on the pyrene core, and starting with S$_6$ several states exhibiting CT from the substituents to the pyrene core are present. From this equilibrium point to an OH distance of 1.39 Å, a strong CT state decreases to S$_5$, exhibiting CT from the O of the photoacid to the H$_2$O/H$_3$O$^+$ moeity. This state continues to decrease so that at the last single point, where deprotonation is fully accomplished, it is the lowest singlet electronically excited state. This is clearly seen in the tables, where the state with a $d_{h\rightarrow e}$ of approximately 4.4 Å and a d_{exc} of about 5.7 Å decreases to be the S$_3$ at a distance of 1.14 Å and finally the S$_1$ post-dissociation. The attachment/detachment densities for the lowest three excited states for the fully dissociated **HPTA** photoacid are shown in 5.13. The states lying below this CT state at points earlier along the dissociation coordinate, for example the S$_1$ and S$_2$ at a distance of 1.14 Å, involve minor CT from the right side of the photoacid, centered on the OH group, to the left

	Gas Phase				C-PCM			
	EE	**fosc**	$\mathbf{d}_{h \to e}$	$\mathbf{d}_{exc}$	**EE**	**fosc**	$\mathbf{d}_{h \to e}$	$\mathbf{d}_{exc}$
S_1	3.37	0.547	0.61	4.39	3.28	0.723	0.54	4.38
S_2	3.82	0.013	0.37	3.95	3.83	0.019	0.35	3.94
S_3	4.60	0.029	0.52	3.89	4.57	0.071	0.51	3.92
S_4	4.64	0.169	0.91	4.11	4.62	0.289	0.75	4.11
S_5	4.81	0.264	0.33	4.17	4.76	0.280	0.24	4.02
S_6	5.04	0.015	2.22	5.05	4.99	0.014	1.88	5.08
S_7	5.21	0.017	1.60	5.22	5.14	0.020	1.88	5.36
S_8	5.30	0.042	0.17	4.26	5.20	0.001	4.83	6.11
S_9	5.39	0.015	2.08	5.10	5.25	0.049	0.41	4.24
S_{10}	5.41	0.016	3.45	5.62	5.40	0.129	0.79	4.50
S_{11}	5.57	0.560	0.46	4.12	5.54	0.694	0.50	4.10
S_{12}	5.66	0.004	0.81	4.69	5.74	0.016	0.46	4.39
S_{13}	5.77	0.050	0.51	4.04	5.77	0.051	0.29	4.03
S_{14}	5.88	0.259	0.22	4.00	5.86	0.247	0.45	4.11
S_{15}	5.93	0.041	1.14	4.81	6.09	0.012	1.17	4.69
S_{16}	5.99	0.001	3.34	5.22	6.14	0.001	4.08	5.33
S_{17}	6.09	0.001	2.54	5.18	6.20	0.019	1.44	4.74
S_{18}	6.15	0.009	1.88	5.00	6.28	0.003	1.57	4.90
S_{19}	6.24	0.000	4.56	5.86	6.31	0.002	0.32	4.21
S_{20}	6.27	0.018	2.42	5.10	6.34	0.005	2.69	5.07

TABLE 5.16: Excited state parameters for the lowest 20 singlet electronically excited states of **HPTA**·H_2O, computed in the gas phase and using C-PCM for water, at the ground state equilibrium OH distance between the H of **HPTA** and the O of water of 1.70 Å. The excitation energies (EE) are given in eV, while the sizes $d_{h \to e}$ and d_{exc} are in Å.

side of the pyrene core away from the site of ESPT. Looking to the case of **HPTA**·H_2O using C-PCM for water, we have corresponding data again in Tables 5.16 and 5.17. In this case, a large crossing of a higher-lying state down to S_1 is not observed in Figure 5.12. Indeed, at an OH distance of 0.96 Å, this CT state is still S_{17}, and the S_4, having a $d_{h \to e}$ of 2.78 Å and a d_{exc} of 4.42 Å , is an $n\pi^*$ state.

Single point calculations were also carried out for **1A**·H_2O in the gas phase and using the C-PCM model for water. The results for these calculations in the gas phase are found in Tables 5.18 (equilibrium OH distance of 1.77 Å) and 5.19 (1.02 Å), i.e. at the end of the dissocation coordinate. **1A** is a stronger photoacid than **HPTA**, so it is useful to look at the presence and location of the large crossing CT state from **HPTA** in this case. Indeed, in the gas phase, this state crosses down less strongly than for **HPTA**, and at a distance of 1.02 Å it is only the S_2. The A/D plots for the lowest six states of **1A** at equilibrium are shown in Figure 5.14, while the lowest six states at a distance of 1.02 Å are shown in Figure 5.15, in both cases in the gas phase. In water, the CT state does not appear to cross down at all. This leads to the strong possibility that this state hinders ESPT in the weaker photoacids, while for stronger ones like **1A**,

| | Gas Phase | | | | C-PCM | | | |
	EE	fosc	$d_{h \to e}$	d_{exc}	EE	fosc	$d_{h \to e}$	d_{exc}
S_1	2.94	0.016	4.41	5.72	2.91	0.652	0.86	4.44
S_2	2.96	0.449	0.95	4.49	3.57	0.048	0.97	4.12
S_3	3.58	0.026	0.89	4.09	4.21	0.023	0.80	3.88
S_4	4.22	0.031	0.80	3.90	4.40	0.001	2.78	4.42
S_5	4.52	0.274	0.74	4.29	4.52	0.328	0.66	4.26
S_6	4.61	0.004	2.72	4.45	4.74	0.010	0.33	3.89
S_7	4.63	0.100	2.49	3.97	4.95	0.194	0.33	4.12
S_8	4.81	0.053	0.68	4.08	5.01	0.020	0.42	4.82
S_9	5.01	0.001	5.15	6.33	5.33	0.026	3.37	5.25
S_{10}	5.04	0.041	1.38	4.86	5.44	0.473	1.33	4.70
S_{11}	5.06	0.007	0.52	4.52	5.48	0.047	4.65	6.06
S_{12}	5.12	0.015	2.88	5.40	5.60	0.189	1.69	4.69
S_{13}	5.32	0.019	3.35	5.30	5.65	0.000	2.67	4.26
S_{14}	5.43	0.000	5.04	6.10	5.76	0.090	0.48	3.86
S_{15}	5.49	0.358	1.79	4.73	5.80	0.500	0.16	3.84
S_{16}	5.59	0.184	1.51	4.52	5.99	0.047	0.94	4.67
S_{17}	5.68	0.000	6.22	7.15	6.01	0.001	4.06	5.45
S_{18}	5.74	0.003	4.40	5.89	6.12	0.009	0.47	4.10
S_{19}	5.76	0.151	0.18	4.24	6.24	0.025	0.72	4.88
S_{20}	5.83	0.015	1.74	4.35	6.28	0.002	3.65	5.13

TABLE 5.17: Excited state parameters for the lowest 20 singlet electronically excited states of **HPTA**·H_2O, computed in the gas phase, at an OH distance between the H of **HPTA** and the O of water of 0.96 Å. The excitation energies (EE) are given in eV, while the sizes $d_{h \to e}$ and d_{exc} are in Å.

it plays much less of a role in the excited state picture. Since it crosses down so strongly for HPTA in the gas phase but less so for **1A**, it is likely the factor that hinders ESPT in HPTA making it less photoacidic. Indeed, it also vanishes in the lower states once implicit solvation is treated.

On the basis of their calculations, Jung et al.[45] hypothesized two main interpretations for the photoacidity of the series, in particular with respect to the S_3-S_5 states in their computations. One suggestion was that these CT states move below the S_1 as a result of the solvent relaxation, forcing ESPT to take place only via thermal depopulation of these states within the fluorescence lifetime of the photoacid. That is, ESPT and intramolecular CT are competing processes. A second suggestion was that these states mix with the S_1, partially transferring their CT character. This mixing would then occur to a lesser extent the larger the difference between the spectroscopically observed S_2 state and the S_1. The computed CT for the spectroscopic S_2 is from the substituents to the pyrene core, which likely works against the ESPT process. On the basis of the computations presented in this thesis, the strong CT state, exhibiting transfer of charge from the O of the photoacid to the water moeity, crosses down more strongly to become the S_1 in weaker photoacids and absent the stabilizing effect of the solvent. This CT
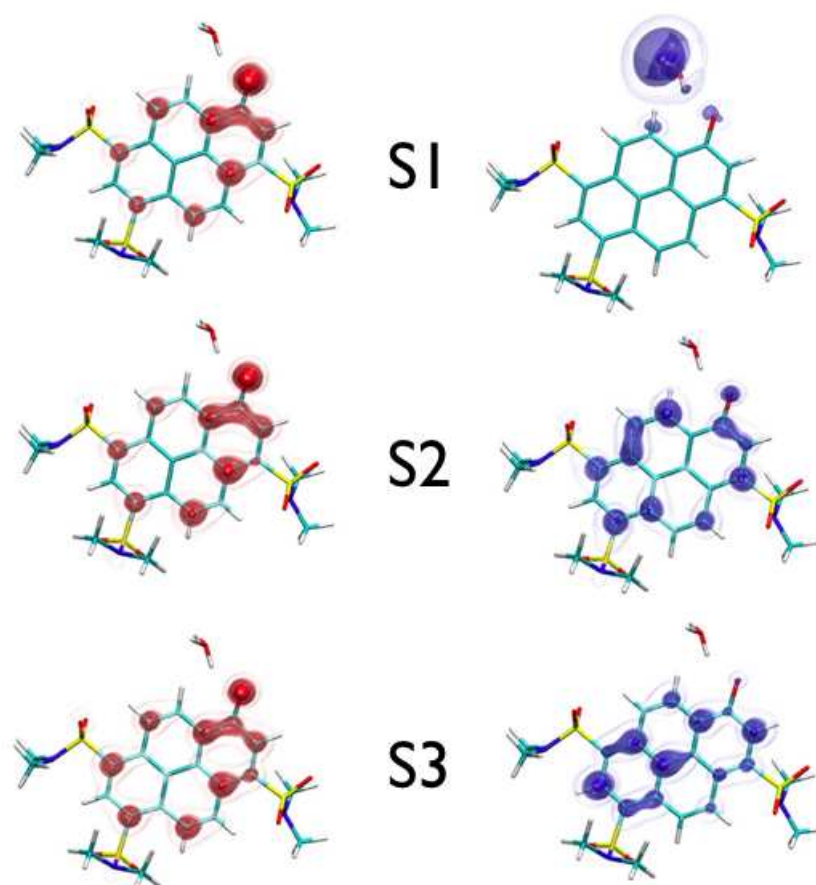
FIGURE 5.13: Detachment (left, red) and attachment (right, blue) densities for the lowest three singlet electronically excited states of **HPTA**·H_2O computed in the gas phase at a distance of 0.96 Å (corresponding in Figure 5.12 to a distance of 1.787 Å).

process therefore likely competes with ESPT, and the steeper it crosses in, i.e. the lesser the energetic difference between this state and the S_1, the more difficult ESPT becomes. In stronger photoacids and, in particular, under stabilizing solvation in water, this state does not cross down to potentially disrupt the ESPT process. Rather, it remains energetically far away from the S_1. The lowest states, S_1 and S_2, involve then small amounts of CT from the OH side of the photoacid to the opposite side of the pyrene core, facilitating ESPT.

The main results thusfar will be summarized as follows. The discussion of the static properties of the photoacid series along with the rigid scans of the deprotonation coordinate of **HPTA** to an explicit water molecule in its vicinity provide two main ideas for how charge transfer effects the differing photoacidities of the pyranine-based series. The lowest 20 singlet electronically excited states for **HPTA** and **1A** exhibit two main classes of CT states. The first, as seen in the discussion of static properties, are the states showing CT from the substituents to the ring. There was a significant positive
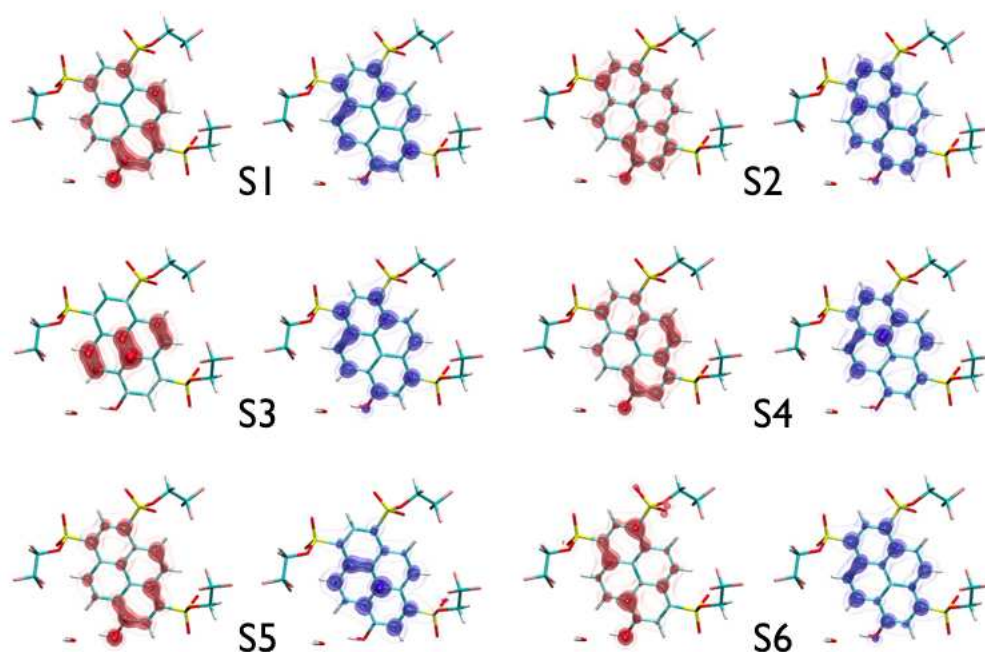
FIGURE 5.14: Detachment (red) and attachment (blue) densities for the lowest six electronically excited states of the neutral **1A**·H_2O system.
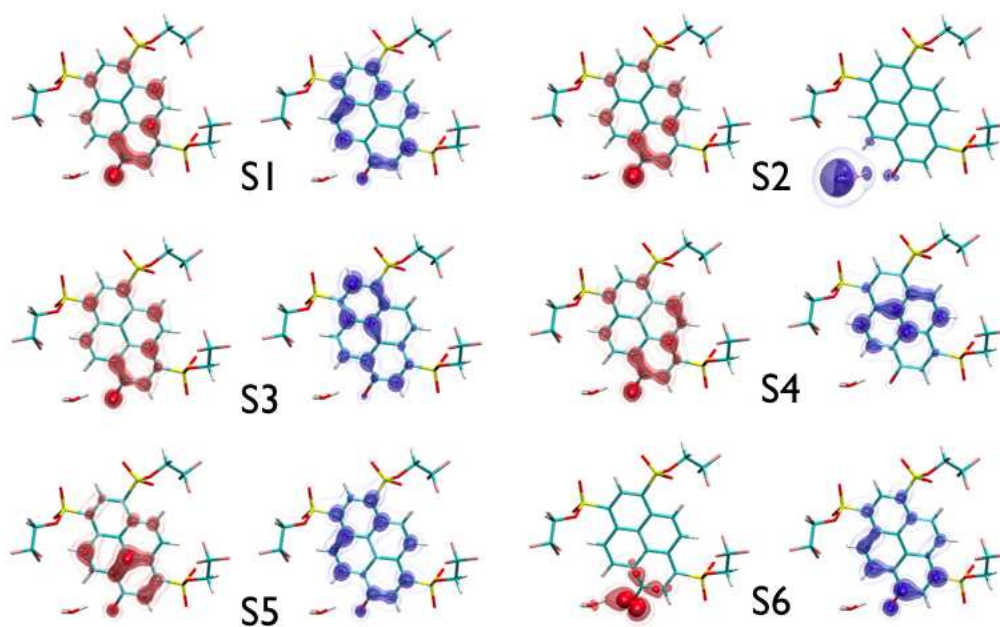
FIGURE 5.15: Detachment (red) and attachment (blue) densities for the lowest six electronically excited states of the deprotonated **1A**·H_3O^+ system.

correlation between the excitation energies of these states and increased photoacidity. Thus, it may be posed that if they cross down during the course of the dissociation co-ordinate, hinderance of the deprotonation may ensue. The rigid scans show a different

	Gas Phase				C-PCM			
	EE	**fosc**	$d_{h\to e}$	d_{exc}	**EE**	**fosc**	$d_{h\to e}$	d_{exc}
S_1	3.31	0.495	0.68	4.37	3.21	0.661	0.67	4.36
S_2	3.85	0.015	0.36	3.92	3.85	0.016	0.38	3.91
S_3	4.43	0.025	0.37	3.84	4.38	0.027	0.40	3.85
S_4	4.67	0.290	0.93	4.16	4.62	0.465	0.83	4.19
S_5	4.83	0.155	0.13	3.96	4.80	0.145	0.08	3.88
S_6	5.26	0.008	0.14	4.46	5.24	0.000	0.19	4.42
S_7	5.32	0.043	0.48	3.87	5.25	0.064	0.65	3.95
S_8	5.65	0.533	0.38	3.94	5.60	0.843	0.17	3.96
S_9	5.76	0.108	0.24	4.02	5.73	0.031	0.47	3.82
S_{10}	5.77	0.023	0.71	4.56	5.84	0.141	0.13	4.13
S_{11}	5.90	0.169	1.09	4.64	5.90	0.118	0.13	4.03
S_{12}	5.92	0.051	1.81	4.89	6.11	0.002	3.13	5.12
S_{13}	5.96	0.032	2.53	4.96	6.16	0.003	3.30	5.28
S_{14}	6.04	0.004	3.19	5.27	6.19	0.000	2.43	5.14
S_{15}	6.13	0.002	1.17	4.60	6.21	0.002	1.21	4.85
S_{16}	6.31	0.001	0.53	3.77	6.28	0.003	0.50	3.96
S_{17}	6.44	0.009	0.24	4.75	6.43	0.023	0.60	4.57
S_{18}	6.46	0.015	1.46	4.89	6.55	0.218	0.35	4.41
S_{19}	6.52	0.001	3.07	5.27	6.58	0.038	0.58	4.03
S_{20}	6.54	0.009	1.16	4.93	6.62	0.223	0.44	4.33

TABLE 5.18: Excited state parameters for the lowest 20 singlet electronically excited states of **1A**·H_2O, computed in the gas phase and using the C-PCM model at the ground state equilibrium OH distance between the H of **1A** and the O of water, 1.77 Å. The excitation energies (EE) are given in eV, while the sizes $d_{h\to e}$ and d_{exc} are in Å.

picture, however. Here, particularly in the destabilized gas phase, a different type of CT state crosses down over the course of the coordinate, reaching eventually the lower states and, in the case of the weaker **HPTA** photoacid, the S_1 position. This state, exhibiting CT from the H_2O/H_3O^+ to the OH/O^- of the photoacid, may compete with acid dissociation, thereby increasing the pK_a^*. These rigid scans provide a strong foundation for further work. Next, optimizations along the bright S_1 state will be presented for the **HPTA**·H_2O acid dissociation coordinate. These relaxed scans were computed both in the gas phase and employing the linear-response, equilibrium C-PCM model to treat solvation in water. These results are shown in Figure 5.16.

Inspecting these curves in Figure 5.16, little difference is observed between the gas phase and C-PCM calculations. Employing C-PCM leads to a very slight stabilization of the S_1 surface by about 0.2 eV, and the potential along this coordinate is almost completely flat in S_1, indicating that ESPT in S_1 occurs very readily. However, at OH distances shorter than 1.09 Å the optimizations in the gas phase broke down and in C-PCM, the surfaces dramatically increased in energy. Still, no crossing behavior was observed. Over the course of the scans shown here, the S_1 is continually a bright HOMO-LUMO transition,

	Gas Phase				C-PCM			
	EE	**fosc**	$\mathbf{d}_{h\rightarrow e}$	$\mathbf{d}_{exc}$	**EE**	**fosc**	$\mathbf{d}_{h\rightarrow e}$	$\mathbf{d}_{exc}$
S_1	2.90	0.437	0.95	4.43	2.82	0.605	0.87	4.44
S_2	3.37	0.001	4.57	5.77	3.62	0.043	1.01	4.12
S_3	3.64	0.019	0.89	4.08	4.25	0.009	0.78	3.90
S_4	4.26	0.021	0.85	3.90	4.29	0.001	2.80	4.43
S_5	4.42	0.220	0.77	4.18	4.39	0.215	0.76	4.14
S_6	4.55	0.002	2.75	4.45	4.62	0.086	0.23	4.01
S_7	4.66	0.031	0.09	4.01	4.94	0.259	0.79	4.24
S_8	4.96	0.255	1.06	3.99	5.06	0.068	0.10	4.41
S_9	5.06	0.052	0.52	4.51	5.57	0.695	0.51	3.91
S_{10}	5.27	0.005	1.88	4.10	5.72	0.004	2.53	4.20
S_{11}	5.45	0.001	5.24	6.31	5.74	0.012	0.70	3.79
S_{12}	5.58	0.305	1.52	4.56	5.81	0.502	0.74	4.14
S_{13}	5.66	0.173	3.40	5.40	5.98	0.029	0.85	4.37
S_{14}	5.78	0.189	0.78	3.87	6.07	0.018	0.19	4.35
S_{15}	5.84	0.007	4.76	5.82	6.22	0.004	3.00	5.22
S_{16}	5.89	0.151	1.04	4.37	6.24	0.003	1.02	4.77
S_{17}	5.93	0.148	1.16	4.34	6.30	0.010	1.79	4.97
S_{18}	5.99	0.017	1.87	4.55	6.37	0.045	0.45	5.10
S_{19}	6.03	0.002	1.30	4.74	6.41	0.007	2.45	5.45
S_{20}	6.10	0.001	5.78	6.91	6.43	0.008	1.20	4.71

TABLE 5.19: Excited state parameters for the lowest 20 singlet electronically excited states of **1A**·H_2O, computed in the gas phase and using the C-PCM model at an OH distance between the H of **1A** and the O of water of 1.02 Å. The excitation energies (EE) are given in eV, while the sizes $d_{h\rightarrow e}$ and d_{exc} are in Å.

showing mainly local excitation centered on the pyrene core. The KS molecular orbitals for this transition are shown in Figure 5.17.

The results for the relaxed S_1 surface scans are qualitatively different from those of the rigid scans, and do not clearly show any CT state crossing down for potential competition with ESPT. Further scans should therefore be an integral part of future work, along with several other points which, due to the complexity of the project, will be proposed in the following section.

5.7   Conclusion and Outlook

Photoacids exhibit enhanced photoacidity in the first electronically excited state compared to the ground state. A class of photoacids called super-photoacids are characterized by a pK_a^* and can undergo ESPT not only in water, but to DMSO, alcohols, and other polar, aprotic solvents as well. Recently, a group of super-photoacids based on the popularly-studied **HPTS** were synthesized and their differing properties investigated in a series of experimental and initial theoretical studies. Of the photoacids considered in this
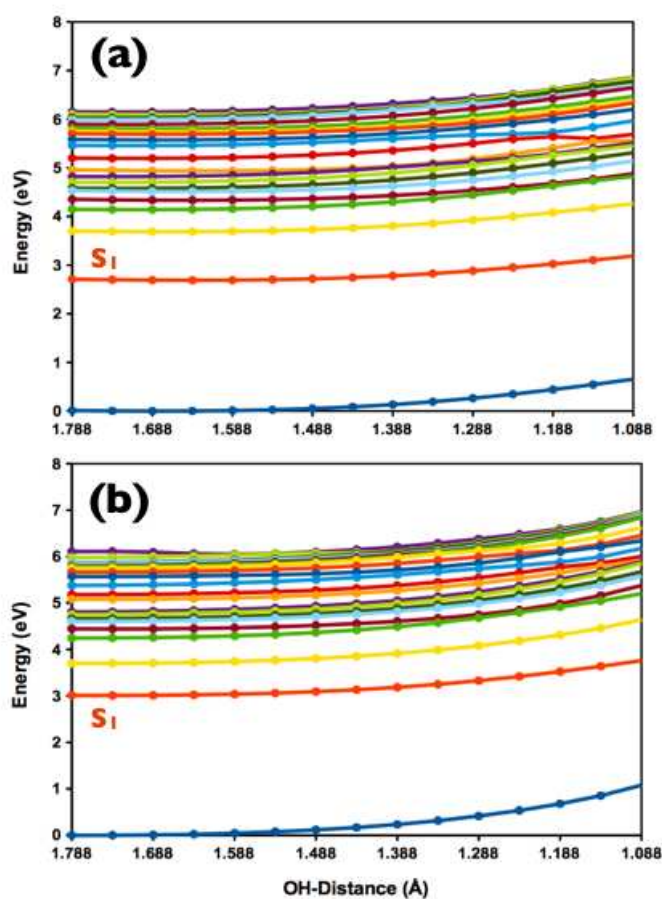
FIGURE 5.16: Relaxed surface scans optimized in the bright S_1 state along the acid dissociation coordinate of **HPTA** in water for the **HPTA**·H_2O system,computed at the TD-DFT/CAM-B3LYP/cc-pVDZ level of theory (a) employing the C-PCM model to treat solvation in water and (b) in the gas phase.
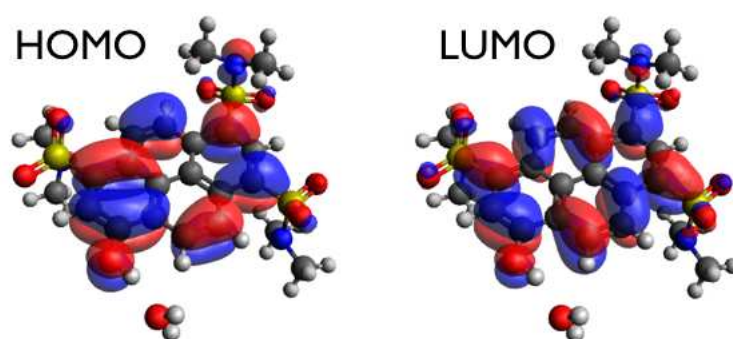
FIGURE 5.17: The frontier molecular orbitals for the HOMO-LUMO transition characterizing the S_1 state along the relaxed S_1 surface scan of the acid dissociation coordinate of **HPTA** in water.

study, **1B** is the strongest with a $pK_a^* = -3.9$, although all photoacids in the series are superphotoacids with a $pK_a^* < 0$. Incidentally, it has the strongest electron-withdrawing groups R. In general, it was found that stronger electron-withdrawing groups lead to

enhanced photoacidites. Among the photoacids studied, both those with a dissociating OH group and their methylated counterparts show similar behavior, as one would expect since the electronic effect of a methyl group and a proton is not appreciably different. The computational study presented in this dissertation began with an overview of the main results and open questions observed by Jung et al[45–47]. The main points of this discussion are summarized in the following paragraph.

A short summary of the results of the studies by Jung et al. that are most pertinent to this investigation are given now. The excitation and emission spectra exhibit bathochromic shifts in solvents of higher polarity, though here the shift is more extreme in emission than in excitation, indicating that the photoacids have higher polarities in the excited state than in the ground state. Also, a large change in the permanent dipole moment was observed for all photoacids upon excitation, which is seen as evidence for charge transfer, leading to increased photoacidity, taking place before ESPT. Previously performed quantum chemical calculations had been interpreted to indicate that the spectroscopically observed S_2 state is made up of the S_3, S_4, and S_5 states, while the real second electronic transition is not visible in experimental spectra. The energy difference between this spectroscopically observed S_2 state was shown to increase as photoacidity increased. This was not observed in my computations, though I did find a strong positive correlation between the energy difference between the lowest CT state and the S_1 and photoacid strength. Overall, electron-withdrawing substituents were found in Jung et al.'s work to lead to increased photoacidity of the compounds.

The computational study performed here began with a benchmarking analysis of a series of exchange-correlation functionals for TD-DFT. This benchmarking procedure encompassed a comparison of a series of excited state descriptors offering a more complete description of the excited state at the TD-DFT level. Benchmarking with TD-DFT for such large systems must be intelligent and go beyond the simple molecular orbital picture, especially since more accurate calculations with ADC(2)-s, for example, are prohibitively expensive and time-consuming. Since the presence of CT was indicated as being an important factor for the photoacidity, it is also pertinent that the description of the excited states also involve CT analysis. Thus, my focus throughout was on two main measures of the amount of CT in an excited state: the mean of the distance between an electron and hole in the exciton picture, and the root-mean-square of this distance. Comparing the results employing the B3LYP, BHLYP, ω-B97X, and CAM-B3LYP functionals, it was apparent that the TD-DFT/CAM-B3LYP level of theory offered the best description of the excited states of the photoacids. For benchmarking the **HPTA** molecule was used. The TD-DFT/CAM-B3LYP/cc-pVDZ level was therefore employed throughout the duration of the study.

First, the static properties of the excited states of the photoacids shown in Figure 5.1 were analyzed on the basis of their excitation energies, oscillator strengths, $d_{h\rightarrow e}$ and d_{exc} distances, and attachment/detachment (A/D) density plots. For the weaker photoacids, an excited state in the S_6 position was found to exhibit strong CT character from the substituents to the ring, as evidenced by the A/D plots and $d_{h\rightarrow e}$ distances on the order of about 2 Å. In the stronger photoacids and in the presence of aqueous solution, as modeled using the C-PCM, this type of CT state was found to be significantly higher lying, at around the S_{12} position. Since CT from the substituents to the pyrene core will logically destabilize ESPT, it is thought that these states may move downward over the course of the ESPT coordinate, interfering with that process.

In order to gain insight into the behavior of the excited states during ESPT, rigid potential surface scans were performed via single point calculations, pulling the acidic proton on **HPTA** and **1A** towards an explicit water molecule in its vicinity. These two photoacids are ideal to study in parallel, as **HPTA** has an experimental $pK_a^* = -1$ and **1A** is a much stronger photoacid with a $pK_a^* = -2.7$. The single point calculations were performed starting from the equilibrium OH distance between the acidic H and the O of water for each system at intervals of 0.05 Å. Here, the TD-DFT/CAM-B3LYP/cc-pVDZ level of theory was used both in the gas phase and employing the linear-response, non-equilibrium C-PCM model for solvation in water. A/D densities and the series of excited state descriptors were inspected. For the **HPTA** in the gas phase, a state of strong CT character showing charge transfer from the OH/O$^-$ of the photoacid to the water/hydroxide moeity decreases over the course of the ESPT coordinate, eventually assuming the S_1 position. When the C-PCM model was employed and when the ESPT rigid coordinate for the stronger **1A** photoacid was computed, this CT state crossed down to a lesser extent, never fully reaching the energetic realm of the S_1. An attempt at gaining more conclusive analysis of this fact was made by performing relaxed surface scans of the **HPTA** ESPT coordinate to an explicit water molecule, both in the gas phase and employing the linear-response, equilibrium C-PCM solvation model to treat solvation in water. The results of these relaxed potential energy surface scans showed a practically flat S_1 potential curve, particularly in the case of solvation in aqueous solution, indicating that ESPT to water from **HPTA** occurs very readily. The S_1 state along the coordinate was a strong HOMO-LUMO transition, characterized by a local excitation involving the pyrene core. No state crossings were observed, and the process played out on a relatively isolated S_1 surface. Since this qualitatively does not support the rigid scan results, more investigation would be necessary to uncover what role the CT state observed in the rigid scan results has on impacting the photoacidity.

The remainder of this conclusion is dedicated to a detailed outlook for the pyranine-based photoacid project, as it has proven to be very intricate. Due to the complexity

of the singlet manifold of the photoacids and the large variety of flavors of pyranine-based photoacids available, much more can be done to delve into this work. First, excited state properties of the neutral excited photoacids were studied. However, such strong photoacids will dissociate rapidly after excitation, forming their conjugate bases. Jung et al. studied the solvatochromism of these anions, finding that, with increasing donating strength of the hydrogen bond, absorption and emission frequencies were both blue-shifted. Here, the effect was stronger in the ground state than in the excited state, as would be expected due to a more negative charge on the oxygen atom in S_0. In addition, the basicity and polarity of the solvent did not measurably alter the absorption or emission wavelengths of the anions. These points should be investigated in further computational studies, particularly since the rapid presence of such anions is a powerful indicator of photoacidity.

The rigid and relaxed potential surfaces computed in this study did not reflect the same trend. The high-lying state exhibiting CT from the oxygen on the photoacid to the water/H_3O^+ moeity that crossed down during the rigid scan in the gas phase must be studied in more depth. Suggestions for this may include looking to where this state crosses in for weaker photoacids, or in the presence of another solvent. It would also be appropriate to perform further relaxed surface scans in solvents to which ESPT is not as easily occuring, such as DMSO and alcohols.

The CT state showing charge transfer from the photoacid oxygen to the explicit solvent molecule moeity is only one type of charge transfer state observed in this study. A group of CT states exhibiting transfer from the substituents to the pyrene core was observed in the analysis of the static properties of the photoacids. Indeed, these states were higher-lying in the stronger photoacids than in the weaker ones, indicating that they may indeed play a role in inhibiting ESPT in some cases. While they were not found to be lower down in the case of acetonitrile versus water for **HPTA** and **MPTA** in my computations, further study employing DMSO and alcohols is warrented. These two types of CT states provide strong leads for further investigation of the photoacidic properties of the series. Finally, two limiting mechanisms were proposed for PT along an H-bond in polar solvents. These are the quantum adiabatic and quantum non-adiabatic, i.e. tunneling, limits. The discussion of these limits in detail is beyond the scope of this thesis, but further investigation into what limit ESPT from the strong photoacids belongs is another suggestion for future work in studying the pyranine-based photoacids presented here.

Chapter 6

Summary and Conclusions

Excited state proton transfer reactions occur in a range of systems with possibilities for a wide variety of applications. Ultrafast ESPT reactions take place, for example, in green fluorescent protein and are responsible for the photostability of DNA. Research into such processes has led to such applications as the development of fluorescent sensors and probes, ultrafast molecular switches, white-light emitting chromophores, and other technologies. While fluorescence-based experimental techniques provide part of the picture in understanding ESPT processes, theoretical calculations can still provide further insight into the electronic picture of a system undergoing ESPT.

Of course, the quantum chemical study of ESPT processes involves going beyond the standard treatment of the electronic ground state to the electronically excited states of a given system. The development and improvement of methods for the quenatum chemical treatment of the excited state is currently a broad and highly active field of resarch. In Chapter 2, an overview of methods used for the study of the excited state were presented. Two of the most commonly employed methods in this study were time-dependent density functional theory (TD-DFT), the analog of DFT for excited states, and the algebraic diagrammatic construction (ADC) for the polarization propagator. TD-DFT is very useful and computationally cheap when appropriately employed, leading to errors in the excitation energies on the order of about 0.1-0.5 eV, which is similar to those found for wave function-based methods. However, the use of TD-DFT is generally problematic when Rydberg or charge transfer states are to be computed. Still, through thorough benchmarking and the use of, for example, long-range corrected functionals, TD-DFT remains broadly applicable.

Another method consistently used throughout this thesis was the ADC scheme, which has proven to be a very effective class of ab initio methods for computing excited states on the basis of perturbation theory. Importantly, ADC methods are ideal for the study

of medium-sized to large molecules because of their size-consistency. Over the course of this work, both TD-DFT and ADC were often used. Indeed, it is often a good idea to compare computational results from different methods to demonstrate the accuracy of the main ones employed. In addition, some methods provide insight beyond others, and using a carefully balanced variety of methods can yield the most complete picture of the excited states of a molecular system.

This work involved the computational investigation of excited state proton transfer processes in a set of very different chemical systems, the first was Pigment Yellow 101 (PY101), which is the subject of Chapter 3. PY101 is one of the few commercially available fluorescent yellow pigments and has long been noted for its unique fluorescent properites and high photostability. The S_1 state of PY101 is a bright HOMO-LUMO $\pi\pi^*$ transition, and previous experimental transient absorption spectra and computed amplitude spectra led to the identification of five time constants were necessary for describing the decay of this S_1 state. In addition, through an extensive search of the potential energy surface, six stable conformers of PY101 thought to reasonably be able to impact the excited state dynamics were identified. These are the *exo-trans*-diol ($\mathbf{A}(\mathbf{x})$), *exo-trans*-keto ($\mathbf{B}(\mathbf{x})$), *endo-trans*-diol ($\mathbf{C}(\mathbf{x})$), *endo-trans*-keto ($\mathbf{D}(\mathbf{x})$), *exo-cis*-diol ($\mathbf{E}(\mathbf{x})$), and *exo-cis*-keto ($\mathbf{F}(\mathbf{x})$), where $\mathbf{x}$ denotes the excited analog of the ground state isomer. In this work, relaxed surface scans were performed connecting these six most stable isomers and energy barriers were estimated on the basis of these curves.

Photoexcitation of PY101 leads to the population of the Franck-Condon region of the S_1 state, from which about 90 % of the PY101 population will remain in the diol form. The rate constant of 63 ps corresponds to fluorescence decay back to the ground state. Rapid depopulation of the Franck-Condon region yields the availability of sufficient excess energy to populate some of the other isomers. Relaxed surface scans connecting these isomers, performed using TD-DFT and optimizing in the bright S_1 state, provide an initial interpretation of the excited state dynamics of PY101 and allow one to make qualitative predictions as to what photochemical processes are feasible. Inspection of these curves and the relative energies of the geometries indicate that isomerization involving ESIPT will likely occur much more readily than those involving dihedral rotation. Overall, the initial excess energy available after depopulation of the Franck-Condon region is sufficient to populate the $\mathbf{Ax}$, $\mathbf{Bx}$, $\mathbf{Ex}$, and $\mathbf{Fx}$ structures. However, since dihedral rotation barriers are prohibitively large and their relative energies are so high, the $\mathbf{Cx}$ and $\mathbf{Dx}$ isomers are unlikely to be reached.

The discussion of PY101 in Chapter 3 also involved the presentation of a simple non-equilibrium adapted rate model for estimating the kinetics and significance of excited state processes. Since the dynamics of PY101 occur on an isolated S_1 surface, it is an

ideal test case for such simple models. For this model, the computed relative energies and estimated energy barriers served as input, and experimental fluorescence lifetimes were taken into account. The energy-dependent Arrhenius rate constants were then calculated for each reaction pathway, and first order kinetic equations for the model were solved by propagation in time under the initial condition that the population of $\mathbf{Ax} = 1$ at $t = 0$. The results of the obtained kinetics agreed surprisingly well with experimental findings and confirmed the hypotheses previously drawn based on qualtitative inspection of the potential energy surfaces. This is an important result, as the development of simple kinetic models like the one presented here can provide an initial peek into the dynamics of large systems where time-dependent quantum dynamcis simulations can not yet be applied.

In Chapter 4, the fluorescence quenching mechanism of benzaldehyde and its derivatives in water is elucidated. This project was initially motivated by the suspicious fluorescence quenching of aldehyde-substituted distyrylbenzenes and cruciform dialdehyde fluorophores in water, which share benzaldehyde as the smallest structural building block common to them. A previously proposed mechanism for the quenching of the aldehydes in water had suggested that ESPT of a proton on water to the carbonyl oxygen was the culprit. In addition, a backdrop of studies presented two conflicting views on the excited state behavior of benzaldehyde, with some claiming it as a photobase, while information on aldehyde photochemistry as it pertains to organic synthesis indicated that it should act as a hydrogen abstractor. A relaxed scan of the S_1 potential energy surface of benzaldehyde with one explicit water molecule along the proton/hydrogen transfer coordinate was carried out at the TD-DFT/CAM-B3LYP level of theory. The relaxed surface scan provided the initial qualitative confirmation that a the proton/hydrogen transfer process opened up a viable non-radiative decay channel. For further elucidation of the electronic processes along the coordinate, advanced tools for computing the Mulliken populations, attachment/detachment densities, and natural transition orbitals at the ADC(2) level of theory were used. Indeed, benzaldehyde acts as a hydrogen abstactor, and ESHT from water to the aldehyde opens up a non-radiative decay route for the system to relax back down to the ground state.

Having described the quenching mechanism for benzaldehyde in water, the study in Chapter 4 was extended to include larger aldehyde chains, growing the systme from one to four rings. It is suspected that aromatic aldehydes exhibiting a lowest $n\pi^*$ state will undergo ESHT as benzaldehyde does. However, for systems of increasing size, the bright $\pi\pi^*$ state decreased to below the $n\pi^*$ state. For a stilbene-like system of two rings, it is expected that dihedral rotation is a possible quenching route. For the system with three rings, the lowest $\pi\pi^*$ singlet state is practically degenerate with the $n\pi^*$ triplet state, opening up the possibility of intersystem crossing. The results presented in

Chapter 4 provide an in-depth understanding of the fluroescence quenching mechanism of the quintessential benzaldehyde in water, while making far-reaching suggestions for the excited state behavior of related systems. Importantly, the question of whether benzaldehyde is a photobase or a hydrogen-abstractor is setted, having broad implications in the field of organic synthesis.

In Chapter 5, the final study of this dissertation is presented. Here, another flavor of ESPT is studied with the complex excited state properties of novel pyranine-based super-photoacids. These so-called super-photoacids become so acidic upon photoexcitation that their excited-state pK_a^* values are < 0. The photoacids studied here are based on the commonly-investigated 8-hydroxypyrene-1,3,6-trisulfonate, or **HPTS**. Among this series of pyranine-based photoacids, the strongest photoacids were those with the most electron-withdrawing substituents. In addition, a large change in the permanent dipole moment of the photoacids upon excitation hinted that charge transfer leading to enhanced photoacidity likely occurs before acid dissociation. Going off of these initial results, the static excited state properties of the photoacids were computed for the lowest 20 singlet electronically excited states of the photoacids. Excited state descriptors at the TD-DFT level of theory were calculated for better indication of the presence of charge transfer excited states. It was found that in the weaker photoacids, excited states exhibiting substantial charge transfer from the substituents to the core were significantly lower-lying than in the stronger photoacids. This provides an initial hint that these states may hinder the ESPT process in the weaker photoacids.

Single point calculations along the acid dissociation coordinate of the simplest photoacid **HPTA** with a $pK_a^* = -1$ revealed the presence of another high-lying state of strong charge transfer character from the solvent molecule moeity to the conjugate-basic oxygen of **HPTA**. This state crossed down as dissociation progressed, eventually taking on the S_1 position. Two scenarios had been previously reported to explain the differing photoacidities of the series. The first was that charge transfer states move down below the S_1 as a result of solvent relaxation, meaning that ESPT could only occur via thermal depopulation of these states within the fluorescence lifetime. The second hypothesis was that the charge transfer states mix with the S_1 and thereby partially transfer their characters. The former scenario most closely matches what was observed on the basis of the single point calculations, and indeed this state did not decrease strongly to below the S_1 in the case of a stronger photoacid derivative than **HPTA**. Still, while one may postulate that this state hinders the ESPT process in weaker photoacids, this excited state behavior was not reflected in relaxed surface scans of the **HPTA** ESPT coordinate to an explicit water molecule. Therefore, more investigation is necessary to fully understand the complex excited state properties and behaviors of the photoacid series, and several promising suggestions are presented at the end of Chapter 5.

Over the course of this work, cutting-edge advancements in quantum chemical methods were applied for treating the excited state proton transfer processes in three very different photochemical scenarios. The TD-DFT in conjunction with more advanced methods like ADC, along with transition and difference density matrix analysis, allows for an in-depth look at the proton and charge transfer processes in a variety of systems of industrial and biological relevance. Another important advancement was applied in Chapter 5, where excited state descriptors based on the exciton wave function were used to reveal more information regarding the charge transfer states so important to pyranine-based photoacid properties. Still, some shortcomings linger. For example, the development of further kinetic rate models like the one presented in Chapter 2, or the extension of time-dependent quantum dynamics simulations to larger systems, present important future challenges. Still, the fervor of research into developing more advanced computational methodologies with farther-reaching applicabilities is promising, and the detail to which one can describe the electronic picture of such a variety of systems and processes already is exemplified in this work.

Bibliography

(1) *Proton-Transfer Reactions*; Caldin, E., Gold, V., Eds.; Springer Science+Business Media: Dordrecht, 1975.

(2) Gutman, M.; Nachliel, E. *Biochim. Biophys. Acta (BBA) - Bioenergetics* **1990**, *1015*, 391–414.

(3) Gerlt, J. A.; Gassman, P. G. *Biochemistry* **1993**, *32*, 11943–11952.

(4) Borgis, D.; Hynes, J. T. In *The Enzyme Catalysis Process: Energetics, Mechanism and Dynamics*; Cooper, A., Houben, J. L., Chien, L. C., Eds.; Springer US: Boston, 1989, pp 293–303.

(5) Bender, M. L.; Kézdy, F. J. In *Proton-Transfer Reactions*; Caldin, E., Gold, V., Eds.; Springer Science+Business Media: Dordrecht, 1975, pp 385–409.

(6) Jarczewski, A.; Hubbard, C. D. *J. Mol. Struct.* **2003**, *649*, 287–307.

(7) Blomberg, M. R. A.; Siegbahn, P. E. M. *Biochim. Biophys. Acta (BBA) - Bioenergetics* **2006**, *1757*, 969–980.

(8) Ishikita, H.; Saito, K. *J. R. Soc. Interface* **2013**, *11*, 20130518.

(9) Capitanio, N.; Capitanio, G.; De Nitto, E.; Boffoli, D.; Papa, S. *Biochemistry* **2003**, *42*, 4607–4612.

(10) Klán, P.; Wirz, J. *Photochemistry of Organic Compounds: From Concepts to Practice*; John Wiley & Sons: West Sussex, 2009.

(11) Liu, Y.-A.; Roca-Sanjuán, D.; Lindh, R. *Photochemistry* **2012**, *40*, 42–72.

(12) Brogaard, R. Y. Molecular Conformation and Organic Photochemistry: Time-resolved Photoionization Studies. Ph.D. Thesis, University of Copenhagen, 2012.

(13) Olivucci, M. *Computational Photochemistry*; Elsevier: Amsterdam, 2005; Vol. 16.

(14) Tsien, R. Y. *Annu. Rev. Biochem.* **1998**, *67*, 509–544.

(15) Stoner-Ma, D.; Jaye, A. A.; Matousek, P.; Towrie, M.; Meech, S. R.; Tonge, P. J. *J. Am. Chem. Soc.* **2005**, *127*, 2864–2865.

(16) Shu, X.; Leiderman, P.; Gepshtein, R.; Smith, N. R.; Kallio, K.; Huppert, D.; Remington, S. J. *Protein Sci.* **2007**, *16*, 2703–2710.

(17) Ormö, M.; Cubitt, A. B.; Kallio, K.; Gross, L. A.; Tsien, R. Y.; Remington, S. J. *Science* **1996**, *273*, 1392–1395.

(18) Sengupta, P. K.; Kasha, M. *Chem. Phys. Lett.* **1979**, *68*, 382–385.

(19) Das, R.; Mitra, S.; Nath, D.; Mukherjee, S. *J. Phys. Chem.* **1996**, *100*, 14514–14519.

(20) Sytnik, A.; Del Valle, J. C. *J. Phys. Chem.* **1995**, *99*, 13028–13032.

(21) Sytnik, A.; Kasha, M. *Proc. Nat. Acad. Sci. U.S.A.* **1994**, *91*, 8627–8630.

(22) Sytnik, A.; Gormin, D.; Kasha, M. *Proc. Nat. Acad. Sci. U.S.A.* **1994**, *91*, 11968–11972.

(23) Sytnik, A.; Litvinyuk, I. *Proc. Nat. Acad. Sci. U.S.A.* **1996**, *93*, 12959–12963.

(24) Heller, H. J.; Blattmann, H. R. *Pure Appl. Chem.* **1973**, *36*, 141–161.

(25) Williams, D. L.; Heller, A. *J. Phys. Chem.* **1970**, *74*, 4473–4480.

(26) Zhao, J.; Ji, S.; Chen, Y.; Guo, H.; Yang, P. *Phys. Chem. Chem. Phys.* **2012**, *14*, 8803–8817.

(27) Tang, K.-C.; Chang, M.-J.; Lin, T.-Y.; Pan, H.-A.; Fang, T.-C.; Chen, K.-Y.; Hung, W.-Y.; Hsu, Y.-H.; Chou, P.-T. *J. Am. Chem. Soc.* **2011**, *133*, 17738–17745.

(28) Scheiner, S. *J. Phys. Chem. A* **2000**, *104*, 5898–5909.

(29) Weller, A. *Z. Phys. Chem. (Munich)* **1958**, *17*, 224–245.

(30) *Ultrafast Hydrogen Bonding Dynamics and Proton Transfer Processes in the Condensed Phase*; Elsaesser, T., Bakker, H. J., Eds.; Kluwer Academic: Dordrecht, 2002.

(31) Förster, T. *Z. Elektrochem.* **1950**, *54*, 531.

(32) Runge, E.; Gross, E. K. U. *Phys. Rev. Lett.* **1984**, *52*, 997–1000.

(33) Casida, M. E. In *Recent Advances in Density Functional Methods, Part I*; Chong, D. P., Ed.; World Scientific: Singapore, 1995, pp 155–192.

(34) Dreuw, A.; Head-Gordon, M. *Chem. Rev.* **2005**, *105*, 4009–4037.

(35) Schirmer, J. *Phys. Rev. A* **1982**, *26*, 2395–2416.

(36) Mertins, F.; Schirmer, J. *Phys. Rev. A* **1996**, *53*, 2140–2152.

(37) Trofimov, A. B.; Schirmer, J *J. Phys. B: At. Mol. Opt. Phys.* **1995**, *28*, 2299–2324.

(38) Trofimov, A. B.; Stelter, G.; Schirmer, J. *J. Chem. Phys.* **1999**, *111*, 9982–9999.

(39) Dreuw, A.; Plötner, J.; Lorenz, L.; Wachtveitl, J.; Djanhan, J. E.; Brüning, J.; Metz, T.; Bolte, M.; Schmidt, M. U. *Angew. Chem. Int. Ed.* **2005**, *44*, 7783–7786.

(40) Plötner, J.; Dreuw, A. *Phys. Chem. Chem. Phys.* **2006**, *8*, 1197–1204.

(41) Lorenz, L.; Plötner, J.; Matylitsky, V. V.; Dreuw, A.; Wachtveitl, J. *J. Phys. Chem. A* **2007**, *111*, 10891–10898.

(42) Plötner, J.; Dreuw, A. *Chem. Phys.* **2008**, *347*, 472–482.

(43) Dopfer, O.; Patzer, A.; Chakraborty, S.; Alata, I.; Omidyan, R.; Broquier, M.; Dedonder, C.; Jouvet, C. *J. Chem. Phys.* **2014**, *140* Art. 124314.

(44) Kumpf, J.; Bunz, U. H. F. *Chem. Eur. J.* **2012**, *18*, 8921–8924.

(45) Spies, C.; Finkler, B.; Acar, N.; Jung, G. *Phys. Chem. Chem. Phys.* **2013**, *15*, 19893–19905.

(46) Spies, C.; Shomer, S.; Finkler, B.; Pines, D.; Pines, E.; Jung, G.; Huppert, D. *Phys. Chem. Chem. Phys.* **2014**, *16*, 9104–9114.

(47) Finkler, B.; Spies, C.; Vester, M.; Walte, F.; Omlor, K.; Riemann, I.; Zimmer, M.; Stracke, F.; Gerhards, M.; Jung, G. *Photochem. Photobiol. Sci.* **2014**, *13*, 548–562.

(48) Harbach, P. H. P. Development and Application of Efficient Theoretical Approaches to Molecular Systems in Photochemistry. Ph.D. Thesis, Ruprecht-Karls Universität Heidelberg, April 2013.

(49) Schrödinger, E. *Phys. Rev.* **1926**, *28*, 1049–1070.

(50) Born, M.; Oppenheimer, R. *Ann. Phys.* **1927**, *389*, 457–484.

(51) Szabo, A.; Ostlund, N. S. *Modern Quantum Chemistry: Introduction to Advanced Electronic Structure Theory*; Dover Publications: Mineola, 1996.

(52) McWeeny, R.; Sutcliffe, B. T. *Methods in Molecular Quantum Mechanics*; Academic Press: London, 1969.

(53) Cramer, C. J. *Essentials of Computational Chemistry*; John Wiley & Sons, Ltd, 2004.

(54) Fernández, F. M. *Introduction to Perturbation Theory in Quantum Mechanics*; CRC press, 2000.

(55) Møller, C.; Plesset, M. S. *Phys. Rev.* **1934**, *46*, 618–622.

(56) Schrödinger, E. *Ann. d. Phys.* **1926**, *385*, 437–490.

(57) Nesbet, R. K. *Proc. R. Soc. A* **1955**, *230*, 312–321.

(58)   Löwdin, P.-O. *Adv. Chem. Phys.* **1959**, *2*, 207–322.

(59)   Bartlett, R. J.; Musiał, M. *Rev. Mod. Phys.* **2007**, *79*, 291–352.

(60)   Schirmer, J.; Trofimov, A. B. *J. Chem. Phys.* **2004**, *120*, 11449–11464.

(61)   Hohenberg, P.; Kohn, W. *Phys. Rev.* **1964**, *136*, B864–B871.

(62)   Kohn, W.; Sham, L. J. *Phys. Rev.* **1965**, *140*, A1133–A1138.

(63)   Sholl, D.; Steckel, J. A. *Density Functional Theory: a Practical Introduction*; John Wiley & Sons: Hoboken, 2009.

(64)   Parr, R. G.; Yang, W. *Density-Functional Theory of Atoms and Molecules*; Oxford Science Publication: New York, 1989.

(65)   Gross, E. K. U.; Dreizler, R. M. *Density Functional Theory*; Springer Science & Business Media: New York, 2013; Vol. 337.

(66)   Baerends, E. J.; Gritsenko, O. V. *J. Phys. Chem. A* **1997**, *101*, 5383–5403.

(67)   Wormit, M. Development and Application of Reliable Methods for the Calculation of Excited States: From Light-Harvesting Complexes to Medium-Sized Molecules. Ph.D. Thesis, Johann Wolfgang Goethe-Universität, January 2009.

(68)   Yarkony, D. R. In *Conical Intersections: Electronic Structure, Dynamics, and Spectroscopy*; W. Domcke, H. K., D. R. Yarkony, Ed.; World Scientific Publishing CO. Pte. Ltd.: Singapore, 2004.

(69)   Keal, T. W.; Koslowski, A.; Thiel, W. *Theor. Chem. Acc.* **2007**, *118*, 837–844.

(70)   Gupta, V. P. *Principles and Applications of Quantum Chemistry*; Academic Press: London, 2015.

(71)   Yarkony, D. R. *J. Phys. Chem. A* **2001**, *105*, 6277–6293.

(72)   Levine, B. G.; Coe, J. D.; Martínez, T. J. *J. Phys. Chem. B* **2008**, *112*, 405–413.

(73)   Maeda, S.; Ohno, K.; Morokuma, K. *J. Chem. Theory Comput.* **2010**, *6*, 1538–1545.

(74)   Bene, J. E. D.; Ditchfield, R.; Pople, J. A. *J. Chem. Phys.* **1971**, *55*, 2236–2241.

(75)   Foresman, J. B.; Head-Gordon, M.; Pople, J. A.; Frisch, M. J. *J. Phys. Chem.* **1992**, *96*, 135–149.

(76)   Levine, B. G.; Ko, C.; Quenneville, J.; Martínez, T. J. *Molecular Physics* **2006**, *104*, 1039–1051.

(77)   Minezawa, N.; Gordon, M. S. *J. Phys. Chem. A* **2011**, *115*, 7901–7911.

(78)   Zhang, X.; Herbert, J. M. *J. Chem. Phys.* **2014**, *141* Art. 064104.

(79)   Zhang, X.; Herbert, J. M. *J. Phys. Chem. B* **2014**, *118*, 7806–7817.

(80) Slater, J. C. *The Self-consistent Field for Molecules and Solids*; McGraw-Hill: New York, 1974; Vol. 4.

(81) *Modern Ideas in Coupled-Cluster Methods*; Bartlett, R. J., Ed.; World Scientific: Singapore, 1997.

(82) Laidig, W. D.; Bartlett, R. J. *Chem. Phys. Lett.* **1984**, *104*, 424–430.

(83) Grimme, S.; Waletzke, M. *J. Chem. Phys.* **1999**, *111*, 5645–5655.

(84) Strodel, P.; Tavan, P. *J. Chem. Phys.* **2002**, *117*, 4667–4676.

(85) Strodel, P.; Tavan, P. *J. Chem. Phys.* **2002**, *117*, 4677–4683.

(86) Pauli, W. *Z. Phys.* **1925**, *31*, 765–783.

(87) Ramachandran, K. I.; Deepa, G.; Namboori, K. *Computational Chemistry and Molecular Modeling: Principles and Applications*; Springer-Verlag: Berlin Heidelberg, 2008.

(88) Ritz, W. *J. Reine Angew. Math.* **1909**, *135*, 1–61.

(89) Ramana, B. V. *Higher Engineering Mathematics*; Tata McGraw-Hill: New Delhi, 2008.

(90) Gustafson, S. J.; Sigal, I. M. In *Mathematical Concepts of Quantum Mechanics*; Springer Berlin Heidelberg: Berlin, Heidelberg, 2011, pp 209–226.

(91) Berazin, F. A. *The Method of Second Quantization*; Academic Press: New York, 1966.

(92) Head-Gordon, M.; Rico, R. J.; Oumi, M.; Lee, T. J. *Chem. Phys. Lett.* **1994**, *219*, 21–29.

(93) Monkhorst, H. J. *Int. J. Quantum Chem.* **1977**, *12*, 421–432.

(94) Mukherjee, D.; Mukherjee, P. K. *Chem. Phys.* **1979**, *39*, 325–335.

(95) Koch, H.; Jørgensen, P. *J. Chem. Phys.* **1990**, *93*, 3333–3344.

(96) Emrich, K. *Nucl. Phys. A* **1981**, *351*, 379–396.

(97) Stanton, J. F.; Bartlett, R. J. *J. Chem. Phys.* **1993**, *98*, 7029–7039.

(98) Koch, H.; Kobayashi, R.; Merás, A. Sanchez de; Jørgensen, P. *J. Chem. Phys.* **1994**, *100*, 4393–4400.

(99) Kállay, M.; Gauss, J. *J. Chem. Phys.* **2004**, *121*, 9257–9269.

(100) Christiansen, O.; Koch, H.; Jørgensen, P. *Chem. Phys. Lett.* **1995**, *243*, 409–418.

(101) Hättig, C.; Weigend, F. *J. Chem. Phys.* **2000**, *113*, 5154–5161.

(102) Hellweg, A.; Grün, S. A.; Hättig, C. *Phys. Chem. Chem. Phys.* **2008**, *10*, 4119–4127.

(103) Christiansen, O.; Halkier, A.; Koch, H.; Jørgensen, P.; Helgaker, T. *J. Chem. Phys.* **1998**, *108*, 2801–2816.

(104) Christiansen, O.; Gauss, J.; Stanton, J. F.; Jørgensen, P. *J. Chem. Phys.* **1999**, *111*, 525–537.

(105) Bartlett, R. J. *Ann. Rev. Phys. Chem.* **1981**, *32*, 359–401.

(106) Dreuw, A.; Wormit, M. *WIREs Comput. Mol. Sci.* **2015**, *5*, 82–95.

(107) Kiełbasiński, A.; Schwetlik, H. *Numerische Lineare Algebra. Eine Computerorientierte Einführung*; Deutscher Verlag der Wissenschaften: Berlin, 1988.

(108) Pople, J. A.; Binkley, J. S.; Seeger, R. *Int. J. Quant. Chem. Symp.* **1976**, *10*, 1–19.

(109) Schirmer, J. *Phys. Rev. A* **1991**, *43*, 4647–4659.

(110) Harbach, P. H. P.; Wormit, M.; Dreuw, A. *J. Chem. Phys.* **2014**, *141* Art. 064113.

(111) Thomas, L. H. *Math. Proc. Cambridge* **1927**, *23*, 542–548.

(112) Fermi, E. *Atti Accad. Naz. Lincei* **1927**, *6*, 602–607.

(113) Dirac, P. A. M. *Math. Proc. Cambridge* **1930**, *26*, 376–385.

(114) *Energy Density Functional Theory of Many-Electron Systems*; Kryachko, E. S., Ludeña, E. V., Eds.; Kluwer Academic Publishers: Dordrecht, 2002.

(115) Rushton, P. P. Towards a Non-Local Density Functional Description of Exchange and Correlation. Ph.D. Thesis, University of Durham, November 2002.

(116) Slater, J. C. *Phys. Rev.* **1951**, *81*, 385–390.

(117) Becke, A. D. *J. Chem. Phys.* **1993**, *98*, 5648–5652.

(118) Becke, A. D. *J. Chem. Phys.* **1993**, *98*, 1372–1377.

(119) Tao, J.; Perdew, J. P.; Staroverov, V. N.; Scuseria, G. E. *Phys. Rev. Lett.* **2003**, *91*, 146401.

(120) Grimme, S. *J. Comput. Chem.* **2006**, *27*, 1787–1799.

(121) Yabana, K.; Bertsch, G. F. *Phys. Rev. B* **1996**, *54*, 4484–4487.

(122) Marques, M. A. L.; Castro, A.; Bertsch, G. F.; Rubio, A. *Comput. Phys. Commun.* **2003**, *151*, 60.

(123) Furche, F. *J. Chem. Phys.* **2001**, *114*, 5982.

(124) Hirata, S.; Head-Gordon, M. *Chem. Phys. Lett.* **1999**, *314*, 291–299.

(125) Eichkorn, K.; Treutler, O.; Öhm, H.; Häser, M.; Ahlrichs, R. *Chem. Phys. Lett.* **1995**, *240*, 283–290.

(126) Jamorski, C.; Casida, M. E.; Salahub, D. R. *J. Chem. Phys.* **1996**, *104*, 5134–5147.

(127) Bauernschmitt, R.; Häser, M.; Treutler, O.; Ahlrichs, R. *Chem. Phys. Lett.* **1997**, *264*, 573–578.

(128) Dierksen, M.; Grimme, S. *J. Chem. Phys.* **2004**, *120*, 3544–3554.

(129) Cai, Z.-L.; Sendt, K.; Reimers, J. R. *J. Chem. Phys.* **2002**, *117*, 5543–5549.

(130) Grimme, S.; Parac, M. *ChemPhysChem* **2003**, *4*, 292–295.

(131) Dreuw, A.; Weisman, J. L.; Head-Gordon, M. *J. Chem. Phys.* **2003**, *119*, 2943–2946.

(132) Dreuw, A.; Head-Gordon, M. *J. Am. Chem. Soc* **2004**, *126*, 4007–4016.

(133) Magyar, R. J.; Tretiak, S. *J. Chem. Theor. Comput.* **2007**, *3*, 976–987.

(134) Tozer, D. J.; Amos, R. D.; Handy, N. C.; Roos, B. O.; Serrano-Andres, L. *Mol. Phys.* **1999**, *97*, 859–868.

(135) Tozer, D. J. *J. Chem. Phys.* **2003**, *119*, 12697–12699.

(136) Perdew, J. P.; Parr, R. G.; Levy, M.; Balduz, J. L. *Phys. Rev. Lett.* **1982**, *49*, 1691–1694.

(137) Plötner, J.; Tozer, D. J.; Dreuw, A. *J. Chem. Theory Comput.* **2010**, *6*, 2315–2324.

(138) Peach, M. J. G.; Benfield, P.; Helgaker, T.; Tozer, D. J. *J. Chem. Phys.* **2008**, *128* Art. 044118.

(139) Peach, M. J. G.; Le Sueur, C. R.; Ruud, K.; Guillaume, M.; Tozer, D. J. *Phys. Chem. Chem. Phys.* **2009**, *11*, 4465–4470.

(140) Wiggins, P.; Williams, J. A. G.; Tozer, D. J. *J. Chem. Phys.* **2009**, *131* Art. 091101.

(141) Yanai, T.; Tew, D. P.; Handy, N. C. *Chem. Phys. Lett.* **2004**, *393*, 51–57.

(142) Chang, R. *Physical Chemistry for the Chemical and Biological Sciences*; University Science Books: Sausalito, 2000.

(143) Willock, D. J. *Molecular Symmetry*; John Wiley and Sons, Ltd: West Sussex, 2009.

(144) Harris, D. C.; Bertolucci, M. D. *Symmetry and Spectroscopy: An Introduction to Vibrational and Electronic Spectroscopy*; Dover Publications: Mineola, 1989.

(145) Turro, N. J.; Ramamurthy, V.; Scaiano, J. C. *Principles of Molecular Photochemistry: An Introduction*; University Science Books: Sausalito, 2009.

(146) Amos, A. T.; Hall, G. G. *Proc. R. Soc. A* **1961**, *263*, 483–493.

(147) Luzanov, A. V.; Sukhorukov, A. A.; Umanskii, V. É. *Theor. Exp. Chem.* **1976**, *10*, 354–361.

(148) Martin, R. L. *J. Chem. Phys.* **2003**, *118*, 4775–4777.

(149) Mayer, I. *Chem. Phys. Lett.* **2007**, *437*, 284–286.

(150) Plasser, F.; Wormit, M.; Dreuw, A. *J. Chem. Phys.* **2014**, *141* Art. 024106.

(151) Climent, T.; González-Luque, R.; Merchán, M. *J. Phys. Chem. A* **2003**, *107*, 6995–7003.

(152) Serrano-Andrés, L.; Merchán, M.; Jabłoński, M. *J. Chem. Phys.* **2003**, *119*, 4294–4304.

(153) Wiberg, K. B.; Hadad, C. M.; Foresman, J. B.; Chupka, W. A. *J. Phys. Chem.* **1992**, *96*, 10756–10768.

(154) Molina, V.; Merchán, M. *J. Phys. Chem. A* **2001**, *105*, 3745–3751.

(155) Head-Gordon, M.; Grana, A. M.; Maurice, D.; White, C. A. *J. Phys. Chem.* **1995**, *99*, 14261–14270.

(156) Grana, A. M.; Lee, T. J.; Head-Gordon, M. *J. Phys. Chem.* **1995**, *99*, 3493–3502.

(157) Halasinski, T. M.; Weisman, J. L.; Ruiterkamp, R.; Lee, T. J.; Salama, F.; Head-Gordon, M. *J. Phys. Chem. A* **2003**, *107*, 3660–3669.

(158) Vaswani, H. M.; Hsu, C.-P.; Head-Gordon, M.; Fleming, G. R. *J. Phys. Chem. B* **2003**, *107*, 7940–7946.

(159) Weisman, J. L.; Head-Gordon, M. *J. Am. Chem. Soc.* **2001**, *123*, 11686–11694.

(160) Oumi, M.; Maurice, D.; Head-Gordon, M. *Spectrochim. Acta Mol. Biomol. Spectrosc.* **1999**, *55*, 525–537.

(161) Reichardt, C. *Solvents and Solvent Effects in Organic Chemistry, 2nd ed.* Wiley-VCH: Weinheim, 1988.

(162) Rivail, J.-L.; Rinaldi, D. In *Computational Chemistry: Review of Current Trends*; Leszczynski, J., Ed.; World Scientific: Singapore, 1995.

(163) Cramer, C. J.; Truhlar, D. G. In *Solvent Effects and Chemical Reactivity*; Tapia, O., Bertrán, J., Eds.; Kluwer Academic Press: Dordrecht, 1996.

(164) Friesner, R. A.; V. Guallar, V. *Annu. Rev. Phys. Chem.* **2005**, *56*, 389–427.

(165) Lin, H.; Truhlar, D. G. *Theor. Chem. Acc.* **2007**, *117*, 185–199.

(166) Senn, H. M.; Thiel, W. *Curr. Opin. Chem. Biol.* **2007**, *11*, 182–187.

(167) Tomasi, J.; Persico, M. *Chem. Rev.* **1994**, *94*, 2027–2094.

(168) Cramer, C. J.; Truhlar, D. G. *Chem. Rev.* **1999**, *99*, 2161–2200.

(169) Li, J.; Zhu, T.; Cramer, C. J.; Truhlar, D. G. *J. Phys. Chem. A* **2000**, *104*, 2178–2182.

(170) Dolney, D. M.; Hawkins, G. D.; Winget, P.; Liotard, D. A.; Cramer, C. J.; Truhlar, D. G. *J. Comput. Chem.* **2000**, *21*, 340–366.

(171) Tomasi, J.; Mennucci, B.; Laug, P. In *Essential Computational Modeling in Chemistry*; Ciarlet, P. G., Bris, C. L., Eds.; Elsevier: Oxford, 2011, pp 5–100.

(172) Mennucci, B. *WIREs Comput. Mol. Sci.* **2012**, *2*, 386–404.

(173) Miertuš, S.; Scrocco, E.; Tomasi, J. *Chem. Phys.* **1981**, *55*, 117–129.

(174) Foresman, J. B.; Keith, T. A.; Wiberg, K. B.; Snoonian, J.; Frisch, M. J. *J. Phys. Chem.* **1996**, *100*, 16098–16104.

(175) Miertuš, S.; Tomasi, J. *Chem. Phys.* **1982**, *65*, 239–245.

(176) Pascual-ahuir, J. L.; Silla, E.; Tuñon, I. *J. Comput. Chem.* **1994**, *15*, 1127–1138.

(177) Cossi, M.; Barone, V.; Cammi, R.; Tomasi, J. *Chem. Phys. Lett.* **1996**, *255*, 327–335.

(178) Barone, V.; Cossi, M.; Tomasi, J. *J. Chem. Phys.* **1997**, *107*, 3210–3221.

(179) Cancès, E.; Mennucci, B.; Tomasi, J. *J. Chem. Phys.* **1997**, *107*, 3032–3041.

(180) Mennucci, B.; Tomasi, J. *J. Chem. Phys.* **1997**, *106*, 5151–5158.

(181) Mennucci, B.; Cancès, E.; Tomasi, J. *J. Phys. Chem. B* **1997**, *101*, 10506–10517.

(182) Barone, V.; Cossi, M. *J. Phys. Chem. A* **1998**, *102*, 1995–2001.

(183) Cossi, M.; Barone, V.; Mennucci, B.; Tomasi, J. *Chem. Phys. Lett.* **1998**, *286*, 253–260.

(184) Barone, V.; Cossi, M.; Tomasi, J. *J. Comput. Chem.* **1998**, *19*, 404–417.

(185) Cammi, R.; Mennucci, B.; J. Tomasi, J. *J. Phys. Chem. A* **1999**, *103*, 9100–9108.

(186) Cossi, M.; Barone, V.; Robb, M. A. *J. Chem. Phys.* **1999**, *111*, 5295–5302.

(187) Tomasi, J.; Mennucci, B.; Cances, E. *J. Mol. Struc.-THEOCHEM* **1999**, *464*, 211–226.

(188) Cammi, R.; Mennucci, B.; Tomasi, J. *J. Phys. Chem. A* **2000**, *104*, 5631–5637.

(189) Cossi, M.; Barone, V. *J. Chem. Phys.* **2000**, *112*, 2427–2435.

(190) Cossi, M.; Barone, V. *J. Chem. Phys.* **2001**, *115*, 4708–4717.

(191) Cossi, M.; Rega, N.; Scalmani, G.; Barone, V. *J. Chem. Phys.* **2001**, *114*, 5691–5701.

(192) Cossi, M.; Scalmani, G.; Rega, N.; Barone, V. *J. Chem. Phys.* **2002**, *117*, 43–54.

(193) Cossi, M.; Rega, N.; Scalmani, G.; Barone, V. *J. Comput. Chem.* **2003**, *24*, 669–681.

(194) Klamt, A.; Schüürmann, G. *J. Chem. Soc., Perkin Trans. 2* **1993**, 799–805.

(195) Klamt, A. *WIREs Comput. Mol. Sci.* **2011**, *1*, 699–709.

(196) Jackson, J. D. *Classical Electrodynamics*; John Wiley and Sons, 1975.

(197) Erk, P. *Angew. Chem. Int. Ed.* **2004**, *43*, 4393–4394.

(198) Blout, E. R.; Gofstein, R. M. *J. Am. Chem. Soc.* **1945**, *67*, 13–17.

(199) Mathur, S. S.; Suschitzky, H. *J. Chem. Soc., Perkin Trans. 1* **1975**, 2479–2483.

(200) Schapiro, N. *Ber. Dtsch. Chem. Ges. (A and B Series)* **1933**, *66*, 1103–1107.

(201) Marcus, R. A.; Rice, O. K. *J. Phys. Chem.* **1951**, *55*, 894–908.

(202) Marcus, R. A. *J. Chem. Phys* **1952**, *20*, 359–364.

(203) Kozuch, S.; Shaik, S. *Acc. Chem. Res.* **2011**, *44*, 101–110.

(204) Atkins, P. W. *Physikalische Chemie*; Wiley-VCH: Weinheim, 1996.

(205) Fletcher, K.; Dreuw, A.; Faraji, S. *Comp. Theor. Chem.* **2014**, *1040*, 177–185.

(206) Neese, F. *WIREs Comput. Mol. Sci.* **2012**, *2*, 73–78.

(207) Shao, Y. et al. *Phys. Chem. Chem. Phys.* **2006**, *8*, 3172–3191.

(208) Dunning, T. H. *J. Chem. Phys.* **1989**, *90*, 1007–1023.

(209) Hättig, C.; Weigend, F. *J. Chem. Phys.* **2000**, *113*, 5154–5161.

(210) Christiansen, O.; Koch, H.; Jørgensen, P. *Chem. Phys. Lett.* **1995**, *243*, 409–418.

(211) Kendall, R. A.; Dunning, T. H.; Harrison, R. J. *J. Chem. Phys.* **1992**, *96*, 6796–6806.

(212) Woon, D. E.; Dunning, T. H. *J. Chem. Phys.* **1993**, *98*, 1358–1371.

(213) Frisch, M. J. et al. *Gaussian 09 Revision D.01*, Gaussian Inc. Wallingford, CT 2013.

(214) Becke, A. D. *Phys. Rev. A* **1988**, *38*, 3098–3100.

(215) Perdew, J. P. *Phys. Rev. B* **1986**, *34*, 7406.

(216) Ahmedova, A.; Simeonov, S. P.; Kurteva, V. B.; Antonov, L. *Chem. Cent. J.* **2013**, *7*, 1–10.

(217) Barbara, P. F.; Walsh, P. K.; Brus, L. E. *J. Phys. Chem.* **1989**, *93*, 29–34.

(218) Braem, O.; Penfold, T. J.; Cannizzo, A.; Chergui, M. *Phys. Chem. Chem. Phys.* **2012**, *14*, 3513–3519.

(219) Sajadi, M.; Weinberger, M.; Wagenknecht, H.-A.; Ernsting, N. P. *Phys. Chem. Chem. Phys.* **2011**, *13*, 17768–17774.

(220) Kovalenko, S. A.; Schanz, R.; Hennig, H.; Ernsting, N. P. *J. Chem. Phys.* **2001**, *115*, 3256–3273.

(221) Bao, B.; Yuwen, L.; Zheng, X.; Weng, L.; Zhu, X.; Zhan, X.; Wang, L. *J. Mater. Chem.* **2010**, *20*, 9628–9634.

(222) Ajayakumar, M. R.; Mukhopadhyay, P. *Chem. Commun.* **2009**, 3702–3704.

(223) Körsten, S.; Mohr, G. J. *Chem. Eur. J.* **2011**, *17*, 969–975.

(224) Greene, N. T.; Shimizu, K. D. *J. Am. Chem. Soc.* **2005**, *127*, 5695–5700.

(225) Zhou, H.; Baldini, L.; Hong, J.; Wilson, A. J.; Hamilton, A. D. *J. Am. Chem. Soc.* **2006**, *128*, 2421–2425.

(226) Yeh, C.-Y.; Lin, S.-J.; Hwang, D.-F. *J. Food Drug Anal.* **2004**, *12*, 128–132.

(227) Cheng, S. G. G.; Merchant, Z. M. In *Characterization of Food: Emerging Methods*; Gaonkar, A. G., Ed.; Elsevier Science: New York, 1995.

(228) Mohr, G. J.; Demuth, C.; Spichiger-Keller, U. E. *Anal. Chem.* **1998**, *70*, 3868–3873.

(229) Mohr, G. J. *Chem. Eur. J.* **2004**, *10*, 1082–1090.

(230) Rakow, N. A.; Sen, A.; Janzen, M. C.; Ponder, J. B.; Suslick, K. S. *Angew. Chem. Int. Ed.* **2005**, *44*, 4528–4532.

(231) Greene, N. T.; Shimizu, K. D. *J. Am. Chem. Soc.* **2005**, *127*, 5695–5700.

(232) Wiskur, S. L.; Ait-Haddou, H.; Lavigne, J. J.; Anslyn, E. V. *Acc. Chem. Res.* **2001**, *34*, 963–972.

(233) Lavigne, J. J.; Anslyn, E. V. *Angew. Chem. Int. Ed.* **1999**, *38*, 3666–3669.

(234) Nelson, T. L.; O'Sullivan, C.; Greene, N. T.; Maynor, M. S.; Lavigne, J. J. *J. Am. Chem. Soc.* **2006**, *128*, 5640–5641.

(235) Maynor, M. S.; Nelson, T. L.; O'Sullivan, C.; Lavigne, J. J. *Org. Lett.* **2007**, *9*, 3217–3220.

(236) Nelson, T. L.; Tran, I.; Ingallinera, T. G.; Maynor, M. S.; Lavigne, J. J. *Analyst* **2007**, *132*, 1024–1030.

(237) Mertz, E.; Zimmerman, S. C. *J. Am. Chem. Soc.* **2003**, *125*, 3424–3425.

(238) Mertz, E.; Beil, J. B.; Zimmerman, S. C. *Org. Lett.* **2003**, *5*, 3127–3130.

(239) Feuster, E. K.; Glass, T. E. *J. Am. Chem. Soc.* **2003**, *125*, 16174–16175.

(240) Secor, K.; Plante, J.; Avetta, C.; Glass, T. *J. Mater. Chem.* **2005**, *15*, 4073–4077.

(241) Phillips, R. L.; Kim, I.-B.; Tolbert, L. M.; Bunz, U. H. F. *J. Am. Chem. Soc.* **2008**, *130*, 6952–6954.

(242) Freudenberg, J.; Kumpf, J.; Schäfer, V.; Sauter, E.; Wörner, S. J.; Brödner, K.; Dreuw, A.; Bunz, U. H. F. *J. Org. Chem.* **2013**, *78*, 4949–4959.

(243) Zucchero, A. J.; McGrier, P. L.; Bunz, U. H. F. *Acc. Chem. Res.* **2010**, *43*, 397–408.

(244) Hauck, M.; Schönhaber, J.; Zucchero, A. J.; Hardcastle, K. I.; Müller, T. J. J.; Bunz, U. H. F. *J. Org. Chem.* **2007**, *72*, 6714–6725.

(245) Zucchero, A. J.; Wilson, J. N.; Bunz, U. H. F. *J. Am. Chem. Soc.* **2006**, *128*, 11872–11881.

(246) Davey, E. A.; Zucchero, A. J.; Trapp, O.; Bunz, U. H. F. *J. Am. Chem. Soc.* **2011**, *133*, 7716–7718.

(247) Schwaebel, T.; Trapp, O.; Bunz, U. H. F. *Chem. Sci.* **2013**, *4*, 273–281.

(248) Gerhardt, W. W.; Zucchero, A. J.; Wilson, J. N.; South, C. R.; Bunz, U. H. F.; Weck, M. *Chem. Commun.* **2006**, 2141–2143.

(249) Tolosa, J.; Solntsev, K. M.; Tolbert, L. M.; Bunz, U. H. F. *J. Org. Chem.* **2010**, *75*, 523–534.

(250) Tolosa, J.; Zucchero, A. J.; Bunz, U. H. F. *J. Am. Chem. Soc.* **2008**, *130*, 6498–6506.

(251) McGrier, P. L.; Solntsev, K. M.; Miao, S.; Tolbert, L. M.; Miranda, O. R.; Rotello, V. M.; Bunz, U. H. F. *Chem. Eur. J.* **2008**, *14*, 4503–4510.

(252) Görner, H.; Kuhn, H. J. *J. Phys. Chem.* **1986**, *90*, 5946–5955.

(253) Ou, Q.; Subotnik, J. E. *J. Phys. Chem. C* **2013**, *117*, 19839–19849.

(254) Cui, G.; Lu, Y.; Thiel, W. *Chem. Phys. Lett.* **2012**, *537*, 21–26.

(255) Ohmori, N.; Suzuki, T.; Ito, M. *J. Phys. Chem.* **1988**, *92*, 1086–1093.

(256) Park, S. T.; Feenstra, J. S.; Zewail, A. H. *J. Chem. Phys.* **2006**, *124* Art. 174707.

(257) Lower, S. K.; El-Sayed, M. A. *Chem. Rev.* **1966**, *66*, 199–241.

(258) Antol, I.; Eckert-Maksić, M.; Klessinger, M. *J. Mol. Struc.-THEOCHEM* **2003**, *664-665*, 309–317.

(259) Levy, J. B. *Struct. Chem.* **2000**, *11*, 141–144.

(260) Bouchoux, G. *Chem. Phys. Lett.* **2010**, *495*, 192–197.

(261) Alata, I.; Omidyan, R.; Dedonder-Lardeux, C.; Broquier, M.; Jouvet, C. *Phys. Chem. Chem. Phys.* **2009**, *11*, 11479–11486.

(262) Turro, N. J. *Modern Molecular Photochemistry*; University Science Books: Sausalito, 1991.

(263) Formosinho, S. J.; Arnaut, L. G. *Adv. Photochem.* **1991**, *16*, 67–117.

(264) Dauben, W. G.; Salem, L.; Turro, N. J. *Acc. Chem. Res.* **1975**, *8*, 41–54.

(265) Silva, C. R.; Reilly, J. P. *J. Phys. Chem.* **1996**, *100*, 17111–17123.

(266) Walsh, A. D. *Trans. Faraday Soc.* **1946**, *42*, 62–65.

(267) Walsh, A. D. In *Proc. R. Soc. A*, 1947, pp 32–38.

(268) Kimura, K.; Nagakura, S. *Theor. Chim. Acta* **1965**, *3*, 164–173.

(269) Abe, H.; Kamei, S.-i.; Mikami, N.; Ito, M. *Chem. Phys. Lett.* **1984**, *109*, 217–220.

(270) Smolarek, J.; Zwarich, R.; Goodman, L. *J. Mol. Spectrosc.* **1972**, *43*, 416–428.

(271) Chai, J.-D.; Head-Gordon, M. *J. Chem. Phys.* **2008**, *128* Art. 084106.

(272) Cammi, R.; Mennucci, B. *J. Chem. Phys.* **1999**, *110*, 9877–9886.

(273) Lange, A. W.; Herbert, J. M. *J. Chem. Phys.* **2010**, *133* Art. 244111.

(274) Lange, A. W.; Herbert, J. M. *Chem. Phys. Lett.* **2011**, *509*, 77–87.

(275) Krylov, A. I.; Gill, P. M. W. *WIREs Comput. Mol. Sci.* **2013**, *3*, 317–326.

(276) Shao, Y. et al. *Mol. Phys.* **2015**, *113*, 184–215.

(277) Lee, S.-H.; Tang, K.-C.; Chen, I.-C.; Schmitt, M.; Shaffer, J. P.; Schultz, T.; Underwood, J. G.; Zgierski, M. Z.; Stolow, A. *J. Phys. Chem. A* **2002**, *106*, 8979–8991.

(278) Dreuw, A.; Plötner, J.; Wormit, M.; Head-Gordon, M.; Dutoi, A. D. *Z. Phys. Chem.* **2010**, *224*, 311–324.

(279) Cammi, R.; Corni, S.; Mennucci, B.; Tomasi, J. *J. Chem. Phys.* **2005**, *122* Art. 104513.

(280) Caricato, M.; Mennucci, B.; Tomasi, J.; Ingrosso, F.; Cammi, R.; Corni, S.; Scalmani, G. *J. Chem. Phys.* **2006**, *124* Art. 124520.

(281) Mewes, J.-M.; You, Z.-Q.; Wormit, M.; Kriesche, T.; Herbert, J. M.; Dreuw, A. *J. Phys. Chem. A* **2015**, *119*, 5446–5464.

(282) Sham, Y. Y.; Joens, J. A. *Spectrochim. Acta Mol. Biomol. Spectrosc.* **1995**, *51*, 247–251.

(283) Kasha, M. *Discuss. Faraday Soc.* **1950**, *9*, 14–19.

(284) Beer, M.; Longuet-Higgins, H. C. *J. Chem. Phys.* **1955**, *23*, 1390.

(285) Hirata, Y.; Lim, E. C. *J. Chem. Phys.* **1978**, *69*, 3292–3296.

(286) Murata, S.; Iwanaga, C.; Toda, T.; Kokubun, H. *Chem. Phys. Lett.* **1972**, *13*, 101–104.

(287) Viswanath, G.; Kasha, M. *J. Chem. Phys.* **1956**, *24*, 574–577.

(288) Poole, J. A.; Dhingra, R. C.; Gelernt, B. *J. Chem. Phys.* **1970**, *52*, 464–465.

(289) Köhler, A.; Bässler, H. *Electronic Processes in Organic Semiconductors: An Introduction*; Wiley-VCH Verlag GmbH & Co. KGaA.: Weinheim, 2015.

(290) Kisch, H. *Semiconductor Photocatalysis: Principles and Applications*; Wiley-VCH Verlag GmbH &Co. KGaA: Weinheim, 2015.

(291) Kwok, W.-M.; Ma, C.; Phillips, D. L. *J. Am. Chem. Soc.* **2006**, *128*, 11894–11905.

(292) Buchvarov, I.; Wang, Q.; Raytchev, M.; Trifonov, A.; Fiebig, T. *Proc. Natl. Acad. Sci.* **2007**, *104*, 4794–4797.

(293) Vayá, I.; Miannay, F.-A.; Gustavsson, T.; Markovitsi, D. *Chem. Phys. Chem.* **2010**, *11*, 987–989.

(294) Kim, J.-M.; Chang, T.-E.; Kang, J.-H.; Park, K. H.; Han, D.-K.; Ahn, K.-D. *Angew. Chem. Int. Ed.* **2000**, *39*, 1780–1782.

(295) Lee, I.; Kim, C. K.; Lee, I. Y.; Kim, C. K. *J. Phys. Chem. A* **2000**, *104*, 6332–6337.

(296) Lasne, J.; Laffon, C.; Parent, P. *Phys. Chem. Chem. Phys.* **2012**, *14*, 15715–15721.

(297) Hochstrasser, R. M. *Pure Appl. Chem.* **1980**, *52*, 2683–2691.

(298) Lewis, G. N.; Magel, T. T.; Lipkin, D. *J. Am. Chem. Soc.* **1940**, *62*, 2973–2980.

(299) Waldeck, D. H. *Chem. Rev.* **1991**, *91*, 415–436.

(300) Saltiel, J. *J. Am. Chem. Soc.* **1967**, *89*, 1036–1037.

(301) Saltiel, J. *J. Am. Chem. Soc.* **1968**, *90*, 6394–6400.

(302) Syage, J. A.; Lambert, W. R.; Felker, P. M.; Zewail, A. H.; Hochstrasser, R. M. *Chem. Phys. Lett.* **1982**, *88*, 266–270.

(303) Greene, B. I.; Farrow, R. C. *J. Chem. Phys.* **1983**, *78*, 3336–3338.

(304) Myers, A. B.; Mathies, R. A. *J. Chem. Phys.* **1984**, *81*, 1552–1558.

(305) Syage, J. A.; Felker, P. M.; Zewail, A. H. *J. Chem. Phys.* **1984**, *81*, 4706–4723.

(306) Abrash, S.; Repinec, S.; Hochstrasser, R. M. *J. Chem. Phys.* **1990**, *93*, 1041–1053.

(307) Todd, D. C.; Jean, J. M.; Rosenthal, S. J.; Ruggiero, A. J.; Yang, D.; Fleming, G. R. *J. Chem. Phys.* **1990**, *93*, 8658–8668.

(308) Frederick, J. H.; Fujiwara, Y.; Penn, J. H.; Yoshihara, K.; Petek, H. *J. Phys. Chem.* **1991**, *95*, 2845–2858.

(309) Pedersen, S.; Bañares, L.; Zewail, A. H. *J. Chem. Phys.* **1992**, *97*, 8801–8804.

(310) Baskin, J. S.; Bañares, L.; Pedersen, S.; Zewail, A. H. *J. Phys. Chem.* **1996**, *100*, 11920–11933.

(311) Baumert, T.; Frohnmeyer, T.; Kiefer, B.; Niklaus, P.; Strehle, M.; Gerber, G.; Zewail, A. H. *Appl. Phys. B* **2001**, *72*, 105–108.

(312) Fuß, W.; Kosmidis, C.; Schmid, W. E.; Trushin, S. A. *Angew. Chem. Int. Ed.* **2004**, *43*, 4178–4182.

(313) Dietl, C.; Papastathopoulos, E.; Niklaus, P.; Improta, R.; Santoro, F.; Gerber, G. *Chem. Phys.* **2005**, *310*, 201–211.

(314) Takeuchi, S.; Ruhman, S.; Tsuneda, T.; Chiba, M.; Taketsugu, T.; Tahara, T. *Science* **2008**, *322*, 1073–1077.

(315) Orlandi, G.; Siebrand, W. *Chem. Phys. Lett.* **1975**, *30*, 352–354.

(316) Vachev, V. D.; Frederick, J. H.; Grishanin, B. A.; Zadkov, V. N.; Koroteev, N. I. *J. Phys. Chem.* **1995**, *99*, 5247–5263.

(317) Bolton, K.; Nordholm, S. *Chem. Phys.* **1996**, *203*, 101–126.

(318) Bearpark, M. J.; Bernardi, F.; Clifford, S.; Olivucci, M.; Robb, M. A.; Vreven, T. *J. Phys. Chem. A* **1997**, *101*, 3841–3847.

(319) Berweger, C. D.; van Gunsteren, W. F.; Müller-Plathe, F. *J. Chem. Phys.* **1998**, *108*, 8773–8781.

(320) Molina, V.; Merchán, M.; Roos, B. O. *Spectrochim. Acta Mol. Biomol. Spectrosc.* **1999**, *55*, 433–446.

(321) Kwasniewski, S. P.; Claes, L.; François, J.-P.; Deleuze, M. S. *J. Chem. Phys.* **2003**, *118*, 7823–7836.

(322) Quenneville, J.; Martínez, T. J. *J. Phys. Chem. A* **2003**, *107*, 829–837.

(323) Leitner, D. M.; Levine, B.; Quenneville, J.; Martínez, T. J.; Wolynes, P. G. *J. Phys. Chem. A* **2003**, *107*, 10706–10716.

(324) Improta, R.; Santoro, F. *J. Phys. Chem. A* **2005**, *109*, 10058–10067.

(325) Debnarova, A.; Techert, S.; Schmatz, S. *J. Chem. Phys.* **2006**, *125* Art. 224101.

(326) Dou, Y.; Allen, R. E. *Chem. Phys. Lett.* **2003**, *378*, 323–329.

(327) Dou, Y.; Allen, R. E. *J. Chem. Phys.* **2003**, *119*, 10658–10666.

(328) Dou, Y.; Allen, R. E. *J. Mod. Opt.* **2004**, *51*, 2485–2491.

(329) Sauer, P.; Allen, R. E. *Chem. Phys. Lett.* **2007**, *434*, 260–264.

(330) Dou, Y.; Wu, W.; Tang, H.; Allen, R. E. *Chem. Phys.* **2008**, *353*, 104–108.

(331) Jiang, C.; Xie, R.; Li, F.; Allen, R. E. *Chem. Phys. Lett.* **2009**, *474*, 263–267.

(332) Lewis, F. D.; Sinks, L. E.; Weigel, W.; Sajimon, M. C.; Crompton, E. M. *J. Phys. Chem. A* **2005**, *109*, 2443–2451.

(333) Freitas, A. A.; Quina, F. H.; Maçanita, A. A. L. *J. Phys. Chem. A* **2011**, *115*, 10988–10995.

(334) Gould, E.-A.; Popov, A. V.; Tolbert, L. M.; Presiado, I.; Erez, Y.; Huppert, D.; Solntsev, K. M. *Phys. Chem. Chem. Phys.* **2012**, *14*, 8964–8973.

(335) Mosquera, M.; Penedo, J. C.; Ríos Rodríguez, M. C.; Rodríguez-Prieto, F. *J. Phys. Chem.* **1996**, *100*, 5398–5407.

(336) Strandjord, A. J. G.; Smith, D. E.; Barbara, P. F. *J. Phys. Chem.* **1985**, *89*, 2362–2366.

(337) Cohen, B.; Álvarez, C. M.; Carmona, N. A.; Organero, J. A.; Douhal, A. *J. Phys. Chem. B* **2011**, *115*, 7637–7647.

(338) Erez, Y.; Gepshtein, R.; Presiado, I.; Trujillo, K.; Kallio, K.; Remington, S. J.; Huppert, D. *J. Phys. Chem. B* **2011**, *115*, 11776–11785.

(339) Steadman, J.; Syage, J. A. *J. Chem. Phys.* **1990**, *92*, 4630–4632.

(340) Syage, J. A.; Steadman, J. *J. Chem. Phys.* **1991**, *95*, 2497–2510.

(341) Syage, J. A. *J. Phys. Chem.* **1993**, *97*, 12523–12529.

(342) Kaneko, S.; Yotoriyama, S.; Koda, H.; Tobita, S. *J. Phys. Chem. A* **2009**, *113*, 3021–3028.

(343) Pines, E. In *The Chemistry of Phenols*; Rappoport, Z., Ed.; John Wiley and Sons, Ltd: West Sussex, 2003.

(344) Martynov, I. Y.; Demyashkevich, A. B.; Uzhinov, B. M.; Kuz'min, M. G. *Russ. Chem. Rev.* **1977**, *46*, 3–31.

(345) Jankowski, A.; Stefanowicz, P.; Dobryszycki, P. *J. Photochem. Photobiol. A* **1992**, *69*, 57–66.

(346) Tolbert, L. M.; Haubrich, J. E. *J. Am. Chem. Soc.* **1990**, *112*, 8163–8165.

(347) Tolbert, L. M.; Haubrich, J. E. *J. Am. Chem. Soc.* **1994**, *116*, 10593–10600.

(348) Kim, S. K.; Breen, J. J.; Willberg, D. M.; Peng, L. W.; Heikal, A.; Syage, J. A.; Zewail, A. H. *J. Phys. Chem.* **1995**, *99*, 7421–7435.

(349) Huppert, D.; Tolbert, L. M.; Linares-Samaniego, S. *J. Phys. Chem. A* **1997**, *101*, 4602–4605.

(350) Solntsev, K. M.; Huppert, D.; Tolbert, L. M.; Agmon, N. *J. Am. Chem. Soc.* **1998**, *120*, 7981–7982.

(351) Knochenmuss, R.; Solntsev, K. M.; Tolbert, L. M. *J. Phys. Chem. A* **2001**, *105*, 6393–6401.

(352) Clower, C.; Solntsev, K. M.; Kowalik, J.; Tolbert, L. M.; Huppert, D. *J. Phys. Chem. A* **2002**, *106*, 3114–3122.

(353) Tolbert, L. M.; Solntsev, K. M. *Acc. Chem. Res.* **2002**, *35*, 19–27.

(354) De Vleeschouwer, F.; Yang, W.; Beratan, D. N.; Geerlings, P.; De Proft, F. *Phys. Chem. Chem. Phys.* **2012**, *14*, 16002–16013.

(355) Prémont-Schwarz, M.; Barak, T.; Pines, D.; Nibbering, E. T. J.; Pines, E. *J. Phys. Chem. B* **2013**, *117*, 4594–4603.

(356) Solntsev, K. M.; Huppert, D.; Agmon, N. *J. Phys. Chem. A* **1999**, *103*, 6984–6997.

(357) Carmeli, I.; Huppert, D.; Tolbert, L. M.; Haubrich, J. E. *Chem. Phys. Lett.* **1996**, *260*, 109–114.

(358) Cohen, B.; Segal, J.; Huppert, D. *J. Phys. Chem. A* **2002**, *106*, 7462–7467.

(359) Solntsev, K. M.; Tolbert, L. M.; Cohen, B.; Huppert, D.; Hayashi, Y.; Feldman, Y. *J. Am. Chem. Soc.* **2002**, *124*, 9046–9047.

(360) Agmon, N. *J. Phys. Chem. A* **2005**, *109*, 13–35.

(361) Pines, D; Nibbering, E. T. J.; Pines, E. *J. Phys.: Condens. Matter* **2007**, *19*, 065134.

(362) Rini, M.; Magnes, B.-Z.; Pines, E.; Nibbering, E. T. J. *Science* **2003**, *301*, 349–352.

(363) Mohammed, O. F.; Pines, D.; Dreyer, J.; Pines, E.; Nibbering, E. T. J. *Science* **2005**, *310*, 83–86.

(364) Tran-Thi, T.-H.; Gustavsson, T.; Prayer, C.; Pommeret, S.; Hynes, J. T. *Chem. Phys. Lett.* **2000**, *329*, 421–430.

(365) Spry, D. B.; Fayer, M. D. *J. Chem. Phys.* **2008**, *128* Art. 084508.

(366) Siwick, B. J.; Cox, M. J.; Bakker, H. J. *J. Phys. Chem. B* **2008**, *112*, 378–389.

(367) Mohammed, O. F.; Pines, D.; Nibbering, E. T. J.; Pines, E. *Angew. Chem. Int. Ed.* **2007**, *46*, 1458–1461.

(368) Mondal, S. K.; Sahu, K.; Sen, P.; Roy, D.; Ghosh, S.; Bhattacharyya, K. *Chem. Phys. Lett.* **2005**, *412*, 228–234.

(369) Mandal, P. K.; Samanta, A. *J. Phys. Chem. A* **2003**, *107*, 6334–6339.

(370) Bhattacharya, B.; Samanta, A. *J. Phys. Chem. B* **2008**, *112*, 10101–10106.

(371) Lustres, J. L. P.; Kovalenko, S. A.; Mosquera, M.; Senyushkina, T.; Flasche, W.; Ernsting, N. P. *Angew. Chem. Int. Ed.* **2005**, *44*, 5635–5639.

(372)   Pérez-Lustres, J. L.; Rodriguez-Prieto, F.; Mosquera, M.; Senyushkina, T. A.; Ernsting, N. P.; Kovalenko, S. A. *J. Am. Chem. Soc.* **2007**, *129*, 5408–5418.

(373)   Zhujun, Z.; Seitz, W. R. *Anal. Chim. Acta* **1984**, *160*, 47–55.

(374)   Tran-Thi, T.-H.; Prayer, C.; Millié, P.; Uznanski, P.; Hynes, J. T. *J. Phys. Chem. A* **2002**, *106*, 2244–2255.

(375)   Schulman, S. G.; Chen, S.; Bai, F.; Leiner, M. J. P.; Weis, L.; Wolfbeis, O. S. *Anal. Chim. Acta* **1995**, *304*, 165–170.

(376)   Spry, D. B.; Goun, A.; Fayer, M. D. *J. Phys. Chem. A* **2007**, *111*, 230–237.

(377)   Mondal, S. K.; Ghosh, S.; Sahu, K.; Sen, P.; Bhattacharyya, K. *J. Chem. Sci.* **2007**, *119*, 71–76.

(378)   Spry, D. B.; Goun, A.; Bell, C. B.; Fayer, M. D. *J. Chem. Phys.* **2006**, *125* Art. 144514.

(379)   Spry, D. B.; Fayer, M. D. *J. Phys. Chem. B* **2009**, *113*, 10210–10221.

(380)   Leiderman, P.; Gepshtein, R.; Uritski, A.; Genosar, L.; Huppert, D. *J. Phys. Chem. A* **2006**, *110*, 9039–9050.

(381)   Wolfbeis, O. S.; Fürlinger, E.; Kroneis, H.; Marsoner, H. *Fresen. Z. Anal. Chem.* **1983**, *314*, 119–124.

(382)   Agmon, N.; Pines, E.; Huppert, D. *J. Chem. Phys.* **1988**, *88*, 5631–5638.

(383)   Simkovitch, R.; Kisin-Finfer, E.; Shomer, S.; Gepshtein, R.; Shabat, D.; Huppert, D. *J. Photochem. Photobiol. A* **2013**, *254*, 45–53.

(384)   Han, J.; Burgess, K. *Chem. Rev.* **2010**, *110*, 2709–2728.

(385)   Plasser, F.; Thomitzni, B.; Bäppler, S. A.; Wenzel, J.; Rehn, D. R.; Wormit, M.; Dreuw, A. *J. Comput. Chem.* **2015**, *36*, 1609–1620.

(386)   Bäppler, S. A.; Plasser, F.; Wormit, M.; Dreuw, A. *Phys. Rev. A* **2014**, *90*, 052521.

(387)   Mewes, S. A.; Plasser, F.; Dreuw, A. *J. Chem. Phys.* **2015**, *143* Art. 171101.

Eidesstattliche Versicherung gemäß §8 der Promotionsordnung der Naturwissenschaftlich-Mathematischen Gesamtfakultät der Universität Heidelberg

1. Bei der eingereichten Dissertation zu dem Thema
   "Quantum Chemical Study of Excited State Proton Transfer in Solvated Organic Molecules"
   handelt es sich um meine eigenständig erbrachte Leistung.

2. Ich habe nur die angegebenen Quellen und Hilfsmittel benutzt und mich keiner unzulässigen Hilfe Dritter bedient. Insbesondere habe ich wörtlich oder sinngemäß aus anderen Werken übernommene Inhalte als solche kenntlich gemacht.

3. Die Arbeit oder Teile davon habe ich bislang nicht an einer Hochschule des In- oder Auslands als Bestandteil einer Prüfungs- oder Qualifikationsleistung vorgelegt.

4. Die Richtigkeit der vorstehenden Erklärungen bestätige ich.

5. Die Bedeutung der eidesstattlichen Versicherung und die strafrechtlichen Folgen einer unrichtigen oder unvollständigen eidesstattlichen Versicherung sind mir bekannt.

Ich versichere an Eides statt, dass ich nach bestem Wissen die reine Wahrheit erklärt und nichts verschwiegen habe.

Ort/Datum   Unterschrift